Size-dependent Vibration, Response and Stability Analyses of Microplates under Localized Mechanical and Thermal Loads

Thesis submitted to

Birla Institute of Technology and Science, Pilani

for the award of the degree

of

Doctor of Philosophy

by

Varun Jain

Under the guidance of

Dr. Rajesh Kumar

DEPARTMENT OF CIVIL ENGINEERING
BIRLA INSTITUTE OF TECHNOLOGY AND SCIENCE, PILANI-333031
(RAJASTHAN) INDIA
April 2024

© 2024, Varun Jain. All rights reserved.

DEDICATION

To my beloved grandfather, who instilled in me a passion for learning and motivated me towards this remarkable journey of pursuing a Ph.D. Your wisdom and encouragement continue to inspire me every day.

To my dearest parents, whose unwavering love, support, and sacrifices have been the cornerstone of my educational journey. Your belief in me has been my greatest motivation.

And to my dedicated supervisor, Dr. Rajesh Kumar, whose guidance, patience, and expertise have been invaluable throughout this research journey. Your mentorship has shaped not only this thesis but also my growth as a scholar.

This thesis is dedicated to you and all those who have been my pillars of strength and inspiration. Your love, wisdom, and guidance have made this achievement possible.

DECLARATION

I certify that

1. The work contained in this thesis is original and has been done by me under the guidance of my supervisor.
2. The work has not been submitted to any other institute for any degree or diploma.
3. I have followed the guidelines provided by the institute in preparing the thesis.
4. I have confirmed to the norms and guidelines given in the ethical code of conduct of the Institute.
5. Whenever I have quoted written materials from the other sources, I have put them under quotation marks and given due credit to the sources by citing them and giving required details in the references.

Varun Jain

BIRLA INSTITUTE OF TECHNOLOGY AND SCIENCE, PILANI

CERTIFICATE

This is to certify that the thesis titled **“Size-dependent Vibration, Response and Stability Analyses of Microplates under Localized Mechanical and Thermal Loads”** submitted by **Varun Jain ID** No **2020PHXF0409P** for award of Ph.D. of the Institute embodies original work done by him under my supervision.

Signature of the Supervisor:
Name in capital letters: Dr. RAJESH KUMAR
Designation: Assistant Professor

Date:

Acknowledgement

This thesis represents the culmination of three years of dedicated work (2021-2023) undertaken at Birla Institute of Technology and Science, Pilani. I am immensely grateful to numerous individuals whose unwavering support and encouragement have been instrumental in the successful completion of this Ph.D. journey.

First and foremost, I extend my deepest and most sincere gratitude to my supervisor, Dr. Rajesh Kumar, whose continuous guidance, motivation, encouragement, and affection have been the guiding lights throughout my research tenure at BITS Pilani. His tireless efforts, profound insights, and the time he dedicated to this thesis are truly commendable, and it is through his invaluable contributions that this thesis has achieved its substance and readability.

I wish to express my heartfelt thanks to Prof. S. N. Patel and Dr. Gaurav Watts, esteemed members of the Doctoral Advisory Committee (DAC), for their invaluable suggestions and constructive feedback at every juncture of this research. Their expertise has been indispensable in shaping the course of this work. Special gratitude is owed to the Head of the Department (HOD) of Civil Engineering, Prof. Anupam Singhal, Dr. Nishant Roy, and Dr. Md. Rushdie Ibne Islam for their valuable insights and unwavering support.

I would like to acknowledge my seniors, Dr. Vishal Singh, Dr. Amit Yadav, Dr. Farhan Mohammad Khan, Mr. Danish Fayaz, and Mr. Anuj Adhikari for their invaluable mentorship. My heartfelt thanks also go out to my colleagues, Mr. Ankit Kumar, Mr. Rakesh Kumar V.G., Mr. Kathir Vadivel, Mr. Harishwar, Mr. Hrishikesh, Mr. Akash Samadhiya, Mr. Anant Mishra, and Mr. Gulshan Yadav, who have made my time at BITS Pilani truly memorable through their support and camaraderie.

I extend my deepest gratitude to God, my parents, my grandfather, my younger brother Devyash, and all other friends and family members who have consistently provided love, inspiration, support, and unwavering encouragement. Words alone cannot convey the depth of my appreciation for my family, who have made numerous sacrifices to enable my academic pursuits and without whom this research endeavour would not have been possible.

VARUN JAIN

Address:

Varun Jain,
1/185/A-8, Parinay Kunj Extension,
Delhi Gate, Agra,
Pin: 282002
Uttar Pradesh, India
Email: varunjain0061@gmail.com

Date of Birth: 23rd July, 1995

Education Qualification:

- **Master of Engineering (M.E)**

  Department of Civil Engineering
  Birla Institute of Technology and Science Pilani, Pilani Campus, Rajasthan
  Year: 2019

- **Bachelor of Technology (B. Tech)**

  Department of Civil Engineering
  Vellore Institute of Technology, Vellore, Tamil Nadu
  Year: 2017

List of publications during PhD.

Referred Journals

1. Jain, Varun, Rajesh Kumar, and Amit Yadav. 2023. "Size-Dependent Nonlinear Vibration and Instability of a Damped Microplate Subjected to In-Plane Parametric Excitation." *Thin-Walled Structures* 184: 110476.
2. Jain, Varun, and Rajesh Kumar. 2023. "Geometrically Nonlinear Dynamic Analysis of a Damped Porous Microplate Resting on Elastic Foundations under Transverse Patch Loadings." *Mechanics of Advanced Materials and Structure*. DOI: 10.1080/15376494.2023.2216273
3. Jain, Varun, Rajesh Kumar, S. N. Patel, and Tanish Dey. 2023. "Geometrically Nonlinear Dynamic Analysis of a Damped Porous Microplate Resting on Elastic Foundations under In-Plane Nonuniform Excitation." *Mechanics Based Design of Structures and Machines*. DOI: 10.1080/15397734.2023.2232845
4. Jain, Varun, Rajesh Kumar, Gaurav Watts, Md. Rushdie Ibne Islam, and Vishal Singh. 2023."Size-Dependent Nonlinear Free and Forced Vibration Analyses of a Functionally Graded Microplate Subjected to Transverse Patch Loading." *Journal of Engineering Mechanics* 149 (10): 04023082.

Conferences

1. Jain, Varun, and Rajesh Kumar. 2023 Size-Dependent Nonlinear Dynamic behaviour of a Damped Microplate under Nonuniform Excitation. International Conference on Nanotechnology for Better Living (ICNBL-2023), 25-29, May 2023, National Institute of Technology, Srinagar and IIT (BHU) Varanasi.

Articles under Review

1. Jain, Varun, Rajesh Kumar, Tanish Dey, S. N. Patel, and Gaurav Watts. 2023. "A Meshfree Formulation for Size-dependent Buckling and Post-Buckling Behaviour of Porous Microplates on Elastic Foundation under Localized Heating" *International Journal of Solids and Structures*.

This thesis presents a comprehensive study of size-dependent vibration, response and stability analyses of microplates using size-dependent continuum mechanics. In this study, the detailed investigation of free vibration, buckling, dynamic instability, nonlinear free and forced vibrations, nonlinear dynamic response and post-buckling of microplates are performed. The various types of loadings such as non-uniform in-plane mechanical loads, transverse patch loads and localized thermal loads, are considered in the present investigation. The size-dependent effects are included using the modified strain gradient theory (MSGT) and the field displacement equations are modelled using the third order shear deformation theory (TSDT) pertaining the von-Kármán nonlinearity. The investigation encompasses modelling of microplates with a range of material properties, including isotropic materials, functionally graded (FG) materials, and porous materials. The resting medium of the microplates is modelled using the Winkler-Pasternak elastic foundations. The impact of viscous damping on these microplates is also included in the investigation.

The analytical expressions for in-plane pre-buckling stresses within the plate due to non-uniform in-plane mechanical loadings / localized thermal loadings are obtained by solving the in-plane stress equilibrium equation in terms of the Airy's stress function (Φ). The governing partial differential equations (PDEs) of the microplate are derived using the Hamilton's principle for dynamic problem and the principle of minimization of total potential energy for the static problem. The PDEs are reduced to approximate closed-form ordinary differential equations (ODEs) for dynamic problem and algebraic equations for static problem using the Galerkin's weighted residual method. The mechanical/thermal buckling load and natural frequencies are calculated by solving the eigenvalue problem of these equations. The dynamic instability regions are plotted using the Bolotin's method. The nonlinear free and forced vibrations behaviour are presented using the frequency-amplitude curves which are obtained using the incremental harmonic balance (IHB) method in conjunction with the pseudo arc-length continuation technique. The post-buckling equilibrium path is obtained using the modified Newton-Raphson method and the nonlinear dynamic response is presented using the time history plots which are obtained using the implicit Newmark-β time integration technique. The validity of the developed semi-analytical methodology is established by comparison of the simpler version of the methodology used in this thesis with prior studies.

An understanding of the impact of the various parameters on microplate behaviour such as mechanical/thermal buckling load, natural frequencies, dynamic instability regions, frequency-amplitude curves, nonlinear dynamic responses, and post-buckling behaviour is attained through extensive parametric analysis. The influence of various parameters such as size-dependent theories, porosity coefficients and distributions, elastic foundation properties, plate dimensions, boundary conditions, and loading parameters on microplate's behaviours is examined. The effect of aspect ratios, boundary conditions and elastic foundation parameters on the mode shape of the plate at the critical buckling load under in-plane mechanical/ thermal loading is also assessed. The influence of initial perturbations on the steady-state response under transverse periodic loading / in-plane periodic loading is explored using time history plots. The findings of this research provide a better understanding of the behaviour of microplates and can be used to improve the design guidelines for microplates and develop further advanced methodologies for the analyses of microplates.

Table of Contents

Title **Page No.**

Dedication iii
Declaration v
Certificate vii
Acknowledgement ix
Curriculum Vitae xi
Abstract xiii
Table of Content xv
List of Figures xxi
List of Tables xxix
List of Symbols xxx

Content

Chapter 1 Introduction 1

1.1 Preamble 1
1.2 Motivations 6
1.3 Aim of the Study 7
1.4 Contribution of the Study 7
1.5 Organization of the Thesis 8

Chapter 2 Literature Review 11

2.1 Introduction 11
2.2 Size-Dependent Continuum Theories 12
    2.2.1 Couple Stress Theories 12
    2.2.2 Strain Gradient Theories 13
    2.2.3 Material Length Scale Parameters 14
    Critical Discussion 14
2.3 Plate Theories 15

2.3.1 Classical Plate Theory 15

2.3.2 First Order Shear Deformation Theory 16

2.3.3 Higher Order Shear Deformation Theory 16

2.3.4 Plate Theories with Nonlinearity 17

Critical Discussion 18

2.4 Solution Methodologies for Governing Equations 19

Critical Discussion 21

2.5 Microplate Material Types 21

2.5.1 Isotropic Microplates 22

2.5.2 Functionally Graded Microplates 22

2.5.3 Porous Microplates 23

2.6 Static Analysis of Microplates 24

2.6.1 Linear Analysis 24

2.6.1.1 Bending 24

2.6.1.2 Buckling 26

2.6.2 Nonlinear Analysis 29

2.6.2.1 Nonlinear Bending 29

2.6.2.2 Post-Buckling 30

2.7 Dynamic Analysis of Microplates 32

2.7.1 Linear Analysis 32

2.7.1.1 Free Vibration 33

2.7.1.2 Dynamic Instability 34

2.7.2 Nonlinear Analysis 35

2.7.2.1 Nonlinear Free Vibration 36

2.7.2.2 Nonlinear Forced Vibration 37

2.7.2.3 Nonlinear Dynamic Response 39

Critical Discussion 40

2.8 Non-Uniform Loading 41

2.9 Research Gaps 41

2.10 Objectives 42

Chapter 3 **Mathematical Formulation** **43**

3.1 Introduction 43

3.2 Material Properties of Microplate 44

3.3 Strain Energy Density Function 48

  3.3.1 Classical Continuum Theory (CCT) 48

  3.3.2 Modified Couple Stress Theory (MCST) 48

  3.3.3 Modified Strain Gradient Theory (MSGT) 49

3.4 Kinematics of Microplate 50

  3.4.1 Field Displacement Equations 50

  3.4.2 Strain-Displacement Equations 51

3.5 Types of Loading 51

  3.5.1 Non-Uniform In-plane Loading 52

  3.5.2 Transverse Patch Loading 54

  3.5.3 Localized Thermal Loading 58

3.6 Estimation of Governing Partial Differential Equations of Motion 59

  3.6.1 Expressions of First Variation of Energy Functions 60

    3.6.1.1 First Variation of Strain Energy 60

    3.6.1.2 First Variation of Strain Energy due to Foundation 73

    3.6.1.3 First Variation of Geometric Strain Energy 73

    3.6.1.4 First Variation of External Work Done 74

    3.6.1.5 First Variation of Damping Energy 74

    3.6.1.6 First Variation of Kinetic Energy 74

  3.6.2 Partial Differential Equations of Motion 75

3.7 Boundary Conditions of Microplate 76

3.8 Analytical Expressions for In-plane Pre-buckling Stresses 78

  3.8.1 Pre-buckling Stresses due to Localized Thermal Loading 78

  3.8.2 Pre-buckling Stresses due to Non-uniform In-plane Mechanical Loading 82

3.9 Methodology for Solving Partial Differential Equations 84

  3.9.1 Basis functions for displacement fields 85

  3.9.2 Governing Ordinary Differential Equations 87

3.10 Rayleigh's Damping Matrix 88

3.11 Solution Methodologies for Various Analyses 88

3.11.1 Free Vibration and Buckling 88

3.11.2 Dynamic Instability 88

3.11.3 Nonlinear Vibration 89

3.11.4 Nonlinear Dynamic Response 92

3.11.5 Post-buckling Response 93

Chapter 4 Nonlinear Vibration and Dynamic Instability of Microplate under In-Plane Mechanical Loading: Results and Discussion 95

4.1 Introduction 95

4.2 Validation Study 95

4.3 Convergence Study 99

4.4 Effect of Different Theories on Buckling Load and Frequency 100

4.5 Non-Linear Vibration and Dynamic Instability Region 102

4.5.1 Effect of Different Strain Gradient Theories 105

4.5.2 Effect of Damping Coefficient 106

4.5.3 Effect of Preloading 107

4.5.4 Effect of Boundary Conditions 108

4.5.5 Effect of Different Loading Conditions 110

Chapter 5 Nonlinear Vibration and Dynamic Response of Microplate under In-plane Mechanical Loading: Results and Discussion 113

5.1 Introduction 113

5.2 Validation Study 113

5.3 Parametric Study of Buckling Mode Shape 117

5.4 Convergence Study 119

5.5 Nonlinear Dynamic Analysis Results 120

5.5.1 Porosity Coefficient 121

5.5.2 Type of Porosity 123

5.5.3 Elastic Foundation 124

5.5.4 Theory 125

5.5.5 Length to Thickness ratio (*a/h*) of the Plate 127

5.5.6 Size of the Plate (*h/l* ratio) 128

5.5.7 Load Concentration 129

5.5.8 Load Profile 130

5.5.9 Damping 131

Chapter 6 Nonlinear Dynamic Analyses of Microplate under Transverse Loading: Results and Discussion 133

6.1 Introduction 133
6.2 Validation and Convergence study 133
6.3 Nonlinear Free and Forced Vibration of FG Microplate 136
  6.3.1 Non-Linear Free Vibration Analysis 137
    6.3.1.1 Effect of power-law index 137
    6.3.1.2 Effect of change in *h/l* ratios 138
  6.3.2 Nonlinear Forced Vibration Analysis 138
    6.3.2.1 Effect of change in length to thickness ratio (*a/h*) 139
    6.3.2.2 Effect of change in modal damping ratios 140
    6.3.2.3 Effect of different boundary conditions 141
    6.3.2.4 Effect of different patch loading positions 142
    6.3.2.5 Effect of different loading concentrations 142
6.4 Nonlinear Dynamic Analyses of PMREF 143
  6.4.1 Effect of Porosity coefficient 145
  6.4.2 Effect of Type of Porosity 146
  6.4.3 Effect of Elastic Foundation Parameters 148
  6.4.4 Effect of Size-Dependent Theory 149
  6.4.5 Load Concentration 150
  6.4.6 Effect of Load Position 151
  6.4.7 Effect of Damping 153

Chapter 7 Thermal Buckling and Post-buckling analyses of Microplate: Results and Discussion 155

7.1 Introduction 155
7.2 Validation and Convergence study 156
7.3 Parametric Analysis 161
7.3.1 Mode Shape Behaviour 161
7.3.2 Buckling Temperature 164
7.3.3 Thermal Post-buckling Response 168

Chapter 8 Conclusions 173

8.1 Introduction 173
8.2 Findings of this Study 174
    8.2.1 Nonlinear Vibration and Dynamic Instability of Microplate under In-Plane Mechanical Loading 176
    8.2.2 Nonlinear Vibration and Dynamic Response of Microplate under In-plane Mechanical Loading 177
    8.2.3 Nonlinear Dynamic Analyses of Microplate under Transverse Loading 178
    8.2.4 Thermal Buckling and Post-buckling analyses of Microplate 179
8.3 Impact of this Study 180
8.4 Strengths of this Study 180
8.5 Limitations of this Study 181
8.6 Future Scope 182

References 183
Biography of Supervisor 199
Biography of Student 201

List of Figures

Figure No.	Description	Page No.
1.1	Size chart depicting scale of things in meters	1
1.2	Applications of micromachined devices in various fields	2
1.3	Schematic representation of accumulation of GNDs at grain boundaries along critical slip plane	4
1.4	Comparison of frequency-amplitude graph of microplates with and without nonlinearity under (a) simple harmonic resonance and (b) parametric resonance	5
3.1	Schematic representation of (a) isotropic microplate subjected to non-uniform in-plane loading	44
3.2	Schematic representation of functionally graded microplate subjected to transverse patch loading	45
3.3	Schematic representation of a porous microplate resting on elastic foundation (PMREF), subjected to (a) non-uniform in-plane loading, (b) transverse patch loading, and, (c) localized heating	46
3.4	Sectional view of the microplate with different types of porosity distributions	47
3.5	Different cases of in-plane harmonic loading profiles on two opposite edges of the microplate (a) uniform loading profile (b) parabolic loading profile (c) partial loading profile	52
3.6	Generalized case of transverse patch loadings	55
3.7	Different positions of transverse patch loadings on the microplate: (a) centre loading, (b) edge loading, and (c) corner loading	58
4.1	Comparison of in-plane longitudinal stress distribution on simply supported isotropic square microplate (b/h=20; a/b=1) using Airy's stress approach and Finite Element (FE) method along (a) $x/a = 0.5$ (b) $x/a = 0.25$ and (c) $x/a = 0$	97
4.2	Comparison of in-plane longitudinal, transverse, and shear stress contours on simply supported isotropic square microplate (b/h=20; a/b=1) obtained using Airy's stress approach and Finite Element (FE) method	98

4.3 Validation study and convergence analysis of free vibration response of a microplate considering the different number of constant terms corresponding to displacement fields 99

4.4 Convergence analysis of nonlinear vibration response of a damped microplate (β=0.2) considering the different number of constant terms corresponding to displacement fields 100

4.5 Comparison of size-effect on (a)buckling load ratio, k_{Ncr} [$Ncr/(h/l)$] and (b) frequency ratio, k_{freq} [$freq/(h/l)$] for MSGT, MCST, and the CCT 101

4.6 (a) Principal instability zone, and (b) non-linear vibration response at β=0.3 for a damped epoxy microplate (a/h=20; h/l=2; ζ_1=4% & ζ_2=2%; MSGT; SSSS) 102

4.7 (a) principal instability zone, (b) width of dynamic instability region, (c) non-linear vibration response, and (d) width of dynamic instability region considering non-linearities at β=0.2 for a damped (ζ_1=4% and ζ_2=2%) and an undamped isotropic epoxy microplate (a/h=100; h/l=1; MSGT; SSSS) 103

4.8 Effect of different strain gradient theories on (a) principal instability zone, (b) width of dynamic instability region, (c) non-linear vibration response, and (d) width of dynamic instability region considering non-linearities at $\beta=0.6$ for a damped isotropic epoxy microplate (a/h=100; h/l=2; ζ_1=3% & ζ_2=1.5%; SSSS) 105

4.9 Effect of damping factor on (a) principal instability zone, (b) width of dynamic instability region, (c) non-linear vibration response, and (d) width of dynamic instability region considering non-linearities at β=0.2 for an isotropic epoxy microplate (a/h=100; h/l=1; MSGT; SSSS). 106

4.10 Effect of preloading on (a) principal instability zone, and (b) width of dynamic instability region for an isotropic epoxy microplate (a/h=100; h/l=1; ζ_1=3% & ζ_2=1.5%; MSGT; SSSS) 107

4.11 Width of dynamic instability region at β=0.2 vs static load factor for different modal damping ratios for an isotropic epoxy microplate (a/h=100; h/l=1; ζ_1=3% & ζ_2=1.5%; MSGT; SSSS) 108

4.12 Effect of boundary conditions on (a) principal instability zone, (b) width of dynamic instability region, (c) non-linear vibration response, and (d) width of dynamic instability region considering non-linearities at β=0.5 for an isotropic epoxy microplate (a/h=100; h/l=1; ζ_1=3% & ζ_2=1.5%; MSGT) 109

4.13 Effect of different loading conditions on (a) principal instability zone, (b) width of dynamic instability region, (c) non-linear vibration 110 response, and (d) width of dynamic instability region considering non-linearities at β=0.6 for an isotropic epoxy microplate (a/h=100; h/l=1; ζ_1=3% & ζ_2=1.5%; MSGT; SSSS)

5.1 In-plane pre-buckling normal and shear stresses contours computed using Airy’s stress method and ABAQUS for simply supported isotropic square plate (b/h=10; a/b=1) 116

5.2 Mode Shape at buckling load for PMREF (e_0=0.2; Symmetric Porosity; $\overline{K_w} = 10$, $\overline{K_p} = 10$; Partial load (d=0.5b); a/h=10; h/l=2; MSGT; SSSS) with different aspect ratios, (a) a/b=1, (b) a/b=2, (c) a/b=4, (d) a/b=6 118

5.3 Variation of critical buckling load for different mode shapes on varying the Winkler and Pasternak elastic foundation parameters for a PMREF (e_0=0.2; symmetric porosity; partial load (d=0.5b); a/h=10; a/b=1; h/l=2; MSGT; SSSS) 118

5.4 Convergence study of a damped PMREF's (β =0.6) nonlinear forced vibration response taking into account the various number of terms corresponding to each displacement field 119

5.5 Non-linear vibration response using frequency-amplitude curve at β=0.6 for a damped PMREF (e_0=0.2; symmetric porosity; $\overline{K_w} = 10$, $\overline{K_p} = 10$; partial load (d=0.5b); a/h=10; h/l=2; ζ_1=4% & ζ_2=2% ; MSGT; SSSS) 120

5.6 Effect of Porosity coefficient on (a) nonlinear vibration response and (b) nonlinear dynamic response (p/ω=2 and w_0=0.2h), at β=0.6 for a damped PMREF (symmetric porosity; $\overline{K_w} = 10, \overline{K_p} = 10$; partial load ($d$=0.5$b$); a/h=10; h/l=2; ζ_1=4% & ζ_2=2%; MSGT; SSSS) 122

5.7 Effect of type of porosity on (a) nonlinear vibration response, and (b) nonlinear dynamic response (p/ω=2.4 and w_0=1.2h), at β=0.6 for a damped PMREF ($\overline{K_w} = 10$, $\overline{K_p} = 10$; partial load (d=0.5b); a/h=10; h/l=2; ζ_1=4% & ζ_2=2%; MSGT; SSSS). 123

5.8 Effect of Winkler-Pasternak elastic foundation parameters on (a)nonlinear vibration response, and (b)nonlinear dynamic response (p/ω=1.5 and w_0=0.2h), at β=0.6 for a damped PMREF (e_0=0.2; 125

symmetric porosity; partial load (d=0.5b); a/h=10; h/l=2; ζ_1=4% & ζ_2=2%; MSGT; SSSS).

5.9 Impact of various small-scale theories on (a) nonlinear vibration response, and (b) nonlinear dynamic response (p/ω=3.5 and w_0=1.6h), at β=0.7 for a damped PMREF (e_0=0.2; symmetric porosity; $\overline{K_w} = 10$, $\overline{K_p} = 10$; partial load (d=0.5b); a/h=10; h/l=2; ζ_1=4% & ζ_2=2%; SSSS). 126

5.10 Effect of length to thickness ratio (a/h) on (a) nonlinear vibration response, and (b) nonlinear dynamic response (p/ω=3.3 and w_0=1.6h), at β=0.7 for a damped PMREF (e_0=0.2; symmetric porosity; $\overline{K_w} = 10$, $\overline{K_p} = 10$; partial load (d=0.5b); a=600μm; h/l=2; ζ_1=4% & ζ_2=2%; MSGT; SSSS) 127

5.11 Effect of thickness to MLSP ratio (h/l) on (a) nonlinear vibration response and (b) nonlinear dynamic response (p/ω=2.2 and w_0=1.3h), at β=0.8 for a damped PMREF (e_0=0.2; symmetric porosity; $\overline{K_w} = 10$, $\overline{K_p} = 10$; partial load (d=0.5b); a/h=10; h=15μm; ζ_1=4% & ζ_2=2%; MSGT; SSSS) 128

5.12 Impact of load concentration on (a)nonlinear vibration response, and (b)nonlinear dynamic response (p/ω=3 and w_0=0.2h), at β=0.4 for a damped PMREF (e_0=0.2; Symmetric porosity; $\overline{K_w} = 10$, $\overline{K_p} = 10$; Partial load; a/h=10; h/l=2; ζ_1=4% & ζ_2=2%; MSGT; SSSS) 129

5.13 Impact of Loading Profile on (a) nonlinear vibration response, and (b) nonlinear dynamic response (p/ω=2 and w_0=1.5h), at β=0.4 for a damped PMREF (e_0=0.2; symmetric porosity; $\overline{K_w} = 10$, $\overline{K_p} = 10$; a/h=10; h/l=2; ζ_1=4% & ζ_2=2%; MSGT; SSSS) 130

5.14 Effect of modal damping ratios on (a) nonlinear vibration response, and (b) nonlinear dynamic response (p/ω=2.5 and w_0=1.5h), at β=0.3 for a damped PMREF (e_0=0.2; symmetric porosity; $\overline{K_w} = 10$, $\overline{K_p} = 10$; partial load(d=0.5b); a/h=10; h/l=2; MSGT; SSSS). 132

6.1 Effect of different power law indices on non-linear free vibration response of square FG microplate(a/h=10; h/l=2; ζ_1=4% & ζ_2=2% ; MSGT; SSSS; f_0 = 0) 138

6.2 Effect of h/l ratio on non-linear free vibration response of square FG microplate(n=1; a/h=10; h=17.6μm; ζ_1=4% & ζ_2=2% ; MSGT; SSSS; f_0 = 0) 138

6.3 Non-linear forced vibration response of a damped FG microplate(n=1; h/l=2; a/h=20; ζ_1=4% & ζ_2=2% ; MSGT; SSSS; f_0 = 2x10^7 N/m^2; loading case 1; a_l=0.5a; b_l = 0.5b) 139

6.4 Effect of length to thickness ratio (a/h) on non-linear free and forced vibration responses of square FG microplate(n=1; a=176μm; h/l=2; ζ_1=4% & ζ_2=2% ; MSGT; SSSS; f_0 = 1x10^7 N/m^2; loading case 4; a_l=0.5a; b_l = 0.5b) 140

6.5 Impact of varying modal damping ratios on non-linear free and forced vibration responses of square FG microplate (n=1; a/h=10; h/l=2; MSGT; SSSS; f_0 =5x10^8 N/m^2; loading case 2; a_l=0.5a; b_l = 0.5b) 140

6.6 Effect of different boundary conditions on non-linear free and forced vibration response of square FG microplate (n=1; a/h=10; h/l=2; MSGT; ζ_1=4% & ζ_2=2%; f_0 =2x10^8 N/m^2; loading case 1; a_l=0.5a; b_l = 0.5b) 141

6.7 Effect of different patch loading positions on non-linear free and forced vibration response of square FG microplate (n=1; a/h=10; h/l=2; MSGT; SCSC; ζ_1=4% & ζ_2=2%; f_0 =5x10^8 N/m^2; a_l=0.5a; b_l = 0.5b) 142

6.8 Effect of different patch loading concentrations on non-linear free and forced vibration response of square FG microplate (n=1; a/h=10; h/l=2; SSSS; MSGT; ζ_1=4% & ζ_2=2%; f_0 =1x10^8 N/m^2; loading case 1) 143

6.9 Non-linear vibration response using frequency-amplitude curve at β=0.6 for a damped PMREF (e_0=0.2; Symmetric Porosity; $\overline{K_w} = 10$, $\overline{K_p} = 10$; a/h=10; h/l=2; ζ_1=4% & ζ_2=2% ; MSGT; SSSS; f_0 = 2x10^8 N/m^2; Centre {(a_l,b_l)= 0.5(a,b)}) 145

6.10 Effect of Porosity coefficient on (a)Nonlinear vibration response, and (b)Nonlinear dynamic response ((ω_{NL}/ω_L) =2 and w_0=0), for a damped PMREF (symmetric porosity; $\overline{K_w} = 10$, $\overline{K_p} = 10$; a/h=10; 146

h/l=2; ζ_1=4% & ζ_2=2%; MSGT; SSSS; f_0 = 2x10^8 N/m^2; Centre {(a_l,b_l)= 0.5(a,b)})

6.11 Effect of type of porosity on (a)Nonlinear vibration response, and (b)Nonlinear dynamic response ((ω_{NL}/ω_L) =1.35 and w_0=1.35h), for a damped PMREF ($\overline{K_w} = 10$, $\overline{K_p} = 10$; *a/h*=10; *h/l*=2; ζ_1=4% & ζ_2=2%; MSGT; SSSS; f_0 = 2x10^8 N/m^2; Centre {(a_l,b_l)= 0.5(a,b)}) 147

6.12 Effect of Winkler-Pasternak elastic foundation parameters on (a)nonlinear vibration response, and (b)nonlinear dynamic response ((ω_{NL}/ω_L) =1.5 and w_0=0.5h), for a damped PMREF (e_0=0.2; Symmetric Porosity; *a/h*=10; *h/l*=2; ζ_1=4% & ζ_2=2%; MSGT; SSSS; f_0 = 2x10^8 N/m^2; Centre {(a_l,b_l)= 0.5(a,b)}) 148

6.13 Effect of different small-scale theories on (a)nonlinear vibration response, and (b)nonlinear dynamic response (ω_{NL}/ω_L =2 and w_0=0.2h), for a damped PMREF (e_0=0.2; symmetric porosity; $\overline{K_w} = 10$, $\overline{K_p} = 10$; *a/h*=10; *h/l*=2; ζ_1=4% & ζ_2=2%; SSSS; f_0 = 2x10^8 N/m^2; Centre {(a_l,b_l)= 0.5(a,b)}) 149

6.14 Effect of Concentration of load on (a)nonlinear vibration response, and (b)nonlinear dynamic response (ω_{NL}/ω_L=0.5 and w_0=h), for a damped PMREF (e_0=0.2; symmetric porosity; $\overline{K_w} = 10$, $\overline{K_p} = 10$; *a/h*=10; *h/l*=2; ζ_1=4% & ζ_2=2%; MSGT; SSSS; f_0 = 5x10^8 N/m^2; Centre) 151

6.15 Impact of Loading Profile on (a)nonlinear vibration response, and (b)nonlinear dynamic response (ω_{NL}/ω_L=2.3 and w_0=0), for a damped PMREF (e_0=0.2; Symmetric Porosity; $\overline{K_w} = 10$, $\overline{K_p} = 10$; *a/h*=10; *h/l*=2; ζ_1=4% & ζ_2=2%; MSGT; SSSS; f_0 = 5x10^8 N/m^2; {(a_l,b_l)= 0.5(a,b)}). 152

6.16 Effect of modal damping ratios on (a)nonlinear vibration response, and (b)nonlinear dynamic response (ω_{NL}/ω_L=1.5 and w_0=h), for a damped PMREF (e_0=0.2; symmetric porosity; $\overline{K_w} = 10$, $\overline{K_p} = 10$; *a/h*=10; *h/l*=2; MSGT; SSSS; f_0 = 3x10^8 N/m^2; Centre {(a_l,b_l)= 0.5(a,b)}) 153

7.1 Comparison of in-plane pre-buckling normalized (a) normal stress $\bar{\sigma}_{xx}$, (b) normal stress $\bar{\sigma}_{yy}$, and (c) shear stress $\bar{\sigma}_{xy}$ computed using the semi-analytical methodology (Airy's Stress Approach) used in this 157 study with numerical method (ABAQUS) for a simply supported macro plate $\left(\frac{a_0}{a} = 0.6; \mathrm{CCT}\right)$.

7.2 Convergence analysis of the PMREF's pre-buckling normalized stress $\bar{\sigma}_{xx}$ with different number of terms in the trigonometric series expressions used to model these stresses $\left(\frac{a_0}{a} = 0.7; \mathrm{SSSS}; \mathrm{MSGT}\right)$ 158

7.3 Contour plots for in-plane pre-buckling normalized (a) normal Stress $\bar{\sigma}_{xx}$, (b) normal Stress $\bar{\sigma}_{yy}$, and (c) shear Stress $\bar{\sigma}_{xy}$ for the PMREF used in this study$\left(\frac{a_0}{a} = 0.7; \mathrm{SSSS}; \mathrm{MSGT}\right)$ 159

7.4 Validation Study of the plate's post-buckling response methodology by comparison of post-buckling equilibrium path of a macro-plate $\left(\frac{a_0}{a} = 1; \mathrm{SSSS}; \mathrm{CCT}\right)$ with results of Prakash et al. (2008) 160

7.5 Convergence analysis of the PMREF's ($\frac{a_0}{a} = 0.6; \mathrm{SSSS}{:}\ \mathrm{MSGT}$) post-buckling response by considering varying count of terms in the basis function associated with each displacement field 161

7.6 Mode Shape at mechanical buckling load((a), (c), (e), and (g)) and thermal buckling load ((b), (d), (f), and (h)) for a SSSS type PMREF with different aspect ratios (MSGT) 162

7.7 Mode Shape at mechanical buckling load ((a), (c), (e), and (g)) and thermal buckling load ((b), (d), (f), and (h)) for an SSSS type PMREF with different aspect ratios (MSGT) 163

7.8 Modification in $\overline{\Delta T_{cr}}$ with change in porosity coefficient of a PMREF ($\frac{a_0}{a} = 0.6; \mathrm{SSSS}; \mathrm{MSGT}$) with different porosity distributions 165

7.9 Modification in nondimensional buckling temperature difference with change in loading concentration of a PMREF (MSGT) for various boundary conditions 165

7.10 Variation of $\overline{\Delta T_{cr}}$ with change in size (*h/l* ratio) of a PMREF (*h*=45μm; $\frac{a}{b} = 1$; $\frac{a_0}{a} = 0.6$; SSSS) modelled with different size-dependent theories 166

7.11 Variation of $\overline{\Delta T_{cr}}$ with change in aspect ratio (*a/b*) of PMREF ($\frac{a_0}{a} = \frac{b_0}{b} = 0.6$; SSSS; MSGT) with different boundary conditions 167

7.12 Modification in $\overline{\Delta T_{cr}}$ with change in length to thickness ratio (*a/h*) of PMREF (*a*=1350μm; *l* varies; *h* varies; $\frac{a_0}{a} = 0.6$; SSSS) with different aspect ratios. 167

7.13(a) Thermal post-buckling response of PMREF (*a*=1350μm; *l* varies; *h* varies; $\frac{a_0}{a} = 0.6$; SSSS) with different thickness (*a/h* ratios) 169

7.13(b) Thermal post-buckling response of a PMREF ($\frac{a_0}{a} = 0.6; \mathrm{SSSS}$). modelled with different size-dependent theories. 169

7.13(c) Thermal post-buckling response of PMREF (*h*=45μm; $\frac{a}{b} = 1$; $\frac{a_0}{a} = 0.6$; SSSS) with different size (*h/l* ratios). 170

7.13(d) Thermal post-buckling response of PMREF ($\frac{a_0}{a} = 0.6; \mathrm{SSSS}; \mathrm{MSGT}$). with different porosity coefficient and porosity distributions. 170

7.13(e) Thermal post-buckling response of PMREF ($\frac{a_0}{a} = 0.6; \mathrm{SSSS}; \mathrm{MSGT}$).with different Winkler and Pasternak elastic foundation parameters. 171

7.14 Thermal post-buckling response of PMREF ($\mathrm{SSSS}; \mathrm{MSGT}$).with different loading concentrations. 172

7.15 Thermal post-buckling response of PMREF ($\frac{a_0}{a} = 0.6; \mathrm{MSGT}$) with different boundary conditions. 172

List of Tables

Table No.	Description	Page No.
4.1	Comparison of frequency and critical buckling load of an SSSS square microplate with different *l/h* ratio	96
5.1	Comparison of dimensionless frequency of a simply supported square thick plate resting on an elastic foundation with different values of $\overline{K_w}$, $\overline{K_p}$ and *a/h* ratios	114
5.2	Validation study of dimensionless buckling load and dimensionless frequency of an SSSS square porous metal foam microplate on varying the *l/h* ratios	115
6.1	Comparison of frequency of an SSSS microplate with varying power-law index and *l*/*h* ratios	134
6.2	Comparison of non-dimensional linear deflection $\left(\frac{10Eh^3w_{lmax}}{f_0a^4}\right)$ of a SSSS microplate with 3D theory and 2D (FSDT) for different *a/h* and *l*/*h* ratios	135
6.3	Validation study of the dimensionless frequency of an SSSS square porous metal foam microplate on varying the *l/h* ratios	135
7.1	Properties of the plates used in this chapter	155
7.2	Comparison of non-dimensional buckling temperature difference $\overline{\Delta T_{cr}}$ obtained from finite element (FE) method and current semi-analytical methodology (Airy's stress approach) (SSSS; CCT)	156
7.3	Comparison of dimensionless buckling load for a SSSS square porous metal foam microplate subjected to uniaxial compressive mechanical loading with varying *l/h* ratios (MSGT)	158

List of Symbols

x-y-z	Cartesian Co-ordinate
a	Length of the plate
b	Breadth of the plate
h	Thickness of the plate
E	Effective Young's modulus
ρ	Effective mass density
v	Poisson's ratio
E_c, ρ_c	Material properties of ceramic
E_m, ρ_m	Material properties of metal
V_c, V_m	Volume fraction of ceramic and metal
n	Power index in power law function
K_w	Winkler elastic foundation parameter
K_p	Pasternak elastic foundation parameter
$\overline{K_w}$ and $\overline{K_p}$	Equivalent Winkler and Pasternak elastic foundation parameters
e_0	Porosity coefficient
e_r	Porosity density coefficient
E_{max}	Maximum value of $E(z)$
ρ_{max}	Maximum value of $\rho(z)$
κ	Function of thickness
ς	Function of porosity coefficient
U	Strain energy density function
σ_{ij}^{c}	Cauchy stress tensor
ε_{ij}	Cauchy strain tensor
r_{ij}	Symmetric couple stress tensor
χ_{ij}^{s}	Symmetric curvature tensor
ψ_i	Dilatation gradient tensor
L_i	Work conjugate of dilatation gradient tensor
$\eta_{ijk}^{(1)}$	deviatoric stretch gradient tensor
$\tau_{ijk}^{(1)}$	Work conjugate of deviatoric stretch gradient tensor

u, v, w	Displacements of a material point (x, y) which is at a distance 'z' away from the middle surface along x, y, z directions, respectively
θ_i	Rotation vector
l	Material length scale parameter
l_0, l_1, l_2	Material length scale parameters corresponding to the symmetric part of the rotation gradient, dilatation gradient, and deviatoric stretch gradient, respectively
δ_{ij}	Kronecker's delta
λ *and* μ	Lame's constants
u^0, v^0, w^0	Displacements of a point at the middle surface along x, y, z directions, respectively
φ_x, φ_y	Rotation of the mid-surface about the x-axis and y-axis, respectively
ϕ_x^0, ϕ_y^0	Rotation of any cross-section perpendicular to x and y axes, respectively
$\varepsilon_{xx}^0, \varepsilon_{yy}^0$ *and* γ_{xy}^0	The strains at the middle surface of the plate
N_{st}	Static load component
N_{dyn}	Dynamic load component
α	Static load factor
β	Dynamic load factor
d	Width of localized loading
$\overline{N}_0$	Magnitude of localized in-plane loading
$N(y)$	Function representing In-plane loading profile
$f(x)$	Generalized Transverse Patch loading function
f_0	Magnitude of Transverse patch loading
'a_l' and 'b_l'	Width of the transverse patch loading in the x and y direction respectively
x_c , y_c	Distance of geometric center of the transverse patch loading from origin
'a_0' and 'b_0'	Width of the localized thermal load in the x and y directions respectively
$\mathbf{N_T}$	Thermal force resultants matrix

$(N_T)_{xx}, (N_T)_{yy}, (N_T)_{xy}$	Thermal force resultants
$\mathbf{M_T}$	Thermal moment resultants matrix
$(M_T)_{xx}, (M_T)_{yy}, (M_T)_{xy}$	Thermal moment resultants
$\boldsymbol{\alpha_T}$	Thermal expansion coefficients matrix
$\alpha_{xx}^T, \alpha_{yy}^T, \alpha_{xy}^T$	Thermal expansion coefficients
$\mathrm{T}(x, y)$	Function expressing the temperature field over plate domain
T_R	Uniform temperature rise for thermal energy equal to that for fully heated plate
$\bar{K}_{ij}$	Plane stress reduced stiffness constants
F	Strain energy due to foundation
G	Geometric strain energy resulting from the applied in-plane loads
T	Kinetic energy
W	External work done
C	Damping energy
$c_{d1}, c_{d2}, c_{d3}, c_{d4}$, and c_{d5}	Components of Damping coefficient matrix
$\delta^{(1)}$	first variation
U_σ^N	Membrane energy
U_σ^M	Bending energy
$U_\sigma^{M^{\mathrm{a}}}$	Additional bending energy
U_σ^S	Shear Energy
$\mathbf{N}, \mathbf{M}^{\boldsymbol{m}}, \mathbf{M}^{\boldsymbol{a}}, \mathbf{S}$	Matrices of stress, moment, additional moment, and shear resultants, respectively.
$\boldsymbol{\varepsilon}^{\mathbf{0}}, \boldsymbol{\xi}, \boldsymbol{\xi}^{\boldsymbol{a}}, \boldsymbol{\gamma}$	Membrane, bending, additional bending, and shear strains, respectively.
$\bar{\mathbf{A}}, \bar{\mathbf{B}}, \bar{\mathbf{C}}, \bar{\mathbf{D}}, \bar{\mathbf{E}}, \bar{\mathbf{F}}, \bar{\mathbf{H}}$	Stiffness matrices
U_σ	energy due to the Cauchy strain tensor
U_r	energy due to the symmetric curvature gradient
U_L	energy due to the dilatation gradient
U_τ	energy due to the deviatoric stretch gradient
Y_{mn}, P_{mn} and Q_{mn}	Work conjugates of the higher-order deformation gradients in the components of U_r, U_L and U_τ , respectively

$\overline{Y_{mn}}$, $\overline{P_{mn}}$ and $\overline{Q_{mn}}$	Work conjugates of first-order deformation gradients in the components of U_r, U_L and U_τ, respectively
N_{ij}, M_{ij}^m, M_{ij}^a, S_{ij}	The stress resultants, moment resultants, additional moment resultants, and shear resultants respectively.
n_{ij}	In-plane pre-buckling stress resultants due to the applied in-plane mechanical loading or thermal loading
$\hat{N}_{ij}$	The net stress resultants
'S'	Simply supported edge
'C'	Clamped edge
t	Time
Φ	Airy's stress function
Φ_{CS}	Complimentary solution
Φ_{PI}	Particular integral
$\Theta^i{}_{mn}(x, y)$	Basis functions
$U_{mn}^*(t), V_{mn}^*(t)$, $W_{mn}^*(t)$, $K_{mn}^*(t)$ and $L_{mn}^*(t)$	Undetermined coefficients independent of spatial coordinates
m, n	Mode number along x and y directions, respectively
$\overline{N}_x$	Applied in-plane loading
p	Excitation frequency of in-plane harmonic loading
N_{cr}	Buckling Load
$\mathbf{F}$	Transverse force vector
ω_{NL}	Forcing frequency of transverse periodic loading/ Natural frequency considering nonlinearities
$\boldsymbol{\delta}$	displacement vector
$(\dot{\ })$	differentiation with respect to time
$(\ddot{\ })$	double differentiation with respect to time
$\mathbf{M}$	Mass matrix
$\mathbf{K}_{\mathrm{NL}}$	Non-linear stiffness
$\mathbf{K}_{\mathrm{L}}$	Linear stiffness matrix
$\mathbf{K}_{\mathrm{G}}$	Geometric stiffness matrix
$\mathbf{C}$	Rayleigh's damping matrix

$\mathbf{K}_{\mathrm{NL2}}$	Quadratic nonlinear stiffness matrix
$\mathbf{K}_{\mathrm{NL3}}$	Cubic nonlinear stiffness matrix
$\mathbf{I}$	Identity matrix
$\bar{a}$ and $\bar{b}$	Mass and linear stiffness proportionality constants for damping
ζ_i	Damping ratios
ω_i	natural frequency of mode shape 'i'
ω or ω_L	Fundamental natural frequency
$freq$	Fundamental natural frequency in Hertz
$\widehat{\omega}$, $\widehat{N_{cr}}$	Dimensionless fundamental natural frequency and dimensionless critical buckling load coefficient, respectively
T	Time period of plate
ΔT_{cr}	Buckling temperature difference
$\overline{\Delta T}_{cr}$	Non- dimensional Buckling temperature difference
σ_{xx}, σ_{yy} and τ_{xy}	Pre-buckling stresses
$\bar{\sigma}_{xx}$, $\bar{\sigma}_{yy}$ and $\bar{\tau}_{xy}$	Normalized pre-buckling stresses
w_{max}	Maximum steady state amplitude
w_{lmax}	Linear Deflection
w_0	Amplitude of initial perturbation
$wDIR^{L}$	Width of linear dynamic instability region
$wDIR^{NL}$	Width of nonlinear dynamic instability region

1

Introduction

1.1 Preamble

Advances in engineering have led to miniaturized structures with optimal properties specific to their application. Systems as small as a few micrometres can now be made because fabrication techniques have greatly improved. Bulk micromachining and surface micromachining are some of the prevalent fabrication techniques for small-scale structures (Gad-el-Hak 2006). One of the most important applications of small-scale structures has been in Microelectromechanical systems (MEMS). These are devices and systems with critical dimensions measuring a few microns. The size chart depicted in Fig. 1.1 illustrates the relative positioning of MEMS structures in relation to the sizes of other well-known entities.

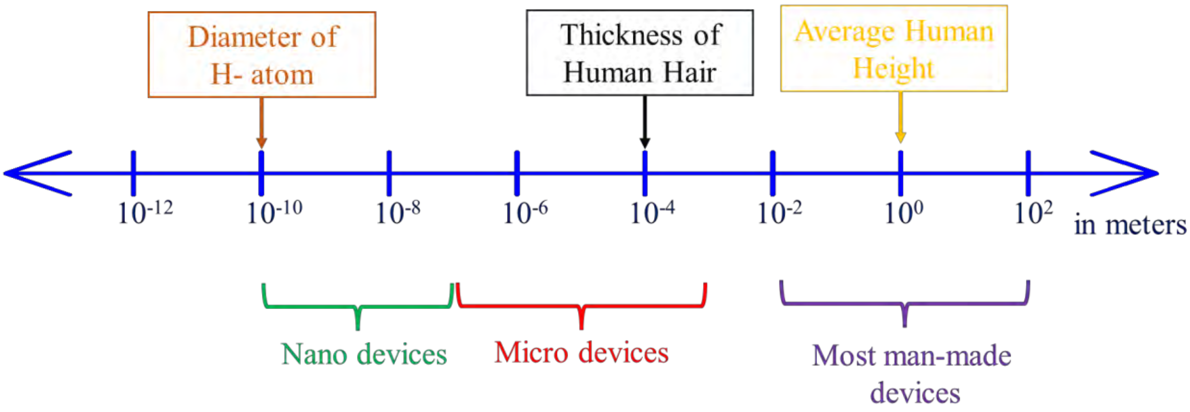

Fig. 1.1: Size chart depicting scale of things in meters

These MEMS are commonly configured as beams and plates, serving as integral components in actuators, tweezers, diaphragms, gears, cantilevers, and probes essential for scanning probe microscopy and highly sensitive sensors (Bashir et al. 2000). Devices employing MEMS technology are often referred to as micromachine devices. The contemporary landscape of micromachined devices encompasses an array of innovations, including gyroscopes, accelerometers, pressure sensors, high-performance mirror displays, micromotors, micro engines, RF switches, valves, pumps, thermally and chemically sensitive membranes, single-chip microfluidic systems (used in applications such as chemical analysis or synthesis), and single-chip micro total-analysis systems, also known as lab-on-a-chip devices, among many others (Mukherjee and Aluru 2006). The MEMS technology enables the miniaturization of mechanical elements in devices and a high-order control of dimensions, which makes them highly sensitive to smaller displacements and forces. They provide a combination of high fundamental frequency along with low force constant. Thereby, enabling high force and displacement sensitivity at ultralow-power. Hence, they have demonstrated remarkable efficiency in scanning surfaces, enabling tasks such as measuring surface roughness, critical dimensions, and 2-D depth profiling (Tortonese 1997). They find utility in examining cells and neurons, serving as lightweight sensors, facilitating precise control in manufacturing processes, enabling high-precision chemical synthesis and various other applications demanding exceptional sensitivity. The micromachined sensors (Yazdi et al. 1998), such as accelerometers, gyroscopes and pressure sensors have become an integral part of the automotives, biomedical applications, consumer electronics, industrial applications, military applications and most recently Internet of Things (IoT). In the automotive industry, they are used in vehicle stability systems, activating safety systems and electronic suspension. There are more than 50 MEMS sensors in a car. In the case of consumer electronics and IoT, they serve as necessary sensors in image stabilization, virtual reality, inertial mouse, and sports equipment. The microcantilevers serve as an integral part of atomic force microscopes, allowing them to detect pico-newton scale intermolecular forces and nanoscale displacements (Alunda and Lee 2020). This capability enables groundbreaking investigations into intermolecular interactions and the study of single living cells.

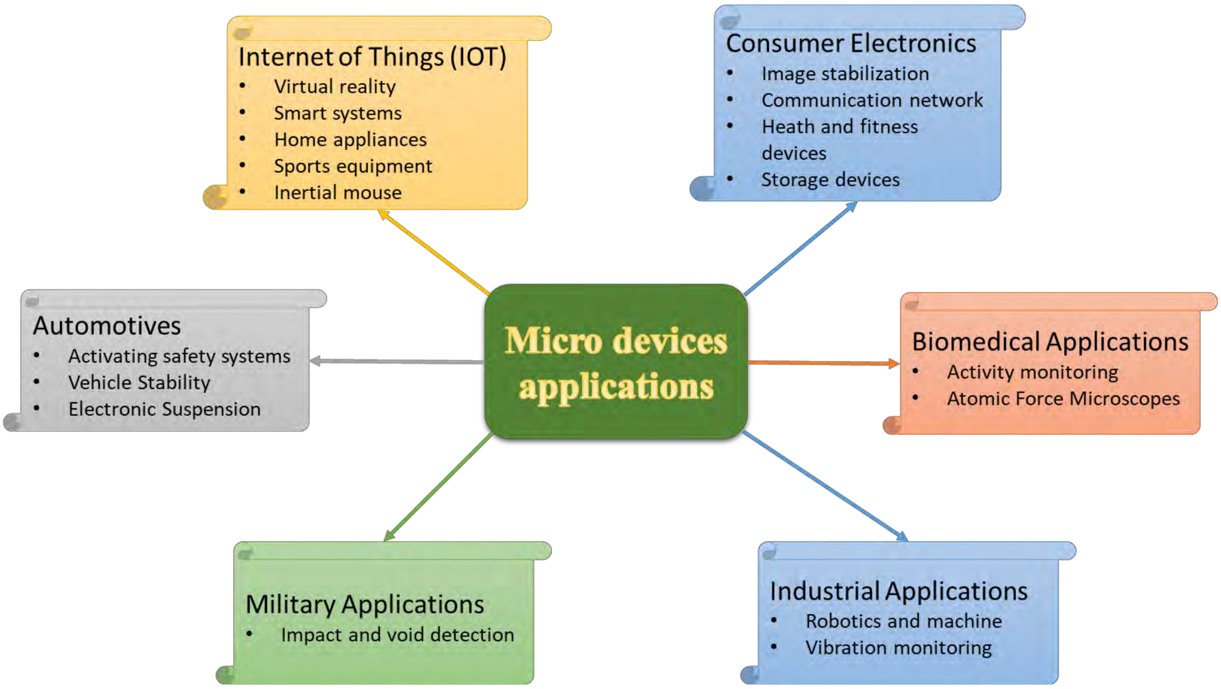
Internet of Things (IOT)
Virtual reality
Smart systems
Home appliances
Sports equipment
Inertial mouse
Consumer Electronics
Image stabilization
Communication network
Heath and fitness devices
Storage devices
Automotives
Activating safety systems
Vehicle Stability
Electronic Suspension
Micro devices applications
Biomedical Applications
Activity monitoring
Atomic Force Microscopes
Military Applications
Impact and void detection
Industrial Applications
Robotics and machine
Vibration monitoring

Fig. 1.2: Applications of micromachined devices in various fields

MEMS devices are also used in wireless communication devices, including mobile phones to serve as excellent bandpass filters because of their large quality factors (Piekarski et al. 2001). The applications of microstructures in diverse fields are illustrated in Fig. 1.2. The large application set of micromachined devices has led to their large-scale commercialization and batch-processing technologies are employed to fabricate the microstructures, aiming to achieve cost optimization. Furthermore, utilizing these microstructures in high-stakes domains such as vehicle safety and military applications necessitates thorough analysis before proceeding with the final fabrication steps.

Microstructures behave differently from macro structures due to prominent distinctions in internal material structure and associated inter-atomic spacing (Behera and Chakraverty 2017). Either experimental research or molecular dynamics (MD) simulation can be used to conduct an accurate study that takes these impacts into account (Rudd and Broughton 1998). The Classical Continuum Theory (CCT) has been unable to accurately model the microstructures as it ignores the changes in behaviour due to size reduction. The hardening of strain is a major factor in microscale structures. This is because, as the distance between the grain boundaries decreases due to a decrease in grain size, the geometrically necessary dislocations (GNDs) (Ashby 1970) pile up at the gradient boundaries due to blockages. Since these GNDs are associated with large plastic strain gradients (Hutchinson 2000), the piling up of GNDs (Fig. 1.3) leads to strain hardening or an increase in yield stress. Although the true behaviour of micro-sized materials considering intermolecular spaces and voids, can only be predicted using molecular dynamic simulations, it is computationally exhausting. A study has shown that corrections from atomistic behaviour emerge at the truly molecular scale (Rudd and Broughton 1998). Continuum theory with certain modifications to incorporate the effects due to small scale (Behera and Chakraverty 2017) such as surface effects, the internal structure of the material, and lattice spacing between the atoms is found to be adequate for most work in micro-scale analysis. Consequently, several researchers have sought to alter the CCT to incorporate size-dependent effects. Strain gradient and couple stress theories have explored the effect of strain hardening, with strain gradients also factored in the strain energy density function. The couple stress theories consider the rotation of grains (couple stress) and the strain gradient theories consider both the rotation of grains and the accumulation of dislocations (strain gradients). The nonlocal effect becomes prominent in nanostructures (Li et al. 2019a). Thus, the nonlocal theories are used to analyse structures at the nano-scale.

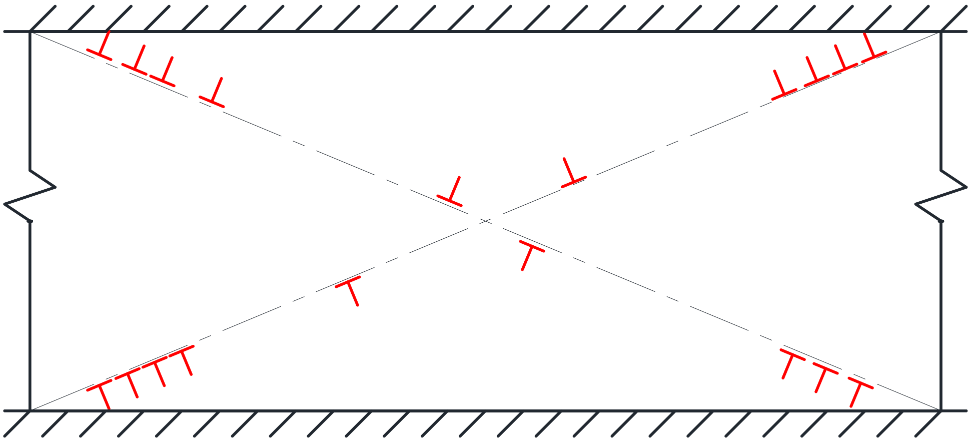

Fig. 1.3: Schematic representation of accumulation of GNDs at grain boundaries along critical slip plane

Micromachined devices, being exceptionally lightweight and slender, are susceptible to failures resulting from surface impacts or other thermal, electrical, and magnetic loads, whether they occur inadvertently or as a routine part of device operation. Such incidents can induce bending or buckling failures, potentially resulting in permanent damage to these devices. The alterations in the response attributes of microcantilevers, including deflection amplitude and quality factor, find valuable applications in diverse fields such as environmental monitoring (Vashist and Holthofer 2010) and the development of read-and-write storage devices (Severi et al. 2009). Consequently, a comprehensive investigation into these response characteristics holds paramount significance within the realm of microstructures. In the static mode of operation, the changes in response depend only on the surface stress variation. However, the potential for microstructure applications and their sensitivity are substantially enhanced when they are employed in the dynamic mode. In this configuration, an external actuation induces oscillations at the microstructure's resonant frequency. The alteration in resonance frequency resulting from shifts in environmental conditions, mass, or damping properties serves as a means to sense these changes. This principle is extensively used in the working of MEMS bandpass filters (Lin et al. 1998; Nguyen 1995), and microcantilevers for biosensors (Patkar et al. 2020). The simple harmonic (SH) resonance is used in accelerometers and mass sensors (Aikele et al. 2001). In the case of SH resonance, an oscillator receives external excitation in the form of a periodic force. This results in a Duffing-type equation, with the oscillator's frequency matching the excitation frequency. Acceleration induces lateral deflection in the oscillator's mass, leading to strain changes within the resonator and a shift in the resonant frequency at peak amplitude. Similarly, in the context of a mass sensor, detecting a change in mass is facilitated by observing shifts in the resonant frequency at peak amplitude. In SH resonance, the response at frequencies significantly different from the resonant frequency is minimal but not entirely absent.

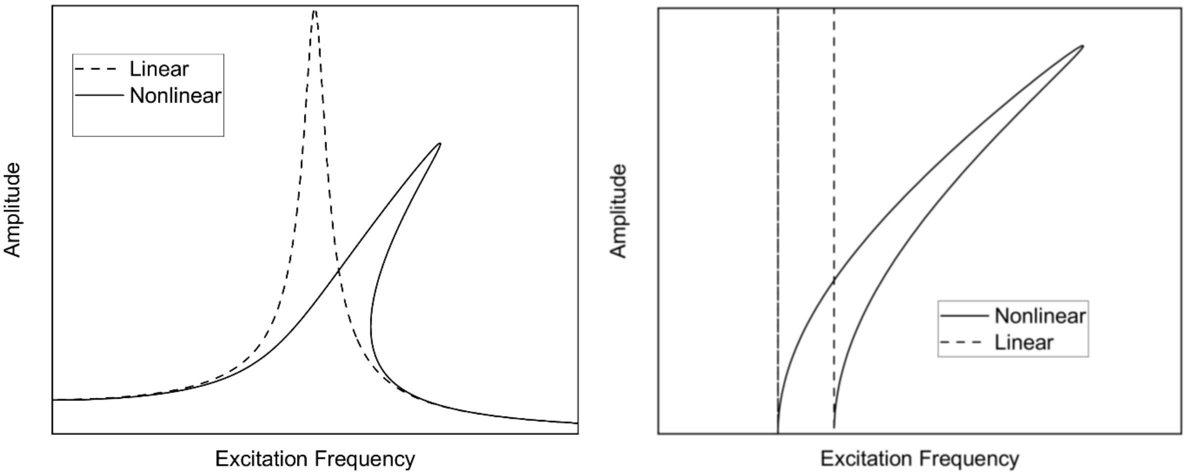

(a) Simple Harmonic Resonance (b) Parametric Resonance

Fig. 1.4: Comparison of frequency-amplitude graph of microplates with and without nonlinearity under (a) simple harmonic resonance and (b) parametric resonance

On the other hand, parametric resonance is employed in various modern oscillators. It exhibits distinct dynamics compared to SH oscillators. Under some combinations of in-plane loading magnitude, loading frequency, and the structure's natural frequency, parametric resonance induces large out-of-plane vibrations at the structure's natural frequency. The response remains zero for all other combinations of frequencies and loads. This leads to a sharp transition in amplitude as the forcing frequency moves from the trivial solution to the sub-harmonic non-trivial solution. This transition point is dependent on various parameters such as mass and geometry, making it particularly valuable in enhancing the sensitivity of mass sensors (Turner and Zhang 2001), MEMS bandpass filters (Rhoads et al. 2005), and parametric amplifiers (Raskin et al. 2000). Mathieu-Hill's equation is employed to model parametric resonance (Cartmell 1990). In the linear parametric resonance region, the amplitude of response is theoretically infinite. The introduction of damping imposes a constraint on the minimum loading required for parametric response. However, it does not limit the amplitude to a finite value. In any practical system, the amplitude is finite and controlled by nonlinearities. Therefore, incorporating geometric nonlinearity is essential to determine the finite amplitude of the steady-state response in non-trivial solutions (Zhang et al. 2002). A comparison of the nature of frequency-amplitude curves of microplates with and without nonlinearity under SH resonance and parametric resonance is shown in Fig. 1.4.

The static and dynamic characteristics of microstructures are dependent upon a variety of parameters. Therefore, prior to embarking on the design and batch fabrication of these structures, it is imperative to conduct a comprehensive modelling and analysis of their properties. A thorough examination of how each parameter influences both static and dynamic behaviours is necessary. Design guidelines should then be formulated based on this analysis to guarantee the effective operation of the manufactured micromachined devices.

1.2 Motivations

Microstructure devices exhibit distinctive characteristics that vary according to their specific applications. These properties encompass factors such as resonant frequency, sensor bandwidth, sensitivity, frequency response, full-scale nonlinearities, and deflection. Microplate parameters such as thickness and support conditions play a key role in controlling these attributes. The damping mass acting on the system also plays a key role in determining the sensor bandwidth. The microplates are fitted to the adjacent structures in different manners. Cantilever support was a popular arrangement (Roylance and Angell 1979). In current times, with prevalent surface micromachining fabrication technology, the sensors are placed in simply supported or clamped conditions along with interface circuits on a single chip. This arrangement is especially adopted in capacitive accelerometers (Peeters et al. 1992; Seidel et al. 1990). These microstructures find critical utility as MEMS devices in essential systems like vehicle safety mechanisms and military operations. Consequently, conducting an exhaustive parametric analysis of these structures is imperative to facilitate their efficient design.

The load acting on the edges or face of microplates is mostly non-uniform and localized due to irregular connections with neighbouring members, partially damaged boundaries during fabrication or connections between stiffened and unstiffened plates (Yazdi and Najafi 1997). Thus, the effect of non-uniform in-plane loadings needs to be included in the modelling. Since most micromachined devices operate under dynamic conditions such as vehicles, the analysis of their dynamic stability also becomes imperative. They also exploit simple harmonic resonance or parametric resonance phenomena, where they are exposed to periodic excitations, in their functionality. Therefore, the inclusion of geometric nonlinearity is mandatory to model vibration amplitudes accurately in the study of these structures. A comprehensive analysis encompassing the study of changes in width and onset points of various frequency regions, as well as the nonlinear hardening characteristics of frequency-amplitude curves due to various parameters is needed. It is crucial to investigate how the point of jump in amplitude of response varies when excitation frequency is swept from low to high and vice versa, taking into account the step size of the frequency. Thus, a thorough examination of the initial amplitude of perturbation is necessary. Over the operational lifespan of microplate elements, they often experience significant thermal stresses that can induce buckling. Like other loads, these loads can also be localized. Therefore, a parametric investigation into buckling loads and post-buckling equilibrium paths of microplates under localized heating is also a requisite component of the analysis.

In response to these multifaceted requirements, this thesis is motivated to present an efficient and accurate methodology that encompasses comprehensive parametric analyses of microplates subjected to diverse types of loading scenarios.

1.3 Aim of the Study

The aim of this study is to establish an efficient and precise methodology for examining the nonlinear static and dynamic behaviours of microplates. These microplates are subjected to diverse loading conditions, including non-uniform in-plane mechanical loading, transverse patch mechanical loading, and localized heating. The study aims to assess the impact of various parameters on critical aspects such as buckling, post-buckling behaviour, dynamic instability zones, nonlinear vibrations, and nonlinear dynamic responses of microplates under the above diverse loading conditions. In pursuit of this objective, the next chapter will conduct a rigorous examination of the existing literature in this field. Simultaneously, it will delineate the precise objectives of the current study, aligning them with the overarching aim.

1.4 Contribution of the Study

This thesis represents a significant contribution to the field of microplate analysis, aiming to enhance comprehension of their static and dynamic behaviours. It offers parametric analyses on the static stability, nonlinear vibration, nonlinear dynamic response, and post-buckling behaviour of microplates under diverse load conditions, employing a semi-analytical approach. The key contributions of this research are outlined as follows:

- Analytical expressions for the partial differential equations of a microplate are given. The microplate is modelled with considerations of size-dependent effects are included in the modelling using the modified strain gradient theory (MSGT), shear deformation effects are included using the third order shear deformation theory (TSDT) and the geometric nonlinearity is included in the form of von-Kármán nonlinearity.
- The ordinary differential equations (ODEs) of motion are obtained using the strong form analytical approximation method (Galerkin's weighted residual method). Thus, the closed form results obtained are very close to the exact solutions.
- The analytical expressions for the in-plane pre-buckling stresses due to non-uniform in-plane mechanical loading and localized thermal loading are derived using Airy's stress function. The transverse patch mechanical and localized thermal loadings are modelled using double Fourier series and expressed analytically in complete domain of plate's surface. However, in-plane localized mechanical edge loading is modelled using single Fourier series and expressed analytically in full edge of the plate.
- The dynamic instability regions are plotted considering damping and a parametric analyses on its depth are presented.
- The non-linear vibrations due to both in-plane loadings and transverse loadings are studied using the frequency-amplitude curves. Both the stable and unstable regions, and the bifurcation points, in the presence of damping are plotted using the incremental harmonic balance (IHB) method in conjunction with the arc-length continuation method.
- The nonlinear dynamic response is presented using the time-history plots. The effect of initial amplitude of perturbation on the steady state response is also studied using these plots.
- A parametric analysis of the different zones of excitation frequencies and the amplitude of vibrations is presented considering various parameters such as porosity, elastic foundations, geometry of plate, damping, and loading parameters.
- A parametric analyses of the buckling and post-buckling characteristics of microplate subjected to localized thermal loads is presented.

1.5 Organization of the Thesis

This thesis comprises eight distinct chapters, each contributing to a comprehensive exploration of the subject matter. This is the first chapter, which introduces the reader to the problem statement and the aim of the research. The second chapter delves into an extensive review of pertinent literature, framing the study's objectives. Chapter three provides an in-depth exploration of the mathematical formulations and solution methodologies applied throughout the investigation. The fourth chapter presents results on dynamic instability and nonlinear vibration of isotropic microplate subjected to non-uniform in-plane mechanical loading. In the fifth chapter, the analysis of nonlinear vibration and nonlinear dynamic response of porous microplate resting on elastic foundation (PMREF) under non-uniform in-plane mechanical loading is presented. Chapter six delves into the study of nonlinear vibration and nonlinear dynamic response of microplates subjected to transverse patch mechanical loading. Moving forward to chapter seven, we present an investigation into the buckling and post-buckling analyses of PMREF subjected to localized thermal loading. This chapter also explores the influence of different parameters on the mode shape of the microplate at the buckling load. Finally, in chapter eight, we offer a synthesis of the key findings from all preceding chapters, drawing conclusions based on the present investigation and providing insights into potential future research directions. The references can be found at the end of the thesis, acknowledging the sources that contributed to this scholarly work.

2

Literature Review

2.1 Introduction

Microstructures, characterized by their diminutive size and increasing applications in microelectromechanical systems (MEMS), nanotechnology, and biotechnology. The huge set of applications of these sensors has led to their large-scale commercialization. They are manufactured using batch manufacturing techniques and thus, detailed attention towards their design and analysis has attracted substantial research attention in recent years. As the structures become smaller, classical continuum theories struggle to accurately describe their mechanical behaviour. Thus, various size-dependent continuum theories have been used to investigate the linear and nonlinear, static and dynamic behaviour of microstructures. This chapter conducts an extensive literature review focusing on the analyses of microstructures using size-dependent continuum theories. It aims to provide a comprehensive overview of the research landscape, highlighting seminal contributions and emerging trends in this field. The literature regarding the research tools used to analyse these structures, such as the size-dependent continuum theories, the modelling tools and the solution methodologies are also reviewed.

In this literature review, we delve into the comprehensive body of research that has focused on the linear and nonlinear static and dynamic analyses of microplates using size-dependent continuum theories. The organization of this literature review is as follows: The literature review on the various size-dependent continuum theories and their origin is discussed in section 2.2. In section 2.3, the literature on different two-dimensional plate theories used in modelling the field-displacement equations of microplates is discussed. Subsequently, in section 2.4, the analytical techniques and numerical methods used by various authors for deriving the governing equations and their solution methodology are explored. In the next section, the various types of microplates and their material properties analysed by the various researchers are looked upon. In section 2.6, the literature review of studies that focused on linear and nonlinear static analyses of microplates is presented. In linear analysis, studies that focused on bending and buckling behaviours are discussed. In nonlinear analysis, studies that focused on nonlinear bending and post-buckling analyses are presented. The literature review on studies that presented linear and nonlinear dynamic analyses of microplates is presented in section 2.7. In linear dynamic analysis, studies that presented the natural frequencies and linear dynamic instability regions of microplates are presented. Studied that analysed nonlinear free vibration behaviour, nonlinear forced vibration behaviour, and nonlinear dynamic responses of microplates are reviewed under nonlinear dynamic analysis. The studied that focused upon localized loading are discussed in section 2.9. The research gaps identified from the literature review are listed in section 2.10. Lastly, the objectives of the current investigation, derived from these research gaps, are presented in section 2.11.

2.2 Size-Dependent Continuum Theories

The size-dependent effects in metals are experimentally observed by several researchers (Fleck et al. 1994; Nix 1989; Stelmashenko et al. 1993; Stölken and Evans 1998). The mechanical behaviour of microstructures departs significantly from classical continuum mechanics due to the influence of size-dependent effects. The most accurate method of modelling these structures is using molecular dynamic (MD) simulations. However, this method is computationally very exhaustive. Thus, several theoretical frameworks have been developed to address this challenge by including necessary size-dependent modifications in the classical continuum theory. The pioneering work related to size-dependent continuum theories was presented by Dell'Isola (Dell'Isola et al. 2014, 2016) and Cosserat brothers (Cosserat and Cosserat 1909). In the present day, several such theories have been developed. These theories are classified into three major theories: The couple stress theories, the strain gradient theories and the nonlocal theories. The couple stress and strain gradient theories are major size-dependent theories used to model microstructures. These are further discussed in the following subsections.

2.2.1 Couple Stress Theories

The classical couple stress theory was originally proposed by Toupin (1962) based on the conception that in addition to the forces driving translations on a material particle, a couple also exists to drive it to rotate. Thus, the higher-order deformation gradients are also included in the deformation metrics. The rotation gradients are the anti-symmetric parts of the strain gradients. Mindlin & Tiersten (1962) and Koiter (1964) further extended this theory providing valuable insights into the role of rotation gradients in microplate mechanics. Mindlin (1964) further demonstrated the surface effects inclusions into the couple stress equations. Yang et al. (2002) proposed a theory by modifying the classical couple stress theories (Koiter 1964; Mindlin, R.D., Tiersten 1962; Mindlin R.D. 1964) to include the small-scale effects and named it as the modified couple stress theory (MCST). In the classical couple stress theory, it was suggested that apart from the force required for a material to translate, a couple is required for it to rotate. However, the couple was unconstrained in position as only conventional equilibrium relations were used. F. Yang et al. (2002) proposed an additional equilibrium relation that restricted the couple stress tensor to be symmetric. Due to this newly introduced symmetric curvature tensor, the number of material length scale parameters required was reduced from two to one.

2.2.2 Strain Gradient Theories

Toupin (1962) observed in his research that the rotation gradient used in the couple stress theories comprises of only eight components of the total eighteen second-order deformation gradients. The remaining ten components are parts of self-equilibrating forces on a particle. Although these forces do not contribute to the forces and couple, their contribution to the potential energy cannot be ignored. In their subsequent work, the authors (Toupin and Gazis 1965) exhibited that in-presence of self-equilibrating stresses, the free surface of a material in atom-lattice, either pulls in or pushes out. This behaviour can be portrayed using the second gradient of strain. Considering the above observations, Mindlin (1965) developed a generalized higher-order stress theory by including the effect of eighteen independent second-order deformation gradient components to the strain energy density function. The number of material length scale parameters corresponding to the first-order strain gradients was five. Fleck & Hutchinson (1997) reformulated the higher-order elasticity theory given by Mindlin (Mindlin 1965) and renamed it as the strain gradient theory. They divided the strain gradients into stretch gradients and rotation gradients. It was further modified by Lam (Lam et al. 2003) and renamed as the modified strain gradient theory(MSGT) where the second-order deformation gradient is further split into two parts, symmetric and anti-symmetric. Similarly, the curvature tensor is also split into anti-symmetric part and symmetric part. The symmetric second-order deformation gradient is further split into a trace part and a traceless part. The trace part is a function of the dilatation gradient and anti-symmetric part of the curvature tensor. The traceless part is also called the deviatoric stretch gradient tensor. The anti-symmetric part of the curvature tensor was neglected as it does not contribute to deformation energy as proposed by F. Yang et al. (2002). Thus, the number of material length scale parameters required was reduced from five to three.

2.2.3 Material Length Scale Parameters

A major challenge while using size-dependent continuum theories is the determination of the size-dependent parameters. Several researchers (Fleck et al. 1994; Gao et al. 1999; Haque and Saif 2003; Hayashi et al. 2011; Lam et al. 2003; Liu et al. 2013; Stölken and Evans 1998; Yang et al. 2002) have used the experimental methods including the nano indentation techniques for the determination of material length scale parameters (MLSPs). (Park and Gao 2006) suggested that the MLSP for epoxy microbeam is 17.6 μm. Chong et al. (2001) suggested that the MLSP is equal to 3 μm for copper wires subjected to torsion. Song and Wei (2020) calibrated the material length scale (MLS) parameters of face-centred cubic, body-centred cubic and hexagonal close-packed metals by linking the strain gradient theory with the molecular Cauchy-Born rule method. Ghorbani et al. (2021) calibrated the MLS and nonlocal parameters of different types of CNTs by comparing the results of natural frequency with those of MD simulations. The dependence of MLS parameters on strain rate and temperature was shown by Voyiadjis and Almasri (2009).

Critical Discussion

The couple stress theories only consider the rotation of grains (couple stress). In contrast, the modified strain gradient theory considers both the rotation of grains and the formation of dislocations (strain gradients). The results of modified strain gradient theory match with those of couple stress theories at larger sizes where the effect of accumulation of dislocations or strain gradients relating to self-equilibrating stresses vanishes (Wang et al. 2011). The nonlocal theories, such as the nonlocal elasticity theory (NET), are more suitable for nanostructures (Tien et al. 2023) because of the characteristic length scale involved with them. In the case of nanostructures, the length scales are in the range of a few nanometres. Thus, the effect of nonlocality becomes prominent (Li et al. 2019a). However, in the case of microstructures, the length scales are larger; thus, the effect of nonlocality becomes insignificant. The nonlocal strain gradient theory (NSGT) can also give results similar to MSGT as it is a combination of strain gradient and nonlocal theories. However, this theory is computationally expensive and challenging to implement for complex microstructures. Thus, Modified Strain Gradient Theory (MSGT) is used in this article as it provides accurate results and is computationally economical for microstructures.

2.3 Plate Theories

The microstructures are available in different shapes, such as beams, columns, plates, or shells. When conducting analytical examinations of these members, it is necessary to categorize them based on their geometries. In the present investigation, the entire analysis centres around plate theories because the focus of this thesis is limited to plate structures. Plates inherently possess a three-dimensional (3D) nature. Therefore, to accurately estimate the stress distribution and displacement within this plate-like structural member, it becomes imperative to employ the principles of three-dimensional elasticity theory, as advocated by several researchers (Noor 1975; Srinivas and Rao 1970). The 3D elasticity theory was used by Salehipour and Shahsavar (2018) to model MSGT based microplates.

However, it is worth noting that the thickness of the plate is significantly smaller in comparison to its other two dimensions. Consequently, plates can be effectively analysed as two-dimensional (2D) plane stress problems, as discussed by Soldatos (1992). Furthermore, adopting a 2D analysis approach also offers the advantage of reducing computational time for problem-solving. The transverse strains are functionally represented in these 2D theories. Based on the function used to represent these transverse strains in the field displacement equations, these theories can be classified as classical, first order or higher order plate theories. Thai and Kim (2015) presented a review article discussing the various plate theories for analyses of FG plates. A review of the literature on these theories used for the analysis of microplates is discussed in the following subsections.

2.3.1 Classical Plate Theory

In 1850s, the German physicist Gustav Kirchhoff came up with the first plate theory based on the assumption that plates can deform without in-plane strains. Later, Love (1888) came up with the Kirchhoff-Love plate theory as an extension of the Euler-Bernoulli beam theory (Timoshenko 1953). This theory is commonly referred to as the classical plate theory (CPT). In this theory, it is assumed that the cross-sections of the plate remain plane after bending and also stay perpendicular to the reference plane, i.e. the middle surface of the plate. The shear deformation effect is considered negligible in this theory as the transverse displacements are assumed to be constant through the thickness. Therefore, this theory is only suitable for thin plates (width to thickness ratio > 50) as it cannot model the shear deformation effect present in the case of moderately thick and thick plates. The first MCST and CPT based isotropic microplate was modelled by G. C. Tsiatas (2009) for its bending analysis. The free vibration analysis of thus MCST and CPT based microplate was performed by Yin et al. (2010). B. Wang et al. (2011) developed one of the earliest CPT based microplates where the size-dependent effects were included using the MSGT. A comparison of the strain gradient and couple stress model was also demonstrated. In recent studies, numerous other authors have used the CPT to model thin microplates (Arefi and Rabczuk 2019; Mirsalehi et al. 2017; Nateghi and Salamat-talab 2013; Tsiatas and Yiotis 2015) to save computational costs associated with other higher order plate theories.

2.3.2 First Order Shear Deformation Theory

In order to include the effect of shear deformation in plate theories, Reissner (1945) and Mindlin (1951) came up with the Reissner-Mindlin plate theory or the first order shear deformation theory (FSDT). In this theory, the plane section remains plane after bending but do not remain perpendicular to the reference plane. The shear deformation effect is taken into consideration as the transverse displacements are assumed to show linear variation through the thickness. However, this leads to non-zero transverse shear strains at the top and bottom surfaces, which is incorrect. The shear correction factor is employed to counter the non-zero transverse stresses at the top and bottom surfaces in this theory. The initial isotropic microplate model employing the MCST and deriving field displacement equations through the FSDT was pioneered by Ma et al. (2011) and Ke et al. (2012b). Meanwhile, the earliest model for microplates incorporating strain gradient effects and adopting the FSDT to formulate field displacement equations was introduced by S. Sahmani & Ansari (2013). Later, several other researchers used the FSDT based field displacement equations to provide a more accurate modelling of the shear deformation effects present in the case of moderately thick microplates (Ansari et al. 2013; Emami and Alibeigloo 2016; Liu et al. 2014; Shenas and Malekzadeh 2016; Yang and Lim 2012).

2.3.3 Higher Order Shear Deformation Theory

Traditional plate theories, such as the Kirchhoff-Love theory and Reissner-Mindlin theory, have limitations in accurately modelling the variation of shear stresses through the plate thickness, which is an important element in modelling moderately thick and thick plates. The Reissner-Mindlin theory does include shear deformation but requires a shear correction factor. In order to address these limitations, higher-order shear deformation theories (HSDTs) have been developed. These theories account for higher-order derivatives of the transverse displacement and provide a better approximation of the shear stress distribution within the plate. The most prevalent higher order theory is Reddy's (Reddy 2006) third order shear deformation theory (TSDT). This theory assumes parabolic variation of the transverse shear strains. After deformation, the initially perpendicular plane sections no longer maintain their perpendicular orientation to the reference plane; instead, they assume a curved cubic shape. This assumption allows for a more realistic representation of the shear deformation behaviour. The first microplate model developed using the TSDT and MCST was given by Gao et al. (2013). Jung & Han (2015) presented an MCST and TSDT model of a FG microplate. S. Sahmani & Ansari (2013) presented the TSDT model of FG microplate where size-dependent effects were included using the strain gradient theory. Recently, microplate models using several other higher order shear deformation theories have been developed. Thai and Vo (2013) developed an MCST based microplate model using the sinusoidal HSDT (Touratier 1991). The simplified strain gradient based FG microplate was developed using the sinusoidal HSDT by Akgöz & Civalek (2015). The refined HSDT model for MCST based microplates was developed by partitioning the shear and bending components (Darijani and Mohammadabadi 2014). The refined plate theory (Shimpi 2002) was used by He et al. (2015) to model MCST based FG microplates. Recently, several other authors have used the HSDTs to model microplates (Arefi and Rabczuk 2019; Karamanli and Vo 2020; Thai et al. 2020a).

2.3.4 Plate Theories with Nonlinearity

Microplates often experience large deflections due to their small size and low rigidity. Consequently, the inclusion of geometric nonlinearity becomes a compulsion to accurately predict their post-buckling behaviour and nonlinear response in both static and dynamic conditions. The Green-Lagrange strain tensor and the von-Kármán nonlinearity are the two most common formulations for incorporating nonlinearity in the plate theories. The Green-Lagrange strains include both material and geometric nonlinearity as it takes into account both linear and shear deformations. The Green-Lagrange strains are included in the 3D theory to model microplates. The von-Kármán nonlinearity, on the other hand, is constrained to geometric nonlinearity (Torabi et al. 2021). It deals with nonlinearities arising from large deformations and rotations that plate structures undergo while maintaining a small strain assumption. This makes the von-Kármán nonlinearity particularly suitable for analysing thin-walled structures modelled using 2D plate theories. Several researchers have used the von-

Kármán nonlinearity to model geometric nonlinearity in microplate models. Earlier several researchers (Ansari et al. 2015a; Farokhi et al. 2013; Şimşek 2014; Wang et al. 2013a, 2015a; b) used the von-Kármán nonlinearity along with beam models to analyse the nonlinear bending, vibration, and post-buckling behaviour of isotropic microbeams. Ke et al. (2012a) and Loghman et al. (2021) studied the nonlinear vibration characteristics of functionally graded (FG) and viscoelastic microbeams, respectively. Geometric nonlinearity was incorporated into microplate models based on CPT and MCST (Asghari 2012; Farokhi and Ghayesh 2015; Wang et al. 2013b, 2014). Similarly, geometric nonlinearity was integrated into microplate models based on FSDT and MCST (Ke et al. 2013, 2014; Reddy and Berry 2012). A microplate model based on TSDT and MCST was also developed to account for geometric nonlinearity (Ghayesh and Farokhi 2016). Reddy and Kim (2012) developed a plate theory model that took into consideration the geometric non-linearity, small-scale effects, and functionally graded behaviour of a plate using the principle of virtual displacements. The small-scale effects were included by MCST, geometric non-linearity by the von-Karman non-linear strains, and functionally graded behaviour by a power law. The existing plate theories could be obtained as special cases of the developed theory, which could further be used to construct finite element models of these plates. Ansari et al. (2015b) studied the nonlinear bending and post-buckling analyses of FG microplates. Zhang et al. (2015a) investigated the axisymmetric bending, buckling, and free vibration analyses of circular/annular microplates.

Critical Discussion

In literature, the formulation for microplates modelled with MCST in combination with CPT, FSDT and TSDT (Thai and Kim 2013; Tran et al. 2022; Trinh et al. 2017) is easily available. Similarly, there is enough work on modified strain gradient theory in combination with CPT and FSDT (Arefi and Zenkour 2017; Shenas and Malekzadeh 2016). However, due to the complex calculations involved in the formulation of microplate based on MSGT and the TSDT, very limited literature is available. While the MSGT captures the size-dependent effects more accurately, the TSDT is found to be more accurate in modelling shear deformation effects in moderately thick plates. Zhang et al. (2020) used the FEM based differential quadrature (DQ) method on MSGT and TSDT-based microplates for their static bending, free vibration and buckling analysis. The author found a single study in literature where an MSGT and TSDT based microplate was modelled with geometric nonlinearity inclusions.

2.4 Solution Methodologies for Governing Equations

Governing equations are essential in understanding and predicting the behaviour of these two-dimensional structural elements under various loads and boundary conditions. These equations serve as the foundation for analysing plate deformations, stresses, and vibrations, making them crucial in engineering and scientific disciplines. In this section, we discuss the solution methodologies employed to derive the governing equations of microplates. In the first stage, the strain energy, kinetic energy and external work done are formulated using the kinematic equations from the plate theories and the size-dependent continuum theory. The governing partial differential equations (PDEs) of the various size-dependent microplate models are obtained using the energy conservation principles. In case of static analyses, the principle of minimization of total potential energy is used. According to this principle, the equilibrium state of the microplate corresponds to the configuration that minimizes its total potential energy. The variation of potential energy with respect to displacement parameters leads to the derivation of the governing PDEs or the Lagrange equations. Most researchers (Darijani and Mohammadabadi 2014; Karamanli and Vo 2020, 2021) have used this principle to derive the governing PDEs of the microplate under static conditions. In dynamic problems, Hamilton's variational principle (Reddy 2017), which is an extension of Lagrangian mechanics, is used to derive the governing PDEs of size-dependent microplate model. The dynamic equations of the system are obtained by varying the path or trajectory between the initial and final points and setting the action integral to be stationary. The actual motion of the plate corresponds to the path that minimized the action integral. The researchers (Ebrahimi et al. 2020; Nateghi and Salamat-talab 2013; Reddy and Kim 2012; Tsiatas and Yiotis 2015) used this principle to derive the governing PDEs of motion for the dynamic analyses of their size-dependent microplate models.

Various numerical and analytical solution methodologies are available to solve these PDEs. The analytical methods such as the Navier's and Levy's methods provide exact closed-form solutions. S. Sahmani & Ansari (2013) evaluated the free vibration response of FG HSDT and MSGT based microplates using Navier's closed form solutions. Afshari & Adab (2020) used the Navier's method to obtain the critical buckling load and natural frequencies of MCST and sinusoidal shear deformation theory based microplates reinforced with graphene nanoplatelets. Babu & Patel (2019b) used Levy's analytical solution to study the static bending of strain gradient and CPT based microplates. These methods provide the most accurate closed form solutions to the governing PDEs. However, formulations involving these methods are very complex and only possible for microplates with simple geometries, loading and boundary conditions. In the practical problems, several irregular geometries, loading, and boundary conditions exist. This, along with the mathematical complexity of the higher order microplate models makes it impossible to find their exact analytical solutions. Thus, the complex geometries and boundary conditions are often modelled using numerical techniques, particularly the finite element method (FEM). These techniques discretize the microplate into finite elements and transform the governing equations into a system of algebraic equations. This approach is most suitable for complex geometries of microplates. Some authors used the FEM-based differential quadrature (DQ) method (Zhang et al. 2020) to solve the PDEs of size-dependent microstructure models. Others used the isogeometric analysis to obtain the ODEs discretized based on Non-Uniform Rational B-Splines (NURBS) (Thai et al. 2018, 2019, 2020b, 2017b). Various other researchers (Babu and Patel 2019b; Ebrahimi et al. 2020; Karamanli et al. 2021; Karamanli and Vo 2020; Mirsalehi et al. 2015, 2017; Nateghi and Salamat-talab 2013) used several other numerical approaches to analyse the mechanical behaviour of these small-scale plate structures subjected to irregular geometries, loadings and boundary conditions. However, a drawback of using these numerical approaches is that they are associated with convergence or discretization errors.

Thus, the meshless analytical approximation solution methodologies have been used to provide a closed form solutions very close to the exact methods. Using these methodologies, the governing PDEs are converted to a set of algebraic equations for the static problem and a set of ordinary differential equations (ODEs) for the dynamic problem. The analytical approximation methods shall be categorized into strong form and weak form methods. A functional, which is an integral expression that implicitly incorporates the differential equations that characterise the system, is required in the weak form approaches. In this functional, the differential equation's differentiability is weakened. This functional is bilinear and symmetric in the case of linear and even order differential equations. The variation of this functional can be readily shown to be zero, and hence variational approaches like the Rayleigh-Ritz method perform exceptionally well for such equations. The functional, however, is not bilinear in the case of nonlinear differential equations. The process of weakening the differentiability and establishing the functional minima and maxima gets quite difficult in such equations. No variational principle could be developed in the situation of unstable thermal conductivity and viscous flow issues (Stolarski et al. 2018). The strong form methods have no such complexity and work well for all types of differential equations. The inclusion of nonlinearity and strain gradients in microplate models leads to both nonlinear and odd-order differential equations. The strong form analytical approximation method, such as the Galerkin's weighted residual method can provide closed form solutions to PDEs with strong nonlinearity considerations as well (Arpanahi et al. 2019, 2023; Sheng and Wang 2019; Sheykhi et al. 2023), with results very close to the exact solutions. However, this method is restrictive regarding the choice of approximating functions. In the case of weak form methods, the secondary variables associated with natural boundary conditions emerge explicitly in the integral while weakening the differentiability. Hence, the approximating functions are required to satisfy only essential boundary conditions, but in the case of strong form, they need to satisfy both the essential and natural boundary conditions. Thus, in the case of irregular geometries or boundary conditions, the choice of approximating functions in this method is complex.

Critical Discussion

In literature review of studies related to analyses of size dependent microplate models, it is observed that most studies used numerical approximation solution techniques to solve the PDEs. Some authors used the FEM-based differential quadrature (DQ) method. Others used the isogeometric analysis to obtain the ODEs discretized based on Non-Uniform Rational B-Splines. The closed-form solution for linear PDEs of MSGT and HSDT-based microplates was found using Navier's closed-form solution. The author found no study where the closed-form solution of PDEs of MSGT and TSDT based microplates with geometric nonlinearity consideration was available.

2.5 Microplate Material Types

The field of microplates has witnessed significant advancements in material types and properties, enabling a wide range of applications in microelectronics, sensing technology, optics, and more. Recent advancements in microplate technology have led to the development of various material types with unique properties and capabilities. This section provides an overview of different types of microplate materials, including isotropic microplates, functionally graded microplates, porous microplates and others, highlighting their applications and significance.

2.5.1 Isotropic Microplates

Isotropic microplates are characterized by uniform material properties in all directions. They are often fabricated using standard microfabrication techniques, offering simplicity and ease of manufacturing. These microplates find applications in micro-optoelectronic devices, microfluidics, and microsensors due to their predictable and consistent behaviour. Their isotropic nature simplifies analytical modelling, making them suitable for a wide range of applications. Silicon (Si) (Gennissen et al. 1997; Rosler 1977) and its compounds, such as Silicon Dioxide (Liu et al. 1999) are one of the earliest used materials for microstructures fabricated using bulk micromachining. Germanium-based materials were earlier used in micromachined transducers. Nowadays, they are used for devices that require the use of low-temperature processes (Franke et al. 2000). Recently, some metals such as Aluminium, Tungsten, Chromium and Nickel have been used in microstructures. Metal thin films made of alloys of these metallic elements exhibit shape-memory effects. This allows the use of these microplates as micro actuators in MEMS devices such as microvalves and micropumps (Hahm et al. 2000). Silicon Carbide and Diamond are used for MEMS applications in harsh environments such as micromachined AFM cantilever probe (Björkman et al. 1999).

2.5.2 Functionally Graded Microplates

Functionally graded materials (FGM) (Jha et al. 2013) have gained popularity because of their advantage of optimal properties from two different materials without the issue of the sudden change in properties, as in the case of laminated composites. Functionally graded microplates exhibit spatially varying material properties, allowing for tailored mechanical and thermal characteristics across their domains. These microplates are particularly useful in optimizing stress distributions, thermal management, and performance enhancements. Applications include MEMS actuators, sensors, and adaptive optics, where the ability to control material properties at the microscale is crucial for achieving desired functionalities. Nano-electro-mechanical systems (NEMS) cantilevers of various geometries were fabricated from nanocomposite alloy films of Al-Mo. Room-temperature co-sputtering was used to synthesize these films (Lee et al. 2006). Functionally graded TiN layer was deposited on TiNi based shape memory alloys to improve their surface properties using the magnetron sputtering system (Fu et al. 2003). Functionally graded NiTi shape memory alloys were prepared using a heat treatment method to improve the controllability of actuator applications (Mahmud et al. 2008). Witvrouw and Mehta (2005) developed a multilayer poly-SiGe deposition process to prepare high-quality functionally graded films with excellent mechanical and electrical properties that can be integrated with electronics. A review of various analytical and numerical methods used for the stress, buckling, and vibration analyses of FGM plates subjected to different cases of loading is discussed by Swaminathan et al. (2015).

Recently functionally graded sandwich microplates (Trinh et al. 2017) have been developed. In these structures, microplates consist of multiple layers with distinct material properties. They are designed to optimize specific mechanical or thermal properties while maintaining a lightweight and compact structure. By varying the materials and layer configurations, these microplates can achieve enhanced stiffness, reduced thermal expansion, or improved damping characteristics. These sandwich microplates are used in organic solar cells to improve their efficiency (Li et al. 2019b).

2.5.3 Porous Microplates

Metal foam materials are increasingly being used in microstructures. Metal foams are created by introducing gas into a metallic melt and solidifying it (Kitazono et al. 2004; Miyoshi et al. 1998; Nakajima 2007). In microstructure applications, these porous metal foam materials provide various benefits. These include increased specific capacity and stability of lithium-ion batteries (Zhang et al. 2014) and improved control of the local chemical environment in gas sensors (Jing and Zhan 2008). Solar cell performance is enhanced (Mohamad 2005) because of the high surface area and higher combustion efficiency of porous media (Mustafa et al. 2022). Thus, it becomes necessary to model the reduction in stiffness of microplates brought on by the incorporation of porosity.

The microplates in chips or organic solar cells are often placed on a flexible medium. The combination of porosity and elastic support in MEMS resonators can enhance their performance by reducing unwanted vibrations and improving sensitivity. Thus, the stiffness provided by the flexible foundation also needs to be modelled. In this regard, Winkler proposed the one-parameter elastic foundation, the simplest model. The foundation is modelled as a collection of independent springs with no coupling effects between them (Winkler 1867). The two-parameter elastic foundation model developed by Pasternak (1954) is still widely used to represent the mechanical interactions of soft plates with varying material property distributions, and it was improved upon by Pasternak's addition of a shear layer over the springs.

2.6 Static Analysis of Microplates

Examining the mechanical characteristics is imperative for fine-tuning the design and enhancing the functionality of microplates. In this section, we embark on a thorough exploration of the extensive research dedicated to scrutinizing the linear and nonlinear static analyses of microplates. The linear static analysis of these structures encompasses a scrutiny of mechanical phenomena, including buckling and bending. Buckling is initiated by in-plane stresses, whereas bending is induced by external out-of-plane loads. The nonlinear analysis of these phenomena incorporates geometric nonlinearity to investigate the nonlinear bending and post-buckling reactions exhibited by microplates. The studies that focused on the nonlinear static analysis of these structures are discussed in the subsequent subsection.

2.6.1 Linear Analysis

2.6.1.1 Bending

The linear stability analysis of the microplates under out-of-plane loading, i.e., bending analysis is studied using many analytical, numerical, and experimental methods by different researchers. These microplates have been modelled based on different plate theories and size-dependent theories. The governing differential equations have been solved by implementing various solution methodologies. In this context, (Tsiatas 2009) developed a MCST and CPT based model to conduct bending analysis on isotropic microplates made with varying shapes. The governing equations were derived through the application of the minimum potential energy principle, and the solution to the boundary value problem was achieved using the method of fundamental solutions, a boundary-type meshless approach. Ma et al. (2011) performed the bending analysis of MCST and FSDT based simply supported microplates. The governing equations were obtained using the Hamilton’s variational principle and were analytically solved to obtain the closed-form solutions. Roque et al. (2013) modelled the MCST and FSDT based simply supported isotropic microplates and performed their static bending analysis using a meshless numerical method. This method used the radial basis functions method along with the collocation method. The results of the numerical method were found to be in close agreement with the analytical solutions. Zhou and Gao (2014) solved the static bending problem of MCST and FSDT based circular microplates under axisymmetric loading. The governing equations were derived using the Hamilton’s method and solved analytically using the Fourier-Bessel series. They concluded that the effect of size-dependent theory is enhanced as the plate thickness decreases. The static bending analysis of MCST and FSDT based sigmoidal FG microplates was performed by Jung et al. (2014b). The microplates were assumed to be resting on Pasternak elastic medium. The governing equations derived using Hamilton's method were analytically solved and subjected to parametric analyses. Alinaghizadeh et al. (2017) performed the bending analysis of MCST and FSDT based FG annular microplates. The power law function was used to model the functionally graded behaviour. The governing equations were derived using the principle of minimum potential energy and further solved using the generalized differential quadrature method. The parametric effect of geometric parameters, length-scale parameters and power-law index was also performed. He et al. (2017) studied the static bending analysis of MCST and FSDT based composite skew laminated plates. The governing equations were derived using the principle of minimum potential energy and the central deflection was obtained using the Rayleigh-Ritz method. The effect of the orientation of the lamina on the small-scale effects was also studied. Gao et al. (2013) used the TSDT along with the MCST for better capture of the shear deformation effects of microplate. The Hamilton-derived governing equations were analytically solved to study the static bending and free vibration behaviour of the microplate. The MCST and TSDT based model for FG microplates was developed by Thai and Kim (2013). The derived governing equations were analytically solved to study the bending and free vibration. The MCST and TSDT based microplate model for composite laminated microplates was first developed by Chen et al. (2012).

Ashoori Movassagh and Mahmoodi (2013) presented the first MSGT and CPT based isotropic simply supported and clamped microplate models to present their static bending analysis. The governing PDEs were derived using the principle of minimum potential energy and further used the extended Kantovorich method to obtain the approximate closed-form solutions. Wang et al. (2016) extended the MSGT and CPT microplate model to study the effect of several other boundary conditions, including those with free edges. The extended Kantovorich method was used to obtain the solutions. Zhang et al. (2015b) developed an FG microplate model using the strain gradient elasticity and the refined shear deformation theory. The governing equations were derived using Hamilton's principle and solved analytically using Navier's method to estimate the bending, buckling and free vibration behaviour. The effect of the two parameter Winkler-Pasternak elastic foundations was also considered. A parametric analysis of the foundation parameters, and shear deformation effects was also performed. A similar study was performed by Akgöz and Civalek (2015) on MSGT based simply supported square microplates using the sinusoidal shear deformation theory. The governing equations were solved analytically using Fourier series solution. The parametric change in shear deformation with the thickness of the microplate was also studied.

Eshraghi et al. (2016) studied the static bending and free vibration analysis of MCST based circular and annular microplates under thermal loading. The shear deformation effects were modelled using a unified theory to present results from CPT, FSDT and TSDT using a single theory. The governing equations were solved using the differential quadrature method and the parametric effect of thermal magnitude, geometry and other parameters was considered. Arefi and Kiani (2020) studied the bending behaviour of the sandwich microplates with exponentially graded core with piezomagnetic face-sheets and modelled using MCST and FSDT. The microplate was assumed to be resting on Pasternak foundations. Farzam and Hassani (2019) examined the thermal bending and buckling behaviour of MSGT based FG microplates. The refined hyperbolic shear deformation theory was used to model the shear deformation effect and the problem was solved using the isogeometric analysis (IGA) with the help of Non-Uniform Rational B-Spline (NURBS) functions.

2.6.1.2 Buckling

Understanding the behaviour of microplates under mechanical loading, specifically their buckling phenomenon, is of paramount importance due to its implications on the reliability and performance of microscale devices. Buckling, in this context, refers to the sudden and often catastrophic deformation that occurs when a microplate undergoes in-plane compressive stresses beyond a critical limit. The buckling behaviour of microplates is a complex and multifaceted phenomenon influenced by numerous factors, including material properties, geometrical configurations, boundary conditions, and environmental conditions. In this context, several researchers have focused on analysing the buckling behaviour of microplates using various size-dependent and plate theories.

Akgöz and Civalek (2013) developed a MCST and CPT based microplate model to analyse their buckling, bending and free vibration. The governing equations were derived via Hamilton’s principle and analytically solved using Navier’s method. The plate’s resting medium was modelled in the form of Winkler foundation. Ke et al. (2012c) studied the buckling, bending and free vibration of FG microplate modelled using the MCST and the FSDT. The governing equations were solved using the differential quadrature method. Annular microplates with hinged-hinged and clamped-clamped microplates were analysed. Jung et al. (2014a) studied the buckling response of MCST and FSDT based sigmoidal FG microplate. The plate was assumed to be resting in a Pasternak elastic medium. The governing equations were derived using minimum potential energy and solved analytically using Navier's approach. Jung and Han (2015) developed a TSDT and MCST based FG microplate model to study their buckling, bending and free vibration. The FG behaviour was included using the sigmoidal power law function. The governing equations were solved using the Navier's approach. The effect of biaxial compression, and tension was also included.

The critical buckling load of a MSGT and CPT based microplate model were obtained by Mohammadi and Fooladi Mahani (2015). The governing equations were solved analytically using the Levy's method. The microplate was assumed to be simply supported on two opposite edges. Hosseini et al. (2016) performed the buckling analysis of an orthotropic multi-microplate system under bi-axial compressive loads in a Pasternak medium. The microplate model was based on MSGT and CPT. They used various systems of boundary conditions and obtained the solutions using Navier's method. They concluded that the increase in number of plates lessened the effect of the Pasternak foundation. Ansari et al. (2015c) developed a FSDT and MSGT based microplate model for circular/annular microplates. The governing equations were derived using Hamilton's principle and the buckling, free vibration and bending results were obtained using the generalized differential quadrature (GDQ) method. In another study, Ansari et al. (2016) performed the buckling, free vibration and bending analysis of FG rectangular microplate models based on MSGT and FSDT. The solutions were obtained using the GDQ method. Zhang et al. (2015a) developed a TSDT and MSGT based microplate model for the buckling, free vibration and bending analysis of FG circular/annular microplates. The governing equations were solved using the GDQ method.

In the case of thermal loads, in-plane stresses develop. These temperature induced stresses also lead to buckling at a certain temperature, known as the critical buckling temperature. Several researchers have studied the buckling of microplates due to these temperature-induced stresses. Ashoori and Sadough Vanini (2016a) developed a MCST and CPT bases FG microplate model for annular microplates. The governing equations were developed in curvilinear coordinates and later converted to polar coordinates. Various forms of thermal loads, including uniform temperature rise, linear temperature rise and heat conduction through the thickness were considered. The elastic foundations were also included in the model. Arshid et al. (2021)

performed thermal buckling analysis of FG graphene nanoplatelet (GNP) reinforced porous microplate resting on Pasternak foundation. The microplate model was based on MCST and FSDT. The effective properties were calculated using the Halpin-Tsai and extended rule of mixtures and the governing equations were solved using the GDQ method. Trinh et al. (2017) performed the thermal buckling analysis of an FG microplate modelled using MCST and a quasi-3D theory. A 2D model using the refined shear deformation theory is also developed. The difference between the results of 2D model and 3D model is presented. The temperature-dependent material properties were considered in the modelling. Khorshidi et al. (2018) developed an exponential shear deformation theory (SDT) and MCST based FG microplate model to study the thermal buckling behaviour of microplates. The microplates are often placed on elastic media and the governing ODEs were obtained using the Rayleigh-Ritz method. Farzam and Hassani (2018) studied thermal buckling and bending behaviour of MCST based microplates modelled using refined hyperbolic SDT and solved using isogeometric analysis (IGA). The thermal buckling problem of porous sandwich microplates under hygro and thermal loads was analytically solved by Sobhy (2020). The microplate was modelled using MCST and a four variable higher order shear deformation theory. Sobhy and Zenkour (2019) extended the above work for exponentially graded microplates resting on Winkler-Pasternak elastic foundation. Fang et al. (2023) studied the thermal buckling and vibration behaviour of MCST and TSDT based FG GNP reinforced porous microplates. The governing equations were derived using the Galerkin’s weak form and solved using the finite element method (FEM).

The thermal buckling analyses of flexural microplates was studied by (Farahmand et al. 2011). The microplate was modelled using MSGT and FSDT. The governing equations were derived using Galerkin’s weak form method and solved using higher continuity p-version finite elements. The mode jumping on variation in aspect ratio of microplate was also discussed. The coupled temperature and displacement field equations of functionally graded (FG) microplate were solved using Navier’s analytical solutions by Emami and Alibeigloo (2016). The microplate model was developed using MSGT and FSDT. Ansari et al. (2013) performed the parametric thermal buckling analysis of MSGT and FSDT based FG microplates due to linear, non-linear and uniform temperature rises. The critical buckling temperature was evaluated for different boundary conditions using the GDQ method. Malekzadeh et al. (2018) performed the thermal buckling analysis of MSGT and FSDT based triangular microplates using Ritz method. The Chebyshev-Ritz method was used to solve the governing equations. The temperature dependent properties were considered and the nonlinear equations were solved using the direct iterative technique. The effect of apex angle on the critical buckling temperature was assessed. Arefi et al. (2019) performed the thermal and mechanical buckling analysis of FG graphene nanoplatelet reinforced microplate modelled using MSGT and several HSDTs including the TSDT. The governing equations were analytically obtained. Various distributions of GNPs and their effect on the buckling load were considered.

2.6.2 Nonlinear Analysis

The microplates are extremely thin and small plates that often experience large deformations, leading to geometric nonlinearity. The linear analysis methods often fail to capture the mechanical behaviour exhibited by microplates when subjected to significant deformations or loads. As the plate bends and stretches, the assumptions of linear elasticity no longer hold. Nonlinear analysis accounts for the changing geometry and provides insights into the microplate's response to these deformations. Thus, nonlinear analysis of microplates is a critical aspect of research and engineering. The static nonlinear analysis of microplates includes the examination of nonlinear bending and post-buckling responses. The literature review of studies that focused on nonlinear bending and post-buckling of microplates is presented in the subsequent subsections.

2.6.2.1 Nonlinear Bending

In the presence of out-of-plane loads, the microplates undergo large deformations. Microplates may experience stretching, twisting, and warping that are not accounted for by linear theory. Nonlinear bending analysis considers these large displacements and provides a more realistic representation of the plate's response to applied loads. The inclusion of geometric nonlinearity is required in the plate models for their nonlinear bending analyses. In this context, Wang et al. (2014) performed the nonlinear bending analysis of MCST and CPT based circular microplate models with the inclusion of von Kármán geometric nonlinearity. The governing equations were reduced to nonlinear algebraic equations using the orthogonal collocation point method and the nonlinear bending curve was obtained numerically using the Newton-Raphson method. Parametric analysis of fixed, clamped and simply supported microplates was presented.

Reddy and Berry (2012) presented a nonlinear formulation for modelling of FSDT and MCST based FG circular microplates. The FG behaviour was included using the power-law function. The nonlinearity was included in the form of von Kármán nonlinear strains. The nonlinear bending results could be obtained using finite element models on this formulation. Thai and Choi (2013) presented a nonlinear MCST model for FG microplate. The CPT and FSDT plate theories were employed and the von Kármán geometric nonlinearity was included. The material properties were varied according to the power law. The buckling, bending and free vibration was computed using the Navier approach and the nonlinear bending solutions were obtained using the Bubnov-Galerking method. Reddy and Kim (2012) developed a MCST and TSDT based formulation including von Kármán geometric nonlinearity for FG microplates. This theory can be used to study the nonlinear bending behaviour of moderately thick microplates as it includes the parabolic variation of transverse stresses along with the geometric nonlinearity considerations. The FG behaviour with two materials was modelled using the power law function.

2.6.2.2 Post-Buckling

In the presence of in-plane compressive stresses, at a certain critical load, the microplates undergo loss of stability as it moves from stable equilibrium to neutral equilibrium, known as buckling. In the presence of a small perturbation, the microplate can undergo large lateral deformations. Post-buckling behaviour refers to the behaviour of a microplate after it has buckled. It involves the plate undergoing further deformation and displacement, but unlike the linear regime, this deformation is highly nonlinear due to the nonlinear geometric stiffness. Understanding the stability of microplates during post-buckling is essential. Engineers and researchers analyse the post-buckling behaviour to determine whether the deformed configuration is stable or whether further deformation may lead to structural failure. In this context, (Taati 2016) developed a MCST and CPT based FG microplate model to study their buckling and post-buckling behaviour. The simply supported and clamped-simply supported boundary conditions were considered along with biaxial compression, in-plane shear, and uniform transverse loads. The parametric results indicate that the aspect ratio of the microplate has a large effect on the post-buckling response. Ke et al. (2014) developed a nonlinear model of MCST and FSDT based rectangular FG microplates. In order to nullify the coupling of bending and stretching in FG plates, the physical neutral plane position was considered. The governing equations were derived using the principle of virtual work and further discretized using the GDQ method. The post-buckling response was obtained using the direct iterative method. Ansari et al. (2015b) also developed a nonlinear model of MCST and FSDT based rectangular FG microplates similar to that of Ke et al. (2014). The post-buckling response was obtained in this study using the pseudo-arclength continuation technique. In this approach, an iterative solver is employed to introduce an extra constraint into the set of nonlinear equations. This constraint is used to locate a point along the specified pseudo-arclength. In another research Ansari et al. (2014a) studied the post-buckling behaviour of MCST and FSDT based FG microplates. The governing equations were derived using the Hamilton’s principle and further discretized using the GDQ method. The post-buckling response of microplates with various support conditions was numerically computed using the pseudo arc-length continuation technique. Further, the free vibration of microplates in the buckled configuration was computed. Malikan (2018) studied the post-buckling analysis of sandwich microplates using the MCST and FSDT based microplate model including the von Kármán nonlinearity. The analytical method was used to get the exact results for different boundary conditions. The research demonstrated that the highest and lowest critical load values are associated with the boundary conditions of the microplate. Wu et al. (2018) examined the post-buckling response of MCST and FSDT based microplate models. The resting medium was modelled with the help of a nonlinear elastic foundation. The derived governing PDEs were solved using the Galerkin’s method to obtain closed form solutions for the buckling load and post-buckling equilibrium path. The effect of in-plane boundary conditions on the buckling and post-buckling behaviours was discussed. Qiu et al. (2020) studied the post-buckling response of porous FG microplate modelled using MCST and TSDT. A power law function with the inclusions of porosity was used to model the material properties of the porous FG microplate. The NURBS based isogeometric method was used for the discretization to satisfy the continuity conditions. A comprehensive parametric analysis including the porosity and boundary conditions was performed.

The in-plane compressive stresses also develop due to thermal loads. Thus, the thermal post-buckling analyses of microplates has also been investigated by some researchers. Ashoori and Sadough Vanini (2016b) developed nonlinear models of MCST and CPT based perfect/imperfect circular FG microplates. The FG behaviour was included using the power law and Voigt’s rule. The Ritz finite element method is used to discretize the governing equations. The snap-through phenomenon in post-buckling in the case of concentrated or uniform lateral loads is also addressed. The post-buckling path is traced using the direct-displacement scheme for bifurcation type instability and the Newton-Raphson method or stable responses. Zandekarimi et al. (2017) studied the post-buckling response of MCST and CPT based FG circular microplate including the von Kármán nonlinearity. The equations were discretized using the GDQ method and the post-buckling path was traced using the direct iterative technique. Uniform temperature rise and clamped boundary conditions were considered for the analysis. The post-buckling strength of MSGT and TSDT based FG microplates, including the von Kármán nonlinearity under mechanical and thermal loads was studied by Thai et al. (2017c). The FG behaviour was modelled using the rule of mixtures and models with both temperature-dependent and temperature independent properties were analysed. The governing equations were discretized using the isogeometric analysis and the post-buckling path was obtained using the Newton-Raphson method. Zuo et al. (2021) examined the thermal post-buckling response of porous FG microplate modelled using MSCT and quasi 3D higher order theory. The microplate was assumed to have a central cutout of varying geometries. The porous and temperature-dependent properties were modelled using the refined power-law function along with the Touloukian scheme. The governing equations are discretized using the NURBS based isogeometric analysis. The results indicate that the central cutout causes a decrease in initial post-buckling strength. Ansari et al. (2014c) used a MSGT and FSDT based model to examine the thermal post-buckling behaviour of FG annular microplates. The governing equations for microplates with different boundary conditions were developed and discretized using the GDQ method. The post-buckling equilibrium path was plotted using the pseudo arc-length continuation method.

2.7 Dynamic Analysis of Microplates

The dynamic analysis of microplates involves the study of their vibrational and oscillatory behaviour, including natural frequencies, mode shapes, and responses to external forces. This analysis is essential for designing microsystems, predicting resonance-related issues, and understanding the dynamic characteristics of microplates in various applications. This section focuses on the research works that are aligned towards the dynamic analysis of microplates. In the first subsection, studies focusing on linear dynamic analysis, i.e., free vibration and linear dynamic instability region are discussed. In the next subsection, studies that focus on the nonlinear dynamic analysis of microplates i.e., analysing their nonlinear free vibration, nonlinear forced vibration and nonlinear dynamic responses are discussed.

2.7.1 Linear Analysis

Linear dynamic analysis of microplates encompasses the study of their vibrational behaviour, both in terms of free vibration (undriven oscillations) and linear dynamic instability (buckling or vibrational instability under external forces). This analysis is essential for understanding how microplates respond to various mechanical and vibrational loads. In the following subsections, the various mathematical models, solution methodologies, microplate characteristics and key results presented by the various research works that discussed linear dynamic analysis of microplates are discussed.

2.7.1.1 Free Vibration

Free vibration analysis involves the study of how microplates vibrate naturally when they are not subjected to any external forces. This analysis helps identify natural frequencies and mode shapes, enabling engineers and researchers to tailor the characteristics of microplates to specific applications and performance requirements. In this context, Yin et al. (2010) and Jomehzadeh et al. (2011) studied the free vibration behaviours of MCST and CPT based microplate models, determining their fundamental frequency. Jomehzadeh et al. (2011) performed the analysis on rectangular and circular microplates with several boundary conditions. The governing equations were derived using the Hamilton's principle and analytically solved using the Levy's method. Akgöz and Civalek (2012) studied the free vibration of single layered graphene sheets modelled using MCST and CPT. The elastic medium was also included in the model using Winkler foundation. The results obtained using Navier's analytical method indicate that the effect of size-dependent theory amplifies for higher modes of vibration. Askari and Tahani (2015) also studied the vibrational analysis of MCST and CPT based fully clamped rectangular microplates. The governing equations were solved analytically using the extended Kantorovich method. Asghari and Taati (2012) performed the free vibration analysis of MCST and CPT based FG microplates with random shapes. The boundary conditions were provided at the smooth parts and the sharp corners of the periphery. Ma et al. (2011) performed the free vibration analysis of MCST and FSDT based simply supported microplates. The governing equations were obtained using the Hamilton's variational principle and were analytically solved to obtain the closed-form solutions. The results are compared with the classical plate theory. (Ke et al. 2012b) also modelled the MCST and FSDT based microplates with simply supported and clamped boundary conditions for their free vibration analysis. The governing equations were numerically solved using the p-version Ritz method. The natural frequencies of MCST and TSDT based simply supported microplates Gao et al. (2013), FG microplates (Thai and Kim 2013) and sandwich microplates (Chen et al. 2012) were analytically solved. Eshraghi et al. (2015) derived governing equations of MCST and TSDT based circular/annular microplate models using Hamilton's principle and obtained the natural frequencies by solving the equations using the GDQ method. Thai and Vo (2013) derived governing equations of MCST and sinusoidal shear deformation theory based FG microplate models and solved them analytically to study their free vibrations. (Darijani and Shahdadi 2015) used a HSDT with separate bending and shear components to accurately model the shear deformation effects while maintaining only four variables. The free vibration of an MCST based microplate was analytically solved using the proposed theory. (2015) also performed free vibration analysis of a MCST based microplate. The field displacement equations were modelled using a HSDT that accounts for parabolic variation of both normal and shear deformations. Fang et al. (2023) studied the buckling and vibration behaviour of MCST and TSDT based FG GNP reinforced porous microplates. The governing equations were discretized using the Galerkin's weak form and finite element method (FEM).

The effect of strain gradient was included in the free vibration analysis of FG quadrilateral microplates by Shenas and Malekzadeh (2016). The microplate model was based on MSGT and FSDT and modelled in a thermal environment. Sahmani and Ansari (2013) obtained analytical solutions of MSGT and TSDT based microplates to study their free vibration behaviour. Zhang et al. (2015b) analytically studied axisymmetric bending, buckling, and free vibration of circular and annular microplates modelled using the MSGT and the refined SDT. The microplates were modelled in a Winkler-Pasternak elastic foundations. The nonlinear free vibration response of functionally graded microplates with cracks was investigated by Nguyen et al. (2019). The microplate was modelled using MCST and the refined FSDT. The linear free vibrational frequency was obtained using the NURBS based isogeometric analysis. Thai et al. (2020b) investigated the free vibration analysis of functionally graded (FG) anisotropic microplates using the MSGT in conjunction with the exponential HSDT. The derived governing equations were discretized using isogeometric analysis. Parametric analysis of the natural frequencies obtained was also performed. Hung et al. (2022) modelled a MSGT and refined HSDT based metal foam microplate. The porosity of different kinds of distributions was included in the model. The governing equations were solved using the isogeometric analysis to obtain the free vibration results.

2.7.1.2 Dynamic Instability

Parametric resonance of microplates is a phenomenon that occurs when thin, flexible plates or beams vibrate in response to an external periodic force or excitation whose frequency is modulated or varies with time. In parametric resonance, under some combinations of the driving frequency of the external force, the load magnitude and natural frequencies of microstructure, the microstructure goes into resonance, causing the amplitude of vibration to grow significantly. This can lead to large deformations, instability, or even failure of the microplate. Understanding and predicting dynamic buckling instability in microplates is essential for the design and optimization of microdevices, sensors, and actuators. Researchers use various analytical and computational techniques, such as finite element analysis (FEA), to simulate and analyse the behaviour of microstructures under dynamic loading conditions.

The dynamic stability of FGM microbeams was studied by Ke and Wang (2011). The microbeam was modelled using MCST and TBT and solved using the GDQ method. The boundaries of the instability region were computed using Bolotin's method. The influence of various parameters such as the gradient-index, length scale parameter, and boundary conditions on the dynamic stability response was also investigated. Gholami et al. (2014) observed the influence of static load factor, axial wave number, length to thickness ratio on the dynamic instability region of an FGM microshell. The PDEs were solved using Navier's method and the instability boundaries using Bolotin's method. Sahmani et al. (2013) performed a parametric study on cylindrical microshells using the higher-order shear deformation shell theory to count for the shear deformation effect. The author found no study where the dynamic buckling instability region of microplates modelled using strain gradient or couple stress based theories was computed.

2.7.2 Nonlinear Analysis

Nonlinear dynamic analysis of microplates is a specialized field of study that focuses on understanding the mechanical behaviours exhibited by plates at the microscale under dynamic conditions. Unlike linear analysis, which assumes linear relationships between forces and displacements, nonlinear analysis takes into account the nonlinearities in the material properties, geometry, and boundary conditions of microplates. In practical situations, the inclusion nonlinearities in the plate models are essential to accurately predict their nonlinear behaviour. In the absence of nonlinearity, the structures undergo unbounded amplitudes when subjected to instabilities. However, this is not the case. The inclusion of nonlinearity can help predict the deformations under these instabilities. The nonlinear analysis is crucial for designing and optimizing microelectromechanical systems (MEMS), microsensors, and other microscale devices where precise control and accurate predictions of mechanical responses are essential. In this section, the studies that focused upon the nonlinear dynamic analysis of microstructures are discussed. The studies that performed nonlinear free vibration analysis of microstructures are discussed in subsection 2.7.2.1. The studies that focused on nonlinear forced vibration analysis are discussed in 2.7.2.2. In subsection 2.7.2.3, the studies where the nonlinear dynamic response of structures is performed using time-history analysis are discussed.

2.7.2.1 Nonlinear Free Vibration

The number of studies pertinent to the analytical schemes for the investigation of the linear free vibration responses of the micro/nano- structures is considerable. In order to investigate the nonlinear behavior of free vibration micro/nano-structures, numerical methods were used by the researchers.

The nonlinear free vibration of FSDT and MCST based FG microbeams was performed by Ke et al. (2012a). The governing equations were derived using Hamilton's method and solved using an iterative differential quadrature method to obtain the nonlinear vibrational frequency versus amplitude curve. Wang et al. (2013b) studied the nonlinear free vibration analysis of circular microplates modelled using the MCST and CPT with clamped and simply supported conditions. The governing PDEs were reduced to ODEs using the Kantorovich method. The frequency versus amplitude curve is plotted using the numerical shooting method and a parametric study of the nonlinear free vibration is presented. Ke et al. (2013) examined the nonlinear free vibration of FG microplate models based on MCST and FSDT, including von Kármán nonlinearity. The nonlinear free vibrations for different boundary conditions were computed using a modified iterative method along with the differential quadrature method. Ansari et al. (2014b) studied the non-linear free vibration response of FSDT and MCST based microplate models. The frequency-amplitude curve was obtained by solving the nonlinear algebraic equations using the pseudo arc-length method. A parametric study of factors such as gradient index, length scale parameter, etc., was done on the nonlinear vibration response. Lou and He (2015) included the effect of elastic foundations for the computation of the nonlinear free vibrations of MCST and FSDT based FG microplates. The stretching-bending coupling was avoided by the assumption of a physical neutral surface. The PDEs were reduced to ODEs using the Galerkin's method and closed form solutions of nonlinear free vibration were obtained using He's variational method. Lou et al. (2016) extended the above work for nonlinear vibrations and bending by modelling the microplate using MCST and a refined FSDT.

The nonlinear free vibration analysis of trapezoidal microplates in a thermal environment was studied by Shenas et al. (2022). The FG microplate was modelled using the four variable refined plate theory and the MSGT including von Kármán nonlinear strains. The FG behavior was modelled using Mori-Tanaka's rule of mixture and the nonlinear vibrational frequency was obtained using a iterative procedure along with the Chebyshev-Ritz method.

2.7.2.2 Nonlinear Forced Vibration

Understanding the nonlinear forced vibration of microplates, both in the context of simple harmonic resonance and parametric resonance, is essential for the design and optimization of MEMS devices, sensors, and other microscale systems. Engineers and researchers have considered the intricate interplay between geometric nonlinearity and resonance conditions to predict and control the response of microplates under external excitations. A review of the literature that focused on nonlinear forced vibration behavior of microplates is presented in this subsection.

In case of out-of-plane external periodic excitations, a duffing type equations is obtained which leads to a simple harmonic resonance condition. The static response of the microstructure under such loading and its variation with the frequency of the excitation has been presented by several authors using the frequency-amplitude curves. Loghman et al. (2021) analyzed the nonlinear vibration response of a viscoelastic microbeam modelled using the MCST and the classical beam theory. The viscoelastic behavior was modelled using the Kelvin-Voigt Model. The finite difference method (FDM) and the Galerkin's method were used to discretize the governing equations. The Shooting method was coupled with the FDM to trace the frequency-amplitude curve. Ghayesh et al. (2013c) examined the nonlinear forced vibration of a microbeam modelled using the MCST and the classical beam theory with geometric nonlinearity considerations. The microplate was subjected to a harmonic transverse excitation. The governing PDEs were reduced to ODEs using the Galerkin's method. The numerical solution of the nonlinear ODEs was obtained to plot the frequency-amplitude curve using the pseudo-arclength continuation technique and the higher mode Galerkin's discretization. The effect of damping was also traced as this method allowed to trace both the stable and unstable curves, including the bifurcation points. Farokhi et al. (2013) further extended the above study by including the effect of initial curvature in the microbeams while computing their nonlinear frequency response under transverse excitations. Farokhi and Ghayesh (2015) extended the above study to the study of microplates. The microplate was modelled using the MCST and the CPT including the von Kármán geometric nonlinearity. Initial curvature was included in the transverse direction and the Lagrange's equations were obtained. The frequency response was computed using the arc-length continuation technique and the effect of initial curvatures, forcing frequencies on the nonlinear steady-state response was analysed. Mirjavadi et al. (2019) studied the nonlinear free and forced vibration response of a microbeam reinforced with graphene nanoplatelets with uniform harmonic loading at its top surface. The material properties were computed using the Halpin-Tsai micromechanical model. The effect of geometric imperfections was included and the MCST and classical beam theory-based model was assumed to be resting on a nonlinear elastic foundation. The nonlinear frequency response of the microbeam was computed using the incremental harmonic balance (IHB) method. The nonlinear systems may consist of various types of nonlinearities. The classical perturbation systems, such as the multiple scales method, can only solve systems with weak nonlinearity (Bajkowski and Szemplińska-Stupnicka 1986). IHB serves as a systematic and reliable computer method for analysing strongly non-linear periodic vibrations of multiple DOF. Ghayesh (2019) analyzed the forced vibration response of a viscoelastic FG microcantilevers resting on elastic foundations. The microcantilever was modelled using the MCST and the classical beam theory. The frequency response was obtained using the Galerkin's technique and analyzed comprehensively with inclusions of internal resonance. Saghir and Younis (2018) examined the forced vibration response of imperfect microplates. The microplate was modelled using the MCST and the CPT and the governing PDEs were solved using the Galerkin's method. The forced frequency response of the plate under a harmonic AC voltage was computed and its variation with the initial curvatures was assessed. Ghayesh et al. (2020) analyzed the frequency response curves of imperfect MCST and CPT based microplates under transverse periodic excitations. The effect of initial curvatures and nonlinear viscoelastic damping was included. The viscoelasticity was modelled using Kelvin-Voigt based model. The frequency response curves illustrated a large impact of imperfection and damping on the bifurcation points and the large amplitude vibrations.

Ghayesh et al. (2013a) studied the nonlinear forced vibration behavior of MCST and first order beam theory based microplate models in order to include the effect of shear deformation for moderately thin microbeams. The governing PDEs were discretized using the Galerkin's method and the frequency response was plotted using the arc-length continuation method. A parametric analysis of the frequency-response and force-response curves was presented. The arc-length continuation method utilized as the incremental method in IHB is a predictor-corrector method in which tangent prediction calculates the predicted point by advancing a specified arc-length in the direction of the tangent (Wu et al. 2022). It can pass through the juncture and continue following the solution branch. This method may easily trace the snap back and snap through cases that cannot be traced using the Newton-Raphson iteration method. Additionally, the arc length method minimizes the required number of iterations to obtain the answer, hence reducing the computing cost. In order to model the shear deformation effects more accurately, Ghayesh et al. (2013b) developed a MCST and TSDT based nonlinear microplate model. The Lagrange's PDEs were reduced to ODEs using an assumed-mode method. The frequency and force responses were plotted using a direct time integration technique and the arc-length continuation method. Time-history response and phase plots were also shown for a more comprehensive dynamic analysis. Das (2019) studied the effect of geometric nonlinearity on FG microbeam modelled with HSDT and MCST. The stable regions of the frequency-amplitude curve were solved by a mixed algorithm of iterative substitution method with successive relaxation and Broyden's method. The beam was assumed to be supported on a three-parameter Winkler-Pasternak-type nonlinear elastic foundation and the influence of change in foundation parameters was observed. Liu et al. (2021) performed a parametric study on the non-linear vibration response of FG piezoelectric cylindrical shells. The shells were subjected to thermo-electro-mechanical load. The multi-mode Galerkin's scheme was used in conjugation with the Pseudo-arc length continuation method to obtain the nonlinear internal resonances and bifurcations of the system.

Timoshin et al. (2021) for the first time investigated the non-linear forced vibration response of microplate modelled using the MSGT and FSDT. The nonlinear forced vibration response was obtained using a finite element method based on rectangular hermitians. Various parametric studies were performed on the forced vibration response.

2.7.2.3 Nonlinear Dynamic Response

Analyzing the nonlinear steady-state and transient dynamic response of microplates using time history plots is a valuable approach to understanding their complex behaviors. Time history plots depict how the response of a microplate changes over time, providing insights into the plate's behavior under various conditions and loads. Researchers and engineers have used these plots to make critical design decisions, optimize microscale systems, and ensure reliable operation. A few research works are available in the literature where the steady-state and transient dynamic response of microplates have been studied. In this context, Şimşek et al. (2015) investigated the nonlinear dynamic response of CPT and MCST based microplate models under a moving load. The governing equations were derived using Lagrange's equations. A polynomial trial function was introduced to model the dynamic deflection, enabling calculating the microplate's dynamic responses. The time history plots were plotted solving the governing equations in time domain using the Newmark-β implicit direct time integration method. Şimşek and Aydın (2017) extended the above research to the study of nonlinear dynamic response of FG microplates modelled using MCST and FSDT under moving load. The effect of porosity was also included and neutral surface concept was used to accurately model for FG plate. The formulation for computing the time history response was the same as that in the previous research. The nonlinear dynamic response of MSGT and TSDT based microplates with von Kármán nonlinearity was first modelled by Thai et al. (2017a). The governing equations were obtained using the Hamilton's principle and further discretized using the numerical NURBS based isogeometric analysis. The dynamic response was plotted under dynamic step loading and exponential blast loading using the Newmark-β time integration method.

Critical Discussion

In literature, several studies are available where the nonlinear forced vibration behavior of couple stress and strain gradient based microplates with simple harmonic resonance was studied. In these studies, analysis of microplates modelled using MCST and TSDT, MSGT and FSDT were available. No study is available, where the nonlinear forced vibration behavior of MSGT and TSDT based microplates were analyzed. More importantly, no study was available where the nonlinear forced vibration behavior of microplates under parametric resonance, i.e., nonlinear Mathieu-Hill equation was studied. A study was available where the transient response of MSGT and TSDT based microplates under step loading and exponential blast loading was studied using the numerical isogeometric analysis. However, no study was found where the nonlinear dynamic response of MSGT and TSDT based microplates was studied, such that the governing ODEs were in exact or approximate closed form solutions.

2.8 Non-Uniform Loading

The loading applied on the microstructures is often localized or with a non-uniform load profile. The in-plane stresses developed are uniform for uniformly loaded plate and non-uniform for localized or non-uniform heating or mechanical loading profile. Some researchers have worked upon the problem of non-uniform loading on plates. FEM has been used to avoid the hassle of computing the analytical expression of in-plane stresses for humped heating profile on rectangular plate (Ko 2004), tent-like temperature distribution (Lal and Singh 2010) and other arbitrarily varying heating profiles on composite plates (Chen et al. 1991; George et al. 2016). Dhotarad and Ganesan (1978) used the finite difference method to solve the problem of plates with various steady state temperature fields. Li et al. (2015) treated the continuous temperature distribution field as discrete temperature distribution elements to avoid analytical expressions. The discrete in-plane stress field was developed by the coupled thermal and elasticity field equations by Ren et al. (2023). Airy' stress function was used to develop the analytical expressions for thermal stresses of functionally graded rectangular plates under localized rectangular heating by Morimoto et al. (2006). Kumar et al. (2017) derived analytical expressions of thermal stress due to doubly symmetric rectangular and circular localized heating profile on composite plate. Swaminathan et al. (2022) investigated the effect of localized edge loadings on the buckling and vibration behavior of porous plates. No study was found in the literature where the analysis of microplates under non-uniform loading was solved using continuum mechanics.

2.9 Research Gaps

Upon conducting an extensive study of the existing literature related to microplate's behaviour, several critical gaps in the current body of research are identified. These are listed below.

1. The exact or approximate closed form solutions of MSGT and TSDT based microplates with geometric nonlinearity inclusions are not available.
2. The dynamic instability analysis of microplates under parametric resonance using non-classical continuum mechanics based on couple stress and strain gradient theories remains unexplored.
3. The analysis of nonlinear free and forced vibrations behaviour of microplates under transverse loading, modelled using MSGT and TSDT based microplates are not available.

4. The nonlinear forced vibration analysis of microplates under in-plane dynamic loading has not been examined using any strain gradient or couple stress theory.
5. The steady-state nonlinear dynamic response of microplates based on MSGT and TSDT has not been examined under periodic loading.
6. The effect of non-uniform or localized in-plane thermal and mechanical loadings has not been considered for analysis of microplates.

2.10 Objectives

The primary objective of the current research is to delve into the vibration, response and stability analyses of microplates using size-dependent continuum theory, when subjected to various forms of localized or non-uniform mechanical loading or thermal loadings. Considering the identified research gaps in the existing literature, the following research objectives are been formulated for the present study.

1. To study the size-dependent buckling and linear dynamic instability region of microplates under localized under non-uniform in-plane loadings.

2. To examine the size-dependent nonlinear forced vibration behaviour and nonlinear dynamic response of isotropic microplates and porous microplates resting on elastic foundations (PMREF) under non-uniform in-plane loading.

3. To investigate the nonlinear free and forced vibrations, and nonlinear dynamic response of FG microplates and PMREF under transverse patch loading.

4. To analyse the thermal buckling and post-buckling behaviours of microplates under localized thermal loading.

3

Mathematical Formulation

3.1 Introduction

Microstructures cannot be modelled using classical continuum theories due to the small-scale effects involved with them. The inclusion of accumulation of dislocations and rotation of grains in the form of strain gradients and couple stress in the continuum theories has allowed modelling of these structures. The microplate structures are modelled in two-dimensional (2D) space as the thickness is very small in comparison to the other dimensions. The three-dimensional (3D) analysis is useful in the case of thick structures with complex geometry, where the transverse shear strains show large variations along the thickness. In 2D analysis, the shear deformation theories are used to model the transverse shear strains with a certain assumption of the variation of the transverse shear strains along the thickness. In this work, the modified strain gradient theory (MSGT) is used to model the small-scale effects of the microplate. The field displacement equations are modelled using the Reddy's third order shear deformation theory (TSDT). The shear deformation effect is thus included with the assumption of parabolic variation of transverse shear strains along the thickness. The strain-displacement equations are obtained with von-Kármán geometric nonlinearity considerations. Different analyses are performed on microplates subjected to localized and non-uniform periodic in-plane mechanical loadings, periodic transverse patch loading, and localized thermal loading. The Rayleigh's damping model is considered to include the damping characteristics of the microplate. The governing partial differential equations (PDEs) are obtained using the Hamilton's principle for the dynamic problem and the principle of minimum total potential energy for the static problem. The pre-buckling stresses due to non-uniform in-plane mechanical and localized thermal loads are also non-uniform. The analytical expressions for these non-uniform stresses are obtained by satisfying the in-plane stress equilibrium equations and solving the strain compatibility condition presented in terms of the Airy's stress function (φ). The nonlinear PDEs are further reduced to nonlinear ODEs for dynamic problem and nonlinear algebraic equations (AEs) for static problem using the strong form Galerkin's weighted residual method.

Various analyses of microplates are done using the ODEs/AEs. The natural frequency and buckling load are calculated by solving the eigenvalue problem. The dynamic instability regions are plotted using the Bolotin's method. The nonlinear free and forced vibrations analyses are performed using the incremental harmonic balance (IHB) method in conjunction with the arc-length continuation method. The nonlinear dynamic response is determined using the implicit Newmark-β time integration technique. The post-buckling equilibrium path is estimated using the modified Newton-Raphson method.

3.2 Material Properties of Microplate

The properties of microplate and loading considered for analysis in this study are: isotropic microplate subjected to non-uniform in-plane loading (Fig. 3.1), functionally graded (FG) microplate subjected to transverse patch loading, porous microplates resting on elastic foundation (PMREF) subjected to non-uniform in-plane loading, PMREF subjected to transverse patch loading, and, PMREF subjected to localized thermal loading. The schematic diagram of isotropic microplate subjected to non-uniform in-plane loading is presented in Fig. 3.1. The functionally graded microplate subjected to transverse patch loading is shown in Fig. 3.2. The PMREF subjected to non-uniform in-plane loading, transverse patch loading and localized thermal loading is presented in Fig. 3.3(a), Fig. 3.3(b), and Fig. 3.3(c) respectively.

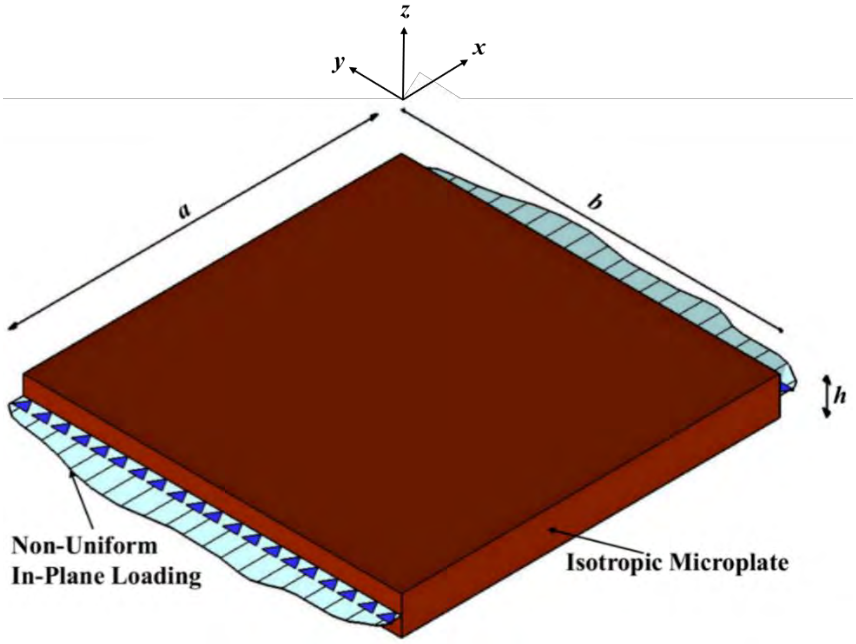

Fig. 3.1 Schematic representation of isotropic microplate subjected to non-uniform in-plane loading

In Fig. 3.1, Fig. 3.2, and Fig. 3.3, the thickness, *h,* of the plate, is considered in the micrometre range. The edge dimensions, ‘*a*’ and ‘*b*’ are considered in certain multiples of the microplate’s thickness. The orthogonal cartesian coordinate system has its origin at the geometric centre of the plate. The material properties of the isotropic microplate (Fig. 3.1) viz. Young’s modulus

‘E’, Poisson’s ratio *‘ν’,* and mass density *‘ρ’*, remain constant throughout the plate, in all directions. The effective material properties of the functionally graded plate and porous microplate are estimated using the equations depicted in the following subsections.

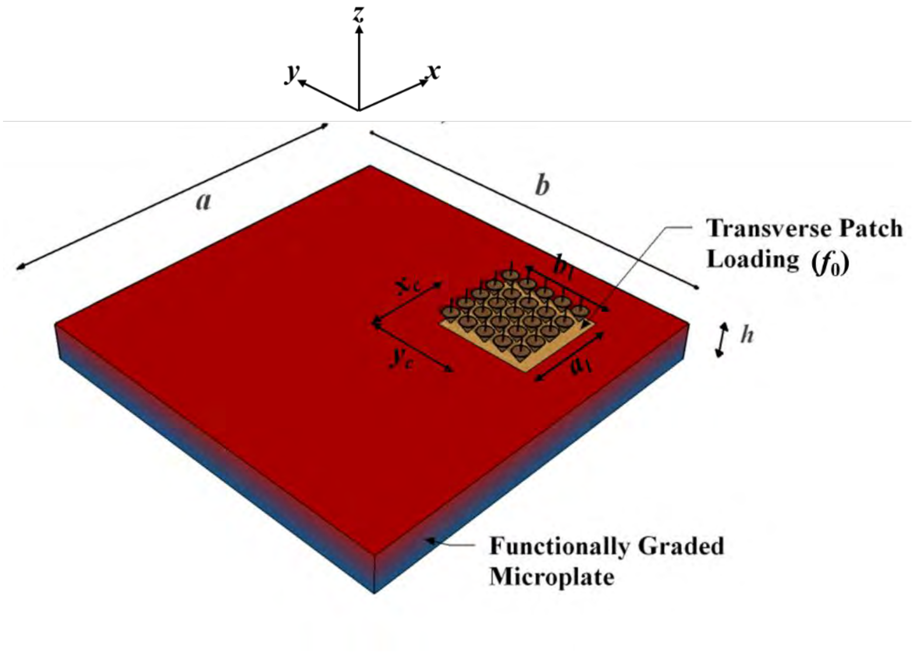
z
y
x
a
b
Transverse Patch Loading (f_0)
b_1
x_c
y_c
a_1
h
Functionally Graded Microplate

Fig. 3.2 Schematic representation of functionally graded microplate subjected to transverse patch loading

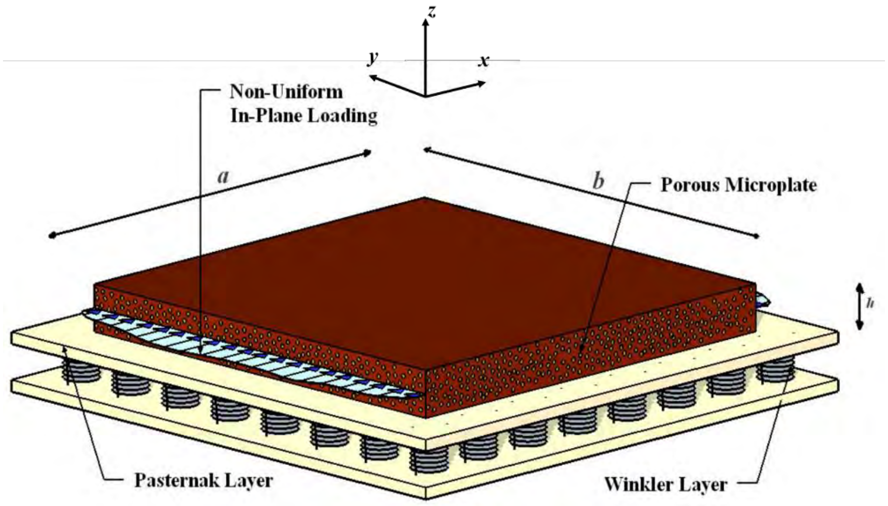
z
y
x
Non-Uniform In-Plane Loading
a
b
Porous Microplate
h
Pasternak Layer
Winkler Layer

(a) PMREF subjected to non-uniform in-plane loading

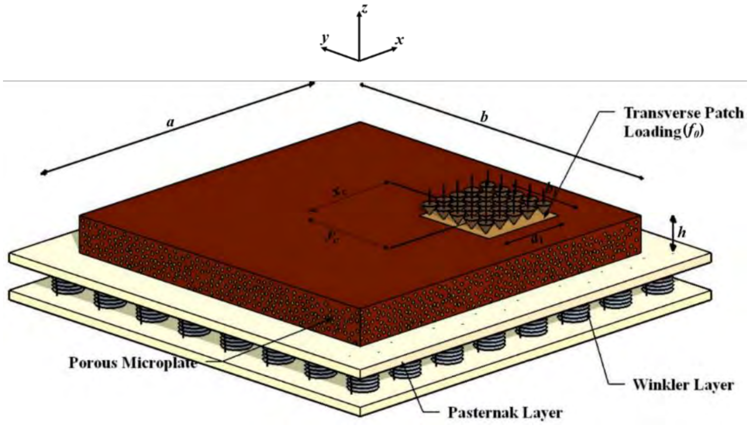
z
y
x
a
b
Transverse Patch Loading(f_0)
h
Porous Microplate
Winkler Layer
Pasternak Layer

(b) PMREF subjected to transverse patch loading

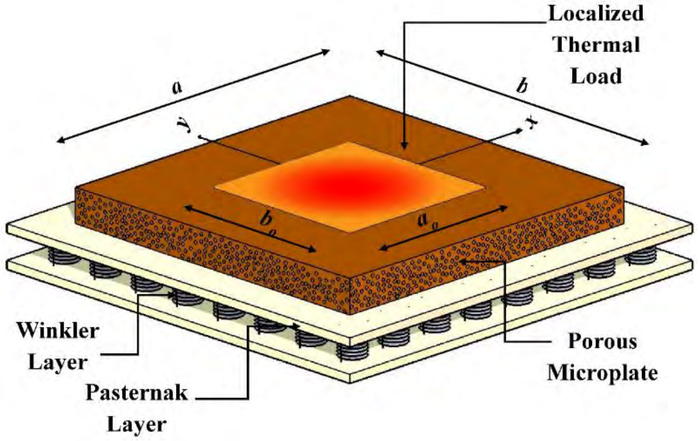
Localized Thermal Load
a
b
y
x
b_0
a_0
Winkler Layer
Pasternak Layer
Porous Microplate

(c) PMREF subjected to localized thermal loading

Fig. 3.3: Schematic representation of a porous microplate resting on elastic foundation (PMREF), subjected to (a) non-uniform in-plane loading, (b) transverse patch loading, and, (c) localized heating

3.2.1 *Material Properties of Functionally Graded (FG) Microplate*

Functionally graded materials (FGM) (Jha et al. 2013) consist of properties from two different materials, metal and ceramic, with effective material properties varying through thickness. The volume fraction of the metal, V_m, and ceramic phase V_c follow the power-law distribution as shown in Eq. (3.1) (Jha et al. 2013). The effective materials properties of the FG microplate (Fig. 3.2) along the thickness viz. Young's modulus *'E(z)'* and mass density *'ρ(z)'*, are related to the metal and ceramic properties as shown in Eq. (3.2) (Jha et al. 2013). The subscript 'c' denotes ceramic properties and 'm' denotes metal properties and 'n' is the power index. The Poisson's ratio, *'ν, '* is assumed to be constant throughout the thickness.

$$V_c(z) = \left(\frac{z}{h} + \frac{1}{2}\right)^n \tag{3.1a}$$

$$V_m(z) = 1 - V_c(z) \tag{3.1b}$$

$$E(z) = E_c V_c(z) + E_m V_m(z) \tag{3.2a}$$

$$\rho(z) = \rho_c V_c(z) + \rho_m V_m(z) \tag{3.2b}$$

3.2.2 *Material Properties of PMREF*

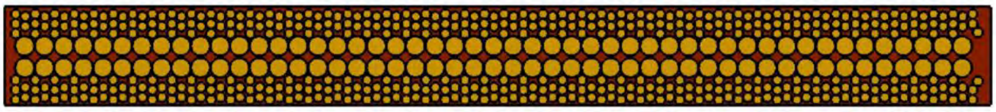

(a) Symmetrically Distributed Porosity

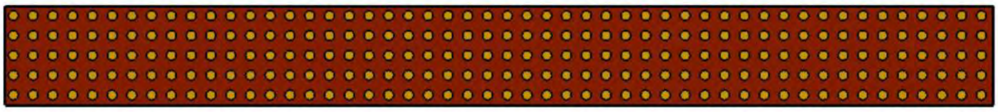

(b) Uniformly Distributed Porosity

Fig. 3.4: Sectional view of the microplate with different types of porosity distributions

The PMREF (Fig. 3.3) rests on Winkler and Pasternak elastic foundations. The Winkler elastic foundation parameter is denoted by K_w and Pasternak elastic foundation parameter is denoted by K_p. It is a porous metal foam microplate with different porosity distributions through the thickness of the plate, such as (a) symmetrically graded and (b) uniformly graded. The sectional view of the microplate with different distributions of porosity is presented in Fig. 3.4. The effective materials properties of the plate along the thickness 'z' viz. Young's modulus *'E(z)'* and mass density *'ρ(z)'*, for symmetric and uniform porosity distributions, are estimated using the relations given in Eq. (3.3a-b) and Eq. (3.4a-b), respectively. The Poisson's ratio 'ν' remains constant throughout the thickness.

$$E(z) = E_{max}[1 - e_0 \kappa] \tag{3.3a}$$

$$\rho(z) = \rho_{max}[1 - e_r \kappa] \tag{3.3b}$$

Where e_0 and e_r are the porosity coefficient and porosity density coefficient, respectively. E_{max} and ρ_{max} are the maximum value of $E(z)$ and $\rho(z)$, as in the case of minimum porosity, with e_0 = 0. The porosity density coefficient is related to the porosity coefficient by the relation given in Eq. (3.3c). κ is a function of thickness defined in Eq. (3.3d).

$$e_r = 1 - \sqrt{1 - e_0} \tag{3.3c}$$

$$\kappa = \cos\left(\frac{\pi z}{h}\right) \tag{3.3d}$$

$$E(z) = E_{max}[1 - e_0 \varsigma] \tag{3.4a}$$

$$\rho(z) = \rho_{max}\left(1 - \sqrt{1 - e_0 \varsigma}\right) \tag{3.4b}$$

Where ς is a function defined in Eq. (3.4c),

$$\varsigma = \frac{1}{e_0} - \frac{1}{e_0}\left(\frac{2}{\pi}\sqrt{1 - e_0} - \frac{2}{\pi} + 1\right)^2 \tag{3.4c}$$

3.3 Strain Energy Density Function

The strain energy density function is computed using various theories. In this work, the MSGT is considered. However, to demonstrate the superior capture of strain hardening effect in small-scale structures using the MSGT, a comparison with the Classical Continuum Theory (CCT) and the Modified Couple Stress Theory (MCST) is also made. The strain energy density function based on the three theories are discussed below.

3.3.1 Classical Continuum Theory (CCT)

$$U = \frac{1}{2}\int_B \left(\sigma_{ij}^c \epsilon_{ij}\right) dB \tag{3.5}$$

In the CCT, the strain energy function only consists of the Cauchy stress tensor, σ_{ij}^c, and its conjugate ε_{ij}, strain tensor, where $i, j, k = (x, y, z)$. The strain energy, U, in volume B using this theory is given in the Eq. (3.5).

3.3.2 Modified Couple Stress Theory (MCST)

According to this model (Lam et al. 2003), the strain energy, U, in volume B is given by the following equation:

$$U = \frac{1}{2}\int_B \left(\sigma_{ij}^c \epsilon_{ij} + \mathrm{r}_{ij}^s \chi_{ij}^s\right) dB \tag{3.6}$$

In Eq. (3.6), σ_{ij}^c is the Cauchy stress tensor, ϵ_{ij} is the strain, r_{ij}^s is the symmetric couple stress tensor and χ_{ij}^s is the symmetric curvature tensor. These components are as defined in the following equations:

$$\varepsilon_{ij} = \frac{1}{2}(u_{i,j} + u_{j,i}) \tag{3.7a}$$

$$\chi_{ij}^{s} = \frac{1}{2}(\theta_{i,j} + \theta_{j,i}) \tag{3.7b}$$

$$\sigma_{ij}^{c} = \lambda\varepsilon_{mm}\delta_{ij} + 2\mu\varepsilon_{ij} \qquad \text{where, } m=(x, y, z) \tag{3.7c}$$

$$r_{ij} = 2l^2\mu\chi_{ij}^{s} \tag{3.7d}$$

$$\theta_x = \frac{1}{2}(\frac{\partial w}{\partial y} - \frac{\partial v}{\partial z}) \tag{3.8a}$$

$$\theta_y = -\frac{1}{2}(\frac{\partial w}{\partial x} - \frac{\partial u}{\partial z}) \tag{3.8b}$$

$$\theta_z = \frac{1}{2}(\frac{\partial v}{\partial x} - \frac{\partial u}{\partial y}) \tag{3.8c}$$

$$\delta_{ij} = \begin{cases} 0 & \text{if } i \neq j \\ 1 & \text{if } i = j \end{cases} \tag{3.9a}$$

$$\lambda(z) = \frac{\nu E(z)}{(1+\nu)(1-2\nu)} \tag{3.9b}$$

$$\mu(z) = \frac{E(z)}{2(1+\nu)} \tag{3.9c}$$

In the Eqs. (3.7a-d), u_i is the displacement vector, θ_i is the rotation vector, δ_{ij} is the Kronecker delta, λ and μ are Lame's constants. The rotation vector, θ is defined in terms of displacement vectors as shown in Eq. (3.8), and 'l' is the length scale parameter that is obtained from calibrations experimentally. The Kronecker's delta and Lame's constants are defined in Eqs. (3.9a-c).

3.3.3 Modified Strain Gradient Theory (MSGT)

The strain energy, *U,* is given by Lam et al. (2003) in volume *B* as :

$$U = \frac{1}{2}\int_B \left(\sigma_{ij}^{c}\epsilon_{ij} + \mathrm{r}_{ij}^{s}\chi_{ij}^{s} + L_i\psi_i + \tau_{ijk}^{(1)}\eta_{ijk}^{(1)}\right) dB \tag{3.10}$$

In the Eq. (3.10), $\eta_{ijk}^{(1)}$ is the traceless part of the symmetric second-order deformation gradient also called the deviatoric stretch gradient tensor, and L_i is the dilatation gradient tensor. L_i, $\tau_{ijk}^{(1)}$ and r_{ij}^{s} are the work-conjugate of ψ_i, $\eta_{ijk}^{(1)}$ and χ_{ij}^{s} respectively.

$$\psi_i = \varepsilon_{mm,i} \tag{3.11a}$$

$$\eta_{ijk}^{(1)} = \frac{1}{3}\left(\varepsilon_{jk,i} + \varepsilon_{ki,j} + \varepsilon_{ij,k}\right) - \frac{1}{15}\delta_{ij}\left(\varepsilon_{mm,k} + 2\varepsilon_{mk,m}\right) \\ - \frac{1}{15}\delta_{jk}\left(\varepsilon_{mm,i} + 2\varepsilon_{mi,m}\right) - \frac{1}{15}\delta_{ki}\left(\varepsilon_{mm,j} + 2\varepsilon_{mj,m}\right) \tag{3.11b}$$

$$L_i = 2\mu l_0^2 \psi_i \tag{3.12a}$$

$$\tau_{ijk}^{(1)} = 2\mu l_1^2 \eta_{ijk}^{(1)} \tag{3.12b}$$

$$r_{ij}^{s} = 2\mu l_2^2 \chi_{ij}^{s} \tag{3.12c}$$

The dilatation gradient tensor and the deviatoric stretch gradient tensor are defined in Eqs. (3.11a-b). The higher-order stress tensors are defined in Eqs. (3.12a-c), where l_0, l_1, and l_2 are the material length scale parameters with respect to the dilatation gradient, deviatoric stretch gradient, and the symmetric part of the rotation gradient, respectively.

3.4 Kinematics of Microplate

3.4.1 Field Displacement Equations

Reddy's third-order shear deformation theory (TSDT) (Reddy and Liu 1985) is used to represent the field displacement equations in this work. The shear deformation effects can be included in the model with the help of this theory. The transverse shear strain is assumed to vary in a parabolic manner, which automatically leads to zero transverse shear strains at the top and bottom surfaces. However, this plate theory is limited to moderately thick plates and thin plates. In the case of thick plates, three-dimensional (3D) mathematical modeling is the most accurate theory to study their mechanical behavior. The field displacement equations of TSDT are expressed as (Reddy and Liu 1985):

$$u = u^0 + z\varphi_x + z^3\left(\frac{4}{3}h^2\right)\left[-\varphi_x - w_{,x}^0\right] \tag{3.13a}$$

$$v = v^0 + z\varphi_y + z^3\left(\frac{4}{3}h^2\right)\left[-\varphi_y - w_{,y}^0\right] \tag{3.13b}$$

$$w = w^0 \tag{3.13c}$$

The terms *u*, *v,* and *w* in the Eqs. (3.13a-c) represent the displacement in *x, y,* and *z* directions of a point (*x*, *y*) that is '*z*' distance away from the center surface of the plate. u^0, $v^0$and w^0 are the displacement of the point on the middle surface, i.e. the reference plane along *x, y,* and *z* directions, respectively. φ_x and φ_y are the rotation of the mid-surface about the *y*-axis and *x*-

axis respectively. The suffix $()_{,x}$ and $()_{,y}$ denote differentiation with respect to x and y respectively.

The above field displacement equations were further simplified by Soldatos (1991) as shown below.

$$u = u^0 - zw^0_{,x} + f(z)\phi^0_x \tag{3.14a}$$

$$v = v^0 - zw^0_{,y} + f(z)\phi^0_y \tag{3.14b}$$

$$w = w^0 \tag{3.14c}$$

Where, $\phi^0_x = \varphi_x + w^0_{,x}$, $\phi^0_y = \varphi_y + w^0_{,y}$ and $f(z) = z\left(1 - \frac{4z^2}{3h^2}\right)$

3.4.2 Strain-Displacement Equations

The strain-displacement equations, as obtained using the field displacement equations (Eqs. 3.14a-c) including the geometric non-linearity based on von Kármán, are (Reddy 2006):

$$\varepsilon_{xx} = \varepsilon^0_{xx} - zw_{,xx} + f(z)\phi^0_{x,x} \tag{3.15a}$$

$$\varepsilon_{yy} = \varepsilon^0_{yy} - zw_{,yy} + f(z)\phi^0_{y,y} \tag{3.15b}$$

$$\gamma_{xy} = \gamma^0_{xy} - 2zw^0_{,xy} + f(z)\phi^0_{x,y} + f(z)\phi^0_{y,x} \tag{3.15c}$$

$$\gamma_{xz} = u_{,z} + w_{,x} = f'(z)\phi^0_x \tag{3.15d}$$

$$\gamma_{yz} = v_{,z} + w_{,y} = f'(z)\phi^0_y \tag{3.15e}$$

The strains at the central reference middle surface of the plate are indicated in Eqs. (3.15a-e) by the symbols, ε^0_{xx}, ε^0_{yy} and γ^0_{xy}. These are further related to displacements in the equations below (Reddy 2006).

$$\varepsilon^0_{xx} = u^0_{,x} + \frac{1}{2}\left(w^0_{,x}\right)^2 \tag{3.16a}$$

$$\varepsilon^0_{yy} = v^0_{,y} + \frac{1}{2}\left(w^0_{,y}\right)^2 \tag{3.16b}$$

$$\gamma^0_{xy} = u^0_{,x} + v^0_{,y} + w^0_{,x}w^0_{,y} \tag{3.16c}$$

3.5 Types of Loading

In this study, analysis of microplates due to three types of loadings is considered: non-uniform in-plane mechanical loading (Fig. 3.1 and Fig. 3.3(a)), transverse patch mechanical loading (Fig. 3.2 and Fig. 3.3(b)), and localized thermal loading (Fig. 3.3(c)). The function depicting these loads over the entire domain of the microplate is depicted in the following subsections.

3.5.1 Non-Uniform In-plane Loading

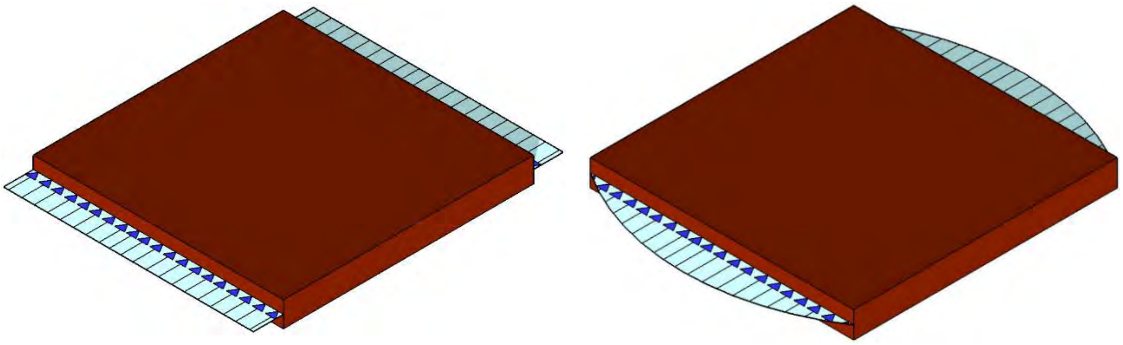

(a) Uniform loading profile (Case I)

(b) Parabolic loading profile (Case II)

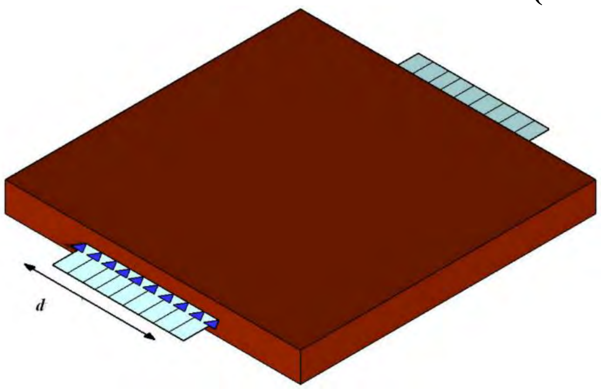

(c) Partial loading profile (Case III)

Fig. 3.5. Different cases of in-plane harmonic loading profiles on two opposite edges of the microplate (a) uniform loading profile (b) parabolic loading profile (c) partial loading profile

The in-plane harmonic mechanical loading is uniaxial and compressive, applied at two opposite edges of the microplate as shown in Fig. 3.1 and Fig 3.3(a). It is of the form $\overline{N}_x = N_{st} + N_{dyn}\cos(pt)$, where the static load, $N_{st} = \alpha N_{cr}$ and dynamic load, $N_{dyn} = \beta N_{cr}$, is applied on two opposite edges. Here, α is the static load factor, β is the dynamic load factor, and p is the in-plane loading frequency. Three in-plane harmonic loading scenarios at the two opposite edges of the plate are considered. In the first case, the profile of harmonic loading is considered uniformly distributed (Fig. 3.5(a)). In the second case, the profile of harmonic loading is assumed to be parabolic (Fig. 3.5(b)) and in the third case the edges are considered to be partially loaded (Fig. 3.5(c)). The total load in all the cases is considered equal, and only the loading profile is varied.

The mathematical representations for the in-plane loads with various loading profiles over the entire length of the edge are presented in the equations below. In the equations below, $\overline{N}_0$ is the magnitude of the load for uniform loading profile.

(1) Uniform loading profile

$$N(y) = \overline{N}_0 \tag{3.17a}$$

(2) Parabolic loading profile

$$N(y) = \frac{3}{2}\overline{N}_0\left(1 - 4\frac{y^2}{b^2}\right) \tag{3.17b}$$

(3) Localized loading profile

The function for in-plane localized loading shown in Fig. 3.5(c), where d is the width of loading, with its centre lying at *x*=0 is:

$$N(y) = \begin{cases} 0 & -\frac{b}{2} < y < -\frac{d}{2} & (3.18a) \\ \overline{N}_0 & -\frac{d}{2} < y < \frac{d}{2} & (3.18b) \\ 0 & \frac{d}{2} < y < \frac{b}{2} & (3.18c) \end{cases}$$

The generalized function for localized in-plane loading along the entire edge of the microplate is represented in terms of Fourier series as follows:

$$N(y) = \left[\frac{a_0}{2} + \sum_{i=1}^{\infty} a_i \cos(\alpha_i y) + \sum_{i=1}^{\infty} b_i \sin(\beta_i y)\right] \tag{3.19}$$

$$a_0 = \frac{2}{b}\int_{-\frac{b}{2}}^{\frac{b}{2}} N(y)dy \tag{3.20a}$$

$$a_0 = \frac{2}{b}\left[\int_{-b/2}^{-d/2} 0\, dy + \int_{-d/2}^{d/2} \overline{N}_0\, dy + \int_{d/2}^{b/2} 0\, dy\right] \tag{3.20b}$$

$$a_0 = \frac{2}{b}\int_{-d/2}^{d/2} \overline{N}_0\, dy \tag{3.20c}$$

$$a_0 = \frac{2\overline{N}_0 d}{b} \tag{3.20d}$$

$$a_i = \frac{2}{b}\int_{-\frac{b}{2}}^{\frac{b}{2}} N(y)\cos\alpha_i y dy \text{ , where, } \alpha_i = \frac{2\pi r}{b} \tag{3.21a}$$

$$a_i = \frac{2}{b}\left[\int_{-b/2}^{-d/2} 0\cos\alpha_i y\, dy + \int_{-d/2}^{d/2} \bar{N}_0 \cos\alpha_i y\, dy + \int_{d/2}^{b/2} 0\cos\alpha_i y dy\right] \tag{3.21b}$$

$$a_i = \frac{2}{b}\int_{-d/2}^{d/2} \bar{N}_0 \cos\alpha_i y\, dy \tag{3.21c}$$

$$a_i = \frac{2\bar{N}_0}{\alpha_i b}\left[\sin\alpha_i\left(\frac{d}{2}\right) - \sin\alpha_i\left(-\frac{d}{2}\right)\right] \tag{3.21d}$$

$$a_i = \frac{2\bar{N}_0}{\pi r}\sin\left(\frac{r\pi d}{b}\right) \tag{3.21e}$$

Similarly,

$$b_i = \frac{2}{b}\int_{-d/2}^{d/2} N(y)\cos\beta_i y\, dy \tag{3.22a}$$

$$b_i = \frac{2\bar{N}_0}{\beta_i b}\left[\cos\beta_i\left(\frac{d}{2}\right) - \cos\beta_i\left(-\frac{d}{2}\right)\right] \tag{3.22b}$$

$$b_i = 0 \tag{3.22c}$$

Thus, using Eq. (3.20d), Eq. (3.21e), and Eq. (3.22c) in Eq. (3.19), we get the generalized equation of the localized in-plane load as follows:

$$N(y) = \bar{N}_0\left(\frac{d}{b} + \sum_{r=1}^{\infty}\frac{2}{\pi}\left(\frac{1}{r}\sin\frac{r\pi d}{b}\cos\frac{2r\pi y}{b}\right)\right) \tag{3.23a}$$

The final form of localized in-plane load becomes,

$$N(y) = \bar{N}_0\frac{b}{d}\left(\frac{d}{b} + \sum_{r=1}^{\infty}\frac{2}{\pi}\left(\frac{1}{r}\sin\frac{r\pi d}{b}\cos\frac{2r\pi y}{b}\right)\right) \tag{3.23b}$$

where, $\frac{b}{d}$ is multiplied to keep the amount of total load the same as in the case of uniform loading profile.

3.5.2 Transverse Patch Loading

Transverse patch loading of the form $f(x, y)\cos(\omega t)$ is applied on the microplate as shown in Fig. 3.2 and Fig. 3.3(b). The geometric center of the transverse patch loading of magnitude 'f_0' is at (x_c, y_c) distance from the origin. The length and width of the transverse patch loading are denoted by 'a_l' and 'b_l', respectively. The transverse patch loading is modelled on the entire domain of the microplate's surface using the double Fourier series expansions (Kumar et al. 2022), which is expanded in both x and y directions.

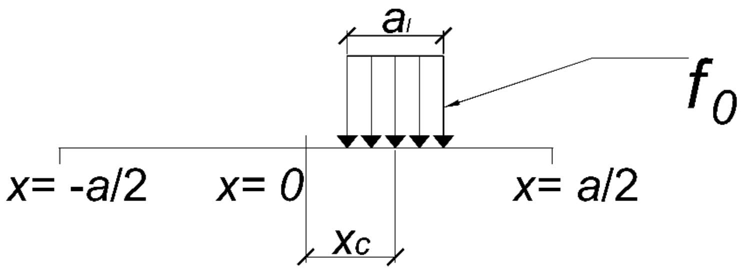

(a) Generalized case of transverse patch loading in the x-direction

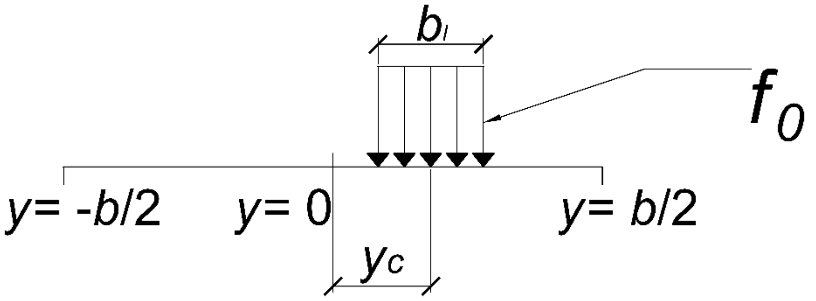

(b) Generalized case of transverse patch loading in the y-direction

Fig. 3.6. Generalized case of transverse patch loadings

The Fourier series expansion of transverse patch loading in both x and y-directions is presented in this section. The domain of the unloaded part will be considered as zero. The general case of transverse patch loading functions is written as per Fig. 3.6(a). The generalized case along the x- and y-axes are calculated separately and then multiplied to obtain the final form of generalized patch loading.

The generalized transverse loading along the x-direction is given as:

$$f(x) = \quad 0 \qquad -\frac{a}{2} < x < x_c - \frac{a_l}{2} \tag{3.24a}$$

$$f(x) = \quad f_0 \qquad x_c - \frac{a_l}{2} < x < x_c + \frac{a_l}{2} \tag{3.24b}$$

$$f(x) = \quad 0 \qquad x_c + \frac{a_l}{2} < x < \frac{a}{2} \tag{3.24c}$$

Where a_l denotes the length of the patch loading area in the x-direction. The above transverse loading along the x-direction is expressed in the total length of the plate via the Fourier series:

$$f(x) \; = \frac{a_0}{2} + \sum_{i=1}^{\infty} a_i \cos\alpha_i x + \sum_{i=1}^{\infty} b_i \sin\alpha_i x \tag{3.25}$$

where,

$$a_0 \; = \frac{2}{a}\int_{-a/2}^{a/2} f_0 \, dy \tag{3.26a}$$

$$= \frac{2}{a}\int_{-a/2}^{x_c-\frac{a_1}{2}} f_0 \, dx + \frac{2}{a}\int_{x_c-\frac{a_1}{2}}^{x_c+\frac{a_1}{2}} f_0 \, dx + \frac{2}{a}\int_{x_c+\frac{a_1}{2}}^{\frac{a}{2}} f_0 \, dx \tag{3.26b}$$

$$= \frac{2}{a}\int_{x_c-\frac{a_1}{2}}^{x_c+\frac{a_1}{2}} f_0 \, dx \tag{3.26c}$$

$$= \frac{2}{a} f_0 \left[x_c + \frac{a_l}{2} - x_c + \frac{a_l}{2}\right] \tag{3.26d}$$

$$= \frac{2}{a} f_0 a_l \tag{3.26e}$$

Again,

$$a_i \; = \frac{2}{a}\int_{-a/2}^{\frac{a}{2}} f_0 \cos\alpha_i x \, dx \tag{3.27a}$$

$$= \frac{2}{a}\int_{-a/2}^{x_c-\frac{a_l}{2}} f_0 \cos\alpha_i x \, dx + \frac{2}{a}\int_{x_c-\frac{a_l}{2}}^{x_c+\frac{a_l}{2}} f_0 \cos\alpha_i x \, dx + \frac{2}{a}\int_{x_c+\frac{a_l}{2}}^{\frac{a}{2}} f_0 \cos\alpha_i x \, dx \tag{3.27b}$$

$$= \frac{2}{a}\int_{x_c-\frac{a_1}{2}}^{x_c+\frac{a_1}{2}} f_0 \cos\alpha_i x \, dx \tag{3.27c}$$

$$a_i = \frac{2f_0}{a\alpha_i}\left[\sin\alpha_i\left(x_c + \frac{a_l}{2}\right) - \sin\alpha_i\left(x_c - \frac{a_l}{2}\right)\right] \tag{3.27d}$$

Similarly,

$$b_i = -\frac{2f_0}{a\alpha_i}\left[\cos\alpha_i\left(x_c + \frac{a_l}{2}\right) - \cos\alpha_i\left(x_c - \frac{a_l}{2}\right)\right] \tag{3.28}$$

Thus, using Eq. (3.25), Eq. (3.26), Eq. (3.27), and Eq. (3.28), we get

$$f(x) = \frac{f_0 a_l}{a} + \sum_{i=1}^{\infty} \frac{2f_0}{a\alpha_i}\left[\sin\alpha_i\left(x_c + \frac{a_l}{2}\right) - \sin\alpha_i\left(x_c - \frac{a_l}{2}\right)\right]\cos\alpha_i x$$
$$-\sum_{i=1}^{\infty} \frac{2f_0}{a\alpha_i}\left[\cos\alpha_i\left(x_c + \frac{a_l}{2}\right) - \cos\alpha_i\left(x_c - \frac{a_l}{2}\right)\right]\sin\alpha_i x \quad (3.29)$$

Similarly, the generalized transverse loading along *y*-direction is given as:

$$f(y) = \frac{f_0 b_l}{b} + \sum_{j=1}^{\infty} \frac{2f_0}{b\chi_j}\left[\sin\chi_j\left(y_c + \frac{b_l}{2}\right) - \sin\chi_j\left(y_c - \frac{b_l}{2}\right)\right]\cos\chi_j y$$
$$-\sum_{j=1}^{\infty} \frac{2f_0}{b\chi_j}\left[\cos\chi_j\left(y_c + \frac{b_l}{2}\right) - \cos\chi_j\left(y_c - \frac{b_l}{2}\right)\right]\sin\chi_j y \quad (3.30)$$

where b_l denotes the width of the patch loading area in the *y*-direction (Fig. 3.6(b))

Thus, the final generalized patch loading on the total area of the plate in the transverse direction of the microplate is defined using Eq. (3.29) and Eq. (3.30) as follows:

$$f(x,y) = \left(\frac{f_0 a_l}{a} + \sum_{i=1}^{\infty} \frac{2f_0}{a\alpha_i}\left[\sin\alpha_i\left(x_c + \frac{a_l}{2}\right) - \sin\alpha_i\left(x_c - \frac{a_l}{2}\right)\right]\cos\alpha_i x - \right.$$
$$\left.\sum_{i=1}^{\infty} \frac{2f_0}{a\alpha_i}\left[\cos\alpha_i\left(x_c + \frac{a_l}{2}\right) - \cos\alpha_i\left(x_c - \frac{a_l}{2}\right)\right]\sin\alpha_i x\right) \times \left(\frac{f_0 b_l}{b} + \right.$$
$$\sum_{j=1}^{\infty} \frac{2f_0}{b\chi_j}\left[\sin\chi_j\left(y_c + \frac{b_l}{2}\right) - \sin\chi_j\left(y_c - \frac{b_l}{2}\right)\right]\cos\chi_j y -$$
$$\left.\sum_{j=1}^{\infty} \frac{2f_0}{b\chi_j}\left[\cos\chi_j\left(y_c + \frac{b_l}{2}\right) - \cos\chi_j\left(y_c - \frac{b_l}{2}\right)\right]\sin\chi_j y\right) \quad (3.31)$$

Since, $\alpha_i = \frac{2\pi i}{a}$ and $\chi_j = \frac{2\pi j}{b}$

The final expression for generalized transverse patch loading becomes,

$$f(x,y) = \left(\frac{f_0 ab}{a_l b_l}\right) \times$$
$$\begin{pmatrix} \frac{a_l}{a} + \sum_{i=1}^{\infty} \frac{1}{\pi i}\left(\sin\alpha_i\left(x_c + \frac{a_l}{2}\right) - \sin\alpha_i\left(x_c - \frac{a_l}{2}\right)\right)\cos\alpha_i x \\ -\sum_{i=1}^{\infty} \frac{1}{\pi i}\left(\cos\alpha_i\left(x_c + \frac{a_l}{2}\right) - \cos\alpha_i\left(x_c - \frac{a_l}{2}\right)\right)\sin\alpha_i x \end{pmatrix} \times \quad (3.32)$$
$$\begin{pmatrix} \frac{b_l}{b} + \sum_{j=1}^{\infty} \frac{1}{\pi j}\left(\sin\chi_j\left(y_c + \frac{b_l}{2}\right) - \sin\chi_j\left(y_c - \frac{b_l}{2}\right)\right)\cos\chi_i y \\ -\sum_{j=1}^{\infty} \frac{1}{\pi j}\left(\cos\chi_j\left(y_c + \frac{b_l}{2}\right) - \cos\chi_j\left(y_c - \frac{b_l}{2}\right)\right)\sin\chi_i y \end{pmatrix}$$

Where, $\left(\frac{ab}{a_l b_l}\right)$ is multiplied to keep the amount of total load the same, although the size of patch loading is varied by varying the values of a_l and b_l.

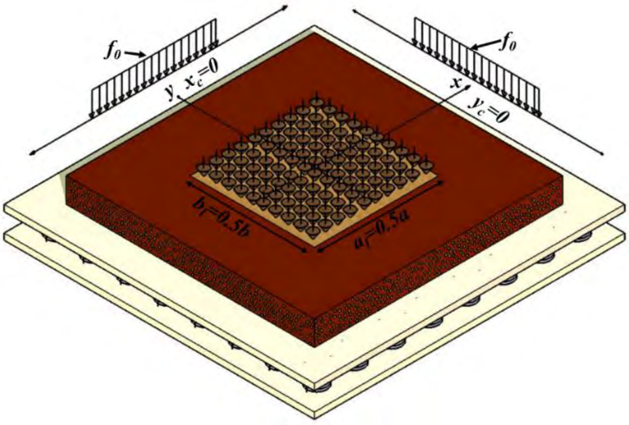

(a) Loading Case 1

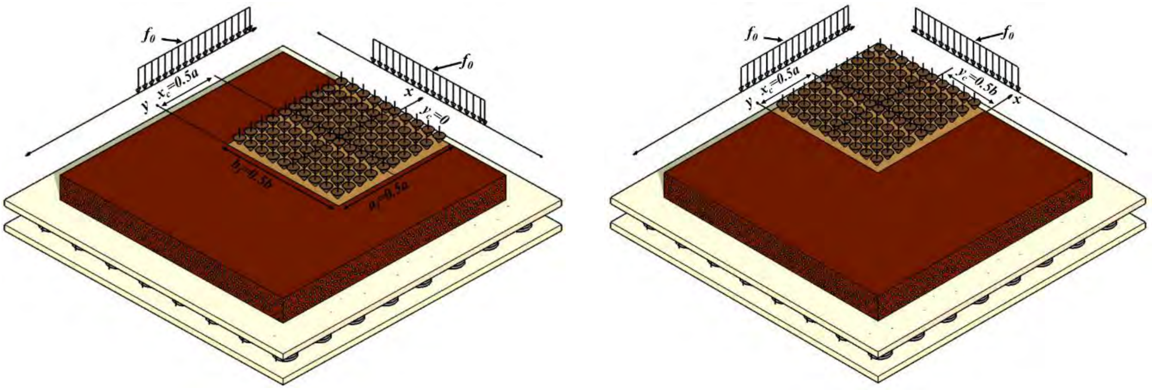

(b) Loading Cases 2 and 3 **(c) Loading Case 4**

Fig. 3.7. Different positions of transverse patch loading on the surface of microplate: (a) centre loading, (b) edge loading, and (c) corner loading

In this study, four different cases of patch loadings with different loading positions are considered, as shown in Fig. 3.7 In the first case (Fig. 3.7(a)), loading is applied at the centre of the plate. In the second case (Fig. 3.7(b)), loading is applied near an edge. In the third case, if SCSC type microplate (one set of edges simply supported and other set clamped) is considered, loading is applied near clamped edge. In the fourth case (Fig. 3.7(c)), loading is applied at a corner.

3.5.3 Localized Thermal Loading

Localized thermal load is applied on microplate as shown in Fig. 3.3(c). The localized thermal load is considered rectangular in shape with its center coinciding with the center of the plate, to maintain symmetry. The width of the loading is 'a_0' and 'b_0' in the x and y directions respectively. The thermal force resultants, $\mathbf{N_T}^{\mathbf{T}} = \{(N_T)_{xx}, (N_T)_{yy}, (N_T)_{xy}\}$ and thermal moment resultants, $\mathbf{M_T} = \{(M_T)_{xx}, (M_T)_{yy}, (M_T)_{xy}\}$ are generated due to heating of the plate. In this study, we are considering uniform temperature rise through the plate thickness and no exchange of heat with surroundings. Thus, thermal moment resultants are not present. The relation of thermal force resultants with the thermal expansion coefficients $(\boldsymbol{\alpha_T})^{\mathbf{T}} = \{\alpha_{xx}^T, \alpha_{yy}^T, \alpha_{xy}^T\}$ is:

$$\mathbf{N_T} = \mathbf{N_C} \cdot \mathrm{T}(x, y) \tag{3.33}$$

In Eq. (3.33), $\mathbf{N_c} = \{N_{xx}^c, N_{yy}^c, N_{xy}^c\}$ is defined as:

$$\mathbf{N_c} = \int_{-h/2}^{h/2} \overline{K}_{ij}\, \boldsymbol{\alpha_T} dz \tag{3.34}$$

where, K_{ij} are the stiffness constants and defined in Eq. (3.42).

In Eq. (3.33), $\mathrm{T}(x, y)$ is the function expressing the temperature field over the entire domain of the plate. In case of partial rectangular heating considered in this study, $\mathrm{T}(x, y)$ is considered symmetric about the origin for less complex analytical calculations. $\mathrm{T}(x, y)$ is defined as:

$$T(x, y) = \begin{cases} T_R & \text{at } \ |x| \leq a_0/2 \ \text{ and } |y| \leq b_0/2 \\ 0 & \text{at } \ a_0/2 < |x| \leq a/2 \ \text{ and } b_0/2 < |y| \leq b/2 \end{cases} \tag{3.35}$$

In Eq. (3.35), T_R is the uniform temperature rise for thermal energy equal to that for fully heated plate. The double Fourier series expansion is used to model this load over the entire domain of the plate as follows:

$$T(x, y) = \sum_{i=1}^{\infty} \sum_{j=1}^{\infty} f_{ij} \cos(\theta_i x) \cos(\beta_j y) \tag{3.36}$$

In Eq. (3.36), $f_{ij} = \frac{16T_R}{ab\theta_i\beta_j} \sin(\theta_i a_0/2) \sin(\beta_j b_0/2)$ and, $\theta_i = \frac{(2i-1)\pi}{a}, \ \ \beta_j = \frac{(2j-1)\pi}{b}$

3.6 Estimation of Governing Partial Differential Equations of Motion

The equations of motion of the microplates analysed in this study are derived using Hamilton's principle (Eq. (3.37)) in case of dynamic problem and using the principle of minimization of total potential energy (Eq. (3.38)) in case of static problem (Reddy 2017).

(a) Hamilton's principle

$$\delta^{(1)}\left(\int_{t_1}^{t2}(U+F-G-W-C-T)\right)=0 \tag{3.37}$$

(b) Minimization of the total potential energy

$$\delta\Pi = \delta^{(1)}(U+F-G)=0 \tag{3.38}$$

According to this principle, for the system to be in equilibrium, the variation ($\delta^{(1)}$) of the total potential energy with respect to the field variables should be zero.

In the above equations, *U* is the strain energy (Sahmani and Ansari 2013), *F* is the strain energy of the foundation (Thai and Choi 2012), *G* is the geometric strain energy due to the in-plane mechanical load or thermal load, *W* is the external work done (Xu et al. 2021) by the transverse loads, *C* is the damping energy, and *T* is the kinetic energy (Kumar et al. 2021) in the time interval t_0 to t_1 whereas $\delta^{(1)}$denotes the first variation. *W* and *G* are not taken together in the calculations. In case of in-plane mechanical loading and thermal loading, where in-plane stresses are developed due to loading, the geometric strain energy is considered and in case of transverse loading, external work done is considered. In the case of static problem, kinetic energy, *T*, and damping energy, *C*, are not present and the principle of minimization of total potential energy, $\Pi = U + F - G$, is used. The first variations of '*U*', '*F*', '*G*', '*W*', '*C*', and '*T*' are defined in the following subsection.

3.6.1 Expressions of First Variation of Energy Functions

3.6.1.1 First Variation of Strain Energy

$$U = U_\sigma + U_r + U_L + U_\tau \tag{3.39a}$$

$$U_\sigma = U_\sigma^N + U_\sigma^M + U_\sigma^{M^{\mathrm{a}}} + U_\sigma^S \tag{3.39b}$$

$$\mathbf{N} = \bar{\mathbf{A}}\boldsymbol{\varepsilon}^{\mathbf{0}} + \bar{\mathbf{B}}\boldsymbol{\xi} + \bar{\mathbf{C}}\boldsymbol{\xi}^{a} - \mathbf{N}_{\mathbf{T}} \tag{3.40a}$$

$$\mathbf{M}^{m} = \bar{\mathbf{B}}\boldsymbol{\varepsilon}^{\mathbf{0}} + \bar{\mathbf{D}}\boldsymbol{\xi} + \bar{\mathbf{E}}\boldsymbol{\xi}^{a} - \mathbf{M}_{\mathbf{T}} \tag{3.40b}$$

$$\mathbf{M}^{a} = \bar{\mathbf{C}}\boldsymbol{\varepsilon}^{\mathbf{0}} + \bar{\mathbf{E}}\boldsymbol{\xi} + \bar{\mathbf{F}}\boldsymbol{\xi}^{a} \tag{3.40c}$$

$$\mathbf{S} = \bar{\mathbf{H}}\boldsymbol{\gamma} \tag{3.40d}$$

The strain energy, calculated based on MSGT, consists of energy due to the Cauchy strain tensor (U_σ), energy due to symmetric curvature gradient tensor (U_r), energy due to dilatation gradient tensor (U_L) and energy due to the deviatoric stretch gradient tensor (U_τ) as shown in Eq. (3.39a). The strain energy density function has five independent components due to U_σ.The strain energy due to Cauchy strain tensor (U_σ) is composed of membrane energy (U_σ^N) due to force resultants $\mathbf{N}^T$=$\{N_{xx}, N_{yy}, N_{xy}\}$, bending energy ($U_\sigma^M$) due to moment resultants $\mathbf{M}^{m^T}$=$\{M_{xx}^m, M_{yy}^m, M_{xy}^m\}$, additional bending energy ($U_\sigma^{M^a}$) due to additional moment resultants due to additional changes in curvatures $\mathbf{M}^{a^T}$=$\{M_{xx}^a, M_{yy}^a, M_{xy}^a\}$ and shear energy (U_σ^S) due to shear resultants $\mathbf{S}^T$=$\{S_{yz}, S_{xz}\}$ as shown in Eq. (3.39b). The above stress resultants are related to the membrane strains $\boldsymbol{\varepsilon}^{\mathbf{0}^T}$=$\{\varepsilon_{xx}^0, \varepsilon_{yy}^0, \varepsilon_{xy}^0\}$, bending strains $\boldsymbol{\xi}^T$=$\{-w_{,xx}^0, -w_{,yy}^0, -2w_{,xy}^0\}$, additional bending strains $\boldsymbol{\xi}^{a^T}$= $\{\phi_{x,x}^0, \phi_{y,y}^0, \phi_{x,y}^0 + \phi_{y,x}^0\}$ and shear strains $\boldsymbol{\gamma}^T$=$\{\gamma_{yz}, \gamma_{xz}\}$, through the constitutive relations (Eqs. (3.40a-d)).

In the Eqs. 3.40(a-d) bold letters are used to denote matrices and vectors. The stiffness matrices $\bar{\mathbf{A}}, \bar{\mathbf{B}}, \bar{\mathbf{C}}, \bar{\mathbf{D}}, \bar{\mathbf{E}}, \bar{\mathbf{F}}$, and $\bar{\mathbf{H}}$ are stated below:

$$\left(\bar{A}_{ij}, \bar{B}_{ij}, \bar{D}_{ij}\right) = \int_{-h/2}^{h/2} \bar{K}_{ij}(1, z, z^2)dz \qquad (i,j) = (1,2,6) \qquad (3.41a)$$

$$\left(\bar{C}_{ij}, \bar{E}_{ij}, \bar{F}_{ij}\right) = \int_{-h/2}^{h/2} \bar{K}_{ij}\left(1, z, f(z)\right)f(z)dz \qquad (i,j) = (1,2,6) \qquad (3.41b)$$

$$\left(\bar{H}_{ij}\right) = \int_{-h/2}^{h/2} \bar{K}_{ij}f'(z)f'(z)dz \qquad (i,j) = (4,5) \qquad (3.41c)$$

where non-zero values of K_{ij} are given below,

$$\bar{K}_{11} = \bar{K}_{22} = \frac{2\lambda\mu}{\nu(\lambda + 2\mu)} \qquad (3.42a)$$

$$\bar{K}_{12} = \bar{K}_{21} = \frac{2\lambda\mu}{\lambda + 2\mu} \qquad (3.42b)$$

$$\bar{K}_{66} = \bar{K}_{44} = \bar{K}_{55} = \mu \qquad (3.42c)$$

The strain energy density function consists of five independent components due to U_r , three independent components due to U_L and ten independent components due to U_τ. The work-conjugate of higher-order deformation gradient tensors in the components of U_r, U_L and U_τ are denoted by Y_{mn}, P_{mn} and Q_{mn} respectively. The work-conjugates of first-order deformation gradients, if any, in the components of U_r, U_L and U_τ are denoted by $\overline{Y_{mn}}$, $\overline{P_{mn}}$ and $\overline{Q_{mn}}$ respectively. In these terms, the suffix *'m'* denotes the index of the component ($m = 1, 2, \ldots., k$ where $k = 5$ for Y_{mn} and $\overline{Y_{mn}}$, $k = 3$ for P_{mn} and $\overline{P_{mn}}$ and $k = 10$ for Q_{mn} and $\overline{Q_{mn}}$), from which it is derived, and the suffix *'n'* represents the index of the displacement or rotation component of which it is a gradient (*n*=1, 2, 3, 4, 5 where $1 \rightarrow u^0$, $2 \rightarrow v^0$, $3 \rightarrow w^0$, $4 \rightarrow \phi_x^0$ and $5 \rightarrow \phi_y^0$).

The non-zero work conjugates, Y_{mn} and $\overline{Y_{mn}}$ of higher-order deformation gradients are defined in the following equations:

$$Y_{13} = l_2^2(2\overline{II}w^0_{,xy} - \overline{LL}\phi^0_{y,x}) \tag{3.43a}$$

$$Y_{15} = l_2^2\left(-\overline{LL}w^0_{,xy} + \frac{1}{2}\overline{MM}\phi^0_{y,x}\right) \tag{3.43b}$$

$$Y_{23} = l_2^2(2\overline{II}w^0_{,xy} - \overline{LL}\phi^0_{x,y}) \tag{3.43c}$$

$$Y_{24} = l_2^2\left(-\overline{LL}w^0_{,xy} + \frac{1}{2}\overline{MM}\phi^0_{x,y}\right) \tag{3.43d}$$

$$Y_{33} = l_2^2(\overline{II}(w^0_{,yy} - w^0_{,xx}) + \frac{1}{2}\overline{LL}(\phi^0_{x,x} - \phi^0_{y,y})) \tag{3.43e}$$

$$Y_{34} = l_2^2\left(\frac{1}{2}\overline{LL}(w^0_{,yy} - w^0_{,xx}) + \frac{1}{4}\overline{MM}(\phi^0_{x,x} - \phi^0_{y,y})\right) \tag{3.43f}$$

$$Y_{35} = -l_2^2\left(\frac{1}{2}\overline{LL}(w^0_{,yy} - w^0_{,xx}) + \frac{1}{4}\overline{MM}(\phi^0_{x,x} - \phi^0_{y,y})\right) \tag{3.43g}$$

$$Y_{41} = -\frac{1}{4}l_2^2(\overline{II}\left(v^0_{,xy} - u^0_{,yy}\right) + \overline{JJ}\left(\phi^0_{y,xy} - \phi^0_{x,yy}\right) + \overline{QQ}\phi^0_x) \tag{3.43h}$$

$$Y_{42} = \frac{1}{4}l_2^2(\overline{II}\left(v^0_{,xy} - u^0_{,yy}\right) + \overline{JJ}\left(\phi^0_{y,xy} - \phi^0_{x,yy}\right) + \overline{QQ}\phi^0_x) \tag{3.43i}$$

$$Y_{44} = -\frac{1}{4}l_2^2(\overline{JJ}\left(v^0_{,xy} - u^0_{,yy}\right) + \overline{KK}\left(\phi^0_{y,xy} - \phi^0_{x,yy}\right) + \overline{QQ}\phi^0_x) \tag{3.43j}$$

$$Y_{45} = \frac{1}{4}l_2^2(\overline{JJ}\left(v^0_{,xy} - u^0_{,yy}\right) + \overline{KK}\left(\phi^0_{y,xy} - \phi^0_{x,yy}\right) + \overline{QQ}\phi^0_x) \tag{3.43k}$$

$$\overline{Y_{44}} = \frac{1}{4}l_2^2(\overline{NN}\left(v^0_{,xy} - u^0_{,yy}\right) + \overline{QQ}\left(\phi^0_{y,xy} - \phi^0_{x,yy}\right) + \overline{PP}\phi^0_x) \tag{3.43l}$$

$$Y_{51} = -\frac{1}{4}l_2^2(\overline{II}\left(v^0_{,xx} - u^0_{,xy}\right) + \overline{JJ}\left(\phi^0_{y,xx} - \phi^0_{x,xy}\right) - \overline{NN}\phi^0_y) \tag{3.43m}$$

$$Y_{52} = \frac{1}{4}l_2^2(\overline{II}\left(v^0_{,xx} - u^0_{,xy}\right) + \overline{JJ}\left(\phi^0_{y,xx} - \phi^0_{x,xy}\right) - \overline{NN}\phi^0_y) \tag{3.43n}$$

$$Y_{54} = -\frac{1}{4}l_2^2(\overline{JJ}\left(v^0_{,xx} - u^0_{,xy}\right) + \overline{KK}\left(\phi^0_{y,xx} - \phi^0_{x,xy}\right) - \overline{QQ}\phi^0_y) \tag{3.43o}$$

$$Y_{55} = \frac{1}{4}l_2^2(\overline{JJ}\left(v^0_{,xx} - u^0_{,xy}\right) + \overline{KK}\left(\phi^0_{y,xx} - \phi^0_{x,xy}\right) - \overline{QQ}\phi^0_y) \tag{3.43p}$$

$$\overline{Y_{55}} = \frac{1}{4}l_2^2(-\overline{NN}\left(v^0_{,xx} - u^0_{,xy}\right) - \overline{QQ}\left(\phi^0_{y,xx} - \phi^0_{x,xy}\right) + \overline{PP}\phi^0_y) \tag{3.43q}$$

The non-zero work conjugates P_{mn} and $\overline{P_{mn}}$, of higher-order deformation gradients are defined in the following equations.

$$P_{11} = 2l_0^2\left(\overline{II}\left(u_{,xx}^0 + v_{,xy}^0\right) - \overline{II^*}\left(w_{,xxx}^0 + w_{,xyy}^0\right) + \overline{JJ}\left(\phi_{x,xx}^0 + \phi_{y,xy}^0\right)\right) \tag{3.44a}$$

$$P_{12} = 2l_0^2\left(\overline{II}\left(u_{,xx}^0 + v_{,xy}^0\right) - \overline{II^*}\left(w_{,xxx}^0 + w_{,xyy}^0\right) + \overline{JJ}\left(\phi_{x,xx}^0 + \phi_{y,xy}^0\right)\right) \tag{3.44b}$$

$$P_{13} = 2l_0^2\left(-\overline{II}\left(u_{,xx}^0 + v_{,xy}^0\right) + \overline{II^{**}}\left(w_{,xxx}^0 + w_{,xyy}^0\right) - \overline{JJ^*}\left(\phi_{x,xx}^0 + \phi_{y,xy}^0\right)\right) \tag{3.44c}$$

$$P_{14} = 2l_0^2\left(\overline{JJ}\left(u_{,xx}^0 + v_{,xy}^0\right) - \overline{JJ^*}\left(w_{,xxx}^0 + w_{,xyy}^0\right) + \overline{KK}\left(\phi_{x,xx}^0 + \phi_{y,xy}^0\right)\right) \tag{3.44d}$$

$$P_{15} = 2l_0^2\left(\overline{JJ}\left(u_{,xx}^0 + v_{,xy}^0\right) - \overline{JJ^*}\left(w_{,xxx}^0 + w_{,xyy}^0\right) + \overline{KK}\left(\phi_{x,xx}^0 + \phi_{y,xy}^0\right)\right) \tag{3.44e}$$

$$P_{21} = 2l_0^2\left(\overline{II}\left(u_{,xy}^0 + v_{,yy}^0\right) - \overline{II^*}\left(w_{,xxy}^0 + w_{,yyy}^0\right) + \overline{JJ}\left(\phi_{x,xy}^0 + \phi_{y,yy}^0\right)\right) \tag{3.44f}$$

$$P_{22} = 2l_0^2\left(\overline{II}\left(u_{,xy}^0 + v_{,yy}^0\right) - \overline{II^*}\left(w_{,xxy}^0 + w_{,yyy}^0\right) + \overline{JJ}\left(\phi_{x,xy}^0 + \phi_{y,yy}^0\right)\right) \tag{3.44g}$$

$$P_{23} = 2l_0^2\left(-\overline{II}\left(u_{,xy}^0 + v_{,yy}^0\right) + \overline{II^{**}}\left(w_{,xxy}^0 + w_{,yyy}^0\right) - \overline{JJ^*}\left(\phi_{x,xy}^0 + \phi_{y,yy}^0\right)\right) \tag{3.44h}$$

$$P_{24} = 2l_0^2\left(\overline{JJ}\left(u_{,xy}^0 + v_{,yy}^0\right) - \overline{JJ^*}\left(w_{,xxy}^0 + w_{,yyy}^0\right) + \overline{KK}\left(\phi_{x,xy}^0 + \phi_{y,yy}^0\right)\right) \tag{3.44i}$$

$$P_{25} = 2l_0^2\left(\overline{JJ}\left(u_{,xy}^0 + v_{,yy}^0\right) - \overline{JJ^*}\left(w_{,xxy}^0 + w_{,yyy}^0\right) + \overline{KK}\left(\phi_{x,xy}^0 + \phi_{y,yy}^0\right)\right) \tag{3.44j}$$

$$P_{33} = 2l_0^2\left(\overline{II}\left(w_{,xx}^0 + w_{,yy}^0\right) - \overline{LL}\left(\phi_{x,x}^0 + \phi_{y,y}^0\right)\right) \tag{3.44k}$$

$$P_{34} = 2l_0^2\left(-\overline{LL}\left(w_{,xx}^0 + w_{,yy}^0\right) + \overline{MM}\left(\phi_{x,x}^0 + \phi_{y,y}^0\right)\right) \tag{3.44l}$$

$$P_{35} = 2l_0^2\left(-\overline{LL}\left(w_{,xx}^0 + w_{,yy}^0\right) + \overline{MM}\left(\phi_{x,x}^0 + \phi_{y,y}^0\right)\right) \tag{3.44m}$$

The non-zero work conjugates Q_{mn} and $\overline{Q_{mn}}$, of higher-order deformation gradients are defined in the following equations.

$$\begin{aligned} Q_{11} = \frac{2}{25}l_1^2\Big(&\overline{II}\left(2u_{,xx}^0 - u_{,yy}^0 - 2v_{,xy}^0\right) + \overline{II^*}\left(-2w_{,xxx}^0 + 3w_{,xyy}^0\right) \\ &+ \overline{JJ}\left(2\phi_{x,xx}^0 - \phi_{x,yy}^0 + 2\phi_{y,xy}^0\right) + \overline{NN}\left(-\phi_x^0\right)\Big) \end{aligned} \tag{3.45a}$$

$$\begin{aligned} Q_{12} = \frac{2}{25}l_1^2\Big(&\overline{II}\left(2u_{,xx}^0 - u_{,yy}^0 - 2v_{,xy}^0\right) + \overline{II^*}\left(-2w_{,xxx}^0 + 3w_{,xyy}^0\right) \\ &+ \overline{JJ}\left(2\phi_{x,xx}^0 - \phi_{x,yy}^0 + 2\phi_{y,xy}^0\right) + \overline{NN}\left(-\phi_x^0\right)\Big) \end{aligned} \tag{3.45b}$$

$$\begin{aligned} Q_{13} = \frac{2}{25}l_1^2\Big(&\overline{II^*}\left(2u_{,xx}^0 - u_{,yy}^0 - 2v_{,xy}^0\right) + \overline{II^{**}}\left(-2w_{,xxx}^0 + 3w_{,xyy}^0\right) \\ &+ \overline{JJ^*}\left(2\phi_{x,xx}^0 - \phi_{x,yy}^0 + 2\phi_{y,xy}^0\right) + \overline{NN^*}\left(-\phi_x^0\right)\Big) \end{aligned} \tag{3.45c}$$

$$\begin{aligned} Q_{14} = \frac{2}{25} l_1^2 \Big(& \overline{JJ}\left(2u^0_{,xx} - u^0_{,yy} - 2v^0_{,xy}\right) + \overline{JJ^*}\left(-2w^0_{,xxx} + 3w^0_{,xyy}\right) \\ & + \overline{KK}\left(2\phi^0_{x,xx} - \phi^0_{x,yy} + 2\phi^0_{y,xy}\right) + \overline{QQ}\left(-\phi^0_x\right)\Big) \end{aligned} \tag{3.45d}$$

$$\begin{aligned} Q_{15} = \frac{2}{25} l_1^2 \Big(& \overline{JJ}\left(2u^0_{,xx} - u^0_{,yy} - 2v^0_{,xy}\right) + \overline{JJ^{**}}\left(-2w^0_{,xxx} + 3w^0_{,xyy}\right) \\ & + \overline{KK}\left(2\phi^0_{x,xx} - \phi^0_{x,yy} + 2\phi^0_{y,xy}\right) + \overline{QQ}\left(-\phi^0_x\right)\Big) \end{aligned} \tag{3.45e}$$

$$\begin{aligned} \overline{Q_{14}} = \frac{2}{25} l_1^2 \Big(& \overline{NN}\left(2u^0_{,xx} - u^0_{,yy} - 2v^0_{,xy}\right) + \overline{NN^*}\left(-2w^0_{,xxx} + 3w^0_{,xyy}\right) \\ & + \overline{QQ}\left(2\phi^0_{x,xx} - \phi^0_{x,yy} + 2\phi^0_{y,xy}\right) + \overline{PP}\left(-\phi^0_x\right)\Big) \end{aligned} \tag{3.45f}$$

$$\begin{aligned} Q_{21} = \frac{2}{25} l_1^2 \Big(& \overline{II}\left(-2u^0_{,xy} - v^0_{,xx} + 2v^0_{,yy}\right) + \overline{II^*}\left(3w^0_{,xyy} - 2w^0_{,yyy}\right) \\ & + \overline{JJ}\left(-2\phi^0_{x,xy} - \phi^0_{y,xx} + 2\phi^0_{y,yy}\right) + \overline{NN}\left(-\phi^0_y\right)\Big) \end{aligned} \tag{3.45g}$$

$$\begin{aligned} Q_{22} = \frac{2}{25} l_1^2 \Big(& \overline{II}\left(-2u^0_{,xy} - v^0_{,xx} + 2v^0_{,yy}\right) + \overline{II^*}\left(3w^0_{,xyy} - 2w^0_{,yyy}\right) \\ & + \overline{JJ}\left(-2\phi^0_{x,xy} - \phi^0_{y,xx} + 2\phi^0_{y,yy}\right) + \overline{NN}\left(-\phi^0_y\right)\Big) \end{aligned} \tag{3.45h}$$

$$\begin{aligned} Q_{23} = \frac{2}{25} l_1^2 \Big(& \overline{II^*}\left(-2u^0_{,xy} - v^0_{,xx} + 2v^0_{,yy}\right) + \overline{II^{**}}\left(3w^0_{,xxy} - 2w^0_{,yyy}\right) \\ & + \overline{JJ^*}\left(-2\phi^0_{x,xy} - \phi^0_{y,xx} + 2\phi^0_{y,yy}\right) + \overline{NN^*}\left(-\phi^0_y\right)\Big) \end{aligned} \tag{3.45i}$$

$$\begin{aligned} Q_{24} = \frac{2}{25} l_1^2 \Big(& \overline{JJ}\left(-2u^0_{,xy} - v^0_{,xx} + 2v^0_{,yy}\right) + \overline{JJ^*}\left(3w^0_{,xyy} - 2w^0_{,yyy}\right) \\ & + \overline{KK}\left(-2\phi^0_{x,xy} - \phi^0_{y,xx} + 2\phi^0_{y,yy}\right) + \overline{QQ}\left(-\phi^0_y\right)\Big) \end{aligned} \tag{3.45j}$$

$$\begin{aligned} Q_{25} = \frac{2}{25} l_1^2 \Big(& \overline{JJ}\left(-2u^0_{,xy} - v^0_{,xx} + 2v^0_{,yy}\right) + \overline{JJ^*}\left(3w^0_{,xyy} - 2w^0_{,yyy}\right) \\ & + \overline{KK}\left(-2\phi^0_{x,xy} - \phi^0_{y,xx} + 2\phi^0_{y,yy}\right) + \overline{QQ}\left(-\phi^0_y\right)\Big) \end{aligned} \tag{3.45k}$$

$$\begin{aligned} \overline{Q_{25}} = \frac{2}{25} l_1^2 \Big(& \overline{NN}\left(-2u^0_{,xy} - v^0_{,xx} + 2v^0_{,yy}\right) + \overline{NN^*}\left(3w^0_{,xyy} - 2w^0_{,yyy}\right) \\ & + \overline{QQ}\left(-2\phi^0_{x,xy} - \phi^0_{y,xx} + 2\phi^0_{y,yy}\right) + \overline{PP}\left(-\phi^0_y\right)\Big) \end{aligned} \tag{3.45l}$$

$$Q_{33} = \frac{2}{25} l_1^2 \left(\overline{II}\left(w^0_{,xx} + w^0_{,yy}\right) + \overline{LL}\left(-2\phi^0_{x,x} - 2\phi^0_{y,y}\right)\right) \tag{3.45m}$$

$$Q_{34} = \frac{2}{25} l_1^2 \left(\overline{LL}\left(w^0_{,xx} + w^0_{,yy}\right) + \overline{MM}\left(-2\phi^0_{x,x} - 2\phi^0_{y,y}\right)\right) \tag{3.45n}$$

$$Q_{35} = \frac{2}{25} l_1^2 \left(\overline{LL}\left(w^0_{,xx} + w^0_{,yy}\right) + \overline{MM}\left(-2\phi^0_{x,x} - 2\phi^0_{y,y}\right)\right) \tag{3.45o}$$

$$\begin{aligned} Q_{41} = \frac{2}{75} l_1^2 \Big(& \overline{II}\left(8u^0_{,xy} + 4v^0_{,xx} - 3v^0_{,yy}\right) + \overline{II^*}\left(-12w^0_{,xyy} + 3w^0_{,yyy}\right) \\ & + \overline{JJ}\left(8\phi^0_{x,xy} + 4\phi^0_{y,xx} - 3\phi^0_{y,yy}\right) + \overline{NN}\left(-\phi^0_y\right)\Big) \end{aligned} \tag{3.45p}$$

$$\begin{aligned} Q_{42} = \frac{2}{75} l_1^2 \Big(& \overline{II}\left(8u^0_{,xy} + 4v^0_{,xx} - 3v^0_{,yy}\right) + \overline{II^*}\left(-12w^0_{,xyy} + 3w^0_{,yyy}\right) \\ & + \overline{JJ}\left(8\phi^0_{x,xy} + 4\phi^0_{y,xx} - 3\phi^0_{y,yy}\right) + \overline{NN}\left(-\phi^0_y\right)\Big) \end{aligned} \tag{3.45q}$$

$$\begin{aligned} Q_{43} = \frac{2}{75} l_1^2 \Big(& \overline{II^*}\left(8u^0_{,xy} + 4v^0_{,xx} - 3v^0_{,yy}\right) + \overline{II^{**}}\left(-12w^0_{,xxy} + 3w^0_{,yyy}\right) \\ & + \overline{JJ^*}\left(8\phi^0_{x,xy} + 4\phi^0_{y,xx} - 3\phi^0_{y,yy}\right) + \overline{NN^*}\left(-\phi^0_y\right)\Big) \end{aligned} \tag{3.45r}$$

$$\begin{aligned} Q_{44} = \frac{2}{75} l_1^2 \Big(& \overline{JJ}\left(8u^0_{,xy} + 4v^0_{,xx} - 3v^0_{,yy}\right) + \overline{JJ^*}\left(-12w^0_{,xyy} + 3w^0_{,yyy}\right) \\ & + \overline{KK}\left(8\phi^0_{x,xy} + 4\phi^0_{y,xx} - 3\phi^0_{y,yy}\right) + \overline{QQ}\left(-\phi^0_y\right)\Big) \end{aligned} \tag{3.45s}$$

$$\begin{aligned} Q_{45} = \frac{2}{75} l_1^2 \Big(& \overline{JJ}\left(8u^0_{,xy} + 4v^0_{,xx} - 3v^0_{,yy}\right) + \overline{JJ^*}\left(-12w^0_{,xyy} + 3w^0_{,yyy}\right) \\ & + \overline{KK}\left(8\phi^0_{x,xy} + 4\phi^0_{y,xx} - 3\phi^0_{y,yy}\right) + \overline{QQ}\left(-\phi^0_y\right)\Big) \end{aligned} \tag{3.45t}$$

$$\begin{aligned} \overline{Q_{45}} = \frac{2}{75} l_1^2 \Big(& \overline{NN}\left(8u^0_{,xy} + 4v^0_{,xx} - 3v^0_{,yy}\right) + \overline{NN^*}\left(-12w^0_{,xyy} + 3w^0_{,yyy}\right) \\ & + \overline{QQ}\left(8\phi^0_{x,xy} + 4\phi^0_{y,xx} - 3\phi^0_{y,yy}\right) + \overline{PP}\left(-\phi^0_y\right)\Big) \end{aligned} \tag{3.45u}$$

$$Q_{53} = \frac{2}{75} l_1^2 \Big(\overline{II}\left(-4w^0_{,xx} + w^0_{,yy}\right) + \overline{LL}\left(8\phi^0_{x,x} - 2\phi^0_{y,y}\right)\Big) \tag{3.45v}$$

$$Q_{54} = \frac{2}{75} l_1^2 \Big(\overline{LL}\left(-4w^0_{,xx} + w^0_{,yy}\right) + \overline{MM}\left(8\phi^0_{x,x} - 2\phi^0_{y,y}\right)\Big) \tag{3.45w}$$

$$Q_{55} = \frac{2}{75} l_1^2 \Big(\overline{LL}\left(-4w^0_{,xx} + w^0_{,yy}\right) + \overline{MM}\left(8\phi^0_{x,x} - 2\phi^0_{y,y}\right)\Big) \tag{3.45x}$$

$$\begin{aligned} Q_{61} = \frac{2}{75} l_1^2 \Big(& \overline{II}\left(-3u^0_{,xx} + 4u^0_{,yy} + 8v^0_{,xy}\right) + \overline{II^*}\left(3w^0_{,xxx} - 12w^0_{,xyy}\right) \\ & + \overline{JJ}\left(-3\phi^0_{x,xx} + 4\phi^0_{x,yy} + 8\phi^0_{y,xy}\right) + \overline{NN}\left(-\phi^0_x\right)\Big) \end{aligned} \tag{3.45y}$$

$$\begin{aligned} Q_{62} = \frac{2}{75} l_1^2 \Big(& \overline{II}\left(-3u^0_{,xx} + 4v^0_{,yy} + 8v^0_{,xy}\right) + \overline{II^*}\left(3w^0_{,xxx} - 12w^0_{,xyy}\right) \\ & + \overline{JJ}\left(-3\phi^0_{x,xx} + 4\phi^0_{x,yy} + 8\phi^0_{y,xy}\right) + \overline{NN}\left(-\phi^0_x\right)\Big) \end{aligned} \tag{3.45z}$$

$$\begin{aligned} Q_{63} = \frac{2}{75} l_1^2 \Big(& \overline{II^*}\left(-3u^0_{,xx} + 4v^0_{,yy} + 8v^0_{,xy}\right) + \overline{II^{**}}\left(3w^0_{,xxx} - 12w^0_{,xyy}\right) \\ & + \overline{JJ^*}\left(-3\phi^0_{x,xx} + 4\phi^0_{x,yy} + 8\phi^0_{y,xy}\right) + \overline{NN^*}\left(-\phi^0_x\right)\Big) \end{aligned} \tag{3.45aa}$$

$$Q_{64}=\frac{2}{75}l_1^2\Big(\overline{JJ}\big(-3u^0_{,xx}+4v^0_{,yy}+8v^0_{,xy}\big)+\overline{JJ^*}\big(3w^0_{,xxx}-12w^0_{,xyy}\big)+\overline{KK}\big(-3\phi^0_{x,xx}+4\phi^0_{x,yy}+8\phi^0_{y,xy}\big)+\overline{QQ}(-\phi^0_x)\Big) \tag{3.45ab}$$

$$Q_{65}=\frac{2}{75}l_1^2\Big(\overline{JJ}\big(-3u^0_{,xx}+4v^0_{,yy}+8v^0_{,xy}\big)+\overline{JJ^*}\big(3w^0_{,xxx}-12w^0_{,xyy}\big)+\overline{KK}\big(-3\phi^0_{x,xx}+4\phi^0_{x,yy}+8\phi^0_{y,xy}\big)+\overline{QQ}(-\phi^0_x)\Big) \tag{3.45ac}$$

$$\overline{Q_{64}}=\frac{2}{75}l_1^2\Big(\overline{NN}\big(-3u^0_{,xx}+4v^0_{,yy}+8v^0_{,xy}\big)+\overline{NN^*}\big(3w^0_{,xxx}-12w^0_{,xyy}\big)+\overline{QQ}\big(-3\phi^0_{x,xx}+4\phi^0_{x,yy}+8\phi^0_{y,xy}\big)+\overline{PP}(-\phi^0_x)\Big) \tag{3.45ad}$$

$$Q_{73}=\frac{2}{75}l_1^2\Big(\overline{II}\big(w^0_{,xx}-4w^0_{,yy}\big)+\overline{LL}\big(-2\phi^0_{x,x}+8\phi^0_{y,y}\big)\Big) \tag{3.45ae}$$

$$Q_{74}=\frac{2}{75}l_1^2\Big(\overline{LL}\big(w^0_{,xx}-4w^0_{,yy}\big)+\overline{MM}\big(-2\phi^0_{x,x}+8\phi^0_{y,y}\big)\Big) \tag{3.45af}$$

$$Q_{75}=\frac{2}{75}l_1^2\Big(\overline{LL}\big(w^0_{,xx}-4w^0_{,yy}\big)+\overline{MM}\big(-2\phi^0_{x,x}+8\phi^0_{y,y}\big)\Big) \tag{3.45ag}$$

$$Q_{81}=\frac{2}{75}l_1^2\Big(\overline{II}\big(-3u^0_{,xx}-u^0_{,yy}-2v^0_{,xy}\big)+\overline{II^*}\big(3w^0_{,xxx}+3w^0_{,xyy}\big)+\overline{JJ}\big(-3\phi^0_{x,xx}-\phi^0_{x,yy}-2\phi^0_{y,xy}\big)+\overline{NN}(4\phi^0_x)\Big) \tag{3.45ah}$$

$$Q_{82}=\frac{2}{75}l_1^2\Big(\overline{II}\big(-3u^0_{,xx}-u^0_{,yy}-2v^0_{,xy}\big)+\overline{II^*}\big(3w^0_{,xxx}+3w^0_{,xyy}\big)+\overline{JJ}\big(-3\phi^0_{x,xx}-\phi^0_{x,yy}-2\phi^0_{y,xy}\big)+\overline{NN}(4\phi^0_x)\Big) \tag{3.45ai}$$

$$Q_{83}=\frac{2}{75}l_1^2\Big(\overline{II^*}\big(-3u^0_{,xx}-u^0_{,yy}-2v^0_{,xy}\big)+\overline{II^{**}}\big(3w^0_{,xxx}+3w^0_{,xyy}\big)+\overline{JJ^*}\big(-3\phi^0_{x,xx}-\phi^0_{x,yy}-2\phi^0_{y,xy}\big)+\overline{NN^*}(4\phi^0_x)\Big) \tag{3.45aj}$$

$$Q_{84}=\frac{2}{75}l_1^2\Big(\overline{JJ}\big(-3u^0_{,xx}-u^0_{,yy}-2v^0_{,xy}\big)+\overline{JJ^*}\big(3w^0_{,xxx}+3w^0_{,xyy}\big)+\overline{KK}\big(-3\phi^0_{x,xx}-\phi^0_{x,yy}-2\phi^0_{y,xy}\big)+\overline{QQ}(4\phi^0_x)\Big) \tag{3.45ak}$$

$$Q_{85}=\frac{2}{75}l_1^2\Big(\overline{JJ}\big(-3u^0_{,xx}-u^0_{,yy}-2v^0_{,xy}\big)+\overline{JJ^*}\big(3w^0_{,xxx}+3w^0_{,xyy}\big)+\overline{KK}\big(-3\phi^0_{x,xx}-\phi^0_{x,yy}-2\phi^0_{y,xy}\big)+\overline{QQ}(4\phi^0_x)\Big) \tag{3.45al}$$

$$\overline{Q_{84}}=\frac{2}{75}l_1^2\Big(\overline{NN}\big(-3u^0_{,xx}-u^0_{,yy}-2v^0_{,xy}\big)+\overline{NN^*}\big(3w^0_{,xxx}+3w^0_{,xyy}\big)+\overline{QQ}\big(-3\phi^0_{x,xx}-\phi^0_{x,yy}-2\phi^0_{y,xy}\big)+\overline{PP}(4\phi^0_x)\Big) \tag{3.45am}$$

$$\begin{aligned} Q_{91} = \frac{2}{75} l_1^2 \Big(& \overline{II}\left(-2u^0_{,xy} - v^0_{,xx} - 3v^0_{,yy}\right) + \overline{II^*}\left(3w^0_{,xxy} + 3w^0_{,yyy}\right) \\ & + \overline{JJ}\left(-2\phi^0_{x,xy} - \phi^0_{y,xx} - 3\phi^0_{y,yy}\right) + \overline{NN}\left(4\phi^0_{y}\right)\Big) \end{aligned} \tag{3.45an}$$

$$\begin{aligned} Q_{92} = \frac{2}{75} l_1^2 \Big(& \overline{II}\left(-2u^0_{,xy} - v^0_{,xx} - 3v^0_{,yy}\right) + \overline{II^*}\left(3w^0_{,xxy} + 3w^0_{,yyy}\right) \\ & + \overline{JJ}\left(-2\phi^0_{x,xy} - \phi^0_{y,xx} - 3\phi^0_{y,yy}\right) + \overline{NN}\left(4\phi^0_{y}\right)\Big) \end{aligned} \tag{3.45ao}$$

$$\begin{aligned} Q_{93} = \frac{2}{75} l_1^2 \Big(& \overline{II^*}\left(-2u^0_{,xy} - v^0_{,xx} - 3v^0_{,yy}\right) + \overline{II^{**}}\left(3w^0_{,xxy} + 3w^0_{,yyy}\right) \\ & + \overline{JJ^*}\left(-2\phi^0_{x,xy} - \phi^0_{y,xx} - 3\phi^0_{y,yy}\right) + \overline{NN^*}\left(4\phi^0_{y}\right)\Big) \end{aligned} \tag{3.45ap}$$

$$\begin{aligned} Q_{94} = \frac{2}{75} l_1^2 \Big(& \overline{JJ}\left(-2u^0_{,xy} - v^0_{,xx} - 3v^0_{,yy}\right) + \overline{JJ^*}\left(3w^0_{,xxy} + 3w^0_{,yyy}\right) \\ & + \overline{KK}\left(-2\phi^0_{x,xy} - \phi^0_{y,xx} - 3\phi^0_{y,yy}\right) + \overline{QQ}\left(4\phi^0_{y}\right)\Big) \end{aligned} \tag{3.45aq}$$

$$\begin{aligned} Q_{95} = \frac{2}{75} l_1^2 \Big(& \overline{JJ}\left(-2u^0_{,xy} - v^0_{,xx} - 3v^0_{,yy}\right) + \overline{JJ^*}\left(3w^0_{,xxy} + 3w^0_{,yyy}\right) \\ & + \overline{KK}\left(-2\phi^0_{x,xy} - \phi^0_{y,xx} - 3\phi^0_{y,yy}\right) + \overline{QQ}\left(4\phi^0_{y}\right)\Big) \end{aligned} \tag{3.45ar}$$

$$\begin{aligned} \overline{Q_{95}} = \frac{2}{75} l_1^2 \Big(& \overline{NN}\left(-2u^0_{,xy} - v^0_{,xx} - 3v^0_{,yy}\right) + \overline{NN^*}\left(3w^0_{,xxy} + 3w^0_{,yyy}\right) \\ & + \overline{QQ}\left(-2\phi^0_{x,xy} - \phi^0_{y,xx} - 3\phi^0_{y,yy}\right) + \overline{PP}\left(4\phi^0_{y}\right)\Big) \end{aligned} \tag{3.45as}$$

$$Q_{103} = \frac{4}{3} l_1^2 \left(-\overline{II} w^0_{,xy} + \overline{LL}\left(2\phi^0_{x,y} + \phi^0_{y,x}\right)\right) \tag{3.45at}$$

$$Q_{104} = \frac{4}{3} l_1^2 \left(-\overline{LL} w^0_{,xy} + \overline{MM}\left(2\phi^0_{x,y} + \phi^0_{y,x}\right)\right) \tag{3.45au}$$

$$Q_{105} = \frac{4}{3} l_1^2 \left(-\overline{LL} w^0_{,xy} + \overline{MM}\left(2\phi^0_{x,y} + \phi^0_{y,x}\right)\right) \tag{3.45av}$$

The functions $\overline{II}$, $\overline{JJ}$, $\overline{KK}$, $\overline{LL}$, $\overline{MM}$, $\overline{NN}$, $\overline{PP}$, $\overline{QQ}$, $\overline{II^*}$, $\overline{II^{**}}$, $\overline{JJ^*}$, and $\overline{NN^*}$ used in the Eqs. (3.43), Eqs. (3.44), and Eqs. (3.45) are defined in the equations below.

$$\overline{II} = \int_{-h/2}^{h/2} \mu \, dz \tag{3.46a}$$

$$\overline{JJ} = \int_{-h/2}^{h/2} \mu f(z) \, dz \tag{3.46b}$$

$$\overline{KK} = \int_{-h/2}^{h/2} \mu f(z)^2 \, dz \tag{3.46c}$$

$$\overline{LL} = \int_{-h/2}^{h/2} \mu f'(z)\, dz \tag{3.46d}$$

$$\overline{MM} = \int_{-h/2}^{h/2} \mu \big(f'(z)\big)^2\, dz \tag{3.46e}$$

$$\overline{NN} = \int_{-h/2}^{h/2} \mu f''(z)\, dz \tag{3.46f}$$

$$\overline{PP} = \int_{-h/2}^{h/2} \mu \big(f''(z)\big)^2\, dz \tag{3.46g}$$

$$\overline{QQ} = \int_{-h/2}^{h/2} \mu f(z) f''(z)\, dz \tag{3.46h}$$

$$\overline{II^*} = \int_{-h/2}^{h/2} \mu z\, dz \tag{3.46i}$$

$$\overline{II^{**}} = \int_{-h/2}^{h/2} \mu z^2\, dz \tag{3.46j}$$

$$\overline{JJ^*} = \int_{-h/2}^{h/2} \mu z f(z)\, dz \tag{3.46k}$$

$$\overline{NN^*} = \int_{-h/2}^{h/2} \mu z f''(z)\, dz \tag{3.46l}$$

The first variation of components of strain energy *'U'* in the region '*B'* are provided below.

The first variation of components of strain energy due to Cauchy strain are:

$$\begin{aligned}\delta^{(1)}U_\sigma = \frac{1}{2}\int_B \big(&\sigma_{xx}\delta^{(1)}\epsilon_{xx} + \sigma_{yy}\delta^{(1)}\epsilon_{yy} + \sigma_{xy}\delta^{(1)}\gamma_{xy} + \sigma_{xz}\delta^{(1)}\gamma_{xz} \\ &+ \sigma_{yz}\delta^{(1)}\gamma_{yz}\big)\, dB\end{aligned} \tag{3.47}$$

$$\begin{aligned}\delta^{(1)}U_\sigma^N = \frac{1}{2}\int_{-a/2}^{a/2}\int_{-b/2}^{b/2} \Big(&N_{xx}\big(\delta^{(1)}u_{,x}^0 + w_{,xx}^0\delta^{(1)}w^0\big) \\ &+ N_{yy}\big(\delta^{(1)}v_{,y}^0 + w_{,yy}^0\delta^{(1)}w^0\big) \\ &+ N_{xy}\big(\delta^{(1)}u_{,y}^0 + \delta^{(1)}v_{,x}^0 + w_{,x}^0\delta^{(1)}w_{,y}^0 + w_{,y}^0\delta^{(1)}w_{,x}^0\big)\Big)\, dx\, dy\end{aligned} \tag{3.47a}$$

$$\begin{aligned}\delta^{(1)}U_\sigma^M = \frac{1}{2}\int_{-a/2}^{a/2}\int_{-b/2}^{b/2} \Big(&M_{xx}\big(-\delta^{(1)}w_{,xx}^0\big) + M_{yy}\big(-\delta^{(1)}w_{,yy}^0\big) \\ &+ M_{xy}\big(-2\delta^{(1)}w_{,xy}^0\big)\Big)\, dx\, dy\end{aligned} \tag{3.47b}$$

$$\delta^{(1)}U_\sigma^{M^{\mathrm{a}}} = \frac{1}{2}\int_{-a/2}^{a/2}\int_{-b/2}^{b/2}\Big(M_{xx}^{a}\big(\delta^{(1)}\phi_{x,x}^{0}\big) + M_{yy}^{a}\big(\delta^{(1)}\phi_{y,y}^{0}\big) + M_{xy}^{a}\big(\delta^{(1)}\phi_{x,y}^{0} + \delta^{(1)}\phi_{y,x}^{0}\big)\Big)\,dx\,dy \tag{3.47c}$$

$$\delta^{(1)}U_\sigma^{S} = \frac{1}{2}\int_{-a/2}^{a/2}\int_{-b/2}^{b/2}\Big(S_{yz}\big(\delta^{(1)}\gamma_{yz}\big) + S_{xz}\big(\delta^{(1)}\gamma_{xz}\big)\Big)\,dx\,dy \tag{3.47d}$$

The first variation of components of strain energy due to symmetric curvature gradient tensor (U_r) are

$$\delta^{(1)}U_r = \frac{1}{2}\int\limits_B \big(r_{xx}\delta^{(1)}\chi_{xx}^{s} + r_{yy}\delta^{(1)}\chi_{yy}^{s} + 2r_{xy}\delta^{(1)}\chi_{xy}^{s} + 2r_{yz}\delta^{(1)}\chi_{yz}^{s} + 2r_{xz}\delta^{(1)}\chi_{xz}^{s}\big)\,dB \tag{3.48}$$

The independent components of Eq. (3.48) are defined in Eqs. (3.48a-e).

$$\frac{1}{2}\int\limits_B r_{xx}\delta^{(1)}\chi_{xx}^{s}\,dB = \frac{1}{2}\int_{-a/2}^{a/2}\int_{-b/2}^{b/2}\big(Y_{13,xy}\delta^{(1)}w^{0} + Y_{15,x}\delta^{(1)}\phi_{y}^{0}\big)\,dx\,dy \tag{3.48a}$$

$$\frac{1}{2}\int\limits_B r_{yy}\delta^{(1)}\chi_{yy}^{s}\,dB = \frac{1}{2}\int_{-a/2}^{a/2}\int_{-b/2}^{b/2}\big(Y_{23,xy}\delta^{(1)}w^{0} + Y_{24,y}\delta^{(1)}\phi_{x}^{0}\big)\,dx\,dy \tag{3.48b}$$

$$\frac{1}{2}\int\limits_B 2r_{xy}\delta^{(1)}\chi_{xy}^{s}\,dB = \frac{1}{2}\int_{-a/2}^{a/2}\int_{-b/2}^{b/2}\Big(\big(Y_{33,yy}\delta^{(1)}w^{0} - Y_{33,xx}\delta^{(1)}w^{0}\big) + Y_{34,x}\delta^{(1)}\phi_{x}^{0} + Y_{35,y}\delta^{(1)}\phi_{y}^{0}\Big)\,dx\,dy \tag{3.48c}$$

$$\frac{1}{2}\int\limits_B 2r_{yz}\delta^{(1)}\chi_{yz}^{s}\,dB = \frac{1}{2}\int_{-a/2}^{a/2}\int_{-b/2}^{b/2}\Big(\big(Y_{41,yy}\delta^{(1)}u^{0} + Y_{42,xy}\delta^{(1)}v^{0}\big) + Y_{45,xy}\delta^{(1)}\phi_{y}^{0} + Y_{44},yy\delta^{(1)}\phi_{x}^{0} + \overline{Y_{44}}\delta^{(1)}\phi_{x}^{0}\Big)\,dx\,dy \tag{3.48d}$$

$$\frac{1}{2}\int\limits_B 2r_{xz}\delta^{(1)}\chi_{xz}^{s}\,dB = \frac{1}{2}\int_{-a/2}^{a/2}\int_{-b/2}^{b/2}\Big(\big(Y_{51,xy}\delta^{(1)}u^{0} + Y_{52,xx}\delta^{(1)}v^{0}\big) + Y_{54,xy}\delta^{(1)}\phi_{x}^{0} + Y_{55,xx}\delta^{(1)}\phi_{y}^{0} + \overline{Y_{55}}\delta^{(1)}\phi_{y}^{0}\Big)\,dx\,dy \tag{3.48e}$$

The first variation of components of strain energy due to dilatation gradient tensor (U_L)

$$U_L = \frac{1}{2}\int_B \left(L_x \delta^{(1)} \psi_x + L_y \delta^{(1)} \psi_y + L_z \delta^{(1)} \psi_z\right) dB \tag{3.49}$$

The independent components of Eq. (3.49) are defined in Eqs. (3.49a-c).

$$\begin{aligned}
&\frac{1}{2}\int_B L_x \delta^{(1)} \psi_x \, dB \\
&= \frac{1}{2}\int_{-a/2}^{a/2}\int_{-b/2}^{b/2} \left(P_{11,xx} \delta^{(1)} u^0 + P_{12,xy} \delta^{(1)} v^0\right. \\
&+ \left(P_{13,xxx} \delta^{(1)} w^0 + P_{13,xyy} \delta^{(1)} w^0\right) + P_{14,xx} \delta^{(1)} \phi_x^0 \\
&\left.+ P_{15,xy} \delta^{(1)} \phi_y^0\right) dx\, dy
\end{aligned} \tag{3.49a}$$

$$\begin{aligned}
&\frac{1}{2}\int_B L_y \delta^{(1)} \psi_y \, dB \\
&= \frac{1}{2}\int_{-a/2}^{a/2}\int_{-b/2}^{b/2} \left(P_{21,xy} \delta^{(1)} u^0 + P_{22,yy} \delta^{(1)} v^0\right. \\
&+ \left(P_{23,xxy} \delta^{(1)} w^0 + P_{23,yyy} \delta^{(1)} w^0\right) + P_{24,xy} \delta^{(1)} \phi_x^0 \\
&\left.+ P_{25,yy} \delta^{(1)} \phi_y^0\right) dx\, dy
\end{aligned} \tag{3.49b}$$

$$\begin{aligned}
&\frac{1}{2}\int_B L_z \delta^{(1)} \psi_z \, dB \\
&= \frac{1}{2}\int_{-a/2}^{a/2}\int_{-b/2}^{b/2} \left(\left(P_{33,xx} \delta^{(1)} w^0 + P_{33,yy} \delta^{(1)} w^0\right) + P_{34,x} \delta^{(1)} \phi_x^0\right. \\
&\left.+ P_{35,y} \delta^{(1)} \phi_y^0\right) dx\, dy
\end{aligned} \tag{3.49c}$$

The first variation of components of strain energy due to the deviatoric stretch gradient tensor (U_τ) are

$$\begin{aligned}
\delta^{(1)} U_\tau = \frac{1}{2}\int_B &\left(\tau_{xxx}^{(1)} \delta^{(1)} \eta_{xxx}^{(1)} + \tau_{yyy}^{(1)} \delta^{(1)} \eta_{yyy}^{(1)} + \tau_{zzz}^{(1)} \delta^{(1)} \eta_{zzz}^{(1)} + 3\tau_{xxy}^{(1)} \delta^{(1)} \eta_{xxy}^{(1)}\right. \\
&+ 3\tau_{xxz}^{(1)} \delta^{(1)} \eta_{xxz}^{(1)} + 3\tau_{yyx}^{(1)} \delta^{(1)} \eta_{yyx}^{(1)} + 3\tau_{yyz}^{(1)} \delta^{(1)} \eta_{yyz}^{(1)} \\
&\left.+ 3\tau_{zzx}^{(1)} \delta^{(1)} \eta_{zzx}^{(1)} + 3\tau_{zzy}^{(1)} \delta^{(1)} \eta_{zzy}^{(1)} + 6\tau_{xyz}^{(1)} \delta^{(1)} \eta_{xyz}^{(1)}\right) dB
\end{aligned} \tag{3.50}$$

The independent components of Eq. (3.50) are defined in following equations:

$$
\begin{aligned}
&\frac{1}{2}\int_{B} \tau_{xxx}^{(1)}\delta^{(1)}\eta_{xxx}^{(1)}\,dB \\
&\quad = \frac{1}{2}\int_{-a/2}^{a/2}\int_{-b/2}^{b/2}\Big(\big(2Q_{11,xx}\delta^{(1)}u^{0} - Q_{11,yy}\delta^{(1)}u^{0}\big) \\
&\quad - 2Q_{12,xy}\delta^{(1)}v^{0} + \big(-2Q_{13,xxx}\delta^{(1)}w^{0} + 3Q_{13,xyy}\delta^{(1)}w^{0}\big) \\
&\quad + \big(2Q_{14,xx}\delta^{(1)}\phi_{x}^{0} - Q_{14,yy}\delta^{(1)}\phi_{x}^{0}\big) + 2Q_{15,xy}\delta^{(1)}\phi_{y}^{0} \\
&\quad - \overline{Q_{14}}\delta^{(1)}\phi_{x}^{0}\Big)\,dx\,dy
\end{aligned}
\tag{3.50a}
$$

$$
\begin{aligned}
&\frac{1}{2}\int_{B} \tau_{yyy}^{(1)}\delta^{(1)}\eta_{yyy}^{(1)}\,dB \\
&\quad = \frac{1}{2}\int_{-a/2}^{a/2}\int_{-b/2}^{b/2}\big(-2Q_{21,xy}\delta^{(1)}u^{0} \\
&\quad + \big(-Q_{22,xx}\delta^{(1)}v^{0} + 2Q_{22,yy}\delta^{(1)}v^{0}\big) \\
&\quad + \big(3Q_{23,xxy}\delta^{(1)}w^{0} - 2Q_{23,yyy}\delta^{(1)}w^{0}\big) - 2Q_{24,xy}\delta^{(1)}\phi_{x}^{0} \\
&\quad + \big(-Q_{25,xx}\delta^{(1)}\phi_{y}^{0} + 2Q_{25,yy}\delta^{(1)}\phi_{y}^{0}\big) - \overline{Q_{25}}\delta^{(1)}\phi_{y}^{0}\big)\,dx\,dy
\end{aligned}
\tag{3.50b}
$$

$$
\begin{aligned}
&\frac{1}{2}\int_{B} \tau_{zzz}^{(1)}\delta^{(1)}\eta_{zzz}^{(1)}\,dB \\
&\quad = \frac{1}{2}\int_{-a/2}^{a/2}\int_{-b/2}^{b/2}\Big(\big(Q_{33,xx}\delta^{(1)}w^{0} + Q_{33,yy}\delta^{(1)}w^{0}\big) - 2Q_{34,x}\delta^{(1)}\phi_{x}^{0} \\
&\quad - 2Q_{35,y}\delta^{(1)}\phi_{y}^{0}\Big)\,dx\,dy
\end{aligned}
\tag{3.50c}
$$

$$
\begin{aligned}
&\frac{1}{2}\int_{B} 3\tau_{xxy}^{(1)}\delta^{(1)}\eta_{xxy}^{(1)}\,dB \\
&\quad = \frac{1}{2}\int_{-a/2}^{a/2}\int_{-b/2}^{b/2}\big(8Q_{41,xy}\delta^{(1)}u^{0} \\
&\quad + \big(4Q_{42,xx}\delta^{(1)}v^{0} - 3Q_{42,yy}\delta^{(1)}v^{0}\big) \\
&\quad + \big(-12Q_{43,xxy}\delta^{(1)}w^{0} + 3Q_{43,yyy}\delta^{(1)}w^{0}\big) + 8Q_{44,xy}\delta^{(1)}\phi_{x}^{0} \\
&\quad + \big(4Q_{45,xx}\delta^{(1)}\phi_{y}^{0} - 3Q_{45,yy}\delta^{(1)}\phi_{y}^{0}\big) - \overline{Q_{45}}\delta^{(1)}\phi_{y}^{0}\big)\,dx\,dy
\end{aligned}
\tag{3.50d}
$$

$$\frac{1}{2}\int_{B} 3\tau_{xxz}^{(1)}\delta^{(1)}\eta_{xxz}^{(1)}\,dB$$

$$= \frac{1}{2}\int_{-a/2}^{a/2}\int_{-b/2}^{b/2}\Big(\big(-4Q_{53,xx}\delta^{(1)}w^0 + Q_{53,yy}\delta^{(1)}w^0\big) + 8Q_{54,x}\delta^{(1)}\phi_x^0 - 2Q_{55,y}\delta^{(1)}\phi_y^0\Big)\,dx\,dy \tag{3.50e}$$

$$\frac{1}{2}\int_{B} 3\tau_{yyx}^{(1)}\delta^{(1)}\eta_{yyx}^{(1)}\,dB$$

$$\begin{aligned}= \frac{1}{2}\int_{-a/2}^{a/2}\int_{-b/2}^{b/2}\Big(&\big(-3Q_{61,xx}\delta^{(1)}u^0 + 4Q_{61,yy}\delta^{(1)}u^0\big)\\ &+ 8Q_{62,xy}\delta^{(1)}v^0 + \big(3Q_{63,xxx}\delta^{(1)}w^0 - 12Q_{63,xyy}\delta^{(1)}w^0\big)\\ &+ \big(-3Q_{64,xx}\delta^{(1)}\phi_x^0 + 4Q_{64,yy}\delta^{(1)}\phi_x^0\big) + 8Q_{65,xy}\delta^{(1)}\phi_y^0\\ &- \overline{Q_{64}}\delta^{(1)}\phi_x^0\Big)\,dx\,dy\end{aligned} \tag{3.50f}$$

$$\frac{1}{2}\int_{B} 3\tau_{yyz}^{(1)}\delta^{(1)}\eta_{yyz}^{(1)}\,dB$$

$$= \frac{1}{2}\int_{-a/2}^{a/2}\int_{-b/2}^{b/2}\Big(\big(Q_{73,xx}\delta^{(1)}w^0 - 4Q_{73,yy}\delta^{(1)}w^0\big) - 2Q_{74,x}\delta^{(1)}\phi_x^0 + 8Q_{75,y}\delta^{(1)}\phi_y^0\Big)\,dx\,dy \tag{3.50g}$$

$$\frac{1}{2}\int_{B} 3\tau_{zzx}^{(1)}\delta^{(1)}\eta_{zzx}^{(1)}\,dB$$

$$\begin{aligned}= \frac{1}{2}\int_{-a/2}^{a/2}\int_{-b/2}^{b/2}\Big(&\big(-3Q_{81,xx}\delta^{(1)}u^0 - Q_{81,yy}\delta^{(1)}u^0\big)\\ &- 2Q_{82,xy}\delta^{(1)}v^0 + \big(3Q_{83,xxx}\delta^{(1)}w^0 + 3Q_{83,xyy}\delta^{(1)}w^0\big)\\ &+ \big(-3Q_{84,xx}\delta^{(1)}\phi_x^0 - Q_{84,yy}\delta^{(1)}\phi_x^0\big) - 2Q_{85,xy}\delta^{(1)}\phi_y^0\\ &- \overline{Q_{84}}\delta^{(1)}\phi_x^0\Big)\,dx\,dy\end{aligned} \tag{3.50h}$$

$$\frac{1}{2}\int_B 3\tau_{zzy}^{(1)}\delta^{(1)}\eta_{zzy}^{(1)}\,dB$$

$$\begin{aligned}&=\frac{1}{2}\int_{-a/2}^{a/2}\int_{-b/2}^{b/2}\Big(-2Q_{91,xy}\delta^{(1)}u^0\\&+\left(-Q_{92,xx}\delta^{(1)}v^0-3Q_{92,yy}\delta^{(1)}v^0\right)\\&+\left(3Q_{93,xxy}\delta^{(1)}w^0+3Q_{93,yyy}\delta^{(1)}w^0\right)-2Q_{94,xy}\delta^{(1)}\phi_x^0\\&+\left(-Q_{95,xx}\delta^{(1)}\phi_y^0-3Q_{95,yy}\delta^{(1)}\phi_y^0\right)+4\overline{Q_{95}}\delta^{(1)}\phi_y^0\Big)\,dx\,dy\end{aligned}\tag{3.50i}$$

$$\frac{1}{2}\int_B 3\tau_{xyz}^{(1)}\delta^{(1)}\eta_{xyz}^{(1)}\,dB$$

$$\begin{aligned}&=\frac{1}{2}\int_{-a/2}^{a/2}\int_{-b/2}^{b/2}\Big(-Q_{103,xy}\delta^{(1)}w^0+Q_{104,y}\delta^{(1)}\phi_x^0\\&+Q_{105,x}\delta^{(1)}\phi_y^0\Big)\,dx\,dy\end{aligned}\tag{3.50j}$$

3.6.1.2 First Variation of Strain Energy due to Foundation

The expression for the foundation strain energy *'F'* in the region *'B'* due to Winkler and Pasternak elastic foundation parameters, K_w and K_p is given in Eq. (3.51a), and its first variation is provided in Eq. (3.51b).

$$F=\frac{1}{2}\int_{-a/2}^{a/2}\int_{-b/2}^{b/2}\left[K_w\frac{1}{2}(w^0)^2+K_p\frac{1}{2}\left\{\left(w^0{}_{,x}\right)^2+\left(w^0{}_{,y}\right)^2\right\}\right]dx\,dy\tag{3.51a}$$

$$\delta^{(1)}F=\frac{1}{2}\int_{-a/2}^{a/2}\int_{-b/2}^{b/2}\left(\left(K_w w^0-K_p\left(w_{,xx}^0+w_{,yy}^0\right)\right)\delta^{(1)}w^0\right)dx\,dy\tag{3.51b}$$

3.6.1.3 First Variation of Geometric Strain Energy

The expression for the geometric strain energy *'G'* because of in-plane pre-buckling stresses is given in Eq. (3.52a) and its first variation is given in Eq. (3.52b) and Eq. (3.52c).

$$G=\frac{1}{2}\int_{-a/2}^{a/2}\int_{-b/2}^{b/2}\left(\frac{1}{2}n_{xx}\left(w_{,x}^0\right)^2+\frac{1}{2}n_{yy}\left(w_{,y}^0\right)^2+n_{xy}\left(w_{,x}^0w_{,y}^0\right)\right)dx\,dy\tag{3.52a}$$

$$\begin{aligned}\delta^{(1)}G=\frac{1}{2}\int_{-a/2}^{a/2}\int_{-b/2}^{b/2}&\Big(n_{xx}w_{,x}^0\delta^{(1)}w_{,x}^0+n_{yy}w_{,y}^0\delta^{(1)}w_{,y}^0\\&+n_{xy}\left(w_{,x}^0\delta^{(1)}w_{,y}^0+w_{,y}^0\delta^{(1)}w_{,x}^0\right)\Big)\,dx\,dy\end{aligned}\tag{3.52b}$$

$$\delta^{(1)}G = \frac{1}{2}\int_{-a/2}^{a/2}\int_{-b/2}^{b/2}\Bigg(\Big(\left(n_{xx}w_{,x}^{0}\right)_{,x} + \left(n_{yy}w_{,y}^{0}\right)_{,y} + \left(n_{xy}w_{,x}^{0}\right)_{,y} + \left(n_{xy}w_{,y}^{0}\right)_{,x}\Big)\,\delta^{(1)}w^{0}\Bigg)\,dx\,dy \tag{3.52c}$$

In the above equation, n_{ij}, where *i,j*=(*x,y*), denote the in-plane pre-buckling stress resultants.

3.6.1.4 First Variation of External Work Done

The expression for the first variation of work done due to the transverse patch loading applied on the microplate is provided in Eq. (3.53).

$$\bar{\delta}W = \frac{1}{2}\int_{-a/2}^{a/2}\int_{-b/2}^{b/2}\left(f(x,y)\bar{\delta}w^{0}\right)dx\,dy \tag{3.53}$$

3.6.1.5 First Variation of Damping Energy

The expression for the damping energy *'C'* in the region *'B'* is given in Eq. (3.54a), and its first variation is provided in Eq. (3.54b).

$$C = \frac{1}{2}\int_{-a/2}^{a/2}\int_{-b/2}^{b/2}\left(c_{d1}\dot{u}^{0}\cdot u^{0} + c_{d2}\dot{v}^{0}\cdot v^{0} + c_{d3}\dot{w}^{0}\cdot w^{0} + c_{d4}\dot{\phi}_{x}^{0}\cdot\phi_{x}^{0} + c_{d5}\dot{\phi}_{y}^{0}\cdot\phi_{y}^{0}\right)dx\,dy \tag{3.54a}$$

$$\delta^{(1)}C = \frac{1}{2}\int_{-a/2}^{a/2}\int_{-b/2}^{b/2}\left(c_{d1}\dot{u}^{0}\delta^{(1)}u^{0} + c_{d2}\dot{v}^{0}\delta^{(1)}v^{0} + c_{d3}\dot{w}^{0}\delta^{(1)}w^{0} + c_{d4}\dot{\phi}_{x}^{0}\delta^{(1)}\phi_{x}^{0} + c_{d5}\dot{\phi}_{y}^{0}\delta^{(1)}\phi_{y}^{0}\right)dx\,dy \tag{3.54b}$$

The terms, c_{d1}, c_{d2}, c_{d3}, c_{d4}, and c_{d5} are obtained from the damping coefficient matrix computed using Rayleigh's damping method. In the above equations and anywhere else in the thesis, the accent "$(\dot{\ })$" indicates differentiation with respect to time '*t*' and "$(\ddot{\ })$" indicates double differentiation with respect to time '*t*'.

3.6.1.6 First Variation of Kinetic Energy

The expression for the Kinetic energy *'T'* in the region *'B'* is given in Eq. (3.55a), and its first variation is provided in Eq. (3.55b) and Eq. (3.55c).

$$T = \frac{1}{2}\int_{B} \left(\rho\left\{\frac{1}{2}(\dot{u})^2 + \frac{1}{2}(\dot{v})^2 + \frac{1}{2}(\dot{w})^2\right\}\right) dB \tag{3.55a}$$

$$\delta^{(1)}T = \frac{1}{2}\int_{B} \left(\rho\left\{\dot{u}\delta^{(1)}\dot{u} + \dot{v}\delta^{(1)}\dot{v} + \dot{w}\delta^{(1)}\dot{w}\right\}\right) dB \tag{3.55b}$$

$$\begin{aligned}\delta^{(1)}T = \frac{1}{2}\int_{-a/2}^{a/2}\int_{-b/2}^{b/2} \Big(&\rho_g\ddot{u}^0\delta^{(1)}u^0 + \rho_g\ddot{v}^0\delta^{(1)}v^0 + \rho_g\ddot{w}^0\delta^{(1)}w^0 \\ &+ \rho_h\ddot{\phi}_x^0\delta^{(1)}\phi_x^0 + \rho_h\ddot{\phi}_y^0\delta^{(1)}\phi_y^0\Big)\, dx\, dy\end{aligned} \tag{3.55c}$$

The inertia terms ρ_g and ρ_h are defined in the following equations

$$\rho_g = \int_{-h/2}^{h/2} \rho dz \tag{3.55d}$$

$$\rho_h = \int_{-h/2}^{h/2} \rho z^2 dz \tag{3.55e}$$

3.6.2 Partial Differential Equations of Motion

In dynamic problem, on substituting the formulations of strain energy, foundation strain energy, geometric strain energy, external work done, damping energy and kinetic energy's first variation in Hamilton's variational equation, and setting the coefficients of $\delta^{(1)}u^0$, $\delta^{(1)}v^0$, $\delta^{(1)}w^0$, $\delta^{(1)}\phi_x^0$ and $\delta^{(1)}\phi_x^0$ to zero, we get five governing partial differential equations. These are illustrated below.

$$\begin{aligned}N_{xx,x} + \mathrm{N}_{xy,y} - Y_{41,yy} - Y_{51,xy} - P_{11,xx} - P_{21,xy} - 2Q_{11,xx} + Q_{11,yy} + 2Q_{21,xy} \\ - 8Q_{41,xy} + 3Q_{61,xx} - 4Q_{61,yy} + 3Q_{81,xx} + Q_{81,yy} + 2Q_{91,xy} \\ = \rho_g\ddot{u}^0 + c_{d1}\dot{u}^0\end{aligned} \tag{3.56a}$$

$$\begin{aligned}N_{xy,x} + N_{yy,y} - Y_{42,xy} - Y_{52,xx} - P_{12,xy} - P_{22,yy} + Q_{12,xy} + Q_{22,xx} - 2Q_{22,yy} - \\ 4Q_{42,xx} + 3Q_{42,yy} - 8Q_{62,xy} + 2Q_{82,xy} + Q_{92,xx} + 3Q_{92,yy} = \rho_g\ddot{v}^0 + c_{d2}\dot{v}^0\end{aligned} \tag{3.56b}$$

$$\begin{aligned}M^m_{xx,xx} + 2M^m_{xy,xy} + M^m_{yy,yy} + \left(\hat{N}_{xx}w_{,x} + \hat{N}_{xy}w_{,y}\right)_{,x} + \left(\hat{N}_{xy}w_{,x} + \hat{N}_{yy}w_{,y}\right)_{,y} \\ - Y_{13,xy} - Y_{23,xy} - Y_{33,yy} + Y_{33,xx} + P_{13,xxx} + P_{13,xyy} + P_{23,xxy} \\ + P_{23,yyy} - P_{33,xx} - P_{33,yy} - 2Q_{13,xxx} + 3Q_{13,xyy} + 3Q_{23,xxy} \\ - 2Q_{23,yyy} - Q_{33,xx} - Q_{33,yy} - 12Q_{43,xxy} + 3Q_{43,yyy} + 4Q_{53,xx} \\ - Q_{53,yy} + 3Q_{63,xxx} - 12Q_{63,xyy} - Q_{73,xx} + 4Q_{73,yy} + 3Q_{83,xxx} \\ + 3Q_{83,xyy} + 3Q_{93,xxy} + 3Q_{93,yyy} + Q_{103,xy} - K_w w^0 \\ + K_p\left(w^0_{,xx} + w^0_{,yy}\right) + f(x,y) = \rho_g\ddot{w}^0 + c_{d3}\dot{w}^0\end{aligned} \tag{3.56c}$$

$$\begin{aligned}M^a_{xx,x} + M^a_{xy,y} - S^a_{xz} + Y_{24,y} + Y_{34,x} - Y_{54,xy} - Y_{44,yy} - \overline{Y_{44}} - P_{14,xx} - P_{24,xy} + \\ P_{34,x} - 2Q_{14,xx} + Q_{14,yy} + \overline{Q_{14}} + 2Q_{24,xy} - 2Q_{34,x} - 8Q_{44,xy} + 8Q_{54,x} +\end{aligned} \tag{3.56d}$$

$$3Q_{64,xx} - 4Q_{64,yy} + \overline{Q_{64}} - 2Q_{74,x} + 3Q_{84,xx} + Q_{84,yy} - 4\overline{Q_{84}} + 2Q_{94,xy} + Q_{104,y} = \rho_h \ddot{\phi}_x^0 + c_{d4}\dot{\phi}_x^0$$

$$M_{xy,x}^a + M_{yy,y}^a - S_{yz}^a + Y_{15,x} + Y_{35,y} - Y_{45,xy} - Y_{55,xx} - \overline{Y_{55}} - P_{15,xy} - P_{25,yy} + P_{35,y} + 2Q_{15,xy} - 2Q_{25,yy} + \overline{Q_{25}} + Q_{25,xx} - 2Q_{35,y} - 4Q_{45,xx} + 3Q_{45,yy} - 2Q_{55,y} - 8Q_{65,xy} + \overline{Q_{45}} + 8Q_{75,y} + 2Q_{85,xy} + Q_{95,xx} - 4\overline{Q_{95}} + 3Q_{95,yy} + Q_{105,x} = \rho_h \ddot{\phi}_y^0 + c_{d5}\dot{\phi}_y^0 \quad (3.56e)$$

In Eq. (3.56c), $\hat{N}_{ij} = [N_{ij} - n_{ij}]$, where $i, j = (x, y)$ and n_{ij} are the in-plane pre-buckling stress resultants due to the applied localized in-plane loading or localized thermal loads, and N_{ij} are the stress resultants.

Note:

- In the present investigation, dynamic or static problems are solved under the presence of either in-plane localized mechanical/thermal loading or transverse patch loading. Any combination of loads are not considered in the present study.
- In case of transverse patch loadings, the in-plane pre-buckling stress resultants are not present ($n_{ij} = 0$). Thus in Eq. (3.56c), $\hat{N}_{ij} = N_{ij}$.
- In the case of in-plane loading/thermal loading, transverse loading is absent. Thus, $f(x, y) = 0$.
- In case elastic foundation is not considered, $K_w = K_p = 0$.
- In case of static problems, principle of minimization of total potential energy is used. The governing PDEs are obtained by taking the functional derivative of the total potential energy with respect to each field variable and setting it equal to zero. The equations obtained are same as Eqs. (3.56a-e) The terms due to kinetic energy and damping energy are not present. Thus, $\rho_g \ddot{u}^0 = c_{d1}\dot{u}^0 = \rho_g \ddot{v}^0 = c_{d2}\dot{v}^0 = \rho_g \ddot{w}^0 = c_{d3}\dot{w}^0 = \rho_h \ddot{\phi}_x^0 = c_{d4}\dot{\phi}_x^0 = \rho_h \ddot{\phi}_y^0 = c_{d5}\dot{\phi}_y^0 = 0$.

3.7 Boundary Conditions of Microplate

In the present investigation, four different types of boundary conditions i.e., CCCC, CSCS, SCSC, and SSSS, are considered. In the above notation of boundary conditions, the four letters represent the restraint applied at the edges of the microplate in the counterclockwise direction, beginning from the left edge. The letter 'S' denotes a simply supported edge, while the letter 'C' denotes clamped edge. The boundary conditions to be satisfied at the edges of the plate for different conditions are denoted by the following equations:

(a) Simply supported (**S**) at $x = -{}^{a}/_{2}$ and ${}^{a}/_{2}$

i. In case of in-plane mechanical loading,

$$\hat{N}_{xx} = \overline{N_0}(t, y), M_{xx}^{a} = M_{xx} = v^0 = w^0 = \phi_y^0 = 0 \tag{3.57a}$$

$\overline{N_0}(t, y)$ denotes the in-plane edge loading expression.

ii. In case of transverse loading

$$M_{xx}^{a} = M_{xx} = v^0 = w^0 = \phi_y^0 = 0 \tag{3.57b}$$

iii. In case of thermal loading

$$M_{xx}^{a} = M_{xx} = u^0 = v^0 = w^0 = \phi_y^0 = 0 \tag{3.57c}$$

(b) Simply supported (**S**) at $y = -{}^{b}/_{2}$ and ${}^{b}/_{2}$

i. In case of in-plane mechanical loading,

$$\hat{N}_{yy} = 0, M_{yy}^{a} = M_{yy} = u^0 = w^0 = \phi_x^0 = 0 \tag{3.58a}$$

ii. In case on transverse loading

$$M_{yy}^{a} = M_{yy} = u^0 = w^0 = \phi_x^0 = 0 \tag{3.58b}$$

iii. In case of thermal loading

$$M_{yy}^{a} = M_{yy} = u^0 = v^0 = w^0 = \phi_x^0 = 0 \tag{3.58c}$$

(c) Clamped (**C**) at $x = -{}^{a}/_{2}$ and ${}^{a}/_{2}$

i. In case of in-plane mechanical loading,

$$\hat{N}_{xx} = \overline{N_0}(t, y), v^0 = w^0 = \phi_x^0 = \phi_y^0 = 0 \tag{3.59a}$$

ii. In case of transverse loading

$$v^0 = w^0 = \phi_x^0 = \phi_y^0 = 0 \tag{3.59b}$$

iii. In case of thermal loading

$$u^0 = v^0 = w^0 = \phi_x^0 = \phi_y^0 = 0 \tag{3.59c}$$

(d) Clamped (**C**) at $y = -{}^{b}/_{2}$ and ${}^{b}/_{2}$

i. In case of in-plane mechanical loading,

$$\hat{N}_{yy} = 0, u^o = w^o = \phi_x^0 = \phi_y^0 = 0 \tag{3.60a}$$

$\overline{N_0}$ denotes the magnitude of in-plane loading at 'y' distance from the origin at time 't'

ii. In case on transverse loading

$$u^o = w^o = \phi_x^0 = \phi_y^0 = 0 \tag{3.60b}$$

iii. In case of thermal loading

$$u^0 = v^0 = w^0 = \phi_x^0 = \phi_y^0 = 0 \tag{3.60c}$$

3.8 Analytical Expressions for In-plane Pre-buckling Stresses

The analytical expressions for in-plane pre-buckling stresses due to in-plane mechanical load or thermal loads are obtained by satisfying the in-plane stress equilibrium equation and solving the strain compatibility condition in terms of the Airy's stress function (ϕ). The methodology to deduce these expressions are discussed in the following sub-sections.

3.8.1 Pre-buckling Stresses due to Localized Thermal Loading

The analytical expressions for pre-buckling internal thermal stress resultants, n_{ij}, due to localized heating on an isotropic plate are computed by solving the thermoelastic problem discussed in this section. In pre-buckling condition for isotropic plate $\boldsymbol{\xi}$ and $\boldsymbol{\xi}^{\boldsymbol{a}}$ are null. Thus, Eq. (3.40a) and Eq. (3.40b) can be written as:

$$\mathbf{N} = \mathbf{A}\boldsymbol{\varepsilon}^{\mathbf{0}} - \mathbf{N_T} \tag{3.62a}$$

$$\mathbf{M}^{m} = \mathbf{B}\boldsymbol{\varepsilon}^{\mathbf{0}} - \mathbf{M_T} \tag{3.62b}$$

The influence of thermal stresses is only considered on the classical stress components.

The pre-buckling strains due to partial thermal load are related to the thermal stress resultants using Eq. (3.62a) as:

$$\varepsilon_{xx}^0 = \frac{1}{E}\{(N_T)_{xx} + n_{xx}\} - \frac{\nu}{E}\{(N_T)_{yy} + n_{yy}\} \tag{3.63a}$$

$$\varepsilon_{yy}^0 = -\frac{\nu}{E}\{(N_T)_{xx} + n_{xx}\} + \frac{1}{E}\{(N_T)_{yy} + n_{yy}\} \tag{3.63b}$$

$$\gamma_{xy}^0 = \frac{2(1+\nu)}{E}\{(N_T)_{xy} + n_{xy}\} \tag{3.63c}$$

The internal thermal stress resultants are assumed in terms of Airy's stress function (φ) as:

$$n_{xx} = \frac{\partial^2 \Phi}{\partial y^2},\ n_{yy} = \frac{\partial^2 \Phi}{\partial x^2},\ n_{xy} = -\frac{\partial^2 \Phi}{\partial x \partial y} \tag{3.64}$$

The above expressions of stress resultants in terms of Airy's stress function automatically satisfy the equilibrium equations. Hence, to obtain explicit expressions of internal stress resultants (n_{xx}, n_{yy}, and n_{xy}) strain compatibility conditions need to be solved.

The strain compatibility condition for a plate is:

$$\frac{\partial^2 \varepsilon_{xx}^0}{\partial y^2} + \frac{\partial^2 \varepsilon_{yy}^0}{\partial x^2} = \frac{\partial^2 \gamma_{xy}^0}{\partial x \partial y} \tag{3.65}$$

The internal thermal stress resultants in terms of Airy's stress function (φ) (Eq. (3.64)) are included in Eqs. (3.63a-c) and used in Eq. (3.65) to obtain the following equilibrium equation:

$$\begin{aligned} &\frac{\partial^4 \Phi}{\partial x^4} + 2\frac{\partial^4 \Phi}{\partial x^2 \partial y^2} + \frac{\partial^4 \Phi}{\partial y^4} \\ &\quad = 2(1+\nu)\frac{\partial^2 (N_T)_{xy}}{\partial x \partial y} + \nu\left(\frac{\partial^2 (N_T)_{xx}}{\partial x^2} + \frac{\partial^2 (N_T)_{yy}}{\partial y^2}\right) \\ &\quad - \left(\frac{\partial^2 (N_T)_{yy}}{\partial x^2} + \frac{\partial^2 (N_T)_{xx}}{\partial y^2}\right) \end{aligned} \tag{3.66}$$

The component of $(N_T)_{xy}$ is absent in Eq. (3.66) as α_{xy}^T=0 for an isotropic plate. The internal thermal stress resultants are then computed by addressing the in-plane stress equilibrium equation in Eq.(3.66). As Eq. (3.66) is a non-homogeneous partial differential equation, its solution (Φ) consists of complimentary solution (Φ_{CS}) and the particular integral (Φ_{PI}), $\Phi = \Phi_{\mathrm{CS}} + \Phi_{\mathrm{PI}}$. The complimentary solution is assumed in terms of trigonometric series as (Morimoto et al. 2006),

$$\Phi_{\mathrm{CS}}(x,y) = \textstyle\sum_{i=1}^{\infty} r_i\,(y)\cos(\,\theta_i x) + \sum_{j=1}^{\infty} s_j\,(x)\cos(\,\beta_j y) \tag{3.67}$$

In the above equation, $\theta_i = \frac{(2i-1)\pi}{a}$, and $\beta_j = \frac{(2j-1)\pi}{b}$. On substituting Eq. (3.67) in Eq. (3.66), we get two ordinary differential equations from coefficients of $\cos(\,\theta_i x)$ and $\cos(\,\beta_j y)$ respectively. These are:

$$\frac{d^4 r_i(y)}{dy^4} - 2{\theta_i}^2\frac{d^2 r_i(y)}{dy^2} + {\theta_i}^4 r_i(y) = 0 \tag{3.68a}$$

$$\frac{d^4 s_j(x)}{dx^4} - 2{\beta_j}^2\frac{d^2 s_j(x)}{dx^2} + {\beta_j}^4 s_j(x) = 0 \tag{3.68b}$$

If $r_i(y) = e^{k_1 y}$ and $s_j(x) = e^{k_2 y}$ in Eq. (3.68a) and Eq. (3.68b), $k_1 = \pm\theta_i$, $\pm\theta_i$ and $k_2 = \pm\beta_j$, $\pm\beta_j$. Considering symmetry about the coordinate axes, $r_i(y) = r_i(-y)$ and $s_j(x) = s_j(-x)$. Thus, the solution for Eqs. (3.68a-b) are:

$$r_i(y) = R_{i1}\cosh(\theta_i y) + R_{i2} y \sinh(\theta_i y) \tag{3.69a}$$

$$s_j(x) = S_{j1}\cosh(\beta_j x) + S_{j2} x \sinh(\beta_j x) \tag{3.69b}$$

On substituting Eqs. (3.69a-b) in Eq. (3.67), we get

$$\begin{aligned} \Phi_{\mathrm{CS}}(x,y) = &\sum_{i=1}^{\infty}\{R_{i1}\cosh(\theta_i y) + R_{i2} y \sinh(\theta_i y)\}\cos(\theta_i x) \\ &+ \sum_{j=1}^{\infty}\{S_{j1}\cosh(\beta_j x) + S_{j2} x \sinh(\beta_j x)\}\cos(\beta_j y) \end{aligned} \tag{3.70}$$

The particular integral for Eq. (3.66) is:

$$\begin{aligned} &\Phi_{\mathrm{PI}}(x,y) \\ &= -\sum_{i=1}^{\infty}\sum_{j=1}^{\infty}\frac{(-\nu N_{xx}^{c} + N_{yy}^{c})\theta_i^{\,2} + (-\nu N_{yy}^{c} + N_{xx}^{c})\beta_j^{\,2}}{\theta_i^{\,4} + 2\theta_i^{\,2}\beta_j^{\,2} + \beta_j^{\,4}} f_{ij}\cos(\theta_i x)\cos(\beta_j y) \end{aligned} \tag{3.71}$$

Thus, on including the solution of Φ in Eq. (3.64), we get the internal thermal stress resultants as follows:

$$\begin{aligned} &n_{xx} = \textstyle\sum_{i=1}^{\infty}\cos(\theta_i x)\{R_{i1}\cosh(\theta_i y)\theta_i^{\,2} + R_{i2}(2\theta_i\cosh(\theta_i y) + \\ &\theta_i^{\,2} y\sinh(\theta_i y))\} - \textstyle\sum_{j=1}^{\infty}\cos(\beta_j y)\{S_{j1}\cosh(\beta_j x) + S_{j2} x\sinh(\beta_j x)\}\beta_j^{\,2} - \\ &\textstyle\sum_{i=1}^{\infty}\sum_{j=1}^{\infty}\frac{(-\nu N_{xx}^{c}+N_{yy}^{c})\theta_i^{\,2}+(-\nu N_{yy}^{c}+N_{xx}^{c})\beta_j^{\,2}}{\theta_i^{\,4}+2\theta_i^{\,2}\beta_j^{\,2}+\beta_j^{\,4}} f_{ij}\cos(\theta_i x)\cos(\beta_j y)\,\beta_j^{\,2} \end{aligned} \tag{3.72a}$$

$$\begin{aligned} &n_{yy} = -\textstyle\sum_{i=1}^{\infty}\cos(\theta_i x)\{R_{i1}\cosh(\theta_i y) + R_{i2} y\sinh(\theta_i y)\}\theta_i^{\,2} + \\ &\textstyle\sum_{j=1}^{\infty}\cos(\beta_j y)\{S_{j1}\cosh(\beta_j x)\beta_j^{\,2} + S_{j2}(2\beta_j\cosh(\beta_j x) + \beta_j^{\,2} x\sinh(\beta_j x))\} - \\ &\textstyle\sum_{i=1}^{\infty}\sum_{j=1}^{\infty}\frac{(-\nu N_{xx}^{c}+N_{yy}^{c})\theta_i^{\,2}+(-\nu N_{yy}^{c}+N_{xx}^{c})\beta_j^{\,2}}{\theta_i^{\,4}+2\theta_i^{\,2}\beta_j^{\,2}+\beta_j^{\,4}} f_{ij}\cos(\theta_i x)\cos(\beta_j y)\,\theta_i^{\,2} \end{aligned} \tag{3.72b}$$

$$\begin{aligned} &(n)_{xy} = \textstyle\sum_{i=1}^{\infty}\sin(\theta_i x)\theta_i\{R_{i1}\sinh(\theta_i y)\theta_i + R_{i2}(\sinh(\theta_i y) + \\ &\theta_i y\cosh(\theta_i y))\} + \textstyle\sum_{j=1}^{\infty}\sin(\beta_j y)\beta_j\{S_{j1}\sinh(\beta_j x)\beta_j + S_{j2}(\sinh(\beta_j x) + \\ &\beta_j x\cosh(\beta_j x))\} - \\ &\textstyle\sum_{i=1}^{\infty}\sum_{j=1}^{\infty}\frac{(-\nu N_{xx}^{c}+N_{yy}^{c})\theta_i^{\,2}+(-\nu N_{yy}^{c}+N_{xx}^{c})\beta_j^{\,2}}{\theta_i^{\,4}+2\theta_i^{\,2}\beta_j^{\,2}+\beta_j^{\,4}} f_{ij}\sin(\theta_i x)\sin(\beta_j y)\,\beta_j\theta_i \end{aligned} \tag{3.72c}$$

On integrating the expressions in Eqs. (3.63a-c), we get the in-plane deformations $u(x,y)$ and $v(x,y)$ as,

$$
\begin{aligned}
&u(x,y) = \\
&-\sum_{i=1}^{\infty}\left[\begin{matrix} R_{i1}\sin(\theta_i x)\cosh(\theta_i y)\frac{\theta_i}{E}(\nu+1)+ \\ R_{i2}\left\{2\sin(\theta_i x)\cosh(\theta_i y))\frac{1}{E}+y\sinh(\theta_i y)\sin(\theta_i x)\frac{\theta_i}{E}(\nu+1)\right\}\end{matrix}\right]+ \\
&\sum_{j=1}^{\infty}\left[\begin{matrix} S_{j1}\cos(\beta_j y)\sinh(\beta_j x)\frac{\beta_j}{E}(\nu+1)+ \\ S_{j2}\left\{\cos(\beta_j y)\sinh(\beta_j x)\frac{1}{E}(\nu-1)+x\cos(\beta_j y)\cosh(\beta_j x)\frac{\beta_j}{E}(\nu+1)\right\}\end{matrix}\right]+ \\
&\sum_{i=1}^{\infty}\sum_{j=1}^{\infty}\frac{\{(1-\nu^2){\theta_i}^2+2(\nu+1){\beta_j}^2\}N_{xx}^{c}-\{1+2\nu+\nu^2\}{\beta_j}^2N_{yy}^{c}}{{\theta_i}^4+2{\theta_i}^2{\beta_j}^2+{\beta_j}^4}f_{ij}\frac{\theta_i}{E}\sin(\theta_i x)\cos(\beta_j y)
\end{aligned}
\tag{3.73a}
$$

$$
\begin{aligned}
&v(x,y) = \\
&\sum_{i=1}^{\infty}\left[\begin{matrix} R_{i1}\cos(\theta_i x)\sinh(\theta_i y)\frac{\theta_i}{E}(\nu+1)+ \\ R_{i2}\left\{\cos(\theta_i x)\sinh(\theta_i y))\frac{1}{E}(\nu-1)+y\cosh(\theta_i y)\cos(\theta_i x)\frac{\theta_i}{E}(\nu+1)\right\}\end{matrix}\right]- \\
&\sum_{j=1}^{\infty}\left[\begin{matrix} S_{j1}\sin(\beta_j y)\cosh(\beta_j x)\frac{\beta_j}{E}(\nu+1)+ \\ S_{j2}\left\{2\sin(\beta_j y)\cosh(\beta_j x)\frac{1}{E}+x\sin(\beta_j y)\sinh(\beta_j x)\frac{\beta_j}{E}(\nu+1)\right\}\end{matrix}\right]- \\
&\sum_{i=1}^{\infty}\sum_{j=1}^{\infty}\frac{\{(1-\nu^2){\beta_j}^2+2(\nu+1){\theta_i}^2\}N_{yy}^{c}-\{1+2\nu+\nu^2\}{\theta_i}^2N_{xx}^{c}}{{\theta_i}^4+2{\theta_i}^2{\beta_j}^2+{\beta_j}^4}f_{ij}\frac{\beta_j}{E}\sin(\beta_j y)\cos(\theta_i x)
\end{aligned}
\tag{3.73b}
$$

In Eqs. (3.73a-b), the coefficients $(R_{i1}, R_{i2}, S_{j1}, S_{j2})$ are calculated by considering the constraints of immovable in-plane displacement boundary conditions, $u = 0$ and $v = 0$ at $x = \pm\frac{a}{2}$ and $y = \pm\frac{b}{2}$. This results in the following four equations which are simultaneously solved to obtain the unknown coefficients.

$$
R_{i2} = -\frac{\cosh\left(\theta_i\frac{b}{2}\right)\frac{\theta_i}{E}(\nu+1)}{\left\{\left(2\cosh\left(\theta_i\frac{b}{2}\right)\frac{1}{E}\right)+\left(\frac{b}{2}\sinh\left(\theta_i\frac{b}{2}\right)\frac{\theta_i}{E}(\nu+1)\right)\right\}}R_{i1}
\tag{3.74a}
$$

$$
S_{j2} = -\frac{\cosh\left(\beta_j\frac{a}{2}\right)\frac{\beta_j}{E}(\nu+1)}{\left\{\left(2\cosh\left(\beta_j\frac{a}{2}\right)\frac{1}{E}\right)+\left(\frac{a}{2}\sinh\left(\beta_j\frac{a}{2}\right)\frac{\beta_j}{E}(\nu+1)\right)\right\}}S_{j1}
\tag{3.74b}
$$

$$
\begin{aligned}
&\frac{4}{b}\sin\left(\theta_i\frac{a}{2}\right)\sin\left(\beta_j\frac{b}{2}\right)\frac{\beta_j}{{\theta_i}^2+{\beta_j}^2}\Bigg[\cosh\left(\theta_i\frac{b}{2}\right)\Bigg\{R_{i1}\frac{\theta_i}{E}(\nu+1)\\
&+R_{i2}\frac{2}{E}\left(1-\frac{{\theta_i}^2(\nu+1)}{{\theta_i}^2+{\beta_j}^2}\right)\Bigg\}+R_{i2}\frac{\theta_i}{E}(\nu+1)\frac{b}{2}\sinh\left(\theta_i\frac{b}{2}\right)\Bigg]\\
&-S_{j1}\sinh\left(\beta_j\frac{a}{2}\right)\frac{\beta_j}{E}(\nu+1)-S_{j2}\left\{\sinh\left(\beta_j\frac{a}{2}\right)\frac{(\nu-1)}{E}+\frac{a}{2}\cosh\left(\beta_j\frac{a}{2}\right)\frac{\beta_j}{E}(\nu+1)\right\}\\
&+\sum_{i=1}^{\infty}\sum_{j=1}^{\infty}f_{ij}\sin\left(\theta_i\frac{a}{2}\right)\frac{\theta_i}{E}\frac{\{(1-\nu^2){\theta_i}^2+2(\nu+1){\beta_j}^2\}N_{xx}^c-\{1+2\nu+\nu^2\}{\beta_j}^2N_{yy}^c}{{\theta_i}^4+2{\theta_i}^2{\beta_j}^2+{\beta_j}^4}
\end{aligned}
\tag{3.74c}
$$

$$
\begin{aligned}
&\frac{4}{a}\sin\left(\beta_j\frac{b}{2}\right)\sin\left(\theta_i\frac{a}{2}\right)\frac{\theta_i}{{\theta_i}^2+{\beta_j}^2}\Bigg[\cosh\left(\beta_j\frac{a}{2}\right)\Bigg\{S_{j1}\frac{\beta_j}{E}(\nu+1)\\
&+S_{j2}\frac{2}{E}\left(1-\frac{{\beta_j}^2(\nu+1)}{{\theta_i}^2+{\beta_j}^2}\right)\Bigg\}+S_{j2}\frac{\beta_j}{E}(\nu+1)\frac{a}{2}\sinh\left(\beta_j\frac{a}{2}\right)\Bigg]\\
&-R_{i1}\sinh\left(\theta_i\frac{b}{2}\right)\frac{\theta_i}{E}(\nu+1)-R_{i2}\left\{\sinh\left(\theta_i\frac{b}{2}\right)\frac{(\nu-1)}{E}+\frac{b}{2}\cosh\left(\theta_i\frac{b}{2}\right)\frac{\theta_i}{E}(\nu+1)\right\}\\
&+\sum_{i=1}^{\infty}\sum_{j=1}^{\infty}f_{ij}\sin\left(\beta_j\frac{b}{2}\right)\frac{\beta_j}{E}\frac{\{(1-\nu^2){\beta_j}^2+2(\nu+1){\theta_i}^2\}N_{yy}^c-\{1+2\nu+\nu^2\}{\theta_i}^2N_{xx}^c}{{\theta_i}^4+2{\theta_i}^2{\beta_j}^2+{\beta_j}^4}
\end{aligned}
\tag{3.74d}
$$

3.8.2 Pre-buckling Stresses due to Non-uniform In-plane Mechanical Loading

The analytical expressions for pre-buckling stresses resultants (σ_{xx}, σ_{yy} and τ_{xy}) for an isotropic plate due to non-uniform in-plane uniaxial compressive loading are determined in this section using a similar methodology used for thermal loading. The equilibrium equation is homogeneous in this problem and expressed as:

$$\frac{\partial^4\Phi}{\partial x^4}+2\frac{\partial^4\Phi}{\partial x^2\partial y^2}+\frac{\partial^4\Phi}{\partial y^4}=0 \tag{3.75}$$

In this, problem, the in-plane stress boundary conditions at all edges of the plate are used to develop the analytical expressions of the pre-buckling stresses. These conditions are:

$$n_{xx}\left(\pm\frac{a}{2},y\right)=N(y),\ n_{xy}\left(\pm\frac{a}{2},y\right)=0,\ n_{xy}\left(x,\pm\frac{b}{2}\right)=0,\ n_{yy}\left(x,\pm\frac{b}{2}\right)=0 \tag{3.76}$$

In Eq. (3.76), $N(y)$ denotes the generalized function representing different load distributions at the edge of the plate discussed earlier in section 3.5.1. The complimentary solution is same as that for thermal loading ($\Phi_{\mathrm{CS}}(x,y)$), given in Eq. (3.70). However, to include the boundary condition of $n_{xx}\left(\pm\frac{a}{2},y\right)=N(y)$, a particular integral ($\Phi_{\mathrm{PI}}(x,y)$) is included as given below.

$$\Phi_{\mathrm{PI}}(x,y) = R_0 y^2 \tag{3.77}$$

Thus, the solution, $\phi(\mathrm{x},y) = \Phi_{\mathrm{CS}}(x,y) + \Phi_{\mathrm{PI}}(x,y)$ is:

$$\begin{aligned}\phi\,(x,y) = &\sum_{i=1}^{\infty}\{R_{i1}\cosh(\theta_i y) + R_{i2} y \sinh(\theta_i y)\}\cos(\theta_i x)\\ &+\sum_{j=1}^{\infty}\{S_{j1}\cosh(\beta_j x) + S_{j2} x \sinh(\beta_j x)\}\cos(\beta_j y) + R_0 y^2\end{aligned} \tag{3.78}$$

where, $\theta_i = \frac{(2i-1)\pi}{a}$, and $\beta_j = \frac{(2j-1)\pi}{b}$. Thus, using Eq. 3.78 in Eq. (3.64), we get the in-plane stress resultants as follows:

$$\begin{aligned}n_{xx} = &\sum_{i=1}^{\infty}\cos(\theta_i x)\{R_{i1}\cosh(\theta_i y){\theta_i}^2 + R_{i2}(2\theta_i\cosh(\theta_i y) + {\theta_i}^2 y \sinh(\theta_i y))\}\\ &-\sum_{j=1}^{\infty}\cos(\beta_j y)\{S_{j1}\cosh(\beta_j x) + S_{j2} x \sinh(\beta_j x)\}{\beta_j}^2 + 2R_0\end{aligned} \tag{3.79}$$

$$\begin{aligned}n_{yy} = &-\sum_{i=1}^{\infty}\cos(\theta_i x)\{R_{i1}\cosh(\theta_i y) + R_{i2} y \sinh(\theta_i y)\}{\theta_i}^2\\ &+\sum_{j=1}^{\infty}\cos(\beta_j y)\{S_{j1}\cosh(\beta_j x){\beta_j}^2\\ &+ S_{j2}(2\beta_j\cosh(\beta_j x) + {\beta_j}^2 x \sinh(\beta_j x))\}\end{aligned} \tag{3.80}$$

$$\begin{aligned}n_{xy} = &\sum_{i=1}^{\infty}\sin(\theta_i x)\theta_i\{R_{i1}\sinh(\theta_i y)\theta_i\\ &+ R_{i2}(\sinh(\theta_i y)\\ &+ \theta_i y \cosh(\theta_i y))\} + \sum_{j=1}^{\infty}\sin(\beta_j y)\beta_j\{S_{j1}\sinh(\beta_j x)\beta_j\\ &+ S_{j2}(\sinh(\beta_j x) + \beta_j x \cosh(\beta_j x))\}\end{aligned} \tag{3.81}$$

In order to obtain the coefficients, $R_{i1}, R_{i2}, S_{j1}, S_{j2}$ in expressions $\eta_{xx}(x,y)$, $\eta_{yy}(x,y)$ and $\eta_{xy}(x,y)$, the in-plane stress boundary conditions in Eq. (3.76) are used. Thus, we get four equations, which can be simultaneously solved to obtain the unknown coefficients.

$$R_{i1} = -\frac{R_{i2}}{\theta_i}\left(\frac{b}{2}\theta_i \cot h\frac{\theta_i b}{2} + 1\right) \tag{3.82}$$

$$S_{j1} = -\frac{S_{i2}}{\beta_j}\left(\frac{a}{2}\beta_j \cot h\frac{\beta_j a}{2} + 1\right) \tag{3.83}$$

$$R_{i2} = S_{j2}\beta_j \cos\frac{\beta_j b}{2}\left(\left(1 - \frac{a}{2}\beta_j \cot h\frac{\beta_j a}{2}\right)I_1 + \beta_j I_2\right) \times$$
$$\left(\frac{2/a}{\left(-{\theta_i}^2 \frac{b}{2}\cot h\frac{\theta_i b}{2} - \theta_i\right)\cos h\frac{\beta_j b}{2} + {\theta_i}^2 \frac{b}{2} sin\, h\frac{\theta_i b}{2}}\right) \tag{3.84}$$

$$S_{j2} = \left(\frac{\frac{2}{b}\cos\frac{\beta_j b}{2}}{{\beta_j}^2 \frac{a}{2} sin\, h\frac{\beta_j a}{2} - \left(\beta_j + \frac{a}{2}{\beta_j}^2 \cot h\frac{\beta_j a}{2}\right)\cos h\frac{\beta_j a}{2}}\right) \times$$
$$\left(-I_0 + \theta_i R_{i2}\cos\frac{\theta_i a}{2}\right)\sum_{n=1}^{\infty}\left(\left(1 - \frac{b}{2}\theta_i \cot h\frac{\theta_i b}{2}\right)I_3 + \theta_i I_4\right) \tag{3.85}$$

Here, $I_0 = \int_{-b/2}^{b/2} N(y)\cos(\beta_j y)\, dy,$ $\quad I_1 = \int_{-a/2}^{a/2} \cos h(\beta_j x)\cos(\theta_i x)\, dx$

$$I_2 = \int_{-a/2}^{a/2} x \sin h(\beta_j x)\cos(\theta_i x)\, dx \qquad I_3 = \int_{-b/2}^{b/2} \cos h(\theta_i y)\cos(\beta_j y)\, dy$$

$$I_4 = \int_{-b/2}^{b/2} y \sin h(\theta_i y)\cos(\beta_j y)\, dy$$

3.9 Methodology for Solving Partial Differential Equations

The Galerkin's weighted residual method is used to convert the governing PDEs of motion (Eqs. (3.56(a-e)) into ODEs. It is a strong form method, where the basis function for each displacement field is assumed such that it fulfils the essential and natural boundary condition requirements. These basis functions also serve as the weighted functions to calculate the weighted integral residue of each governing PDE. The weighted residual in this method is expressed as:

$$\iint_A \mathrm{J}_i(u^o,\ v^o,\ w^o, \phi_x^0, \phi_y^0)\ {\Theta^i}_{mn}(x,y)_j dxdy = 0 \text{ for } i = 1,2,3,4,5 \text{ and } j = 1,2, \ldots M^* \times N^* \tag{3.86}$$

In Eq. (3.86), J_i represents the PDEs and ${\Theta^i}_{mn}(x,y)_j$ represents the assumed basis functions. The overall number of terms along y and x directions are represented using symbols N^* and M^* respectively. Hence, the total number of terms can be represented as $5\ \times N^* \times M^*$.

The basis functions considered in this study for different boundary conditions based on loading conditions are demonstrated in the following subsection.

3.9.1 Basis functions for displacement fields

The basis functions, $\Theta^1{}_{mn}(x,y), \Theta^2{}_{mn}(x,y), \Theta^3{}_{mn}(x,y), \Theta^4{}_{mn}(x,y)$ and $\Theta^5{}_{mn}(x,y)$, are assumed to satisfy the boundary conditions in the field displacement equations expressed below.

$$u^0 = \sum_{m=1}^{M^*}\sum_{n=1}^{N^*} U^*_{mn}(t)\Theta^1{}_{mn}(x,y) \tag{3.87a}$$

$$v^0 = \sum_{m=1}^{M^*}\sum_{n=1}^{N^*} V^*_{mn}(t)\Theta^2{}_{mn}(x,y) \tag{3.87b}$$

$$w^0 = \sum_{m=1}^{M^*}\sum_{n=1}^{N^*} W^*_{mn}(t)\Theta^3{}_{mn}(x,y) \tag{3.87c}$$

$$\phi^0_x = \sum_{m=1}^{M^*}\sum_{n=1}^{N^*} K^*_{mn}(t)\Theta^4{}_{mn}(x,y) \tag{3.87d}$$

$$\phi^0_y = \sum_{m=1}^{M^*}\sum_{n=1}^{N^*} L^*_{mn}(t)\Theta^5{}_{mn}(x,y) \tag{3.87e}$$

In the Eqs. (3.87a-e), $U^*_{mn}(t), V^*_{mn}(t)$, $W^*_{mn}(t)$, $K^*_{mn}(t)$ and $L^*_{mn}(t)$ are unknown coefficients independent of spatial coordinates. The index of the mode along the *y* and *x* directions is represented by the subscripts *n* and *m*, respectively. The basis functions assumed to satisfy the boundary conditions for mechanical loading condition and thermal loading condition are discussed below.

a) For Mechanical Loads

The basis functions adopted to satisfy the boundary conditions for microplate with mechanical loading are expressed as:

$$\Theta^1{}_{mn}(x,y) = \sin\left(\frac{m\pi x}{a}\right)\cos\left(\frac{n\pi y}{b}\right) \tag{3.88a}$$

$$\Theta^2{}_{mn}(x,y) = \cos\left(\frac{m\pi x}{a}\right)\sin\left(\frac{n\pi y}{b}\right) \tag{3.88b}$$

$$\Theta^3{}_{mn}(x,y) = X_m(x)Y_n(y) \tag{3.88c}$$

$$\Theta^4{}_{mn}(x,y) = \sin\left(\frac{m\pi x}{a}\right)\cos\left(\frac{n\pi y}{b}\right) \tag{3.88d}$$

$$\Theta^5{}_{mn}(x,y) = \cos\left(\frac{m\pi x}{a}\right)\sin\left(\frac{n\pi y}{b}\right) \tag{3.88e}$$

The basis function, $\Theta^3{}_{mn}(x,y)$, corresponding to out-of-plane deflection, w^0 comprises of eigen functions $X_m(x)$ and $Y_n(y)$ opted to satisfy the out-of-plane boundary conditions. The Eigen function $X_m(x)$ takes care of the edges at *x* = *-a/2* and *x* = *a/2,* while the eigen function $Y_n(y)$ takes care of the edges *y* = *-b/2* and *y* = *b/2.* The Eigen beam function corresponding to simply supported and clamped beam conditions are expressed as (Warburton 1954):

i. Beam function of simply supported (**S**) at *x* = *-a/2* and *x* = *a/2* (i.e., along two opposite edges)

$$X_m(x) = \cos\frac{m\pi x}{a} \qquad (m = 1,2,3.\ldots.) \tag{3.89}$$

ii. Beam function of clamped support (C) at *x* = *-a/2* and *x* = *a/2* (i.e., along two opposite edges)

$$X_m(x) = \cos\xi_m\frac{x}{a} + \frac{\sin\frac{\xi_m}{2}}{\sinh\frac{\xi_m}{2}}\cosh\xi_m\frac{x}{a} \qquad (for\ m = 2,4,6.\ldots.) \tag{3.90a}$$

where, ξ_m represents the roots of the equation:

$$\tan\frac{\xi_m}{2} + \tanh\frac{\xi_m}{2} = 0 \tag{3.90b}$$

and

$$X_m(x) = \sin\xi_m\frac{x}{a} - \frac{\sin\frac{\xi_m}{2}}{\sinh\frac{\xi_m}{2}}\sinh\xi_m\frac{x}{a} \quad (for\ m = 3,5,7.\ldots.) \tag{3.90c}$$

where, ξ_m are taken as roots of the equation:

$$\tan\frac{\xi_m}{2} - \tanh\frac{\xi_m}{2} = 0 \tag{3.90d}$$

The beam function for edges *y* = *-b/2* and *y* = *b/2,* $Y_n(y)$ can be obtained by replacing 'x', 'a' and 'm' by 'y', 'b 'and 'n' respectively in Eq. (3.89) and Eqs. (3.90).

b) For Thermal Loads

The basis functions adopted to satisfy the boundary conditions for microplate with thermal loading are expressed as:

$$\Theta^1{}_{mn}(x,y) = \sin\left(\frac{2m\pi x}{a}\right)\cos\left(\frac{n\pi y}{b}\right) \tag{3.91a}$$

$$\Theta^2{}_{mn}(x,y) = \cos\left(\frac{m\pi x}{a}\right)\sin\left(\frac{2n\pi y}{b}\right) \tag{3.91b}$$

$$\Theta^3{}_{mn}(x,y) = X_m(x)Y_n(y) \tag{3.91c}$$

$$\Theta^4{}_{mn}(x,y) = \sin\left(\frac{2m\pi x}{a}\right)\cos\left(\frac{n\pi y}{b}\right) \tag{3.91d}$$

$$\Theta^5{}_{mn}(x,y) = \cos\left(\frac{m\pi x}{a}\right)\sin\left(\frac{2n\pi y}{b}\right) \tag{3.91e}$$

The eigen functions $X_m(x)$ and $Y_n(y)$ opted to satisfy the out-of-plane boundary conditions are same as those considered for mechanical loading in Eq. (3.89) and Eqs. (3.90) for both simply supported and clamped conditions.

3.9.2 Governing Ordinary Differential Equations

$$\mathbf{M}\ddot{\boldsymbol{\delta}} + \mathbf{C}\dot{\boldsymbol{\delta}} + \left(\mathbf{K}_{\mathrm{L}} + \mathbf{K}_{\mathrm{NL}} - \left(N_{st} + N_{dyn}\cos pt\right)\mathbf{K}_{\mathrm{G}}\right)\boldsymbol{\delta} = \mathbf{0} \tag{3.92a}$$

$$\mathbf{M}\ddot{\boldsymbol{\delta}} + \mathbf{C}\dot{\boldsymbol{\delta}} + (\mathbf{K}_{\mathrm{L}} + \mathbf{K}_{\mathrm{NL}})\boldsymbol{\delta} = \mathbf{F}\mathbf{cos}(\omega_{NL}t) \tag{3.92b}$$

$$(\mathbf{K}_{\mathrm{L}} + \mathbf{K}_{\mathrm{NL}} - (\Delta T)\mathbf{K}_{\mathrm{G}})\boldsymbol{\delta} = \mathbf{0} \tag{3.92c}$$

The matrix form of the non-linear ODEs generated using Galerkin's method for periodic in-plane loading, periodic transverse loading, and thermal loading are presented in Eq. (3.92a), Eq. (3.92b), and Eq. (3.92c) respectively. In Eq. (3.92a), the applied load N_{xx} is made up of the static part (N_{st}) and dynamic part ($N_{dyn}\cos(pt)$), where p is the excitation frequency. In Eq. (3.92b), the applied transverse force vector is denoted by **F**, and ω_{NL} is the forcing frequency. The symbols **M, C,** $\mathbf{K}_{\mathrm{NL}}$, and $\mathbf{K}_{\mathrm{L}}$, denote the mass, Rayleigh's damping, non-linear stiffness, and linear stiffness matrices in Eq. (3.92). The symbol $\boldsymbol{\delta}$ denotes the displacement vector and the accent "$(\dot{\ })$" indicates differentiation with respect to time '*t*' and "$(\ddot{\ })$" indicates double differentiation with respect to time '*t*'. The components of damping matrix are calculated using the Rayleigh's method discussed in the next section.

3.10 Rayleigh’s Damping Matrix

The Rayleigh’s linear damping matrix (**C**) (Thorby 2008) is considered for analysis of microplate in this study. The expression for Rayleigh’s damping matrix $\mathbf{C}$, is given in below.

$$\mathbf{C} = \bar{a}\mathbf{M} + \bar{b}\mathbf{K}_{\mathrm{L}} \tag{3.93a}$$

In Eq. (3.93a), **M** denotes the mass matrix and $\mathbf{K}_{\mathrm{L}}$ denotes the linear stiffness matrix. The mass and linear stiffness proportionality constants, $\bar{a}$ and $\bar{b}$ are determined using the equation below,

$$\bar{a}\mathbf{I} + \bar{b}[\omega_i^2] = 2[\omega_i\zeta_i] \qquad (i\text{=1,2}) \tag{3.93b}$$

In the Eq. (3.93b) above, **I** stands for the elementary matrix, $[\omega_i^2]$ is a scaling matrix comprising the two lowest natural frequencies considered in this study, i represents the index of the mode shape and ζ_i stands for the damping ratios for the modes corresponding to the natural frequencies considered.

3.11 Solution Methodologies for Various Analyses

3.11.1 Free Vibration and Buckling

$$\mathbf{M}\ddot{\boldsymbol{\delta}} + (\mathbf{K}_{\mathrm{L}} - (N_{\mathrm{cr}})\mathbf{K}_{\mathrm{G}})\boldsymbol{\delta} = \mathbf{0} \tag{3.94a}$$

$$\mathbf{M}\ddot{\boldsymbol{\delta}} + (\mathbf{K}_{\mathrm{L}})\boldsymbol{\delta} = \mathbf{Fcos}(\omega_{NL}t) \tag{3.94b}$$

$$(\mathbf{K}_{\mathrm{L}} - (\Delta T_{\mathrm{cr}})\mathbf{K}_{\mathrm{G}})\boldsymbol{\delta} = \mathbf{0} \tag{3.94c}$$

In order to obtain the natural frequency and buckling loads, the non-linear stiffness is neglected from Eqs. (3.92a-c) to achieve the linear ODEs shown in Eqs. (3.94a-c). The buckling load, N_{cr} is derived by finding the eigenvalue from Eq. (3.94a) while disregarding **M** matrix**.** The natural frequencies are computed by finding the eigenvalue in Eq. (3.94a) and Eq. (3.94b) without considering, $\mathbf{K}_{\mathrm{G}}$, and **F**. The buckling temperature difference, ΔT_{cr}, is obtained by finding the eigenvalue in Eq. (3.94c).

3.11.2 Dynamic Instability

$$\mathbf{M}\ddot{\boldsymbol{\delta}} + \mathbf{C}\dot{\boldsymbol{\delta}} + \big(\mathbf{K}_{\mathrm{L}} - \big(N_{st} + N_{dyn}\cos pt\big)\mathbf{K}_{\mathrm{G}}\big)\boldsymbol{\delta} = \mathbf{0} \tag{3.95}$$

$$\delta(t) = \sum_{k=1,3,5}^{\infty}\left(a_k \sin\frac{kpt}{2} + b_k \cos\frac{kpt}{2}\right) \tag{3.96}$$

The non-linear stiffness is neglected in Eq. (3.92a) to achieve the Mathieu-Hill ODE shown in Eq. (3.95), which has periodic solutions for periods *T* and $2T$. The dynamic instability boundaries of the system are plotted using Bolotin's method on Eq. (3.95). In this method, a Fourier series solution of the form of Eq. (3.96) for period $2T$ is assumed.

$$\left|\mathbf{K}^* \pm 0.5N_{dyn}\mathbf{K_G} \quad -0.25\mathbf{M}p^2\right| = 0 \tag{3.97}$$

$$\begin{vmatrix} \mathbf{K}^* + 0.5N_{dyn}\mathbf{K_G} - 0.25\mathbf{M}p^2 & 0.5\mathbf{C}p \\ -0.5Cp & \mathbf{K}^* - 0.5N_{dyn}\mathbf{K_G} - 0.25Mp^2 \end{vmatrix} = 0 \tag{3.98}$$

where, $\mathbf{K}^* = \mathbf{K_L} - N_{st}\mathbf{K_G}$

On equating the sine and cosine terms and searching for a non-trivial solution, when using Eq. (3.96) in Eq (3.95), we get the upper and lower boundaries of the first-order approximation of the principal dynamic instability region in the form of a homogeneous algebraic equation as shown in Eq. (3.97). If damping is also considered, the dynamic instability boundaries are found by Eq. (3.98).

3.11.3 Nonlinear Vibration

The Incremental Harmonic Balance (IHB) method is used in this study to compute the nonlinear vibration response (frequency-amplitude curve). It was first proposed by Lau and Cheung (Lau and Cheung 1981) and has since been used to study a wide range of nonlinear equations. This method is a combination of the incremental method and the harmonic balance method. The solution is assumed in the form of trigonometric Fourier series. The harmonic balance method (Galerkin averaging method) is used to obtain the algebraic homogeneous equations by nullifying the average of virtual work per period. The homogeneous algebraic equations are then solved using the incremental (arc-length method) method. The nonlinear stiffness terms, $\mathbf{K}_{\mathrm{NL}}$ in Eq. (3.92a) and Eq. (3.92b) are expressed as a sum of nonlinear cubic stiffness, $\mathbf{K}_{\mathrm{NL3}}$, and the nonlinear quadratic stiffness, $\mathbf{K}_{\mathrm{NL2}}$, as shown in the equations below (Amabili 2008; Yadav et al. 2021).

$$\mathbf{M}\ddot{\boldsymbol{\delta}} + \mathbf{C}\dot{\boldsymbol{\delta}} + \left(\mathbf{K}_{\mathrm{L}} + \mathbf{K}_{\mathrm{NL2}} + \mathbf{K}_{\mathrm{NL3}} - \left(N_{st} + N_{dyn}\cos pt\right)\mathbf{K}_{\mathrm{G}}\right)\boldsymbol{\delta} = \mathbf{0} \tag{3.99a}$$

$$\mathbf{M}\ddot{\boldsymbol{\delta}} + \mathbf{C}\dot{\boldsymbol{\delta}} + (\mathbf{K}_{\mathrm{L}} + \mathbf{K}_{\mathrm{NL2}} + \mathbf{K}_{\mathrm{NL3}})\boldsymbol{\delta} = \mathbf{F}\cos(\omega_{NL}t) \tag{3.99b}$$

$$\omega^2\mathbf{M}\boldsymbol{\delta}'' + \omega\mathbf{C}\boldsymbol{\delta}' + \left[(\mathbf{K_L} + \mathbf{K_{NL2}} + \mathbf{K_{NL3}}) - \left(N_{st} + N_{dyn}\cos(\tau)\right)\mathbf{K_G}\right]\boldsymbol{\delta} = 0 \tag{3.100a}$$

$$\omega^2\mathbf{M}\boldsymbol{\delta}'' + \omega\mathbf{C}\boldsymbol{\delta}' + [(\mathbf{K_L} + \mathbf{K_{NL2}} + \mathbf{K_{NL3}})]\boldsymbol{\delta} = \mathbf{F}\cos(\tau) \tag{3.100b}$$

In this approach, for solving the problem, a parameter $\tau = pt$ is added and inserted into Eq. (3.99a) and, $\tau = \omega_{NL}t$ is inserted in Eq. (3.99b), giving us Eq (3.100a) and Eq. (3.100b) for in-plane load and transverse loads respectively. In the above equations, prime ($'$) and double prime ($''$), denote the differentiations and double differentiations with respect to 'τ' respectively. Adding the appropriate increments results in the neighbouring state, as indicated in the following equation.

$$\boldsymbol{\delta}_{\mathbf{j}} = \boldsymbol{\delta}_{\mathbf{j0}} + \boldsymbol{\Delta\delta} \text{ and } p = p_0 + \Delta p\text{ , for in-plane loading} \tag{3.101a}$$

$$\boldsymbol{\delta}_{\mathbf{j}} = \boldsymbol{\delta}_{\mathbf{j0}} + \boldsymbol{\Delta\delta} \text{ and } \omega_{NL} = \omega_{NL_0} + \Delta\omega_{NL}\text{ , for transverse loading} \tag{3.101b}$$

Replacing Eq. (3.101a) and Eq. (3.101b) into Eq. (3.100a) and Eq. (3.100b) respectively and ignoring the small terms leads to Eqs. (3.102a) and Eqs. (3.103a) for in-plane load and transverse load respectively.

a) For In-plane loading:

$$\begin{aligned} & p_0^2\mathbf{M}\boldsymbol{\Delta\delta}'' + p_0\mathbf{C}\boldsymbol{\Delta\delta}' \\ & \quad + \left[(\mathbf{K_L} + 2\mathbf{K_{NL2}} + 3\mathbf{K_{NL3}}) - \left(N_{st} + N_{dyn}\cos(\tau)\right)\mathbf{K_G}\right]\boldsymbol{\Delta\delta} \\ & \quad - [\mathbf{R_e} - 2p_0\mathbf{M}\boldsymbol{\delta_0}''\Delta p - \mathbf{C}\boldsymbol{\delta_0}'\Delta p] = 0 \end{aligned} \tag{3.102a}$$

$$\begin{aligned} \mathbf{R_e} = & -\left(p_0^2\mathbf{M}\boldsymbol{\delta_0}'' + p_0\mathbf{C}\boldsymbol{\delta_0}' + [\mathbf{K_L} + \mathbf{K_{NL2}} + \mathbf{K_{NL3}}]\right. \\ & \left. - \left[N_{st} + N_{dyn}\cos\tau\right]\mathbf{K_G}\right)\boldsymbol{\delta_0} \end{aligned} \tag{3.102b}$$

b) For Transverse Loading:

$$\begin{aligned} & {\omega_{NL}}_0^2\mathbf{M}\boldsymbol{\Delta\delta}'' + \omega_{NL_0}\mathbf{C}\boldsymbol{\Delta\delta}' + [(\mathbf{K_L} + \mathbf{2K_{NL2}} + \mathbf{3K_{NL3}})]\boldsymbol{\Delta\delta} \\ & \quad - \left[\mathbf{R_e} - 2\omega_{NL_0}\mathbf{M}\boldsymbol{\delta_0}''\Delta\omega_{NL} - \mathbf{C}\boldsymbol{\delta_0}'\Delta\omega_{NL}\right] = \mathbf{0} \end{aligned} \tag{3.103a}$$

$$\mathbf{R_e} = \mathbf{F}\cos(\tau) - \left({\omega_{NL}}_0^2\mathbf{M}\boldsymbol{\delta_0}'' + \omega_{NL_0}\mathbf{C}\boldsymbol{\delta_0}' + [\mathbf{K_L} + \mathbf{K_{NL2}} + \mathbf{K_{NL3}}]\right)\boldsymbol{\delta_0} \tag{3.103b}$$

Here, $\mathbf{R_e}$ (Eq. (3.102b) and Eq. (3.103b) represent the residue, which approaches to a negligible value as the solution gets closer to the precise value. The approximate steady-state response of the system is assumed as a truncated Fourier series, as shown in the equations below.

a) For In-plane loading:

$$\boldsymbol{\delta}_{\mathbf{j0}} = \sum_{k=1}^{nc} a_{jk}\cos\frac{2k-1}{2}\tau + \sum_{k=1}^{ns} b_{jk}\sin\frac{2k-1}{2}\tau = \mathbf{TA} \tag{3.104a}$$

$$\boldsymbol{\Delta\delta}_{\mathbf{j}} = \sum_{k=1}^{nc} \Delta a_{jk}\cos\frac{2k-1}{2}\tau + \sum_{k=1}^{ns} \Delta b_{jk}\sin\frac{2k-1}{2}\tau = \mathbf{T\Delta A} \tag{3.104b}$$

where,

$$\mathbf{T} = \left\{\cos\frac{\tau}{2}, \cos\frac{3\tau}{2}, \dots \cos\frac{(2nc-1)\tau}{2}, \sin\frac{\tau}{2}, \sin\frac{3\tau}{2}, \dots \sin\frac{(2ns-1)\tau}{2}\right\} \tag{3.104c}$$

b) For Transverse Loading:

$$\boldsymbol{\delta}_{\mathbf{j0}} = a_{j0} + \sum_{k=1}^{nc} a_{jk} \cos\big((2k-1)\tau\big) + \sum_{k=1}^{ns} b_{jk} \sin\big((2k-1)\tau\big) = \mathbf{TA} \tag{3.105a}$$

$$\boldsymbol{\Delta\delta}_{\mathbf{j}} = \Delta a_{j0} + \sum_{k=1}^{nc} \Delta a_{jk} \cos\big((2k-1)\tau\big) + \sum_{k=1}^{ns} \Delta b_{jk} \sin\big((2k-1)\tau\big) = \mathbf{T\Delta A} \tag{3.105b}$$

where,

$$\mathbf{T} = \{1, \cos(\tau), \cos(2\tau), \ldots \cos(nc\tau), \sin(\tau), \sin(2\tau), \ldots \sin(ns\tau)\} \tag{3.105c}$$

By inserting Eqs. (3.104) and Eqs. (3.105) into Eq. (3.102a) and Eq. (3.103a) respectively, and using the Galerkin's method, a system of homogeneous algebraic equations is created, as shown in the equation below.

$$\mathbf{K_{mc}}\Delta A = \mathbf{R} - \mathbf{R_{mc}}\Delta p \text{ , for in-plane loading problem} \tag{3.106a}$$

$$\mathbf{K_{mc}}\Delta A = \mathbf{R} - \mathbf{R_{mc}}\Delta \omega_{NL} \text{ , for transverse loading problem} \tag{3.106b}$$

The components of Eq. (3.106a) for in-plane loading problem are:

$$\mathbf{A} = \{a_{j1}, a_{j2}, \cdots a_{jnc}, b_{j1}, b_{j2}, \cdots b_{jns}\} \tag{3.107a}$$

$$\boldsymbol{\Delta}\mathbf{A} = \{\Delta a_{j1}, \Delta a_{j2}, \cdots \Delta a_{jnc}, \Delta b_{j1}, \Delta b_{j2}, \cdots \Delta b_{jns}\} \tag{3.107b}$$

$$\mathbf{K_{mc}} = p_0^2 \bar{\mathbf{M}} + p_0 \bar{\mathbf{C}} + (\bar{\mathbf{K}}_{\mathbf{L}} + 2\bar{\mathbf{K}}_{\mathbf{NL2}} + 3\bar{\mathbf{K}}_{\mathbf{NL3}}) \tag{3.107c}$$

$$\mathbf{R} = \{\bar{N}_x - p_0^2 \bar{\mathbf{M}} - p_0 \bar{\mathbf{C}} + (\bar{\mathbf{K}}_{\mathrm{L}} + \bar{\mathbf{K}}_{\mathbf{NL2}} + \bar{\mathbf{K}}_{\mathbf{NL3}})\}\,\mathbf{A} \tag{3.107d}$$

$$\mathbf{R_{mc}} = (2p_0 \bar{\mathbf{M}} + \bar{\mathbf{C}})\mathbf{A} \tag{3.107e}$$

The components of Eq. (3.106b) for transverse loading problem are:

$$\mathbf{A} = \{a_{j0}, a_{j1}, a_{j2}, \cdots a_{jnc}, b_{j1}, b_{j2}, \cdots b_{jnc}\} \tag{3.108a}$$

$$\boldsymbol{\Delta}\mathbf{A} = \{\Delta a_{j0}, \Delta a_{j1}, \Delta a_{j2}, \cdots \Delta a_{jnc}, \Delta b_{j1}, \Delta b_{j2}, \cdots \Delta b_{jnc}\} \tag{3.108b}$$

$$\mathbf{K_{mc}} = \omega_{NL_0}^{\;2} \bar{\mathbf{M}} + \omega_{NL_0} \bar{\mathbf{C}} + (\bar{\mathbf{K}}_{\mathbf{L}} + 2\bar{\mathbf{K}}_{\mathbf{NL2}} + 3\bar{\mathbf{K}}_{\mathbf{NL3}}) \tag{3.108c}$$

$$\mathbf{R} = \{\bar{\mathbf{F}} - \omega_{NL_0}^{\;2} \bar{\mathbf{M}} - \omega_{NL_0} \bar{\mathbf{C}} - (\bar{\mathbf{K}}_{\mathrm{L}} + \bar{\mathbf{K}}_{\mathbf{NL2}} + \bar{\mathbf{K}}_{\mathbf{NL3}})\}\mathbf{A} \tag{3.108d}$$

$$\mathbf{R_{mc}} = (2\omega_{NL_0} \bar{\mathbf{M}} + \bar{\mathbf{C}})\mathbf{A} \tag{3.108e}$$

The bar (¯) in Eqs. (3.107c-e) and Eqs. (3.108c-e) denotes the orthogonalized matrices (Amabili 2008). The orthogonalized matrices $\bar{\mathbf{M}}$, $\bar{\mathbf{C}}$, $\bar{\mathbf{K}}_{\mathbf{L}}$, $\bar{\mathbf{K}}_{\mathbf{NL2}}$, $\bar{\mathbf{K}}_{\mathbf{NL3}}$, $\bar{\mathbf{N}}_{\mathbf{x}}$ and $\bar{\mathbf{F}}$ are defined in the equations below.

$$\bar{\mathbf{M}} = \int_0^{2\pi} \mathbf{S}^{\mathrm{T}}\mathbf{M}\mathbf{S}''\mathrm{d}\tau \tag{3.109a}$$

$$\bar{\mathbf{C}} = \int_0^{2\pi} \mathbf{S}^{\mathrm{T}}\mathbf{C}\mathbf{S}'\mathrm{d}\tau \tag{3.109b}$$

$$(\bar{\mathbf{K}}_{\mathrm{L}}, \bar{\mathbf{K}}_{\mathbf{NL2}}, \bar{\mathbf{K}}_{\mathbf{NL3}}) = \int_0^{2\pi} \mathbf{S}^{\mathrm{T}}(\mathbf{K}_{\mathbf{L}}, \mathbf{K}_{\mathbf{NL2}}, \mathbf{K}_{\mathbf{NL3}})\mathbf{S}\mathrm{d}\tau \tag{3.109c}$$

$$\bar{\mathbf{F}} = \int_0^{2\pi} \mathbf{S}^{\mathbf{T}}\mathbf{F}\cos\big((2m-1)\tau\big)\,\mathrm{d}\tau \tag{3.109d}$$

$$\bar{N}_x = \int_0^{2\pi} \mathbf{S}^{\mathbf{T}}\big(N_{st} + N_{dyn}\cos(\tau)\big)\mathbf{S}\mathrm{d}\tau \tag{3.109e}$$

In Eqs. (3.109a-e), $\mathbf{S}$ is defined as

$$\mathbf{S} = \begin{bmatrix} \mathbf{T} & & \\ & \ddots & \\ & & \mathbf{T} \end{bmatrix} \tag{3.110}$$

In this study, only smooth nonlinearities (quadratic and cubic) exist. The contribution of higher harmonics is very minimal in these systems (Lee et al. 1997). Therefore, the system can be easily assumed solely in terms of the fundamental harmonics of the Fourier series (Cheung et al. 1990), making this method computationally very effective. This method is, however, avoided for systems with non-smooth nonlinearities, such as free play or hysteresis nonlinearities (Liu et al. 2015). In such systems, the contribution of higher harmonics is significant, which leads to substantial computational costs. It is also not suitable for systems with strong mode coupling.

3.11.4 Nonlinear Dynamic Response

In this section, the nonlinear dynamic response of the microplate under in-plane or transverse periodic loading is obtained using the implicit time-dependent Newmark-β direct time integration method (Subbaraj and Dokainish 1989). In the implicit method, the solution at a time step requires the solving of equilibrium conditions at that time step. The nonlinear equilibrium ODE for in-plane/transverse periodic loading is given in Eq. (3.99a) and Eq. (3.99b). The acceleration in each time step is considered as the average of the accelerations at both the ends of the time step. The dynamic equilibrium equation considered at each time step is,

$$\mathbf{M}\ddot{\boldsymbol{\delta}}_{i+1} + \mathbf{C}\dot{\boldsymbol{\delta}}_{i+1} + \mathbf{K}(\boldsymbol{\delta}_i, \bar{N}_x)\boldsymbol{\delta}_{i+1} = \mathbf{F} \tag{3.111}$$

where, $\mathbf{M}\ddot{\boldsymbol{\delta}}_{i+1}$, $\mathbf{C}\dot{\boldsymbol{\delta}}_{i+1}$, $\mathbf{K}(\boldsymbol{\delta}_i, N_x)\boldsymbol{\delta}_{i+1}$ and $\mathbf{F}$ represent the inertial force, the damping force, the elastic internal resisting force, and force vector, respectively. In the case of plate exposed to in-plane loading only, the force vector $\mathbf{F}$ is assumed to be absent. If the plate is exposed to only transverse load then $\bar{N}_x$(in-plane loading) is assumed to be zero in Eq. (3.111). Here, further discussion is chosen for only in-plane loading. In Eq. (3.111), $\boldsymbol{\delta}_{i+1}$ represents the column vector with unknown coefficients $U_{mn}^*(t), V_{mn}^*(t), W_{mn}^*(t), K_{mn}^*(t)$ and $L_{mn}^*(t)$ at time step t_{i+1}. The stiffness matrix $\mathbf{K}(\boldsymbol{\delta}_i, \overline{N}_x)$ of the restoring force, as given in Eq. (3.111), is represented as,

$$\mathbf{K}(\boldsymbol{\delta}_i, \overline{N}_x) = \mathbf{K}_{\mathrm{L}} + \mathbf{K}_{\mathrm{NL}}(\boldsymbol{\delta}_i) - \left(N_{st} + N_{dyn}\cos pt\right)\mathbf{K}_{\mathrm{G}} \tag{3.112}$$

The restoring force for nonlinear systems is determined based on the history of displacement as follows:

$$\mathbf{K}(\boldsymbol{\delta}_i, \overline{N}_x)\boldsymbol{\delta}_{i+1} = \mathbf{K}(\boldsymbol{\delta}_i, \overline{N}_x)\boldsymbol{\delta}_i + \mathbf{K}_{\mathrm{T}}(\boldsymbol{\delta}_i, \overline{N}_x)\Delta\boldsymbol{\delta}_i \tag{3.113}$$

Here, $\mathbf{K}_{\mathrm{T}}(\boldsymbol{\delta}_i, \overline{N}_x)\Delta\boldsymbol{\delta}_i$ is an incremental restoring force for time increment $\Delta t = t_{i+1} - t_i$. The governing equation is obtained by substituting Eq. (3.113) in Eqs. (3.111) and (3.112) at the time step t_{i+1} and is written as,

$$\mathbf{M}\ddot{\boldsymbol{\delta}}_{i+1} + \mathbf{C}\dot{\boldsymbol{\delta}}_{i+1} + \mathbf{K}_{\mathrm{T}}(\boldsymbol{\delta}_i, \overline{N}_x)\Delta\boldsymbol{\delta}_i = -\ \mathbf{K}(\boldsymbol{\delta}_i, \overline{N}_x)\boldsymbol{\delta}_i \tag{3.114}$$

The governing equation is then given in incremental form by expressing the acceleration, $\ddot{\boldsymbol{\delta}}_{i+1}$ at time step t_{i+1}, the velocity, $\dot{\boldsymbol{\delta}}_{i+1}$ at the time step, t_{i+1}, and the incremental displacement $\Delta\boldsymbol{\delta}_i$. The examination of the microplate's dynamic response with damping owing to periodic in-plane/transverse loading is performed by solving the incremental version of the governing equation at each time step. To get the dynamic response of the microplate without damping, the damping matrix C is omitted.

3.11.5 Post-buckling Response

The post-buckling response of microplate due to thermal loading is calculated by solving Eq. (3.94c) using the modified Newton Raphson incremental iterative method. It is a load control method as the load incremental parameter ΔT is kept constant during iterations. A constant approximation of the stiffness matrix is considered at the end of each iteration in the modified Newton Raphson method. This leads to a lower convergence rate but the time consumed in each iteration is significantly reduced. The converged value of the displacements are obtained at each step, returning the deflection corresponding to each load increment.

4

Nonlinear Vibration and Dynamic Instability of Microplate under In-Plane Mechanical Loading: Results and Discussion

4.1 Introduction

In this chapter, the results of non-linear vibration and dynamic instability analyses of a damped square microplate subjected to non-uniform in-plane harmonic loading are presented. Dynamic instability refers to an erratic or unpredictable state that a structure can experience. This state arises when the structure is exposed to periodic loading within its plane, leading to conditions of parametric resonance. Parametric resonance occurs due to a specific combination of loading frequency and amplitude with the natural frequency of the structure. Moreover, nonlinear vibration behaviour illustrates the forced vibration response of a structure subjected to harmonic excitation under external loading. This behaviour is graphically depicted as a frequency-amplitude curve. The subsequent sections elaborate on both dynamic instability and the responses of nonlinear vibration. A comparative study between different theories, such as MSGT, MCST, and the CCT, for the study of vibrational and instability characteristics of the damped microplates, is performed. The effect of change in the size of the plate, modal damping ratios, ζ_1 and ζ_2, and the static load factor, α, is also presented. Investigations on the influence of four different boundary conditions as shown in section 3.7 and three different cases of in-plane harmonic loadings as shown in section 3.5.1 are also presented. The in-plane harmonic edge loading of the form $\overline{N}_x = N_{st} + N_{dyn}\cos(pt)$, where $N_{st} = \alpha Ncr$ and $N_{dyn} = \beta Ncr$, is applied on two opposite edges. Here α is the static load factor, and β is the dynamic load factor. In this chapter, the validation study of free vibration, buckling, the non-uniform loading modelling, and nonlinear free vibration is presented in section 4.2. The convergence study of the Galerkin's methodology used is presented in section 4.3. Section 4.4 shows a comparative study on the free vibration and buckling analysis using different size-dependent theories. The results of dynamic instability and nonlinear vibration are represented in section 4.5.

4.2 Validation Study

The accuracy of the methodology adopted in this study is verified by comparing the frequency and buckling load obtained by using the methodology in this work with that of Mirsalehi et al. (2017). They determined the free vibration and critical buckling load of the plate based on the MSGT and the split finite strip method. The properties of the square microplate taken from Mirsalehi et al. (2017), and the support and loading conditions it is subjected to are as follows:

$E = 380$ GPa; $\rho = 3800$ kg/m^3; $\mu = 0.3$; $l_0 = l_1 = l_2 = l = 17.6$ μm ; $a = 100\times h$;

Support conditions: SSSS; Loading: in-plane uniform harmonic load on two opposite edges

Table 4.1 Comparison of frequency and buckling load of an SSSS square microplate with different *l/h* ratios

l/h	**Vibration frequency (Hz)**		**Buckling load (N/m)**	
	Mirsalehi et al. (2017)	**Present study**	**Mirsalehi et al. (2017)**	**Present study**
0	54020.00	54016.32	2417.90	2417.87
0.5	117240.00	117237.18	11389.40	11389.35
1	215000.00	214999.14	38303.80	38303.77
1.5	316790.00	316748.95	83161.20	83161.15
2	419690.00	419637.28	145961.60	145961.48

The comparison of frequency and critical buckling load for different *l/h* ratios is shown in Table 4.1. It can be seen that the results obtained are in close proximity to those obtained by Mirsalehi et al. (2017). Thus, the validity of the MSGT methodology adopted in this paper is verified.

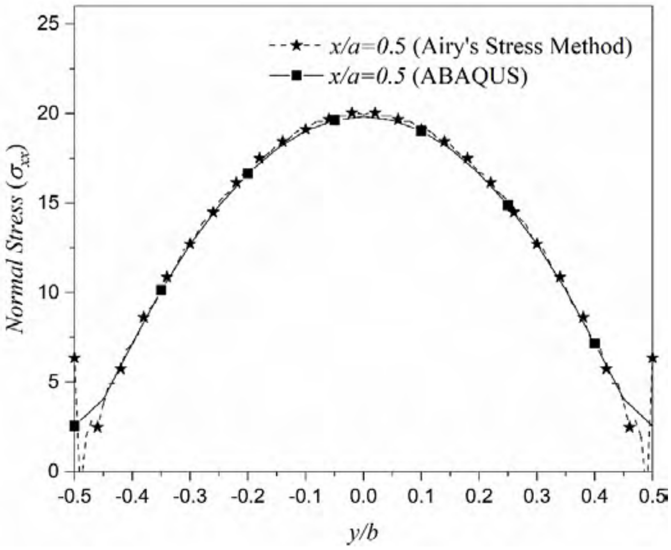

(a) Longitudinal stress distribution at *x/a = 0.5*

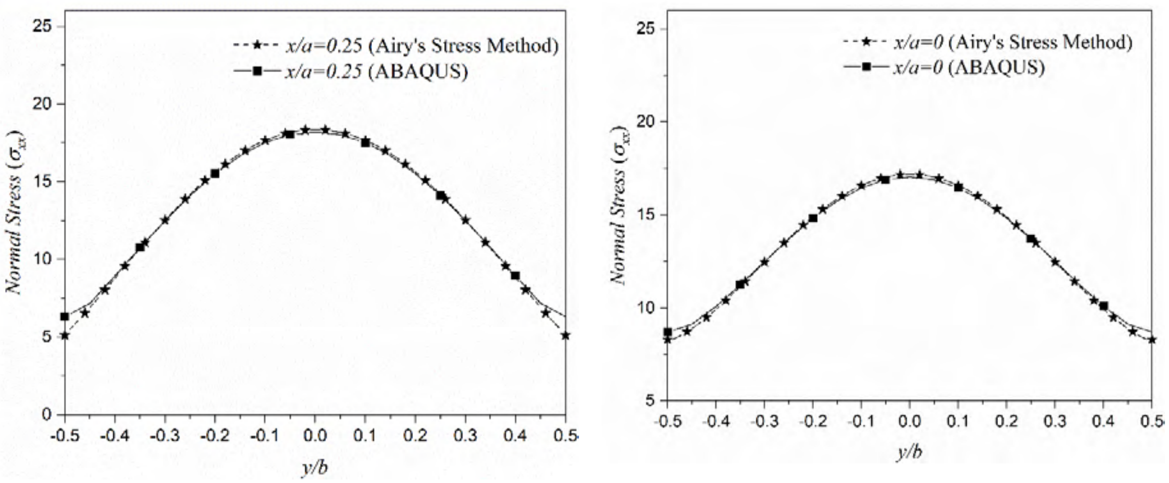

(b) Longitudinal stress distribution at *x/a* = 0.25

(c) Longitudinal stress distribution at *x/a = 0*

Fig. 4.1 Comparison of in-plane longitudinal stress distribution within simply supported isotropic square microplate (*b*/*h*=20; *a*/*b*=1) using Airy's stress approach and finite element (FE) method along (a) *x*/a = 0.5 (b) *x/a* = 0.25 and (c) *x/a* = 0

The reliability of the in-plane stresses obtained using Airy's stress function is validated by comparing the results with the finite element (FE) results obtained using the ABAQUS framework. The distribution of in-plane normal stresses along *x/a* =0.5, *x/a* =0.25 and *x/a*=0 of a simply supported square isotropic microplate (*b*/*h*=20; *a*=*b*) are computed using the present methodology and compared with ABAQUS results in Fig. 4.1(a), Fig. 4.1(b) and Fig. 4.1(c) respectively. The material properties of the microplate used are: E = 1.44 GPa, μ = 0.38, and ρ = 1220 kg/m^3. In-plane non-uniform loading of Case-II with parabolic loading profile (Fig. 3.5(b)) and magnitude unity is applied at a set of opposite edges of the plate. It can be seen from Fig. 4.1 that the results obtained using the Airy's stress approach are in close agreement with those obtained from ABAQUS.

The longitudinal (σ_{xx}), transverse (σ_{yy}), and shear stress (τ_{xy}) contours are also plotted within the domain of the microplate subjected to Case-II type loading (Fig. 3.5(b)) with unit magnitude using Airy's stress approach and finite element method (ABAQUS) in Fig. 4.2. It is evident that the results are very similar to those obtained from ABAQUS. Hence Airy's stress method can be considered a reliable method to model in-plane stresses in this problem.

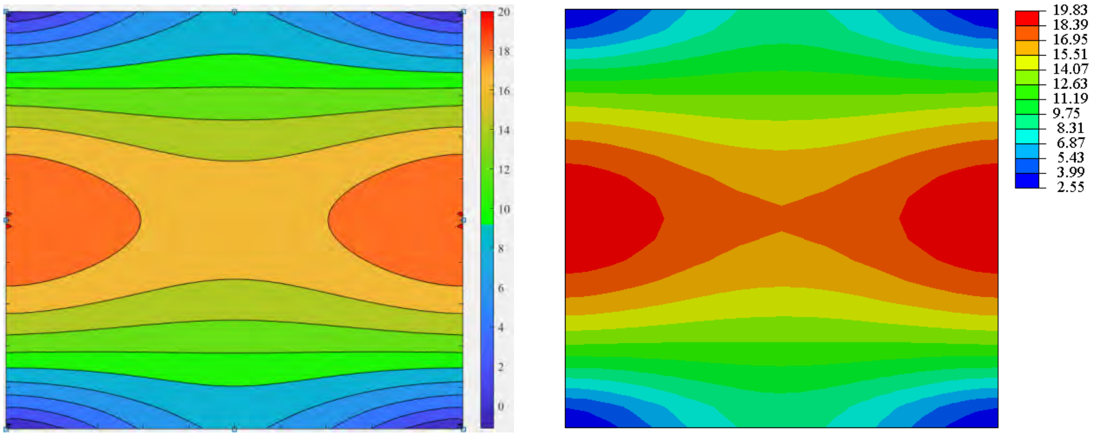

(a)Ariy's stress Method (σ_{xx}) (b) ABAQUS CAE (σ_{xx})

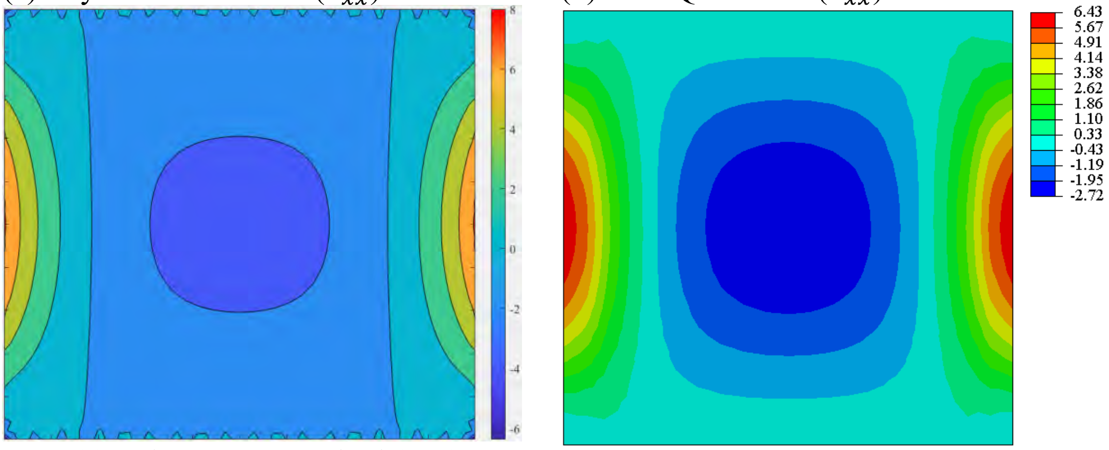

(c) Ariy's stress Method (σ_{yy}) (d) ABAQUS CAE (σ_{yy})

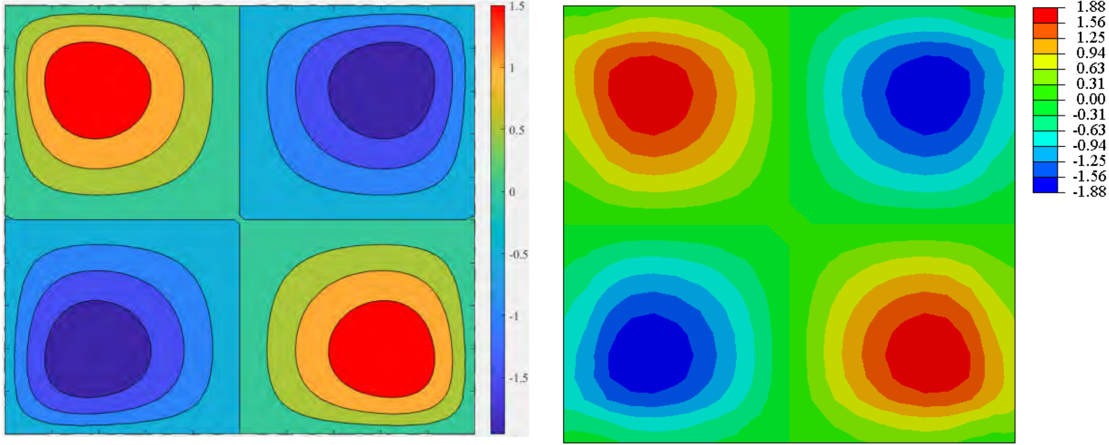

(e) Ariy's stress Method (τ_{xy}) (f) ABAQUS CAE (τ_{xy})

Fig. 4.2 Comparison of in-plane longitudinal, transverse, and shear stress contours on simply supported isotropic square microplate (*b*/*h*=20; *a*/*b*=1) obtained using Airy's stress approach and finite element (FE) method

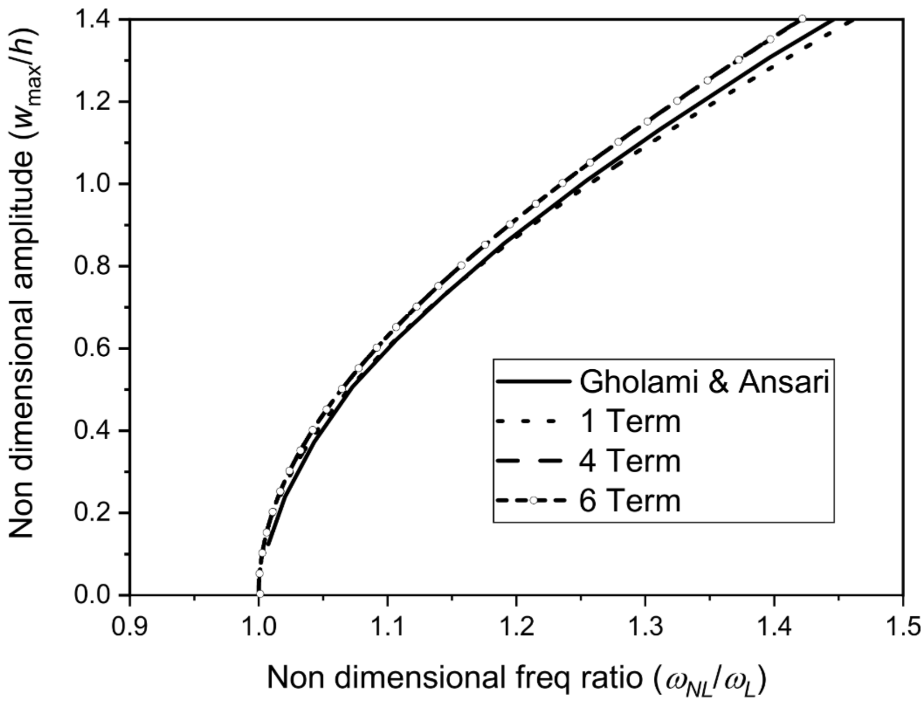

Fig. 4.3. Validation study and convergence analysis of free vibration response of a microplate considering the different number of constant terms corresponding to displacement fields

The methodology used to obtain the frequency-amplitude curve is validated by comparing it to the published results of Gholami and Ansari (2016). The free vibration response obtained from 1, 4, and 6 terms of constants for each displacement field in the present methodology are compared with those given by Gholami and Ansari (2016) (Fig. 4.3). The following microplate properties and parameters are used for this validation and convergence analysis: E = 348.43 GPa; ρ = 2370 kg/m^3; μ = 0.24; $l_0 = l_1 = l_2 = l$ = 15 μm; a = 12 × h; $a = b$; h/l=3; support conditions: SSSS. The non-dimensional frequency ratio used in Fig. 4.3 consists of the natural frequency considering nonlinearity (ω_{NL}) and the fundamental linear natural frequency (ω_L). It can be seen from Fig. 4.3 that the results by Gholami & Ansari are in close agreement with the 1-term solution of this study. However, the curves for the 4-terms solution and 6-terms solution converge completely.

4.3 Convergence Study

For this study, an isotropic epoxy microbeam is considered with the following properties: Young's modulus, E = 1.44 GPa, Poisson's ratio, μ = 0.38, mass density, ρ = 1220 kg/m^3 and the material length scale parameter (MLSP), l = 17.6 μm (Karamanli and Vo 2020). The thickness of the plate, h is considered equal to l and the plate is considered square in shape, with edge length, $a = 100 \times h$. The boundary conditions are assumed to be SSSS (all edges simply-supported) and in-plane uniform harmonic edge loading is considered with static load factor, $\alpha = 0$. The modal damping ratios ζ_1 and ζ_2 for the first and second modes are taken as 3% and 1.5% respectively. All the above conditions are considered all through this study unless explicitly mentioned

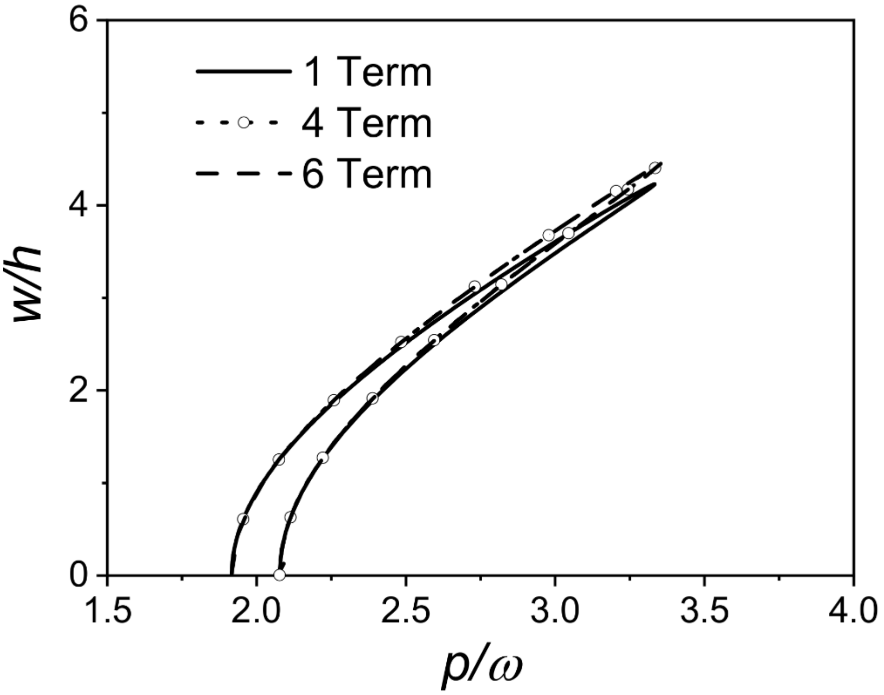

Fig. 4.4 Convergence analysis of nonlinear vibration response of a damped microplate (β=0.2) considering the different number of constant terms corresponding to displacement fields

Convergence analysis is also performed on the forced vibration response to decide the optimum number of terms in each displacement field, which provides accuracy and saves computational costs. It can be seen from Fig. 4.4 that the curve for the 4-terms solution and 6-terms solution converge entirely. Hence, four constants for each displacement field ($u^0, v^0, w^0 \phi_x^0$ and ϕ_y^0), are considered throughout this study (i.e., 4-terms solution). These constants are: U_{11}^*, U_{31}^*, U_{13}^*, U_{33}^*, V_{11}^*, V_{31}^*, V_{13}^*, V_{33}^*, W_{11}^*, W_{31}^*, W_{13}^*, W_{33}^*, K_{11}^*, K_{31}^*, K_{13}^*, K_{33}^*, L_{11}^*, L_{31}^*, L_{13}^*, L_{33}^*.

4.4 Effect of Different Theories on Buckling Load and Frequency

The size effect on the buckling load and frequency in the case of non-macroscopic structures is shown in Fig. 4.5(a) and Fig. 4.5(b), respectively. In the above figures, the buckling load ratio, k_{Ncr} ($\frac{Ncr}{(h/l)}$) and frequency ratio, k_{freq} ($\frac{freq}{(h/l)}$) are plotted against thickness by

MLSP ratio (*h/l*) for MSGT, MCST, and the CCT. Since *l* is constant for a material and $a = 100h$, the size of the plate increases by increasing the *h*/*l* ratio. It is evident from Fig. 4.5(a) that for smaller *h*/*l*, the critical buckling load ratio is higher for MSGT and least for CCT. This is because of hardening due to strain gradients in MSGT. k_{Ncr} for MCST is lower than MSGT due to negligence of dilatant gradient and deviatoric stretch gradient tensors in this theory. k_{Ncr} for CCT remains constant, exhibiting the absence of influence of small-scale effects in this theory. The results of MCST converge with those of CCT at *h*/*l* above 7.5, showing that small-scale effects become insignificant on buckling load in MCST above *h/l*=7.5. In the case of MSGT, the small-scale effects become insignificant on buckling load for *h/l* greater than 15. Similar trends are found in Fig. 4.5(b), where the frequency ratio is found to be maximum in the case of MSGT and least in the case of CCT. The effect of strain gradients was found to vanish for higher *h/l* ratios. Thus, the resonant frequency increases with an increase in size, when the effect of strain gradients or small-scale disappear. However, in the small-scale region, where strain gradients are evident, the resonance frequency increases as the plate size decreases. The sensitivity required is dependent on the resonance bandwidth for a microplate. Thus, depending on the resonance bandwidth required for an application, the size of the plate is reduced in the small-scale region to get a greater resonant frequency.

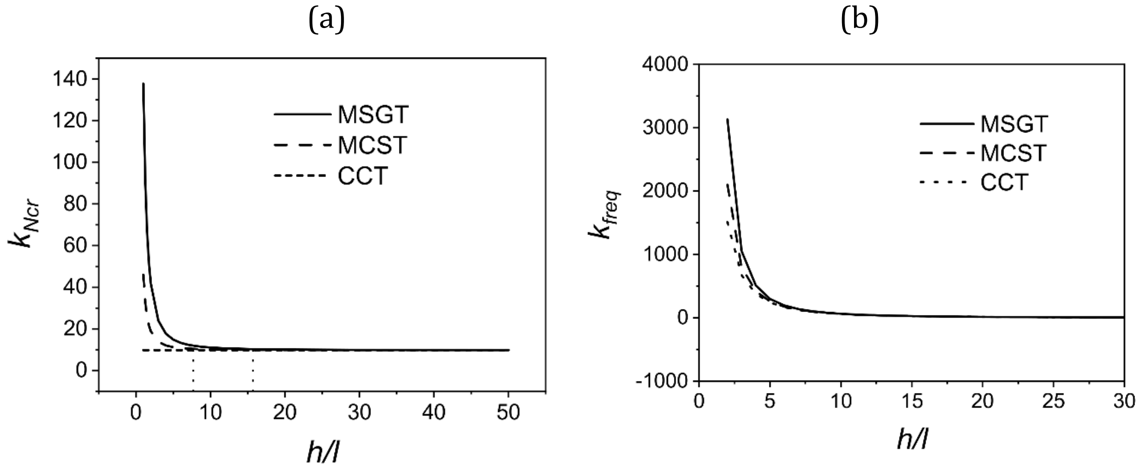

Fig. 4.5 Comparison of size-effect on (a) buckling load ratio, k_{Ncr} [*Ncr*/(*h*/*l*)] and (b) frequency ratio, k_{freq} [*freq*/(*h*/*l*)] for MSGT, MCST, and the CCT

4.5 Non-Linear Vibration and Dynamic Instability Region

The influence of various factors on the dynamic instability and non-linear vibration behavior of a square microplate is discussed in this section. Bolotin's method is used to plot the boundaries of the dynamic instability regions, and a combination of the IHB method and arc length method is used to plot the frequency-amplitude curve for both damped and undamped cases.

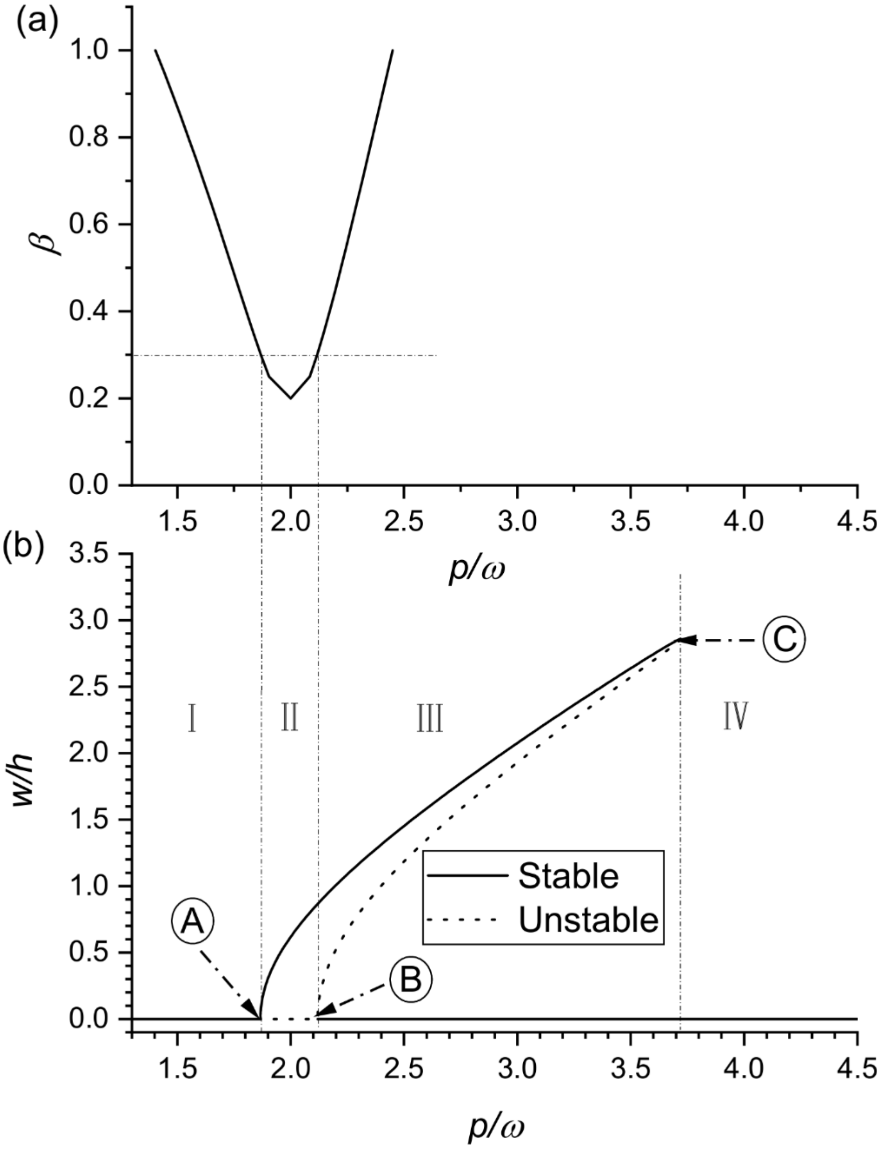

Fig. 4.6 (a) Principal instability zone, and (b) non-linear vibration response at β=0.3 for a damped epoxy microplate (a/h=20; h/l=2; ζ_1=4% & ζ_2=2%; MSGT; SSSS)

The advantage of using the arc-length method is that it gives us both the stable and unstable branches of the frequency-amplitude curve (Fig. 4.6(b)). The curve comprises three bifurcation points, 'A', 'B', and 'C' as shown in the figure. 'A' denotes a supercritical pitchfork bifurcation point, 'B' denotes a subcritical bifurcation point and 'C' is a saddle node bifurcation point. Based on these bifurcation points, the curve can be divided into four regions as indicated in Fig. 4.6(b). Region 'I' consists of one stable solution, region 'II' consists of one stable and one unstable solution, region 'III' consists of two stable and one unstable solution, and region 'IV' consists of one stable solution. The steady-state amplitude attained by a plate when subjected to parametric excitation with forcing frequency in the regions 'I', 'II', and 'IV' is independent of the amplitude of initial displacement due to the presence of only one stable solution.

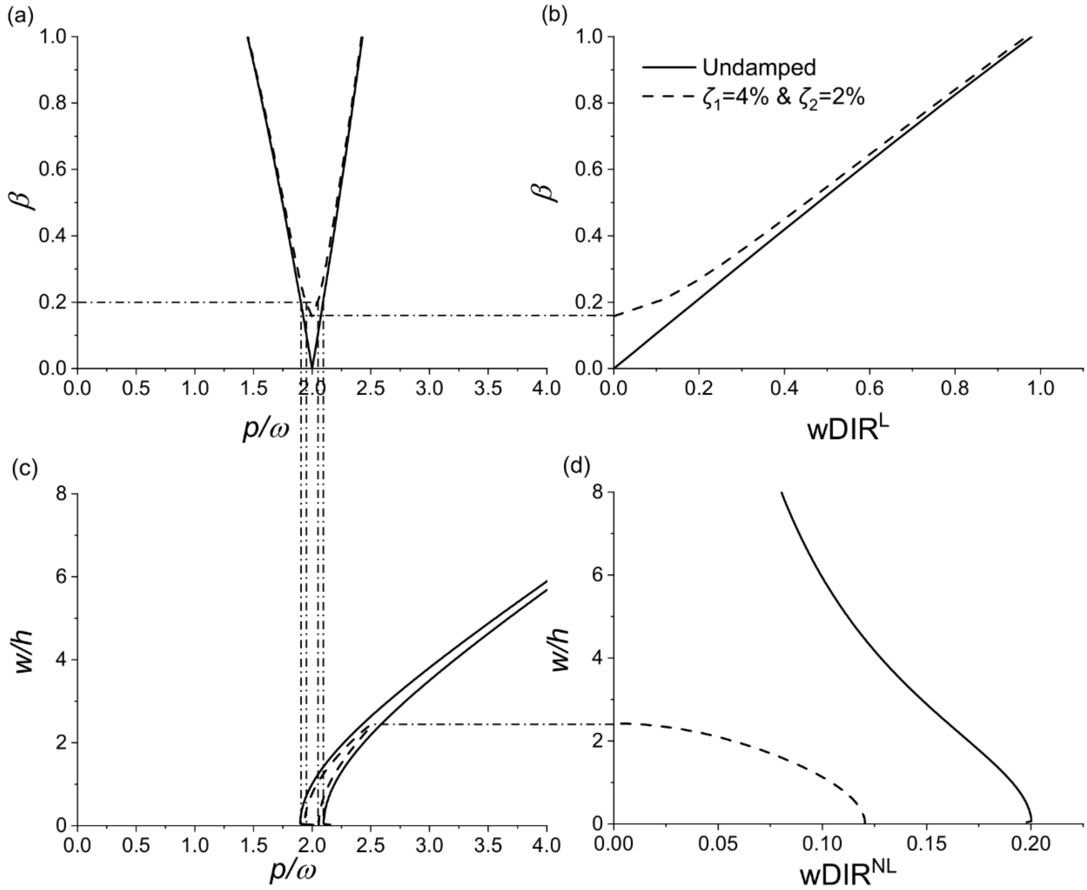

Fig. 4.7 (a) principal instability zone, (b) width of dynamic instability region, (c) non-linear vibration response, and (d) width of dynamic instability region considering non-linearities at β=0.2 for a damped (ζ_1=4% and ζ_2=2%) and an undamped isotropic epoxy microplate (*a/h*=100; *h/l*=1; MSGT; SSSS)

The results in this section are presented with the help of a series of four plots, as shown in Fig. 4.7. The dynamic instability region is shown with the dynamic load factor (β) vs. dimensionless forcing frequency (p/ω) plot in Fig. 4.7(a). The dynamic load factor, β vs. width of dynamic instability region ($wDIR^L$) plot (Fig. 4.7(b)) assists the β vs. (p/ω) plot in expressing the change in the width of the dynamic instability region with the dynamic load factor. The third plot (Fig. 4.7 (c).) is the dimensionless amplitude (*w/h*) vs. dimensionless forcing frequency (*p/ω*) which expresses the non-linear vibration response of the plate at a particular dynamic load factor, *β*. The last plot in the series (Fig. 4.7(d)) traces the dimensionless amplitude (*w/h*) against the width of the non-linear dynamic instability region ($wDIR^{NL}$), i.e., width of the dynamic instability region after considering non-linear stiffness at a particular dimensionless amplitude (*w/h*) and dynamic load factor (*β*). The dynamic instability and non-linear vibration behavior of a damped and undamped epoxy microplate are shown in Fig. 4.7. It can be seen from Fig. 4.7(a) that, while the origin of instability for an undamped microplate starts from $p/\omega = 2$ and $\beta = 0$, the origin of instability for a damped microplate moves a bit in the upward direction, not beginning from $\beta = 0$. Thus, showing that a certain amount of load is needed for a damped plate to display dynamic instability behavior.

It can also be seen from Fig. 4.7(b) that the $wDIR^{L}$ increases with the increase in *β* due to a decrease in stiffness. The $wDIR^{L}$ is less for the damped microplate for smaller values of *β* because of the increase in stiffness due to damping, while it coincides with the $wDIR^{L}$ of the undamped plate at higher values of *β*. The non-linear vibration response is found at $\beta = 0.2$, and it can be seen from Fig. 4.7(c) that the roots of the response (frequency-amplitude) curve coincide with the dynamic instability plot (Fig. 4.7(a)) at $\beta = 0.2$. However, due to the onset of non-linearities in Fig. 4.7(c), the stiffness increases with increasing amplitude (*w*). Thus, the response curve shifts towards the right as non-linear stiffness increases with increasing amplitude, showing hardening behavior. The peak amplitude is infinite in the case of an undamped microplate, while it is finite for a damped microplate. It can also be seen from Fig. 4.7(d) that the $wDIR^{NL}$ decreases on the increase in amplitude due to the increase in non-linear stiffness. It is zero at the finite peak amplitude for the damped microplate and approaches zero at higher amplitudes (infinite) in the case of an undamped microplate.

4.5.1 Effect of Different Strain Gradient Theories

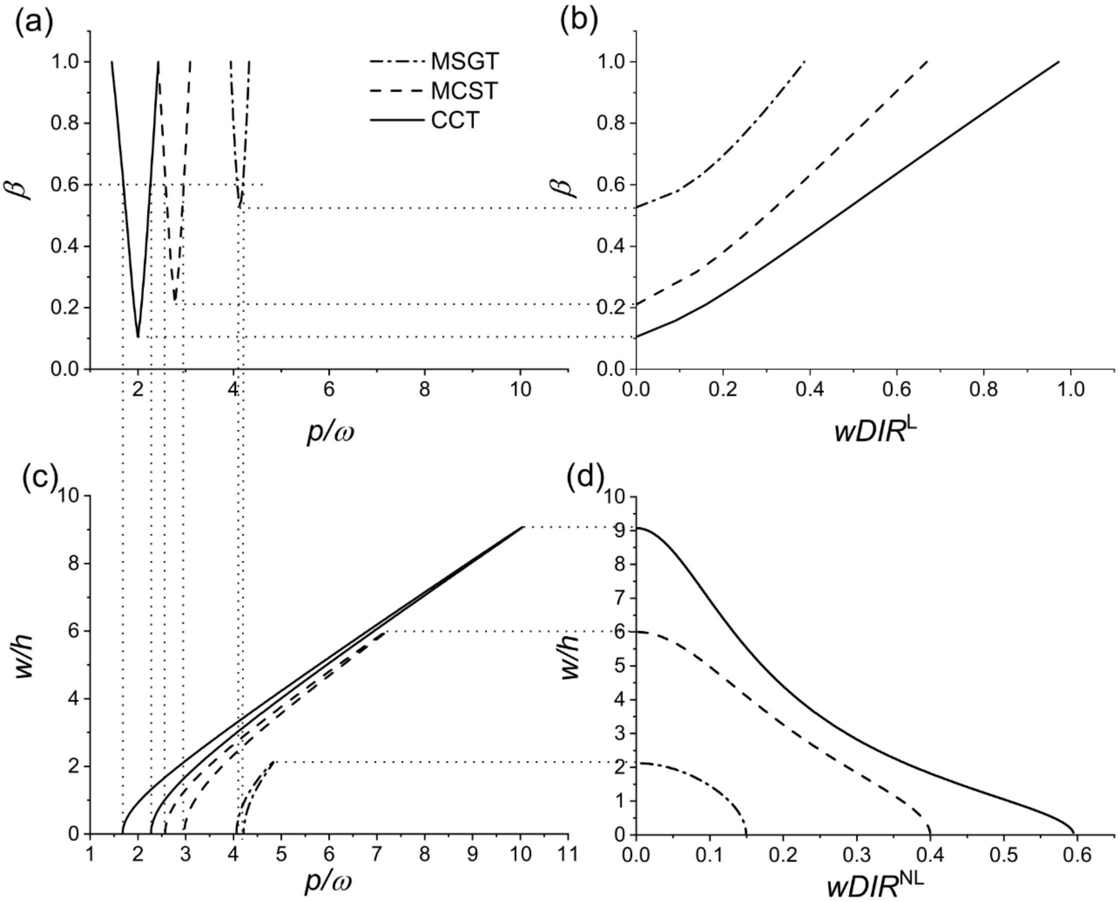

Fig. 4.8 Effect of different strain gradient theories on (a) principal instability zone, (b) width of dynamic instability region, (c) non-linear vibration response, and (d) width of dynamic instability region considering non-linearities at $\beta=0.6$ for a damped isotropic epoxy microplate (a/h=100; h/l=2; ζ_1=3% & ζ_2=1.5%; SSSS)

The difference in dynamic instability and non-linear vibration behavior using the different strain gradient theories is highlighted in Fig. 4.8. The buckling load calculated from CCT is the least, therefore to show fair comparison, the buckling load of CCT is used in the loading function for all methods. The dimensionless natural frequency (p/ω) is calculated using ω calculated from CCT. It can be seen from Fig. 4.8(a). that the origin of instability shifts towards the right in the order CCT<MCST<MSGT. This occurs because of underestimation of stiffness in microplate using MCST due to negligence of dilatant gradient and deviatoric stretch gradient tensors. The results are further underestimated in CCT due to the absence of all the strain gradients and the symmetric curvature tensor. Due to the increase in stiffness, the minimum dynamic load factor required for the onset of instability also increases for MCST and further

for MSGT, despite similar modal damping ratios. Following similar trends, the *wDIR*^{L} also decreases in the same order. The non-linear vibration in Fig. 4.8(c). also shows similar behavior with minimum peak amplitude for MSGT and maximum peak amplitude for CCT, showcasing the higher hardening effect in MCST and MSGT. Similarly, the *wDIR*^{NL} is also maximum for CCT and least for MSGT. The nature of *wDIR*^{NL} is highly nonlinear as the amplitude of the microplate increase for all the theories.

4.5.2 *Effect of Damping Coefficient*

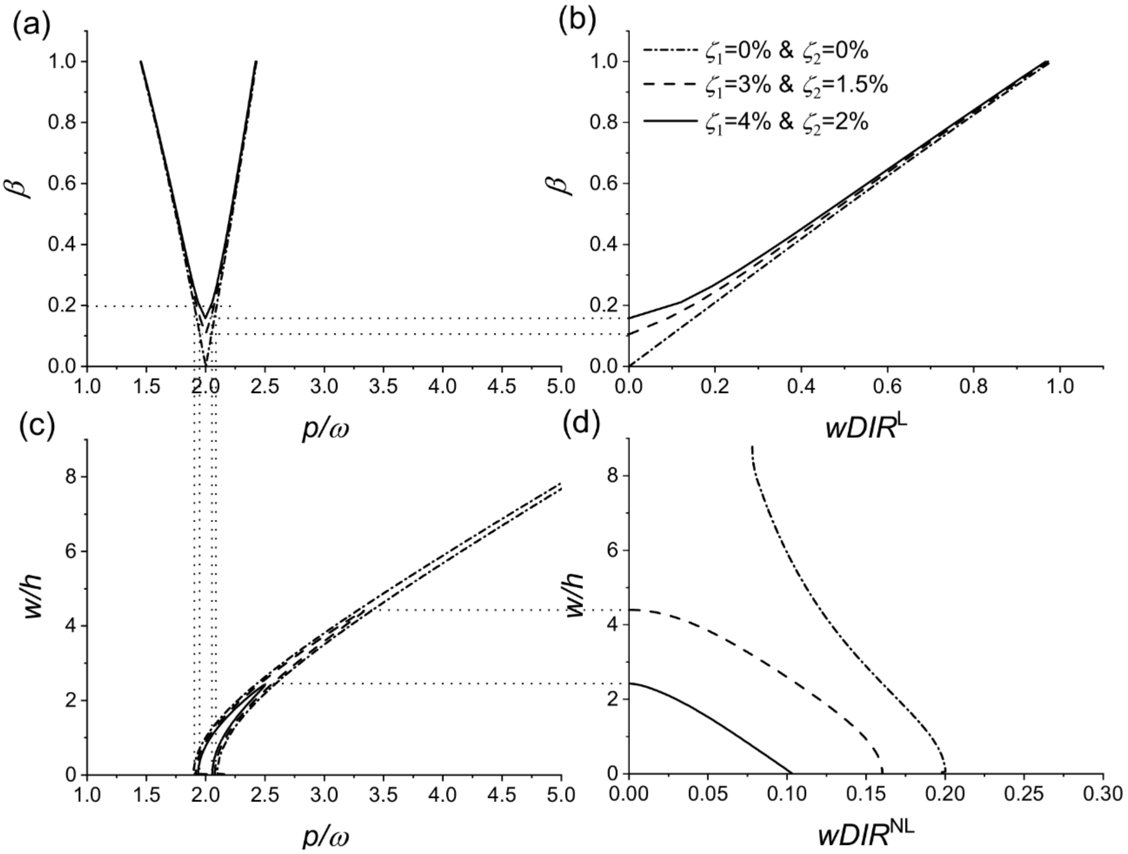

Fig. 4.9. Effect of damping factor on (a) principal instability zone, (b) width of dynamic instability region, (c) non-linear vibration response, and (d) width of dynamic instability region considering non-linearities at β=0.2 for an isotropic epoxy microplate (a/h=100; h/l=1; MSGT; SSSS)

The effect of change in modal damping ratios on dynamic instability and non-linear vibration behavior of microplate is assessed in Fig. 4.9. In the above system of Rayleigh Damping, the mass and stiffness proportional constants are calculated with the help of modal damping ratios, ζ_1 and ζ_2. It is found in Fig. 4.9(a). that on increasing the modal damping ratio, the minimum dynamic load required for the onset of instability increases. The *wDIR*^{L} also decreases for higher modal damping ratios due to an increase in stiffness, and an increase in damping. The peak amplitude and $wDIR^{NL}$ also decrease in the frequency-amplitude curve on an increase in modal damping ratios as evident from Fig. 4.9(c) and Fig. 4.9(d). Thus, it can be concluded that apart from fundamental frequency, damping is also an important factor in determining the sensor bandwidth, especially for lower magnitudes of dynamic load. Thus, to maintain larger bandwidths, the damping on the system also needs to be controlled.

4.5.3 *Effect of Preloading*

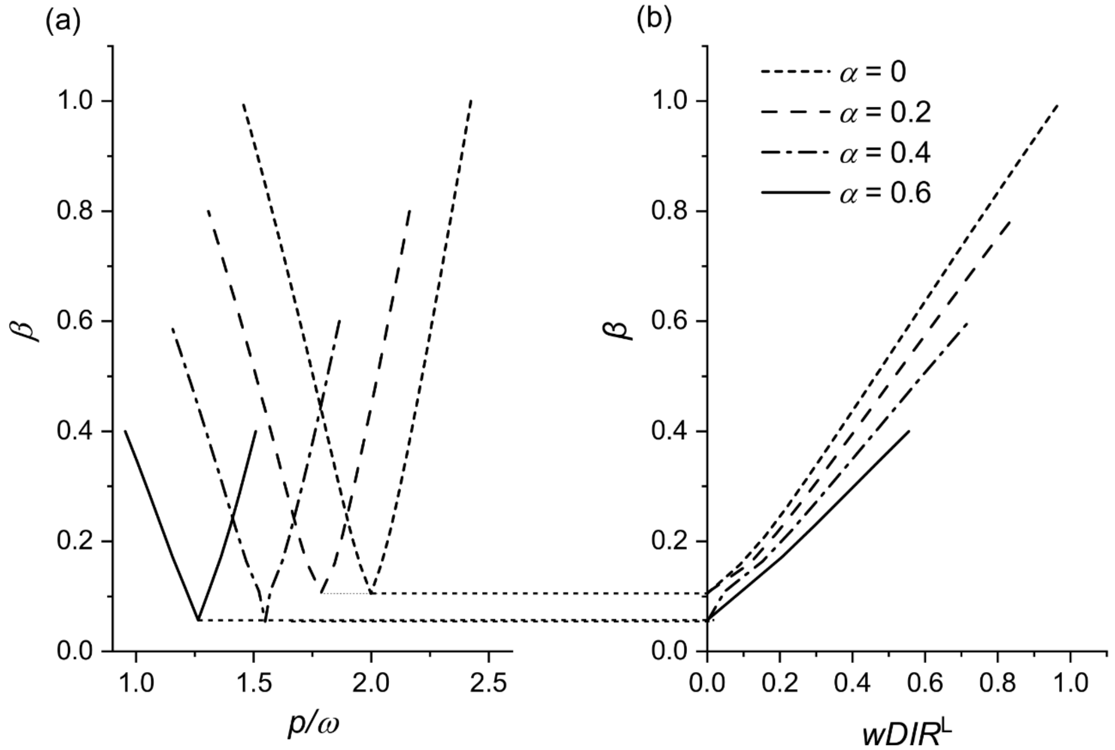

Fig. 4.10 Effect of preloading on (a) principal instability zone, and (b) width of dynamic instability region for an isotropic epoxy microplate (a/h=100; h/l=1; ζ_1=3% & ζ_2=1.5%; MSGT; SSSS)

The effect of the static load factor (i.e., preloading) on the dynamic instability region is shown in Fig. 4.10. The dimensionless natural frequency (p/ω) is calculated using ω calculated for no preloading. The point of origin of instability shifts towards the left in Fig. 4.10(a) due to the drop in stiffness on increasing the static factor. Since the preload is compressive in nature, its addition leads to a drop in stiffness. Following similar grounds, the width of the dynamic instability region also increases with the increase in the static load factor. A representation of the width of the dynamic instability region at β=0.2 and varying the static load factor is shown in Fig. 4.11. It can be seen that with an increase in the static load factor, the $wDIR^L$ increases. The curve is non-linear in nature, and the rate of increase surges with an increase in α. A reduction in $wDIR^L$ is found on increasing the modal damping ratios. However, the difference between $wDIR^L$ for different damping factors diminishes with an increase in the static load factor. Thus, it can be concluded that it is essential to consider preloads for accurate prediction of resonant bandwidths of the microplate. The impact on bandwidth is more significant in less damp systems. Preloads are generally present in any system, and their neglection would lead to an overestimation of the stiffness and origin of resonance bandwidth.

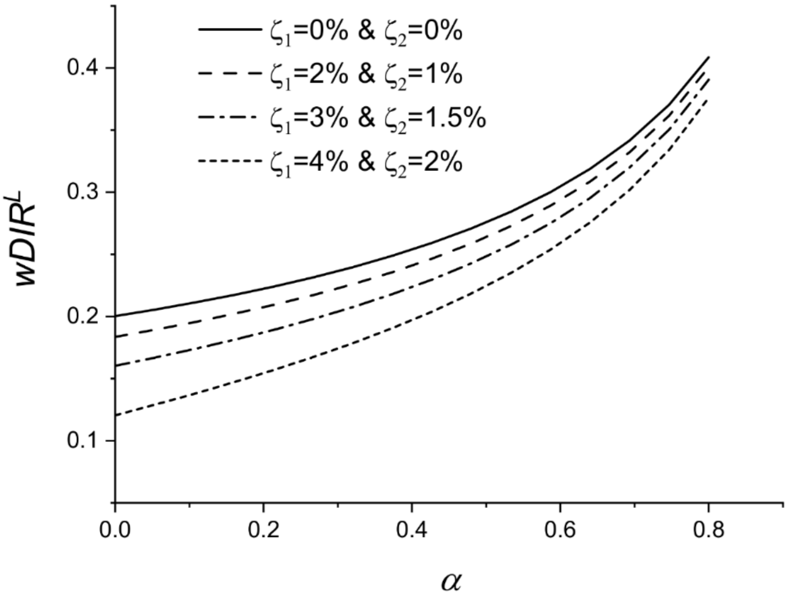

Fig. 4.11. Width of dynamic instability region at β=0.2 vs static load factor for different modal damping ratios for an isotropic epoxy microplate (a/h=100; h/l=1; ζ_1=3% & ζ_2=1.5%; MSGT; SSSS)

4.5.4 *Effect of Boundary Conditions*

The microplates are subjected to various support conditions in practice. The dynamic instability and non-linear vibration behavior of some of the common boundary conditions are plotted in Fig. 4.12. Four different boundary conditions, namely, SSSS (all edges simply supported), SCSC (loaded edges simply supported and non-loaded edges clamped), CSCS (loaded edges clamped and non-loaded edges simply-supported), and CCCC (all edges clamped). The critical buckling load calculated for SSSS is minimum, therefore, to show fair comparison, it is used in the loading function for all methods. The dimensionless natural frequency (p/ω) is also calculated using ω calculated for the SSSS boundary condition. It is observed from Fig. 4.12(a). that the origin of instability shifts towards the right in the order

SSSS→CSCS=SCSC→CCCC. The minimum dynamic load for the onset of instability is also minimum for SSSS and follows the order SSSS<SCSC<CSCS<CCCC. Thus, it can be concluded that the CCCC boundary condition provides the most stiffness to the plate and the SSSS boundary condition provides the least stiffness. The $wDIR^L$ shown in Fig. 4.12(b) also follows a similar trend and is found to be maximum for SSSS and minimum for CCCC support conditions.

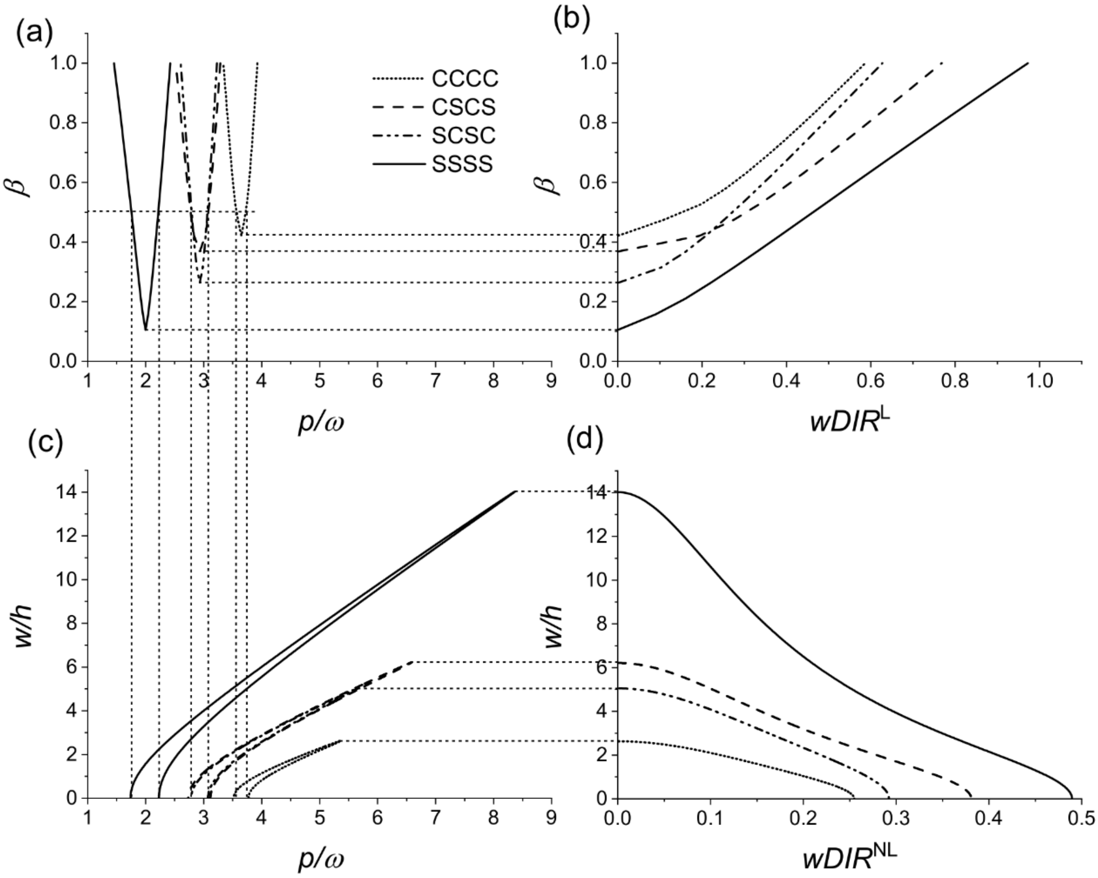

Fig. 4.12. Effect of boundary conditions on (a) principal instability zone, (b) width of dynamic instability region, (c) non-linear vibration response, and (d) width of dynamic instability region considering non-linearities at β=0.5 for an isotropic epoxy microplate (a/h=100; h/l=1; ζ_1=3% & ζ_2=1.5%; MSGT)

Microplate with SCSC boundary condition is found to have lower $wDIR^L$ than with CSCS boundary condition. Similarly, from Fig. 4.12(c) and Fig. 4.12(d). it is observed that peak amplitude and $wDIR^{NL}$ also follow a similar trend and the CCCC support condition provides the maximum stiffness. Thus, it can be concluded that restraints at the boundary conditions not only provide stiffness to the plate but also promote the hardening behavior of the plate. If the size of the plate cannot be reformed, providing restraints at the boundaries may assist in enhancing the resonance frequency of the microplate.

4.5.5 *Effect of Different Loading Conditions*

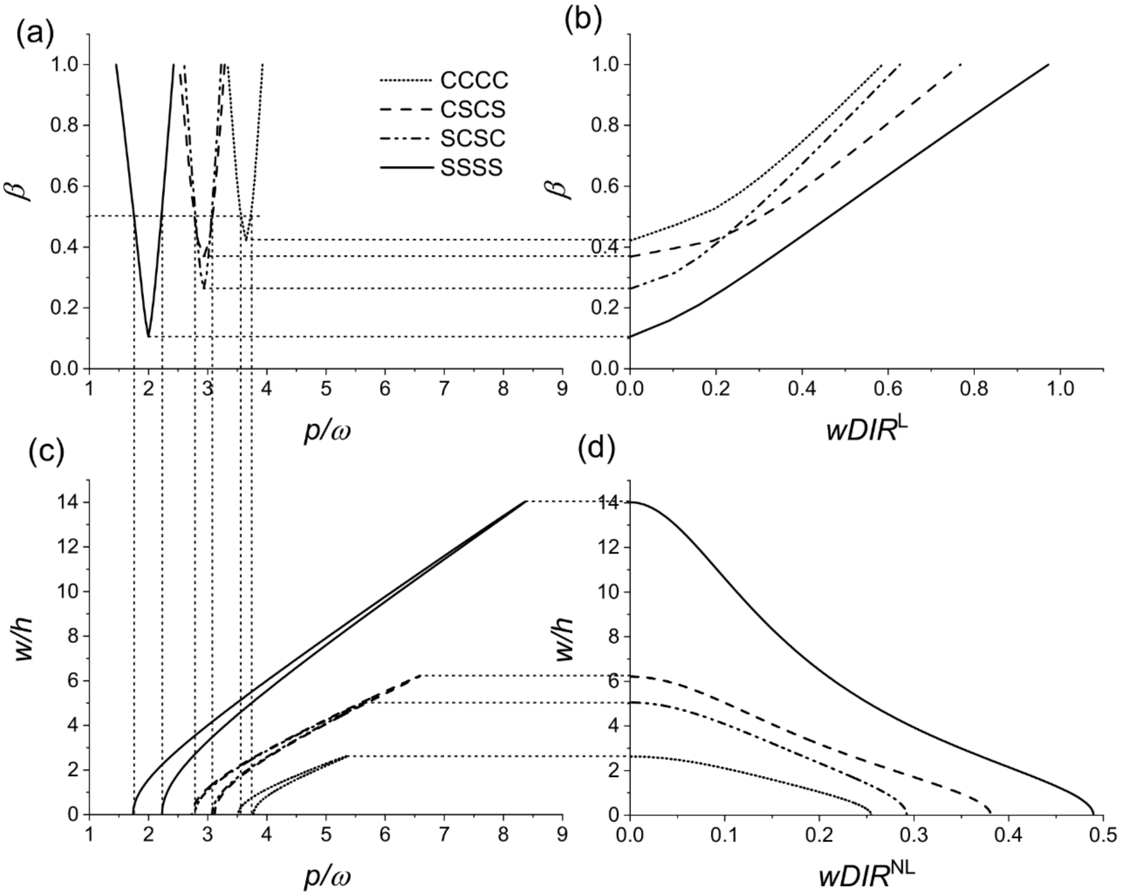

Fig. 4.13. Effect of different loading conditions on (a) principal instability zone, (b) width of dynamic instability region, (c) non-linear vibration response, and (d) width of dynamic instability region considering non-linearities at β=0.6 for an isotropic epoxy microplate (a/h=100; h/l=1; ζ_1=3% & ζ_2=1.5%; MSGT; SSSS)

The loading on the microplate is not always uniform in nature. It might be localized due to localized contact points with the loading device or due to damaged edges. Therefore, a comparison of the effect of uniform, parabolic, and partially loaded edges on dynamic instability and non-linear vibration behavior of microplate is investigated. The magnitude of load in all the cases is equal to the magnitude of load in the uniform load case. The buckling load calculated for the partially loaded edge is minimum, therefore, it is used in the loading function for all methods. The change in loading only affects the geometric stiffness, therefore, there is no change in the origin of instability, as shown in Fig. 4.13(a). The $wDIR^L$ in Fig.

4.13(b) is maximum for partial edge loading and minimum for uniform loading. This is because the geometric stiffness provided is more by partially loaded edges and least for uniformly loaded edges. Since the loading is compressive in nature, higher geometric stiffness leads to lower overall stiffness. Hence, the peak amplitude and $wDIR^{NL}$ are also maximum for partially loaded microplates and minimum for uniformly loaded plates (Fig. 4.13(c) and Fig. 4.13(d)). It can be concluded that the resonance frequency bandwidth varies with the profile of loading considered. The bandwidth would increase for loading profiles where more load is concentrated at the centre of edge.

5

Nonlinear Vibration and Dynamic Response of Microplate under In-Plane Mechanical Loading: Results and Discussion

5.1 Introduction

This chapter presents the combined nonlinear vibration and nonlinear response of a damped porous microplate under nonuniform periodic parametric excitation to understand the complete nonlinear dynamic behaviour of the plate (Fig. 3.3(a)). The plate is supported by a Winkler-Pasternak elastic foundation. The effect of elastic foundation parameters and aspect ratio on mode shape is presented. The steady-state amplitude's dependence on the initial amplitude of perturbation in different zones of excitation frequency is investigated with the help of time history response curves obtained with the use of the Newmark-β method. A parametric study to examine the effect of porosity coefficient, type of porosity, Winkler-Pasternak elastic foundation parameters, different size-dependent theories, size of the plate, thickness of plate, load concentration, loading profile, and modal damping ratios on the nonlinear dynamic behaviour of the porous microplate resting on elastic foundations (PMREF) is presented. The applied loading is of the form shown in section 3.5.1. In this regard, the validation study of the methodology is presented in section 5.2. The parametric study of the mode shape at critical buckling load is presented in section 5.3. Section 5.4 presents the convergence study to determine the optimum number of independent terms to model the field displacement variables. The parametric results for the nonlinear dynamic analyses are presented in section 5.5.

5.2 Validation Study

This section validates the methodology adopted in this study by comparing the results with previous results reported by different studies. The accuracy of the effect of the Winkler-Pasternak elastic foundation on the frequency of simply supported square plate is validated by comparing the results with Baferani et al. (2011), as reported in Table 5.1. They analytically performed the vibration analysis of a thick plate resting on elastic foundations modelled using the TSDT. The mechanical and geometric properties of the plate are E = 380 GPa, ρ = 3800 kg/m^3, ν = 0.3, a/b = 1, and all edges are simply supported (SSSS).

Since the macro-scale plate is considered, CCT is used to obtain the results. It is observed from Table 5.1 that the dimensionless frequency, $\hat{\omega} = \omega h\sqrt{\frac{\rho}{E}}$, obtained from the present study for different equivalent Winkler and Pasternak elastic foundation parameters, $\overline{K_w}$ and $\overline{K_p}$, and *a/h* values match very accurately with that obtained by Baferani et al. (2011). Here, ω stands for the linear fundamental frequency of the plate. The expression for equivalent Winkler and Pasternak elastic foundation parameters, $\overline{K_w}$ and $\overline{K_p}$, is given in Eq. (5.1a) and Eq. (5.1b) respectively.

$$\overline{K_w} = \frac{K_w a^4}{D} \tag{5.1a}$$

$$\overline{K_p} = \frac{K_p a^2}{D} \tag{5.1b}$$

where, $$D = \frac{Eh^3}{12(1-\nu^2)} \tag{5.1c}$$

Table 5.1 Comparison of dimensionless frequency of a simply supported square thick plate resting on an elastic foundation with different values of $\overline{K_w}$, $\overline{K_p}$ and *a/h* ratios

$\overline{K_w}$	$\overline{K_p}$	***a/h***	**Dimensionless frequency**		***a/h***	**Dimensionless frequency**	
			Present study	**Baferani et al. (2011)**		**Present study**	**Baferani et al. (2011)**
0	**0**	**10**	0.1143	0.1134	**20**	0.0292	0.0291
	100		0.1611	0.1599		0.0407	0.0406
100	**0**		0.1171	0.1162		0.0299	0.0298
	100		0.1631	0.1619		0.0412	0.0411

The dimensionless frequency, $\widehat{\omega} = \omega h\sqrt{\frac{\rho}{E}}$ and dimensionless buckling load, $\widehat{N_{cr}} = \frac{N_{cr}a^2}{Eh^3}$, obtained from this study are compared with those given by Hung et al. (2022)**.** It is found that the results obtained from both are very close. They studied the metal foam porous microplate's free vibration and critical buckling load modelled with the help of MSGT and HSDT. The results are compared for different values of *l/h* ratios and types of porosity. The material and geometric properties of the plate are: E = 200 GPa, ρ = 7850 kg/m^3, ν = 0.33, e_0=0.2, l_0= l_1= l_2=15µm, *a/h*=10, *a* = *b*, Support Conditions: all edges are simply supported (SSSS). The formulation for porosity and MSGT is validated by the close results observed between the present study and Hung et al. (2022) in Table 5.2. Thus, the accuracy of the formulation for porosity and modified strain gradient theory in the present study is validated.

Table 5.2 Validation study of dimensionless buckling load and dimensionless frequency of an SSSS square porous metal foam microplate on varying the *l/h* ratios

Type	***l/h***	**Dimensionless critical buckling load**		**Dimensionless frequency**	
		Present Study	**Hung et al. (2022)**	**Present Study**	**Hung et al. (2022)**
Symmetric	**0.1**	3.6579	3.6551	0.0622	0.0617
	0.2	4.9824	4.9697	0.0726	0.072
	0.5	14.2513	13.859	0.1232	0.1215
	1	47.3515	46.2271	0.2245	0.2212
Uniform	**0.1**	3.4716	3.4694	0.0606	0.0601
	0.2	4.7842	4.7734	0.0711	0.0706
	0.5	13.9566	14.153	0.1215	0.1203
	1	46.6882	46.9191	0.2222	0.2196

The in-plane stress resultants are computed analytically in this study using Airy's stress function. The authenticity of these stress resultants is established by matching the stresses computed from them $\left(\sigma_{ij} = \frac{n_{ij}}{h}\right)$ with stresses obtained using the finite element method (ABAQUS). The normal stresses (σ_{xx}, σ_{yy}), and shear stress (τ_{xy}) contours of a simply supported (SSSS) porous microplate resting on an elastic foundation (PMREF) are plotted in Fig. 5.1 using the proposed methodology and ABAQUS. The parameters of the PMREF used are E = 200 GPa, ρ = 7850 kg/m^3, ν = 0.33, a/h=10, a=b, e_0=0.2, symmetric porosity.

A partial loading profile (d=0.25b) of Case-III having unit magnitude is adopted in this validation study. The results are incredibly comparable to those obtained by ABAQUS, as shown in Fig. 5.1. As a result, the analytical approach adopted in this study can be regarded as a dependable methodology for modelling the in-plane pre-buckling stresses.

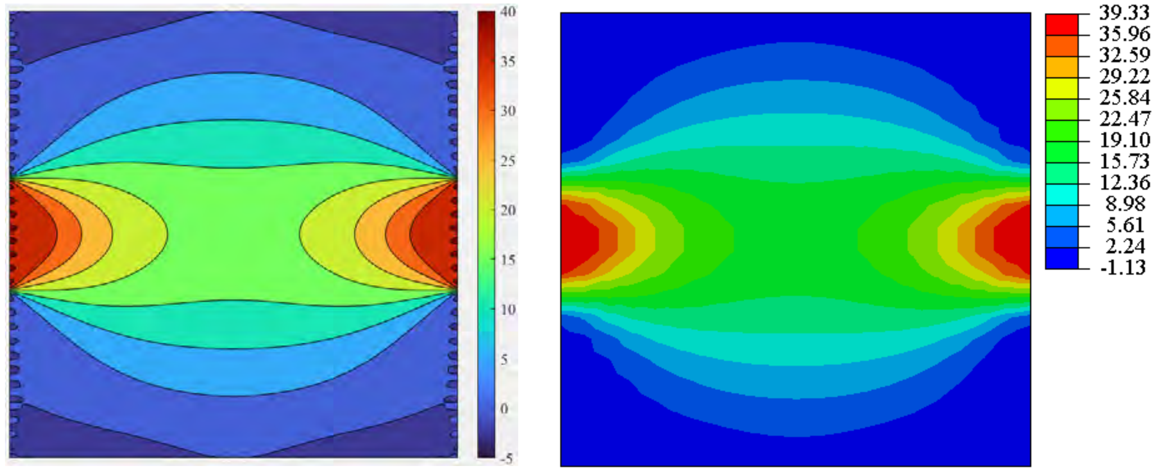

(a)Ariy's stress Method (σ_{xx})

(b) ABAQUS CAE (σ_{xx})

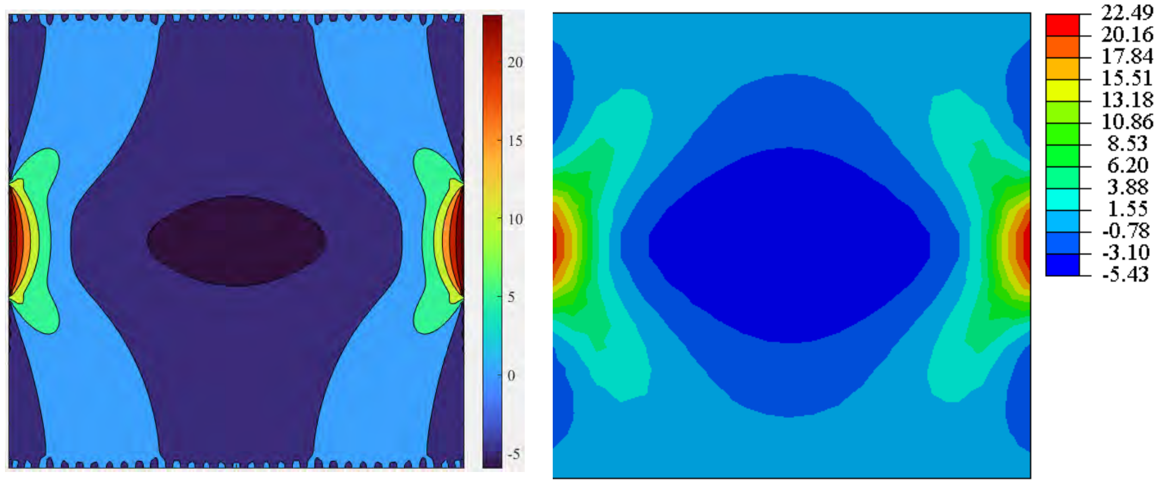

(c) Ariy's stress Method (σ_{yy})

(d) ABAQUS CAE (σ_{yy})

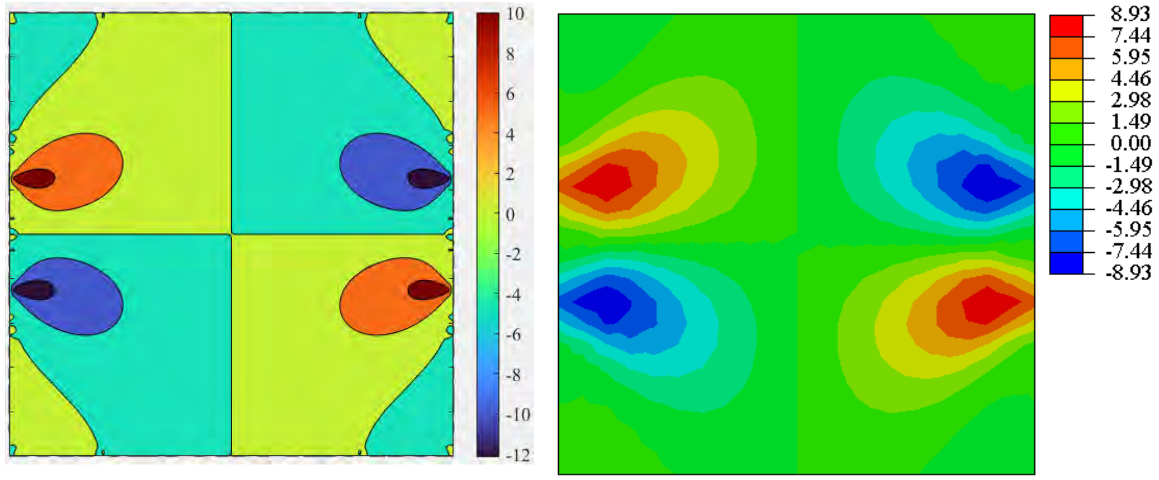

(e) Ariy's stress Method (τ_{xy})

(f) ABAQUS CAE (τ_{xy})

Fig. 5.1. In-plane pre-buckling normal and shear stresses contours computed using Airy's stress method and ABAQUS for simply supported isotropic square plate (*b*/*h*=10; *a*/*b*=1)

5.3 Parametric Study of Buckling Mode Shape

The mode shape at buckling load (i.e., buckling mode shape) for PMREF with different aspect ratios is presented in Fig. 5.2. The square PMREF is buckled in the first mode (m=1, n=1), and the index of the mode shape changes as the aspect ratio increases. This is because, as the aspect ratio increases, the stiffness along one direction is less than the other. This leads to more concentrated stresses across the shorter width in the case of higher aspect ratio plates. Now, as the mode number increases, the number of nodal lines that run across the width of the plate increases. Thus, the vibration in higher modes leads to more localized bending stresses along these nodal lines. These increased localized bending stresses, along with the lower stiffness in one direction for higher aspect ratio plates, lead them to buckle more readily in higher aspect ratio plates. The mode numbers at the buckling load for PMREF with a/b=2, a/b=4, and a/b=6, are obtained as (m=2, n=1), (m=4, n=1), and (m=7, n=1), respectively.

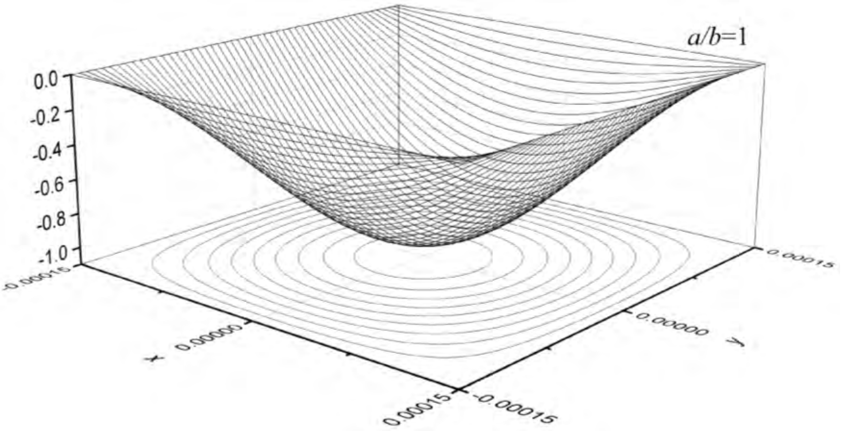

(a)

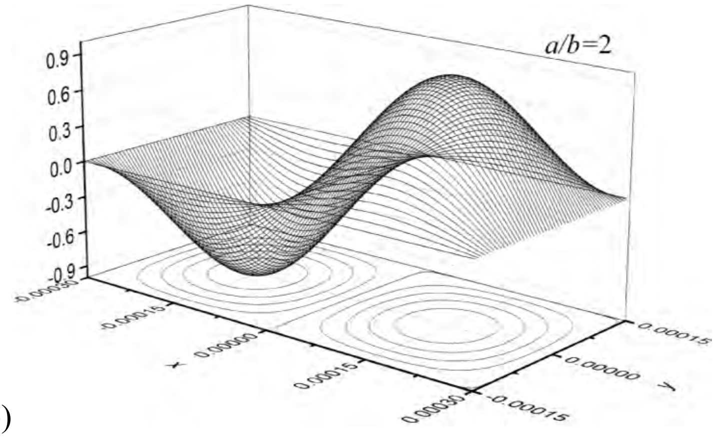

(b)

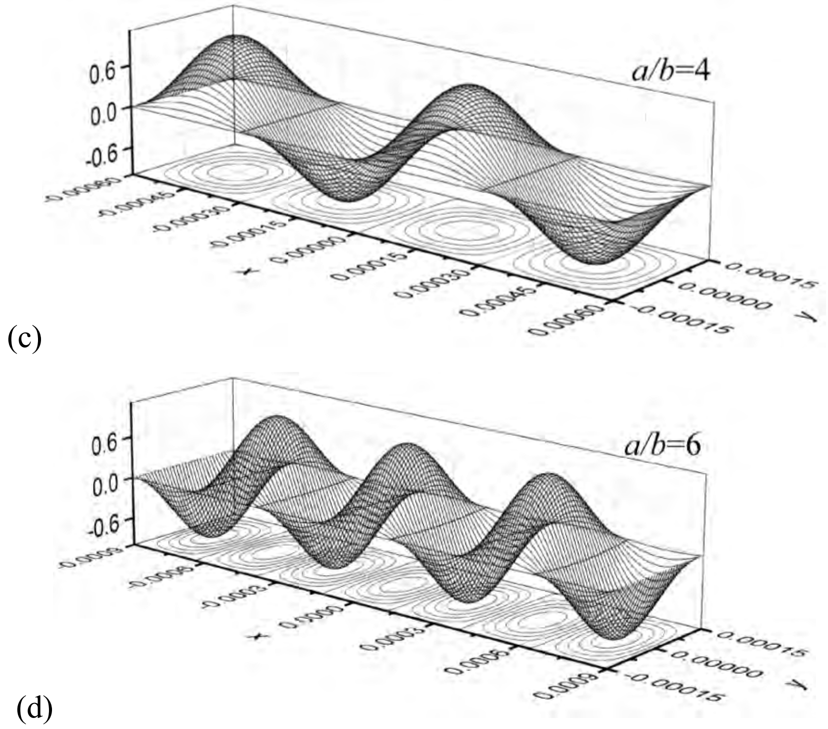

(c)

(d)

Fig. 5.2 Mode shape at buckling load for PMREF (e_0=0.2; Symmetric Porosity; $\overline{K_w} = 10$, $\overline{K_p} = 10$; partial load (*d*=0.5*b*); *a/h*=10; *h/l*=2; MSGT; SSSS) with different aspect ratios, (a) *a/b*=1, (b) *a/b*=2, (c) *a/b*=4, (d) *a/b*=6

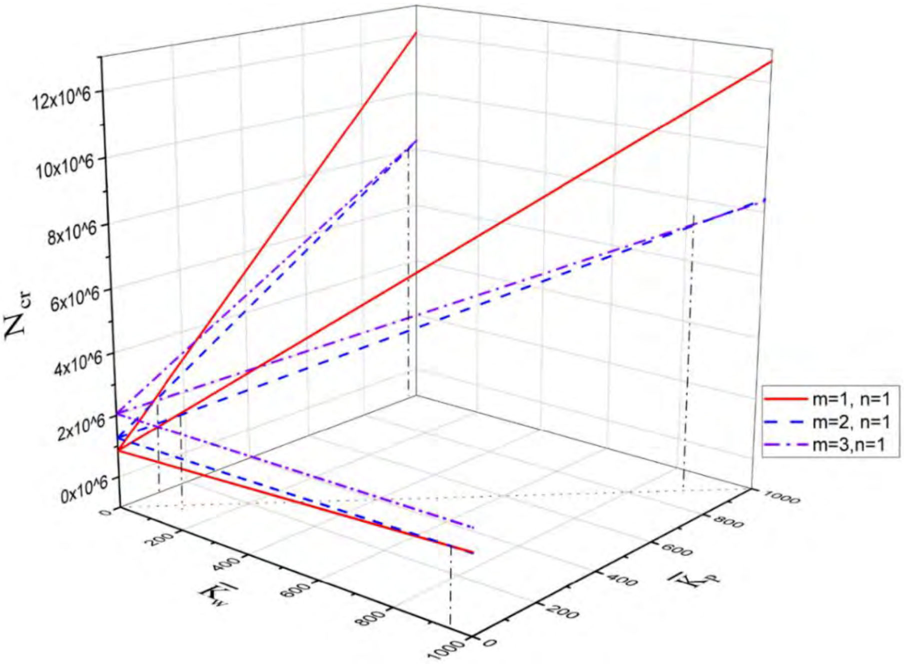

Fig. 5.3 Variation of buckling load for different mode shapes on varying the Winkler and Pasternak elastic foundation parameters for a PMREF (e_0=0.2; symmetric porosity; partial load (*d*=0.5*b*); *a/h*=10; *a/b*=1; *h/l*=2; MSGT; SSSS)

The variation of critical load for a square PMREF at different indexed mode shapes with respect to equivalent Winkler and Pasternak elastic foundation parameters is presented in Fig. 5.3. It is observed that the PMREF buckled in the first mode (*m*=1, *n*=1) for low values of elastic foundation parameters. However, the corresponding indexed buckling mode shapes changed as these parameters increased. The change of mode happens prior on increasing the value of $\overline{K_p}$, than the value of $\overline{K_w}$. When $\overline{K_w}$ is not present, the mode of buckling shifts from (*m*=1, *n*=1) to (*m*=2, *n*=1) near $\overline{K_p} = 100$, and from (*m*=2, *n*=1) to (*m*=3, *n*=1) near $\overline{K_p} = 1000$. On the other hand, when $\overline{K_p}$ is not present, the mode of buckling shifts from (*m*=1, *n*=1) to (*m*=2, *n*=1) near $\overline{K_w} = 1000$. If both $\overline{K_w}$ and $\overline{K_p}$ are increased linearly, the shift from (*m*=1, *n*=1) to (*m*=2, *n*=1) takes place near $\overline{K_w} = \overline{K_p} = 50$, and the shift from (*m*=2, *n*=1) to (*m*=3, *n*=1) takes place near $\overline{K_w} = \overline{K_p} = 900$.

5.4 Convergence Study

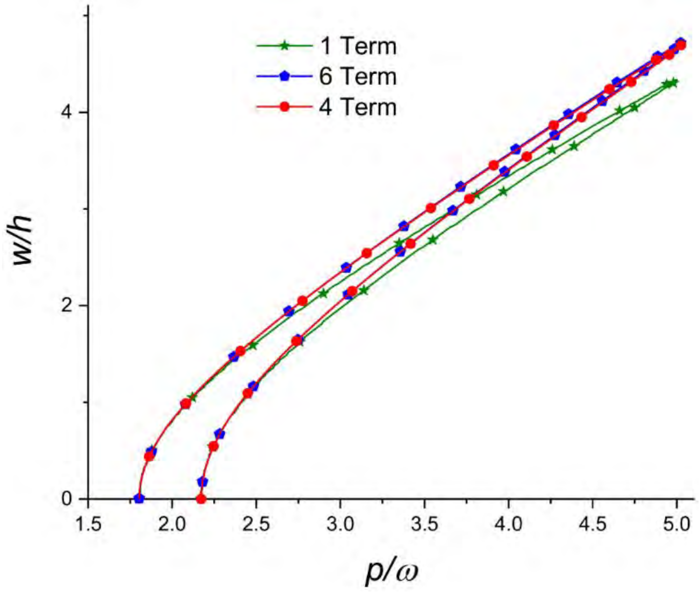

Fig. 5.4 Convergence study of a damped PMREF's (β =0.6) nonlinear forced vibration response taking into account the various number of terms corresponding to each displacement field

In this investigation, the frequency vs amplitude is plotted for nonlinear forced vibration responses with the Incremental Harmonic Balance (IHB) method. The incremental part in IHB is tended to by the arc-length method. The convergence study is performed in Fig. 5.4 for the forced vibration response of the PMREF in this work to determine the optimal number of terms for each displacement field to provide accurate results while maintaining computing efficiency.

The convergence of solution is observed in Fig. 5.4 for 4-terms and 6-terms in the displacement field. Therefore, 4-terms are considered for each displacement field (u^0, v^0, w^0, ϕ_x^0 and ϕ_y^0) all through this study. The four constants for each displacement field are: U_{11}^*, U_{31}^*, U_{13}^*, U_{33}^*, V_{11}^*, V_{31}^*, V_{13}^*, V_{33}^*, W_{11}^*, W_{31}^*, W_{13}^*, W_{33}^*, K_{11}^*, K_{31}^*, K_{13}^*, K_{33}^*, L_{11}^*, L_{31}^*, L_{13}^*, L_{33}^*. The parameters of the PMREF used in this study are E = 200 GPa, ν = 0.33, and ρ = 7850 kg/m^3, a/h=10, a=b, Theory: MSGT, $l_0 = l_1 = l_2 = l$ = 15 µm, h/l=2, e_0=0.2, Symmetric Porosity, $\overline{K_w} = 10$, $\overline{K_p} = 10$, Loading: Partial (d=0.5b), modal damping ratios: ζ_1=4% & ζ_2=2%. Support conditions: All edges are simply supported (SSSS). All these parameters are used throughout this study unless explicitly mentioned.

5.5 Nonlinear Dynamic Analysis Results

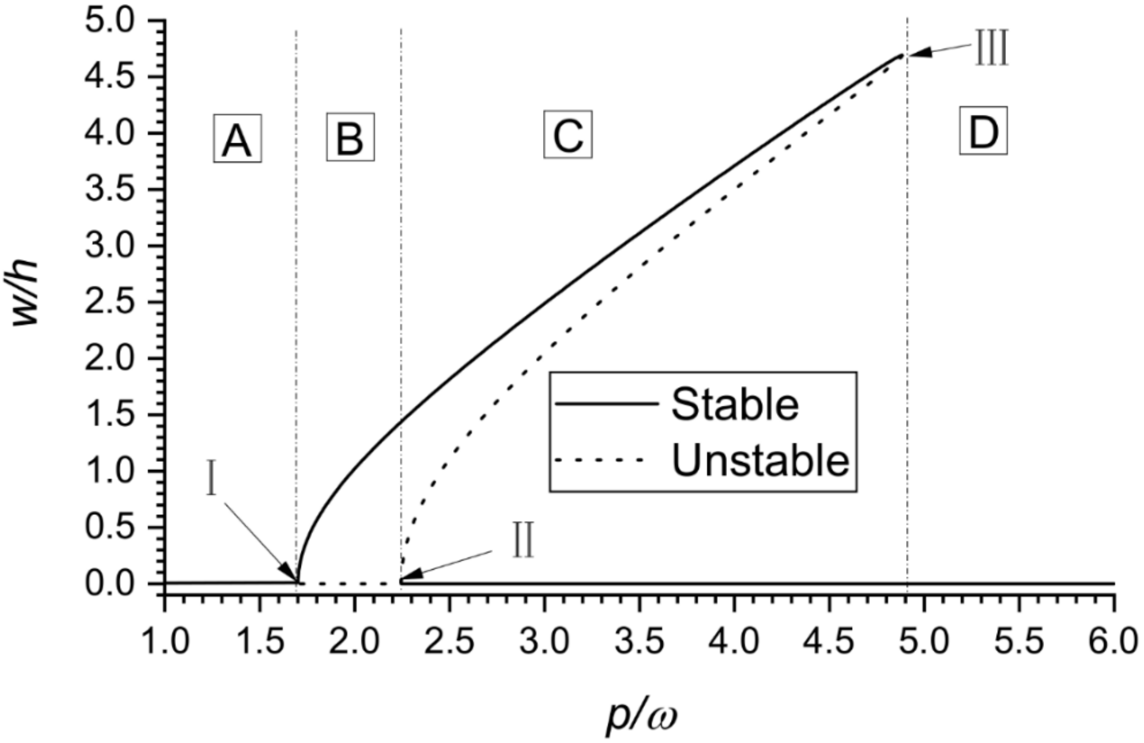

Fig. 5.5 Non-linear vibration response using frequency-amplitude curve at β=0.6 for a damped PMREF (e_0=0.2; Symmetric Porosity; $\overline{K_w} = 10$, $\overline{K_p} = 10$; Partial load (d=0.5b); a/h=10; h/l=2; ζ_1=4% & ζ_2=2%; MSGT; SSSS)

The nonlinear vibration of the PMREF is depicted in Fig. 5.5 by the frequency-amplitude curve. The curve is plotted between w/h and p/ω, where w is the steady state amplitude, p is the frequency of the applied harmonic loading, and ω stands for the linear fundamental frequency. The harmonic load, N_{dyn} applied on the plate is of the form $N_{dyn} =$

βN_{cr}, where β is the dynamic load factor and N_{cr} is the buckling load of the plate. The use of the arc-length technique in IHB provides the frequency-amplitude curve's unstable branch also, along with the stable branch. The diagram shows that the curve has three bifurcation points labeled I, II, and III. Points I and II are pitchfork-type bifurcation points. While I is a supercritical type, II is a subcritical type of pitchfork bifurcation. The bifurcation point III is a saddle-node type point. Four zones may be identified on the curve of forcing frequency based on these bifurcation points, as shown in Fig. 5.5. Region 'A' and 'D' consist of a singular stable solution. On the other hand, region 'B' is comprised of one stable and unstable curve each, and region 'C' is comprised of one unstable and two stable curves.

The existence of a single stable solution in regions 'A', 'B', and 'D', makes the steady-state amplitude in these regions independent of the initial perturbation amplitude. The availability of two stable solutions in region 'C' makes the steady state amplitude attained by forcing frequencies in this region depend on the initial amplitude. Regarding the stability of response, region 'B' is found to be most critical as it leads to high steady-state amplitude for any value of initial displacement amplitude. Region 'C' also shows high amplitude values in Fig. 5.5, but only for large perturbation amplitudes. Regions 'A' and 'D' of forcing frequency are most stable where the steady state amplitude decays to zero for any initial amplitude value.

In this section, the nonlinear dynamic behaviour of the PMREF is analyzed with the help of a frequency-amplitude plot and the time-history response plot. The effect of various parameters such as porosity coefficient, type of porosity, Winkler-Pasternak elastic foundation parameters, size-dependent theories, the concentration of loading, loading profile, and modal damping ratio are examined in the subsections below. The effect of these parameters on the geometric nonlinearity, regions of stability, and overall stiffness is studied with the nonlinear vibration (amplitude vs. frequency plots) and the nonlinear dynamic response (amplitude vs. time plots). The effect of amplitude of initial perturbation, 'w_0', in different regions of forcing frequency is also studied from the time-history analysis.

5.5.1 *Porosity Coefficient*

The impact of change in porosity coefficient on the nonlinear dynamic behaviour of the PMREF is illustrated in Fig. 5.6. The critical buckling load for $e_0=0.6$ is minimum, thus adopted as the magnitude of loading, N_{cr}, for all curves. The excitation frequency ratio (p/ω) and dimensionless time ratio (t/T) are made non-dimensional using 'ω' and 'T' of $e_0=0.6$. Here,

'T' represents the time period of a plate, which is related to 'ω' as $T = 2\pi/\omega$. It is noticed from Fig. 5.6(a) that the lowest frequency of region 'B' moves towards a lower excitation frequency ratio but no shift in the right origin of region 'B' on increasing the porosity coefficient, depicting a decrease in linear stiffness for more porous plates. The width of the region of stability 'B' and 'C' also increases on increasing the porosity coefficient. The increase in porosity coefficient indicates the increase in pores in the material, which in turn results in the reduction of material property parameters such as Young's modulus and shear modulus. The reduction of these parameters reduces both the linear and nonlinear stiffness of the PMREF.

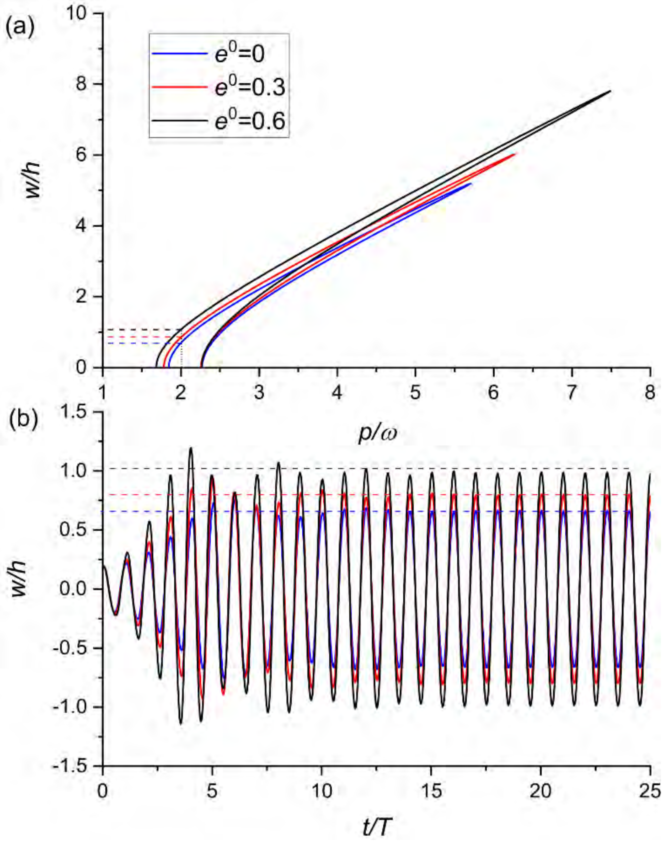

Fig. 5.6 Effect of porosity coefficient on (a) nonlinear vibration response and (b) nonlinear dynamic response (p/ω=2 and w_0=0.2h), at β=0.6 for a damped PMREF (symmetric porosity; $\overline{K_w} = 10$, $\overline{K_p} = 10$; partial load (d=0.5b); a/h=10; h/l=2; ζ_1=4% & ζ_2=2%; MSGT; SSSS)

The effect of geometric nonlinearities on nonlinear stiffness is more evident in less porous PMREF. This is illustrated by the increasing difference in steady-state amplitudes of more porous and less porous plates on increasing the forcing frequency. The forcing frequency for all three curves in the time-history response lies in the region 'B' with a very low amplitude of initial perturbation, w_0. It is observed that the amplitude of the time-history plot increases for all three curves to reach the steady-state amplitude as depicted by their upper stable curves

(Fig. 5.6(b)). The steady-state amplitude is maximum for the most porous plate and minimum for the least porous plate.

5.5.2 *Type of Porosity*

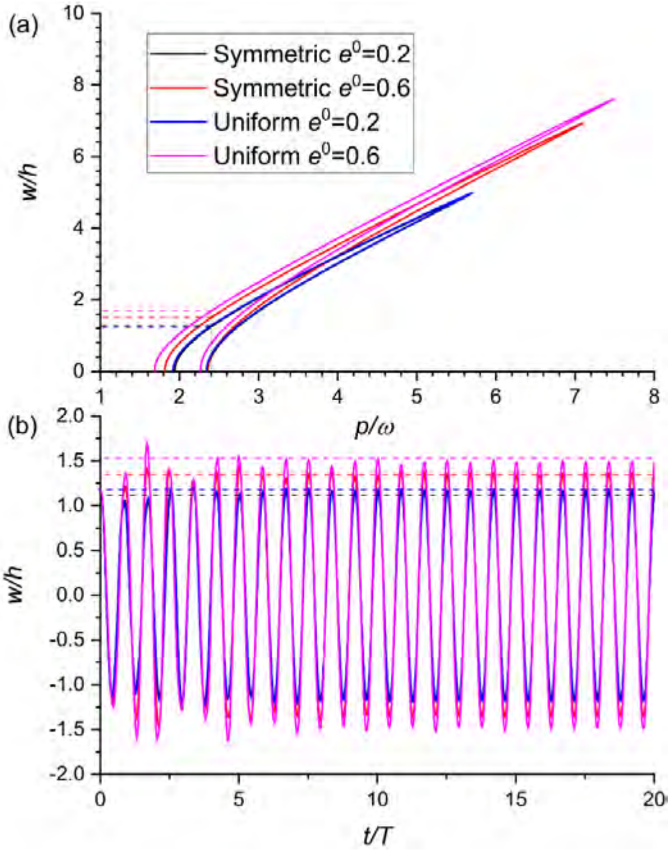

Fig. 5.7 Effect of type of porosity on (a) nonlinear vibration response, and (b) nonlinear dynamic response (p/ω=2.4 and w_0=1.2h), at β=0.6 for a damped PMREF ($\overline{K_w} = 10$, $\overline{K_p} = 10$; partial load (d=0.5b); a/h=10; h/l=2; ζ_1=4% & ζ_2=2%; MSGT; SSSS)

The effect of the type of porosity for different porosity coefficients on the nonlinear dynamic behaviour of the PMREF is illustrated in Fig. 5.7. The magnitude of loading, N_{cr}, 'ω' for dimensionless excitation frequency ratio (p/ω) and 'T' for dimensionless time ratio (t/T) are taken equal to the buckling load, fundamental natural frequency and fundamental time period of PMREF with uniform porosity distribution and e_0=0.6. It is observed from Fig. 5.7(a) that for a particular coefficient of porosity, region 'B' shifts towards a lower excitation frequency ratio when the distribution of porosity is changed from symmetric to uniform. Thus, indicating a reduction in linear stiffness. This is because uniform porosity distribution tends to have a more pronounced effect on reducing Young's modulus because it leads to more uniform stress distribution, reduced effective contact area, increased void interactions, and enhanced stress concentration compared to symmetric porosity distribution. These factors collectively contribute to a higher decrease in the material's stiffness. It can also be seen that the difference in stiffness between a uniform distribution and symmetric porosity distribution is more evident for higher values of the porosity coefficient. Following similar trends, it is also observed that the width of regions 'B' and 'C' is also more for uniform porosity distribution. However, no significant difference is found in the hardening behaviour, indicating significantly less effect on nonlinear stiffness. The time-history plot is plotted for all the porosity distributions with different porosity coefficients corresponding to the forcing frequency in region 'C'. The initial amplitude is chosen near the upper stability curve for all the time-history plots. Thus, the steady-state amplitude for all the time-history plots attained is equal to the amplitude corresponding to their upper stable curve and becomes constant.

5.5.3 *Elastic Foundation*

The effect of Winkler-Pasternak elastic foundation parameters on the nonlinear dynamic behaviour of the PMREF is presented in Fig. 5.8. The magnitude of loading, N_{cr}, 'ω' for dimensionless excitation frequency ratio (p/ω) and 'T' for dimensionless time ratio (t/T) are taken equal to the buckling load, fundamental natural frequency and fundamental time period of PMREF with $\overline{K_w} = 0$, $\overline{K_p} = 0$. It can be noted from Fig. 5.8(a) that the lowest frequency of region 'B' moves towards a higher excitation frequency ratio, and the width of regions 'B' and 'C' decreases on increasing the equivalent elastic foundation parameters $\overline{K_w}$ and $\overline{K_p}$. However, it is seen that the effect of the Winkler parameter on the enhancement of stiffness is negligible in comparison with the Pasternak parameter. This is because, while the Winkler foundation is a model of an array of vertical springs, the Pasternak parameter models the horizontal stiffness provided by the foundation. Since plates are subjected to bending in most cases, the resistance to horizontal displacements provides a greater resistance to bending. The Pasternak parameter also resists the transverse shear deformations, which are detrimental in the case of these plates. The hardening nature of the frequency-amplitude curve is lesser for higher values of elastic foundation parameters, as shown by the diminishing difference between steady-state amplitudes of the upper stable curve on increasing excitation frequency in region 'C'. This indicates that the effect of geometric nonlinearity gets suppressed as the elastic foundation parameters become more prominent. The time-history response is plotted in Fig. 5.8(b) for the excitation frequency of all models in the region 'A' corresponding to a low initial amplitude.

It is observed that the steady-state amplitude for all models decays to zero. The decay for high elastic foundation parameters with greater stiffness occurs earlier than other weaker PMREFs.

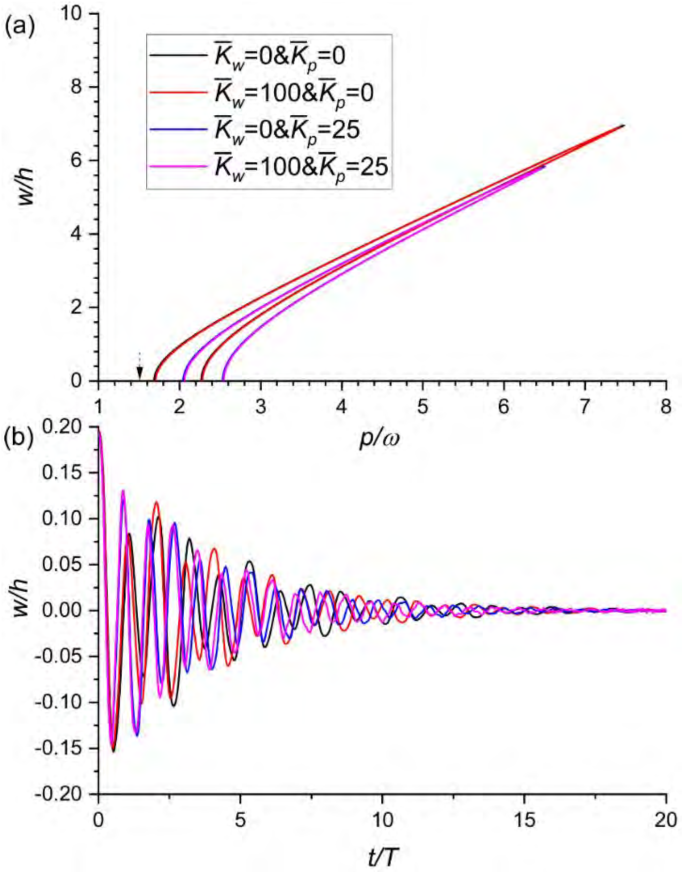

Fig. 5.8 Effect of Winkler-Pasternak elastic foundation parameters on (a)nonlinear vibration response, and (b)nonlinear dynamic response (p/ω=1.5 and w_0=0.2h), at β=0.6 for a damped PMREF (e_0=0.2; symmetric porosity; Partial load (d=0.5b); a/h=10; h/l=2; ζ_1=4% & ζ_2=2%; MSGT; SSSS)

5.5.4 *Theory*

The nonlinear vibration and dynamic responses of PMREF modelled by employing MSGT, MCST, and CCT are presented in Fig. 5.9(a) and Fig. 5.9(b), respectively. The magnitude of loading, N_{cr}, *'ω' for* dimensionless excitation frequency ratio (p/ω), and *'T'* for dimensionless time ratio (t/T) are taken equal to the buckling load, fundamental natural frequency, and fundamental period of PMREF based on CCT. The origin of region 'B' shifts towards a higher excitation frequency ratio on the inclusion of the effect of rotation gradients in the MCST model. The shift is more significant in magnitude due to the MSGT model indicating a more significant contribution in stiffness of the dilatant and deviatoric stretch gradients in MSGT. The width of regions ‘B’ and ‘C’ is also less for the MSGT model and maximum for the CCT model due to the addition of linear stiffness from the hardening of strain gradients in MSGT and MCST models. However, the hardening nature of the upper stable curve in regions ‘B’ and ‘C’ is less for MCST and even lesser in the MSGT model. This is because the effect of geometric nonlinearities gets inferior in the presence of stiffer strain gradient models of MCST and MSGT. The forcing frequency used to obtain the time history response plot lies in region ‘B’ for the MSGT model and region ‘C’ for MCST and CCT models. The initial displacement amplitude is chosen near the upper stable curves of CCT and MCST models. It is observed from Fig. 5.9(b) that the steady state amplitude attained by MCST and CCT does not decay to zero as the initial amplitude nears the upper stable curve. However, in the case of MSGT, although the initial amplitude is not near the upper stable curve, the steady state amplitude still does not decay to zero because of this model's excitation frequency lying in the region ‘B’.

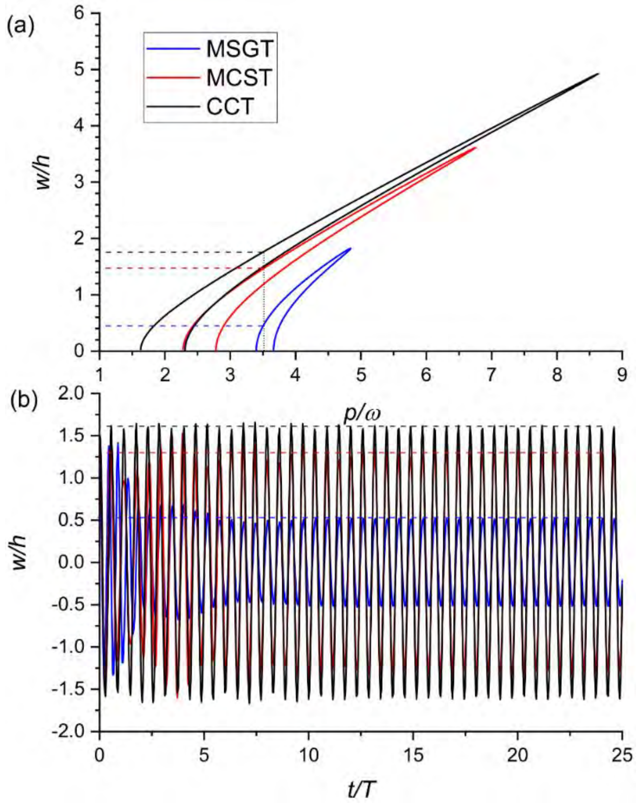

Fig. 5.9 Impact of various small-scale theories on (a) Nonlinear vibration response, and (b) Nonlinear dynamic response (p/ω=3.5 and w_0=1.6h), at β=0.7 for a damped PMREF (e_0=0.2; Symmetric Porosity; $\overline{K_w} = 10$, $\overline{K_p} = 10$; Partial load (d=0.5b); a/h=10; h/l=2; ζ_1=4% & ζ_2=2%; SSSS)

5.5.5 *Length to Thickness ratio (a/h) of the Plate*

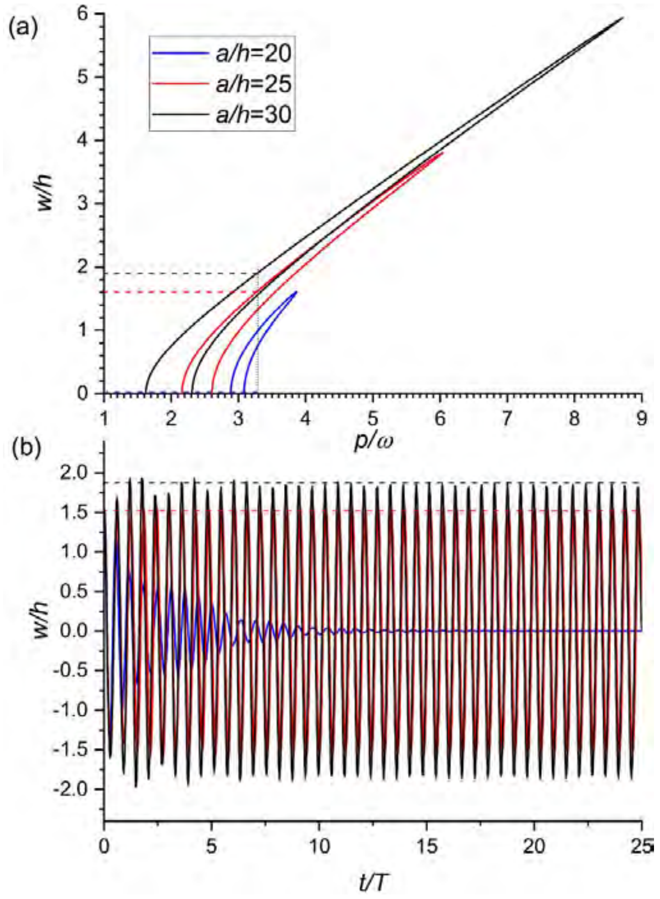

Fig. 5.10 Effect of length to thickness ratio (a/h) on (a) nonlinear vibration response, and (b) nonlinear dynamic response (p/ω=3.3 and w_0=1.6h), at β=0.7 for a damped PMREF (e_0=0.2; symmetric porosity; $\overline{K_w} = 10$, $\overline{K_p} = 10$; partial load (d=0.5b); a=600μm; h/l=2; ζ_1=4% & ζ_2=2%; MSGT; SSSS)

The effect of variation in length to thickness ratio (a/h ratio) of the PMREF on the nonlinear vibration and dynamic response is presented in Fig. 5.10 to study the effect of shear deformation. The edge length 'a' is kept constant at 600 μm, and the thickness of the plate is changed. The value of l is also changed accordingly to maintain an h/l ratio of 2. The nondimensional amplitude (w/h) is calculated using h of the PMREF with a/h=20 i.e., 30μm. The magnitude of loading, N_{cr}, 'ω' for dimensionless excitation frequency ratio (p/ω) and 'T' for dimensionless time ratio (t/T) is taken equal to the buckling load, fundamental natural frequency and fundamental period of PMREF with a/h=30. It can be seen that the origin of region 'B' shifts towards the right, and the widths of regions' B' and 'C' also decrease with an increase in the thickness of the plate. This is because the shear deformation effects become more prominent with an increase in the thickness of the plate. The hardening nature of the curves also decreases with an increase in thickness as the impact of geometric nonlinearity gets suppressed due to the addition of the shear deformation effect. The forcing frequency for Fig. 5.10(b) lies in region 'C' for all three curves, and the amplitude of initial perturbation is near the upper stable curves of *a/h*=30 and *a/h*=25, while away from the upper stable curve of PMREF with *a/h*=20. Therefore, the steady-state amplitude for the PMREF with *a/h*=30 and *a/h*=25 becomes equal to amplitude obtained from their upper stable curves, and it decays to zero for *a/h*=20, exhibiting the dependence of initial perturbation on the steady-state amplitude.

5.5.6 *Size of the Plate (h/l ratio)*

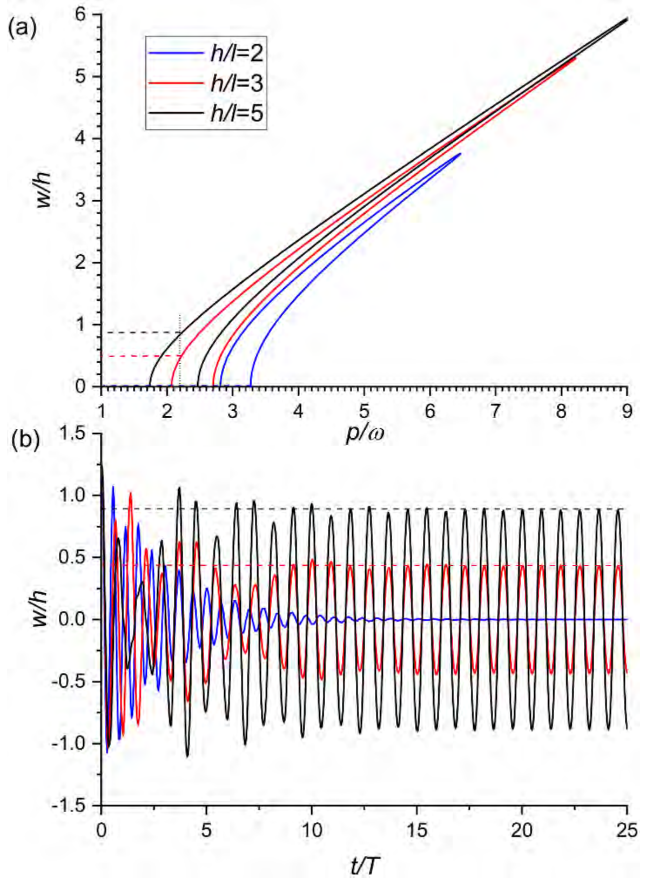

Fig. 5.11 Effect of thickness to MLSP ratio (*h*/*l*) on (a) nonlinear vibration response and (b) nonlinear dynamic response (p/ω=2.2 and w_0=1.3h), at β=0.8 for a damped PMREF (e_0=0.2; symmetric porosity; $\overline{K_w} = 10$, $\overline{K_p} = 10$; partial load (d=0.5b); a/h=10; h=15µm; ζ_1=4% & ζ_2=2%; MSGT; SSSS)

The effect of the size of the plate on the nonlinear vibration and nonlinear dynamic response is presented in Fig. 5.11. The influence of *h*/*l* is studied by keeping the thickness of the plate constant to ignore the effects due to shear deformation. The magnitude of loading, N_{cr}, 'ω' for dimensionless excitation frequency ratio (p/ω), and 'T' for dimensionless time ratio (t/T) is taken equal to the buckling load, fundamental natural frequency, and fundamental period of PMREF with h/l=5. The regions' B' and 'C' shift towards the right and show a decrease in width as the thickness of the plate gets closer to the MLSP (Fig. 5.11(a)). This is because the size-dependent effects get intensified as the size of the plate decreases. The nonlinear hardening nature is also suppressed in the presence of these amplified size-dependent effects. The forcing frequency for the time history response (Fig. 5.11(b)) is taken in region 'B' for PMREF with h/l=5 and h/l=3, and in the region 'A' for h/l=2. Thus, the steady-state amplitude is null in the case of PMREF with h/l=2 and equal to the amplitude from the upper stable curves of the other two plates with no dependence on the initial perturbation.

5.5.7 *Load Concentration*

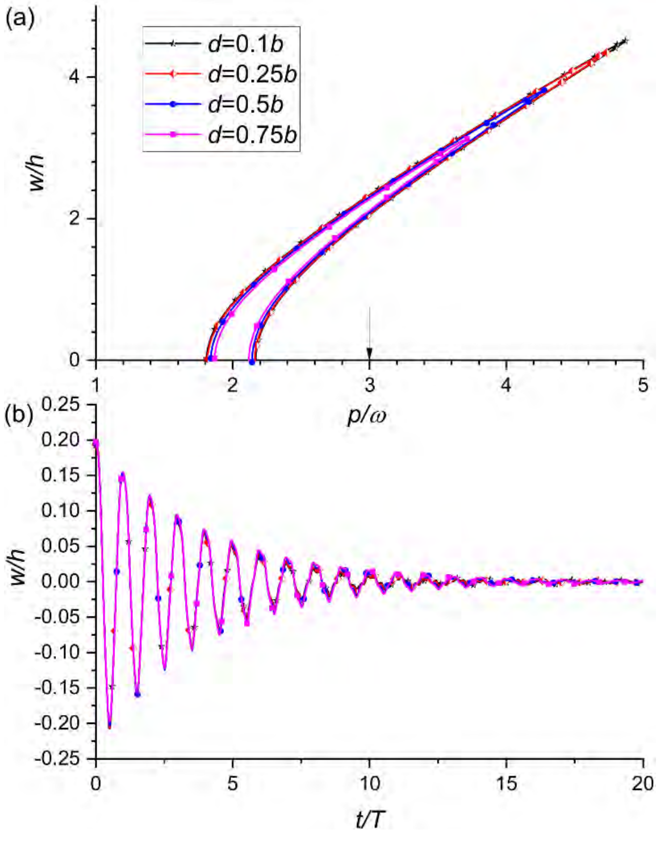

Fig. 5.12 Impact of load concentration on (a)nonlinear vibration response, and (b)nonlinear dynamic response (p/ω=3 and w_0=0.2h), at β=0.4 for a damped PMREF (e_0=0.2; symmetric porosity; $\overline{K_w} = 10$, $\overline{K_p} = 10$; partial load; a/h=10; h/l=2; ζ_1=4% & ζ_2=2%; MSGT; SSSS)

Fig. 5.12 depicts the influence of the concentration of load, *'d'*, in the partial load profile on the nonlinear dynamic behaviour of the PMREF. The buckling load (N_{cr}) due to d=0.1b loading concentration is chosen as a reference. The loading concentration does not affect the linear stiffness and nonlinear stiffness of the PMREF. Thus, the origin of region 'B' and the hardening nature of the curve remains unaffected by loading concentration. It is, however, observed that the steady-state amplitude of the upper stable curve, width of region 'B' and region 'C', increases with the concentration of load. This is because of the greater impact of higher concentrations of load on the linear geometric stiffness due to the in-plane load of the PMREF. The excitation frequency considered for the time-history response (Fig. 5.12(b)) falls in region 'C' for all the loading concentrations. A very small initial amplitude of perturbation has been considered. Thus, the steady-state amplitude for the lower stable curve is adopted for all the loading concentrations, where the response decays completely. Since the linear stiffness in all the cases is unaffected, the decay takes place concurrently for all cases of concentrations.

5.5.8 *Load Profile*

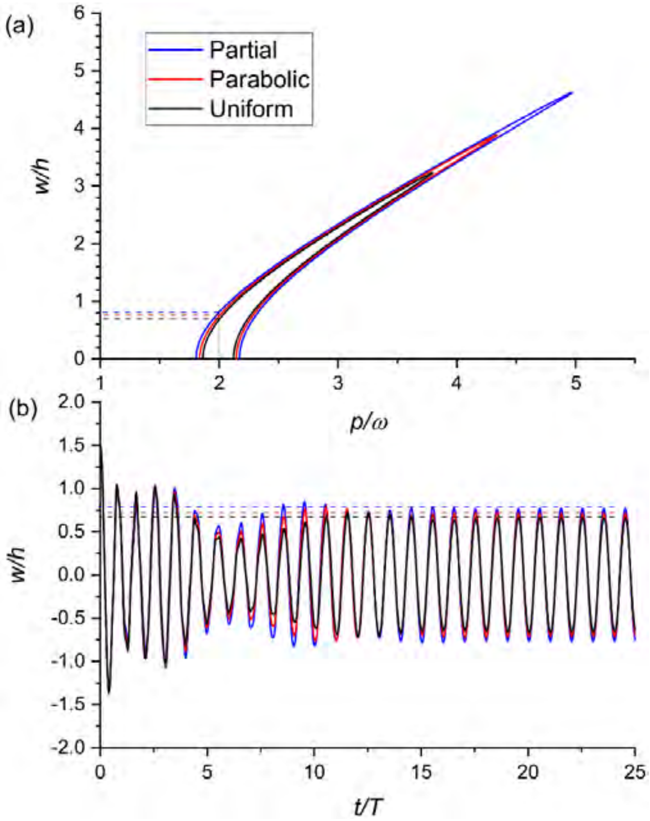

Fig. 5.13 Impact of loading profile on (a) nonlinear vibration response, and (b) nonlinear dynamic response (p/ω=2 and w_0=1.5h), at β=0.4 for a damped PMREF (e_0=0.2; symmetric porosity; $\overline{K_w} = 10$, $\overline{K_p} = 10$; a/h=10; h/l=2; ζ_1=4% & ζ_2=2%; MSGT; SSSS)

The impact of the loading profile of in-plane harmonic load on the nonlinear dynamic behaviour of the PMREF is depicted in Fig. 5.13. The magnitude of loading, N_{cr}, is taken equal to the buckling load due to partial loading profile (d=0.5b). The loading profile has no effect on the linear stiffness and nonlinear stiffness of the PMREF. Thus, the origin of region 'B' and the hardening nature of the curve remains unaffected by the loading profile. The width of region 'B' and region 'C' is most for the partial loading profile and least for the uniform loading profile. This implies that the uniform loading profile has the least impact on the geometric linear stiffness due to in-plane load, followed by parabolic and partial loading profiles. The time history response is plotted for excitation frequency in the region 'B' for all the loading profiles and large initial amplitude of perturbation (Fig. 5.13(b)). It is observed that the response decays from a large initial amplitude of vibration to its steady state amplitude, shown by the stable curve in region 'B'. The steady-state amplitude is highest for the partial loading profile and least for the uniform loading profile, following their order of contribution to geometric stiffness.

5.5.9 *Damping*

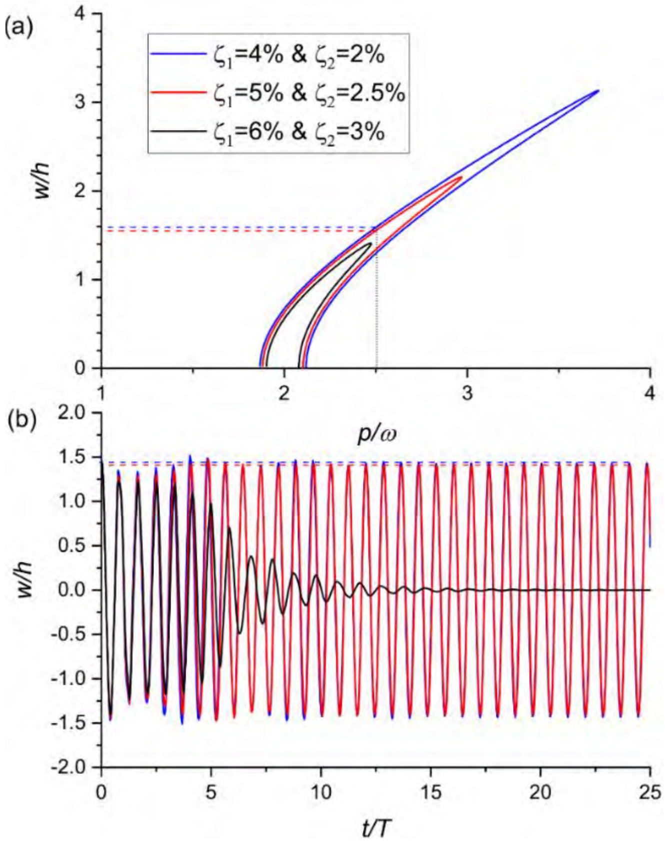

Fig. 5.14. Effect of modal damping ratios on (a) nonlinear vibration response, and (b) nonlinear dynamic response (p/ω=2.5 and w_0=1.5h), at β=0.3 for a damped PMREF (e_0=0.2; symmetric porosity; $\overline{K_w} = 10$, $\overline{K_p} = 10$; partial load(d=0.5b); a/h=10; h/l=2; MSGT; SSSS)

The influence of modal damping ratios on the nonlinear dynamic behaviour of the PMREF is presented in Fig. 5.14. It is observed from Fig. 5.14(a) that an increase in modal damping ratios leads to major mitigation of the width of region 'C'. The width of region 'B' is also lessened but only marginally. The forcing frequency for the time history response falls in region 'D' for a system with ζ_1=6% & ζ_2=3% and in region 'C' for the other two damping systems. The initial amplitude is taken close to the upper stable curves. Thus, the time history response reaches the steady-state response for ζ_1=4% & ζ_2=2%, and ζ_1=5% & ζ_2=2.5%. It decays completely for the ζ_1=6% & ζ_2=3% systems as it falls in the region 'D'. It is also observed that the steady-state response is reached earlier for a higher modal damping ratio system.

6

Nonlinear Dynamic Analyses of Microplate under Transverse Loading: Results and Discussion

6.1 Introduction

In this chapter, the nonlinear dynamic analyses of microplates under periodic transverse patch loadings are studied. The transverse patch loading is considered of the form illustrated in Fig. 3.7. This chapter is divided into three major sections. In section 6.2, the validation and convergence study of the methodology adopted in this chapter is shown. In section 6.3, the parametric analysis of nonlinear free and forced vibration behaviour of functionally graded (FG) microplate subjected to periodic transverse patch loading is presented. In section 6.4, the nonlinear dynamic analyses of porous microplate resting on elastic foundation (PMREF) subjected to periodic transverse patch loading is presented. The frequency-amplitude plots are used to illustrate the nonlinear vibration and time history plots are used to present the nonlinear dynamic response of the PMREF. The effect of different parameters on the nonlinear vibration and the initial amplitude on the dynamic response is studied.

6.2 Validation and Convergence study

By comparing the natural frequency obtained using the methods discussed in this research with that of Mirsalehi et al. (2017), the validity of the mathematical tools for arriving at ODEs utilized in this work is demonstrated. Mirsalehi et al. (2017) calculated the plate's natural frequencies using MSGT and the split finite strip method. The square microplate's properties used in this reference study are the same as those used in this study. The plate's edge length has been taken to be a hundred times its thickness. Table 6.1 compares the fundamental natural frequency in MHz (Ω) for various power-law indices and *l/h* ratios. As can be seen, the results obtained are very similar to those obtained by Mirsalehi et al. 2017. Thus, it is confirmed that the method used in this study is accurate.

The non-dimensional linear deflection $\left(\frac{10Eh^3 w_{lmax}}{f_0 a^4}\right)$ obtained from the present study is compared with the non-dimensional linear deflection computed by Torabi et al. (2021) using the three-dimensional (3D) theory and the plate theory using the FSDT (Table 6.2). The linear deflection is denoted by w_{lmax}. The small-scale effects are modelled using the MCST. The microplate utilized for this comparison in Table 6.2 has the following properties: $E = 14.4$ GPa; $\nu = 0.38$; $\rho = 12200$ kg/m^3; $l_0 = l = 17.6$ μm, $l_1 = l_2 = 0$; $a = b$; Support conditions: All edges simply supported (SSSS). It can be observed from Table 6.2, that the results of the present study are quite close to those by Torabi et al. 2021 for moderately thin (*a/h*=20) and moderately thick (*a/h*=10) plates. The results are closer to 3D results than those given by FSDT plate theory, indicating more accurate modeling of the transverse shear strains than the FSDT. However, for thick plates (*a/h*=5), the plate theories show significant divergence in results from the 3D theory. Thus indicating that plate theories are not suitable for such plates.

Table 6.1 Comparison of frequency of an SSSS microplate with varying power-law index and *l*/*h* ratios

n	***l/h***	**Vibration frequency (MHz)**	
		Mirsalehi et al. (2017)	**This study**
0	0	0.05402	0.05402
	0.5	0.11724	0.11724
	1	0.21500	0.21500
	1.5	0.31679	0.31675
	2	0.41969	0.41964
1	0	0.04121	0.04121
	0.5	0.09584	0.09584
	1	0.17790	0.17788
	1.5	0.26284	0.26284
	2	0.34856	0.34851
5	0	0.03553	0.03553
	0.5	0.07630	0.07630
	1	0.13964	0.13964
	1.5	0.20566	0.20565
	2	0.27242	0.27241
10	0	0.03440	0.03440
	0.5	0.07051	0.07051
	1	0.12781	0.12780
	1.5	0.18781	0.18781
	2	0.24857	0.24859

Comparing the dimensionless frequency, $\hat{\omega} = \omega h\sqrt{\frac{\rho}{E}}$ with Hung et al. (2022) validates the accuracy of the formulation for porosity and modified strain gradient theory in the present work. Utilizing the MSGT, they investigated the free vibration of the metal foam porous microplate and refined the higher-order shear deformation plate theory. The findings for various *l/h* ratios and types of porosity are compared in Table 6.3. These are the plate characteristics utilized in this table:

E = 200 GPa, ρ = 7850 kg/m^3, μ = 0.33, e_0=0.2, l_0= l_1= l_2=15μm, *a/h*=10*,* a = b, Support

Conditions: Simply Supported.

Table 6.2 Comparison of non-dimensional linear deflection $\left(\frac{10Eh^3w_{lmax}}{f_0a^4}\right)$ of a SSSS microplate with 3D theory and 2D (FSDT) for different *a/h* and *l/h* ratios

l/h	*a/h*								
	20			**10**			**5**		
	3D model (Torabi et al. 2021)	**2D HSDT Model (Present Study)**	**2D FSDT Model (Torabi et al. 2021)**	**3D model (Torabi et al. 2021)**	**2D HSDT Model (Present Study)**	**2D (FSDT) Model (Torabi et al. 2021)**	**3D model (Torabi et al. 2021)**	**2D HSDT Model (Present Study)**	**2D (FSDT) Model (Torabi et al. 2021)**
0	0.422	0.422	0.421	0.446	0.440	0.44	0.546	0.512	0.512
0.2	0.363	0.367	0.367	0.377	0.381	0.383	0.437	0.436	0.446
0.4	0.26	0.264	0.265	0.27	0.271	0.276	0.314	0.302	0.324
0.6	0.178	0.179	0.178	0.186	0.184	0.191	0.228	0.200	0.226
0.8	0.124	0.124	0.123	0.132	0.126	0.134	0.173	0.136	0.162
1	0.09	0.09	0.091	0.098	0.090	0.0972	0.141	0.096	0.123

Table 6.3 Validation study of the dimensionless frequency of an SSSS square porous metal foam microplate on varying the *l/h* ratios

Type	***l/h***	**Dimensionless frequency**	
		Present Study	**Hung et al. (2022)**
Symmetric	**0.1**	0.0622	0.0617
	0.2	0.0726	0.072
	0.5	0.1232	0.1215
	1	0.2245	0.2212
Uniform	**0.1**	0.0606	0.0601
	0.2	0.0711	0.0706
	0.5	0.1215	0.1203
	1	0.2222	0.2196

The similarity between the results of this investigation and those of Hung et al. (2022) validates the formulation for porosity and MSGT.

The frequency-amplitude curve is plotted using the IHB method, where the arc-length method acts as the incremental method. The validation of this methodology is already shown in Fig. 4.3 of chapter 4 by comparing the nonlinear free vibration response (i.e., backbone curve).

6.3 Nonlinear Free and Forced Vibration of FG Microplate

The non-linear vibration results of a damped square functionally graded (FG) microplate (Fig. 3.2) are presented in this section. Study of the effects of five various transverse patch loading concentrations, four different positions as shown in section 3.5.2 (Fig. 3.7), and three different boundary conditions (CCCC, SCSC, and SSSS), depicted in section 3.7, is performed. For this study, a FG microplate, with Alumina and Aluminum as the constituent materials, is considered (Mirsalehi et al. 2017). The properties of the plate are as follows: E_c = 380 GPa, ρ_c = 3800 kg/m^3, E_m = 70 GPa , ρ_m = 2707 kg/m^3 and ν = 0.3, power-law index, n=1 and the thickness, h = 35.2 μm. It is known that material length scale parameters (MLSP) have been calibrated by comparing vibration or bending results from nonclassical continuum theory with those obtained from experimental methods such as micro/nano indentation tests or molecular dynamic simulations. In the case of functionally graded materials, no such experimental or atomistic simulation results are available to calibrate the length-scale parameters. Therefore, in this study, the length scale parameters are assumed to provide effective qualitative results, enabling us to study the qualitative effect of various parameters on geometric nonlinearity and stiffness of moderately thick microplates (Gholami et al. 2020). The material length scale parameter, l is assumed to be half the thickness of the plate, h, and, a = 10h, a =b. In the case of modified strain gradient theory, all three MLSPs, l_0, l_1, and l_2, are regarded as equal, suggesting that the three strain gradient tensors—rotation gradient, dilatant gradient, and deviatoric stretch gradient—all contribute equally. In the context of MCST, the effects of the dilatant gradient and deviatoric stretch gradient are not taken into account. Therefore, l_1 and l_2 are considered to be zero. SSSS support conditions and transverse loading of the form $\mathbf{F}\cos(\omega_{NL}t)$ is applied on the face of the plate in the transverse direction. The loading is considered to be uniformly distributed in the patch region (a_l=0.5a, b_l = 0.5b) for the different loading cases (Fig. 3.2). The modal damping ratios ζ_1 and ζ_2 are considered equal to 4% and 2% respectively. All of the aforementioned conditions are taken into account throughout this investigation, unless otherwise stated.

A parametric study on the non-linear vibration characteristics of a square functionally graded microplate using the non-dimensional amplitude (w/h) vs. non-dimensional frequency ratio (ω_{NL}/ω_L) is presented in the following subsections. The non-dimensional frequency ratio is the ratio of the resonating frequency considering the nonlinear stiffness to the linear fundamental natural frequency of the FG microplate. The resonating frequency considering the nonlinear stiffness, equals the forcing frequency for harmonic transverse loading.

The effect of parameters such as power-law index and *h*/*l* ratio on free vibration response (backbone curve) is studied. Furthermore, the effects of change in thickness (*a*/*h* ratio), modal damping ratios, boundary conditions, position, and concentration of patch loading on the forced vibration response, are discussed in the sections below. The fundamental natural frequencies in MHz (Ω) are also given in the figures. It can be seen from the figures that the FG microplate exhibits a hardening type of non-linearity due to the addition of stiffness owing to geometric nonlinearities. It is observed that the hardening behavior magnifies with the increase in amplitude. Thus, nonlinear vibration analysis is essential for the design of microplates used in small-scale devices subjected to large amplitude deflections.

6.3.1 *Non-Linear Free Vibration Analysis*

6.3.1.1 *Effect of power-law index*

It can be seen from Fig. 6.1 that the natural frequencies decrease on the increase in the power-law index due to a decrease in the stiffness of the FG microplates. However, the hardening behavior of the backbone curves with different power-law indices does not follow a particular trend. The hardening nature is maximum for *n*=1 and minimum for *n*=10. The hardening nature for *n*=0 is found to be lesser than the microplate with *n*=1. The difference between the hardening behaviors is not significant enough, therefore showing the unsubstantial influence of the power-law index on the nonlinear hardening behavior of the microplate.

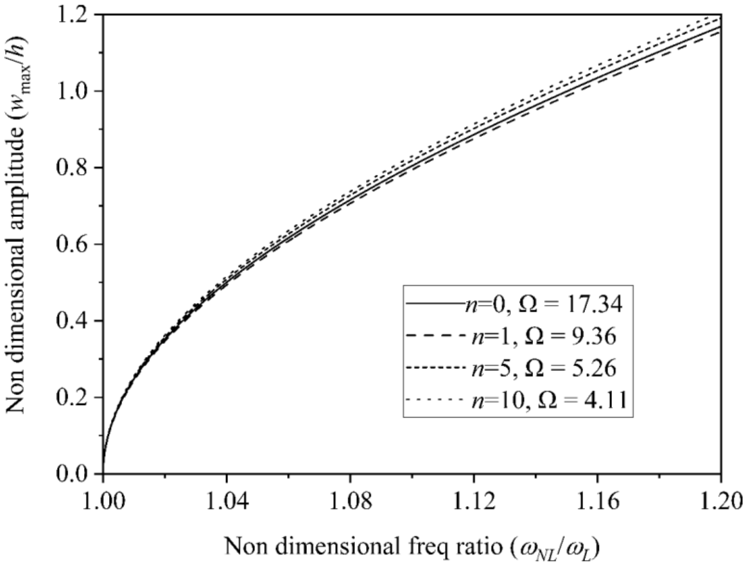

Fig. 6.1 Effect of different power law indices on non-linear free vibration response of square FG microplate(a/h=10; h/l=2; ζ_1=4% & ζ_2=2% ; MSGT; SSSS; $f_0 = 0$)

6.3.1.2 *Effect of change in h/l ratios*

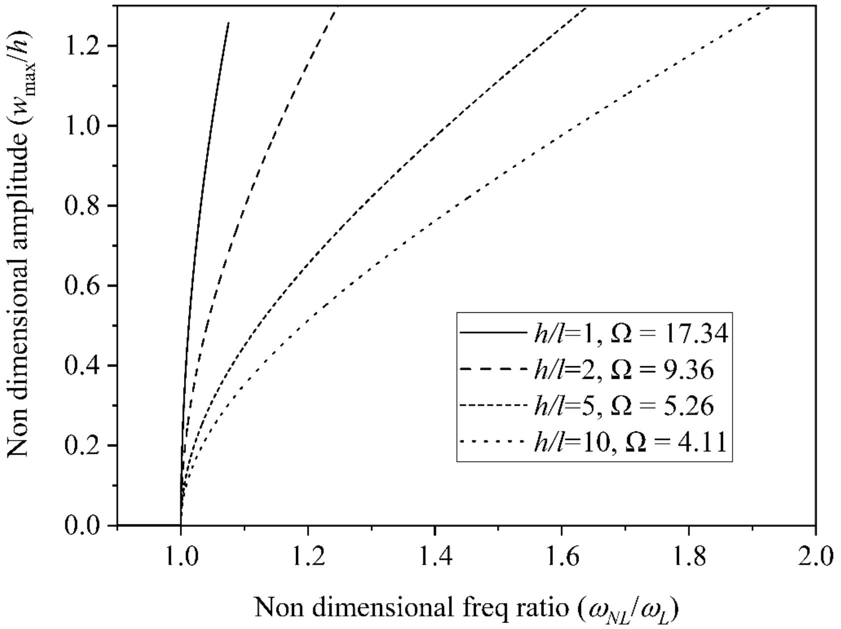

Fig. 6.2 Effect of h/l ratio on non-linear free vibration response of square FG microplate (n=1; a/h=10; h=17.6μm; ζ_1=4% & ζ_2=2% ; MSGT; SSSS; $f_0 = 0$)

Fig. 6.2 represents the free nonlinear free vibration response of FG microplates with different h/l ratios. The influence of h/l is studied by keeping the thickness of the plate constant to ignore the effects due to shear deformation. The natural frequency is higher for a smaller h/l ratio due to the hardening of stiffness owing to the enhancement of small-scale effects. The free vibration frequency decreases as the small-scale effect disappears on increasing the h/l ratio. The nonlinear hardening behaviour due to geometric nonlinearities decreases in smaller h/l ratio microplates as the structural model becomes stiffer, reducing the impact of geometric nonlinearities. Due to this reason, the dimensionless resonance frequency ratio at higher amplitudes is lesser for smaller h/l ratio microplates.

6.3.2 *Nonlinear Forced Vibration Analysis*

The frequency-amplitude curve (Fig. 6.3) comprises of two bifurcation points, ‘A’, and ‘B’ as shown in Fig. 6.3. ‘A’ and ‘B’ both denote saddle-node bifurcation points. Three frequency zones can be defined on the basis of these saddle nodes. The zones ‘I’ and ‘III’ consists of one stable curve, and zone ‘II’ consists of two stable and one unstable curve. Due to the existence of a single stable curve, the steady state amplitude achieved by a plate under transverse harmonic loading with forcing frequency in zones I and III is independent of the initial perturbation.

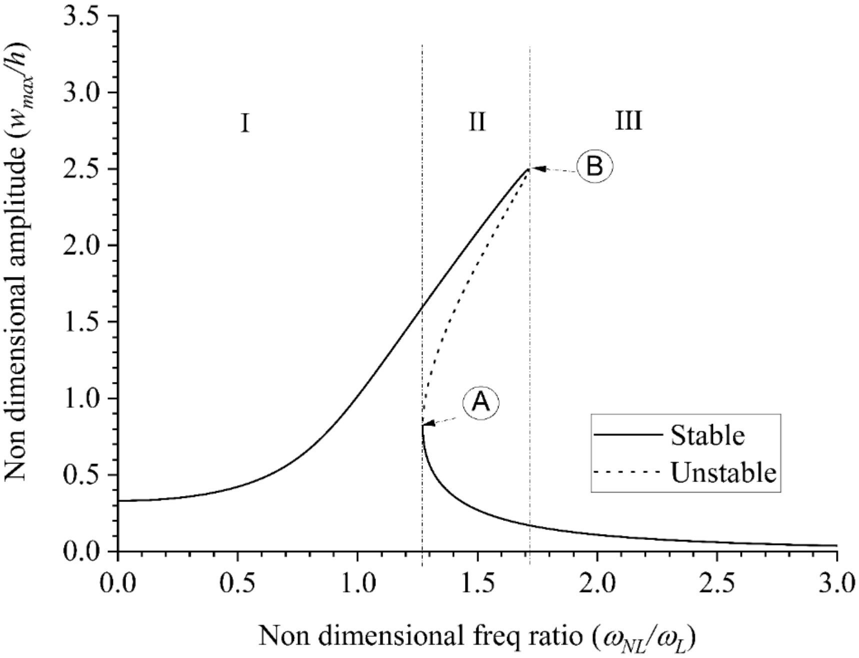

Fig. 6.3 Non-linear forced vibration response of a damped FG microplate(n=1; h/l=2; a/h=20; ζ_1=4% & ζ_2=2% ; MSGT; SSSS; $f_0 = 2\mathrm{x}10^7$ N/m^2; loading case 1; a_l=0.5a; b_l = 0.5b)

6.3.2.1 *Effect of change in length to thickness ratios (a/h)*

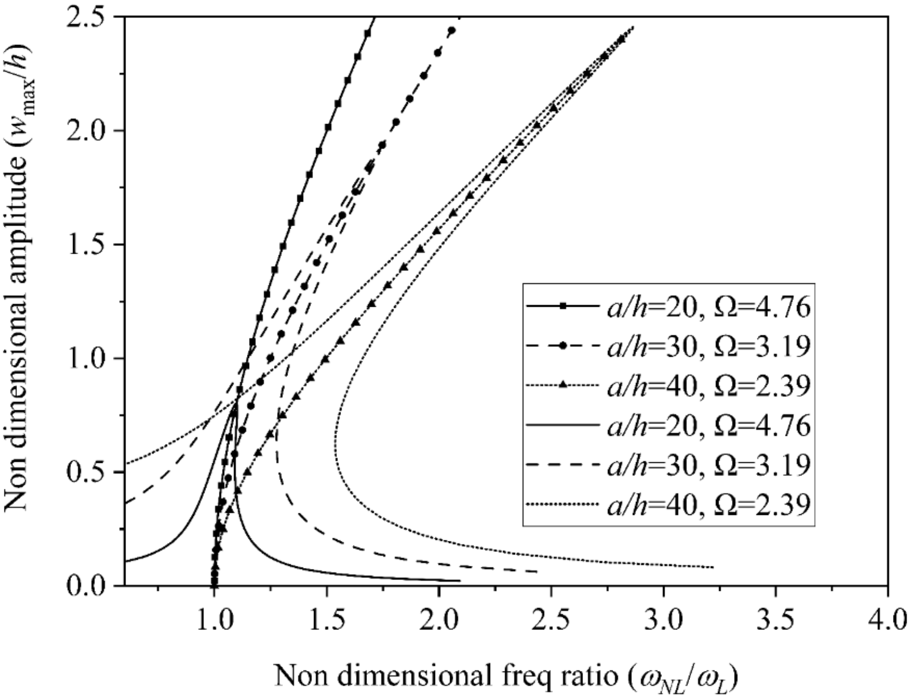

Fig. 6.4 Effect of length to thickness ratio (a/h) on non-linear free and forced vibration responses of square FG microplate(n=1; a=176μm; h/l=2; ζ_1=4% & ζ_2=2% ; MSGT; SSSS; $f_0 = 1\mathrm{x}10^7$ N/m^2; loading case 4; a_l=0.5a; b_l = 0.5b)

The effect of variation in thickness of the microplate on the nonlinear free and nonlinear forced vibration ($f_0 = 1\mathrm{x}10^7$ N/m^2) responses are presented in Fig. 6.4 for a/h =20, 30, and 40. The edge length 'a' is kept constant at 176 μm, and the thickness of the plate is changed. The value of l is also changed accordingly to maintain an h/l ratio of 2. The nondimensional amplitude (w_{max}/h) is calculated using h of the microplate with a/h=20, i.e. 8.8μm. It can be seen from Fig. 6.4 that the natural frequency of the plate decreases by reducing the thickness of the plate. This is because shear deformation becomes more prominent for the thicker plate. The stiffest plate's (a/h =20) peak amplitude is likewise its lowest, while the least stiff (a/h =40) plate's is the highest. The nonlinear hardening characteristic is found to be less for thicker plates as the impact of geometric nonlinearity gets suppressed due to the addition of the shear deformation effect.

6.3.2.2 *Effect of change in modal damping ratios*

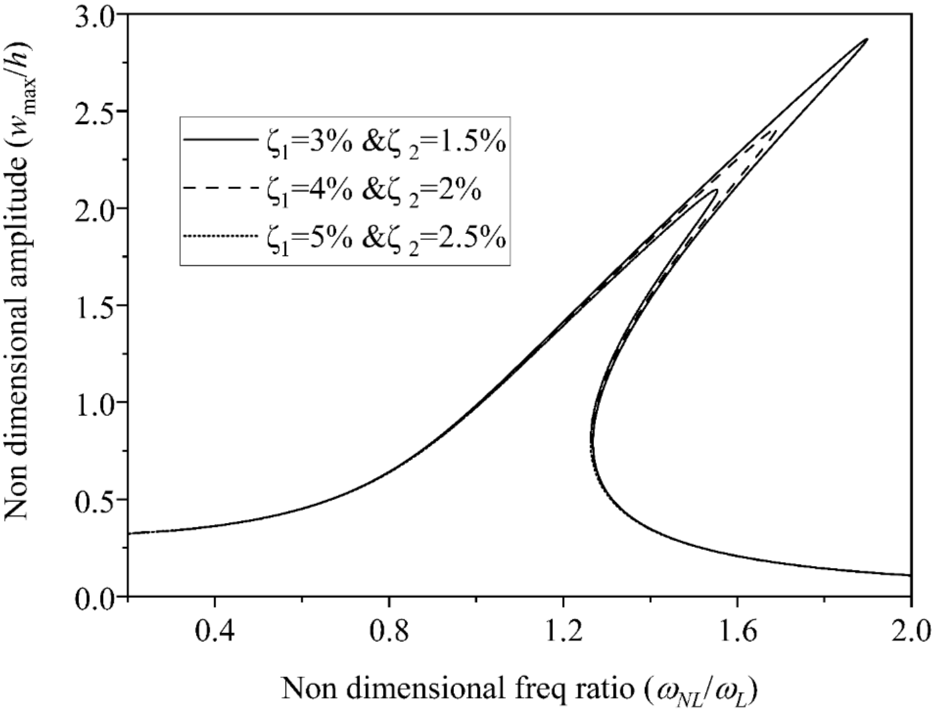

Fig. 6.5 Impact of varying modal damping ratios on non-linear free and forced vibration responses of square FG microplate (n=1; a/h=10; h/l=2; MSGT; SSSS; f_0=5x10^8 N/m^2; loading case 2; a_l=0.5a; b_l = 0.5b)

Fig. 6.5 depicts the influence of varying the values of ζ_1 and ζ_2 on the non-linear forced vibration response of an FG microplate. It is found that the increase in the modal damping ratio considerably lowers the peak amplitude of the forced vibration response. The width of zone II decreases by increasing the modal damping ratios. The hardening characteristics of the curve are unaffected by the change in damping factors.

6.3.2.3 *Effect of different boundary conditions*

In actual use, different support conditions are applied to the microplates. Fig. 6.6 shows the non-linear free and forced vibration responses of some of the typical boundary conditions, namely, CCCC (all edges clamped), SCSC (one set of opposite edges simply supported and other set clamped), and, SSSS (all edges simply-supported). The CCCC microplate has the maximum natural frequency, and SSSS has the least due to the higher stiffness of the plate in the case of clamped supports. Following similar reasons, the maximum amplitude of the CCCC microplate is minimum, and the SSSS microplate is maximum. Since clamped boundary conditions promote a hardening response, the hardening behaviour of the nonlinear vibration response is also maximum for the CCCC plate and least for the SSSS microplate.

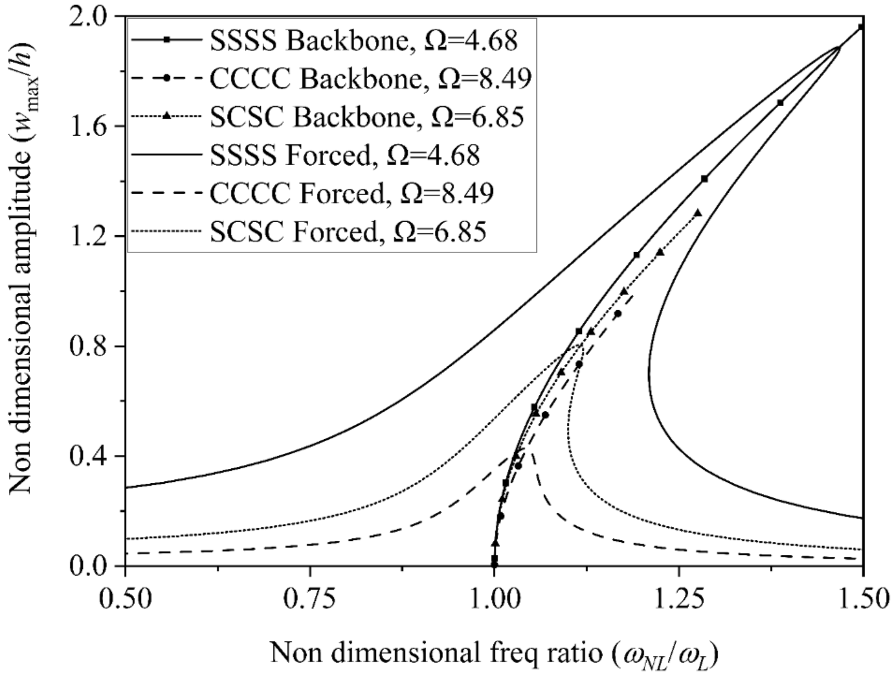

Fig. 6.6 Effect of different boundary conditions on non-linear free and forced vibration response of square FG microplate (n=1; a/h=10; h/l=2; MSGT; ζ_1=4% & ζ_2=2%; f_0=2x10^8 N/m^2; loading case 1; a_l=0.5a; b_l = 0.5b)

6.3.2.4 *Effect of different patch loading positions*

As discussed in section 3.5.2, four different positions of transverse patch loadings (f_0 = 5x10^8 N/m^2) have been considered on an SCSC microplate in this study. The effect of the four loading cases on the forced nonlinear vibration response of the FG microplate is shown in Fig. 6.7. The peak amplitude decreases for the four loading cases in the order Case 1 > Case 3 > Case 2 > Case 4. This shows that the impact of loading decreases as it moves away from the centre of the plate. The peak amplitude for Case 3 > Case 2 shows that loading away from the simply supported edges has a higher impact than loading away from the clamped edge. Following similar reasons, the excitation frequency ratio at which resonance occurs is also minimum for loading at the centre and maximum for loading at corners. The excitation frequency ratios for resonance are almost equal for Case 2 and Case 3 loadings.

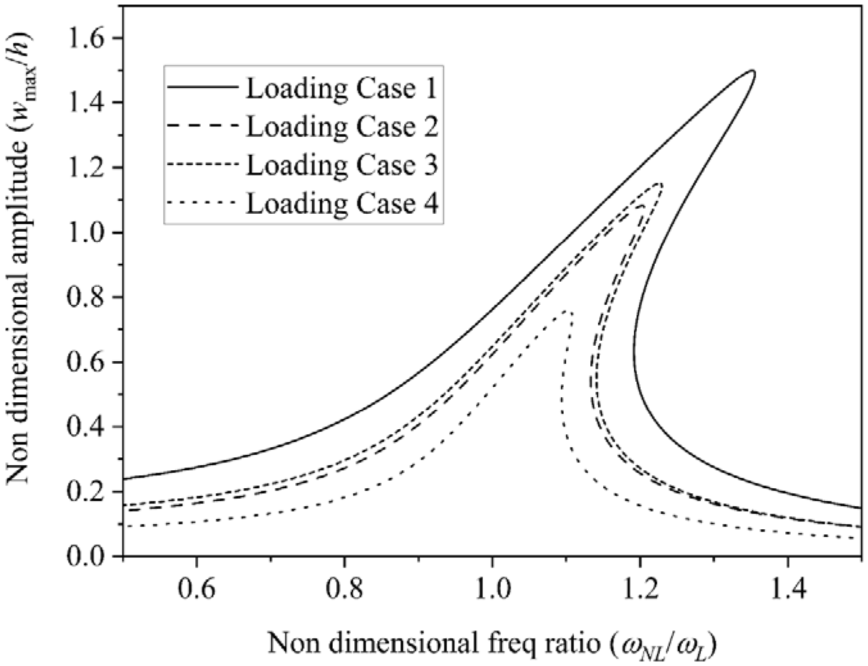

Fig. 6.7 Effect of different patch loading positions on non-linear free and forced vibration response of square FG microplate (n=1; a/h=10; h/l=2; MSGT; SCSC; ζ_1=4% & ζ_2=2%; f_0 =5x10^8 N/m^2; a_l=0.5a; b_l = 0.5b)

6.3.2.5 *Effect of different loading concentrations*

The influence of different concentrations of patch loadings on the nonlinear vibration behavior is portrayed in Fig. 6.8. Different loading concentrations are applied at loading position 1 (Fig. 3.7), and their impact is assessed. It can be seen that the impact of loading maximizes with the increase in the concentration of the applied loading. The peak amplitude increases with the increase in the concentration of loading and is maximum for a_l=0.1a, b_l = 0.1b. The resonance frequency ratio also decreases with the increase in loading concentration owing to a decrease in stiffness due to the increased loading concentration.

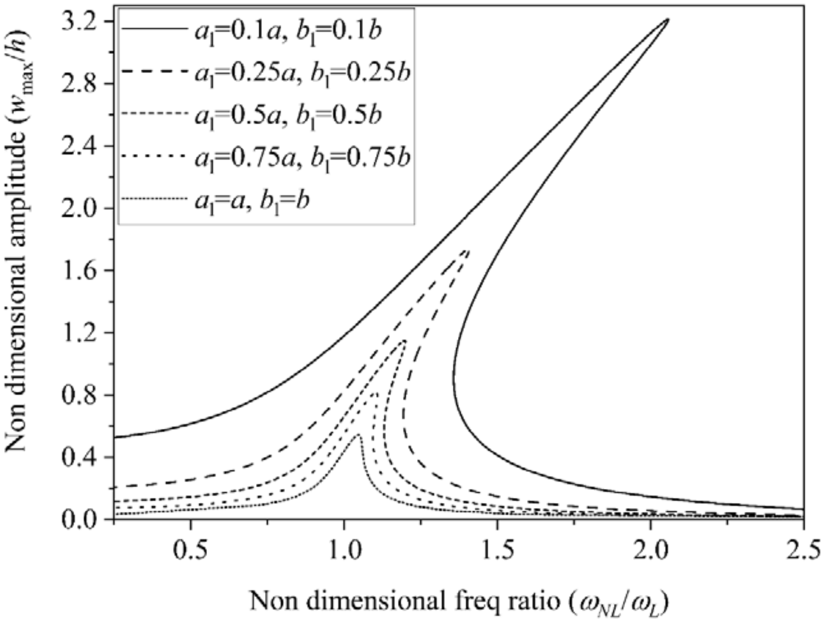

Fig. 6.8 Effect of different patch loading concentrations on non-linear free and forced vibration response of square FG microplate (n=1; a/h=10; h/l=2; SSSS; MSGT; ζ_1=4% & ζ_2=2%; f_0=1x10^8 N/m^2; loading case 1)

6.4 Nonlinear Dynamic Analyses of PMREF

This section does a parametric analysis of the nonlinear vibrations and nonlinear dynamic responses of a porous metal foam microplate supported by a Winkler-Pasternak elastic foundation and exposed to harmonic transverse patch loads.

The parameters of the PMREF used in this study are:

E = 200 GPa, μ = 0.33, and ρ = 7850 kg/m^3, a/h=10, a=b, Theory: MSGT, $l_0 = l_1 = l_2 = l$ = 15 µm, h/l=2, e_0=0.2, Symmetric Porosity, $\overline{K_w} = 10$, $\overline{K_p} = 10$, Loading: Centre (a_l,b_l = 0.5(a,b)), modal damping ratios: ζ_1=4% & ζ_2=2%. Support conditions: All edges simply-supported (SSSS). All these parameters are used throughout this study unless explicitly mentioned.

The nonlinear vibration of the PMREF is illustrated using the nondimensional amplitude (w/h) versus nondimensional frequency ratio, (ω_{NL}/ω_L). The non-dimensional frequency ratio is the ratio between the resonant frequency (ω_{NL}) and the linear fundamental natural frequency (ω_L) of the PMERF. The resonant frequency equals the forcing frequency for harmonic transverse loading when nonlinear stiffness is considered. Utilizing the arc-length approach in IHB yields both unstable and stable frequency-amplitude curves. The curve features two saddle-node bifurcation points, labeled I and II. At point III on the curve, the forcing frequency (ω_{NL}) is equal to the natural frequency (ω_L) for the PMREF, ignoring nonlinearities. Based on these three locations, as illustrated in Fig. 6.9, the plot can be segregated into four regions of forcing frequency. Regions 'A', ‘B’, and 'D' each have one stable curve, but region 'C' contains two stable curves and one unstable curve. Due to the existence of a single stable solution, the steady-state amplitude obtained by a plate under parametric excitation with forcing frequency in regions "A," "B," and "D" is independent of the parametric excitation's initial amplitude. However, due to the existence of two stable solutions, the steady-state amplitude of a plate subjected to a driving frequency in region 'C' depends on the initial amplitude. Region 'B' is the most critical in terms of response stability since it results in a large steady-state amplitude for any initial displacement amplitude. Region 'C' likewise exhibits a high steady-state amplitude, but only for specific high initial displacement amplitude values. The most stable regions of forcing frequency are 'A' and 'D', where the steady-state amplitude decays to nominal values for any initial amplitude.

In the following subsections, the frequency amplitude plot and the time history response plot are utilized to examine the nonlinear dynamic behaviour of the PMREF subjected to transverse patch loading. In order to compare the influence of geometric nonlinearities, the curve of free vibration is also depicted in several frequency amplitude plots. The effect of various parameters, including porosity coefficient, type of porosity, Winkler-Pasternak elastic foundation parameters, size-dependent theory, loading concentration, loading profile, and modal damping ratios, is explored. With nonlinear vibration (frequency-amplitude curve) and nonlinear dynamic response(time-history response plots), the effect of these factors on geometric nonlinearity, the width of regions of forcing frequency, and total stiffness is investigated. From the time-history response plots, the effect of the initial amplitude of perturbation in different regions of forcing frequency is also examined.

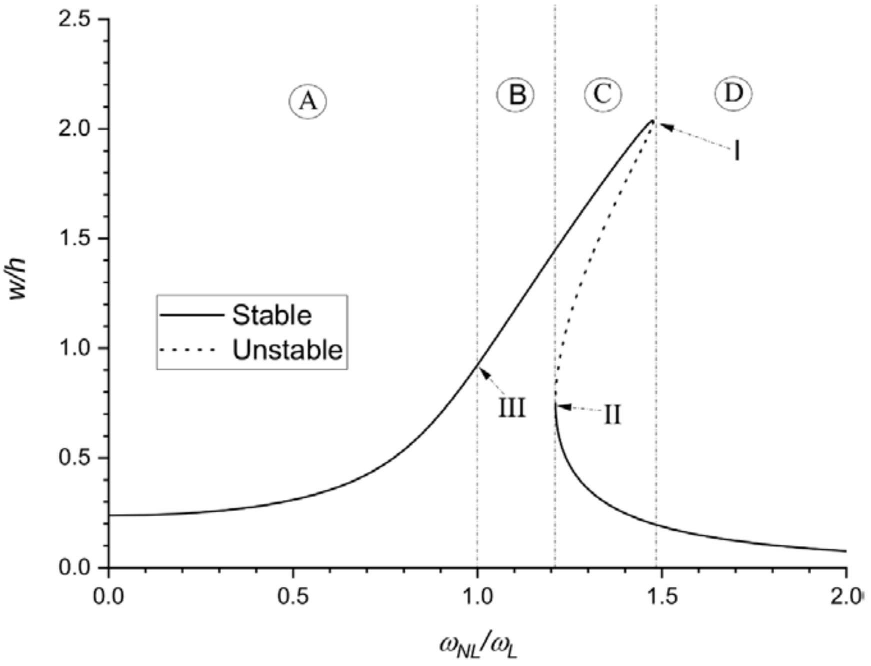

Fig. 6.9 Non-linear vibration response using frequency-amplitude curve at β=0.6 for a damped PMREF (e_0=0.2; symmetric porosity; $\overline{K_w} = 10$, $\overline{K_p} = 10$; a/h=10; h/l=2; ζ_1=4% & ζ_2=2% ; MSGT; SSSS; f_0= 2x10^8 N/m^2; Centre {(a_l,b_l)= 0.5(a,b)})

6.4.1 *Effect of Porosity coefficient*

Fig. 6.10 depicts the influence of a change in the porosity coefficient on the nonlinear dynamic behaviour of the PMREF. The non-dimensional frequency ratio (ω_{NL}/ω_L) and dimensionless time ratio (t/T) is made non-dimensional by using 'ω_L' and 'T' of e_0=0.6. It is observed from Fig. 6.10(a) that on increasing the porosity coefficient, the origin of region 'B' shifts towards a lower excitation frequency ratio, illustrating a drop in linear stiffness for more porous plates. Increasing the porosity coefficient also increases the width of the forcing frequency regions 'B' and 'C'. In less porous PMREF, the effect of geometric nonlinearities on nonlinear stiffness is more pronounced. This is seen by the rising disparity in steady-state amplitudes between more porous and less porous plates when the forcing frequency is increased. The forcing frequency for each of the three curves in the time history response lies in the region 'A' with no initial perturbation. It is noted that the amplitude of the time history plot grows for all three curves to attain their steady-state amplitude (Fig. 6.10(b)). The amplitude at steady state is greatest for the most porous plate and smallest for the least porous plate.

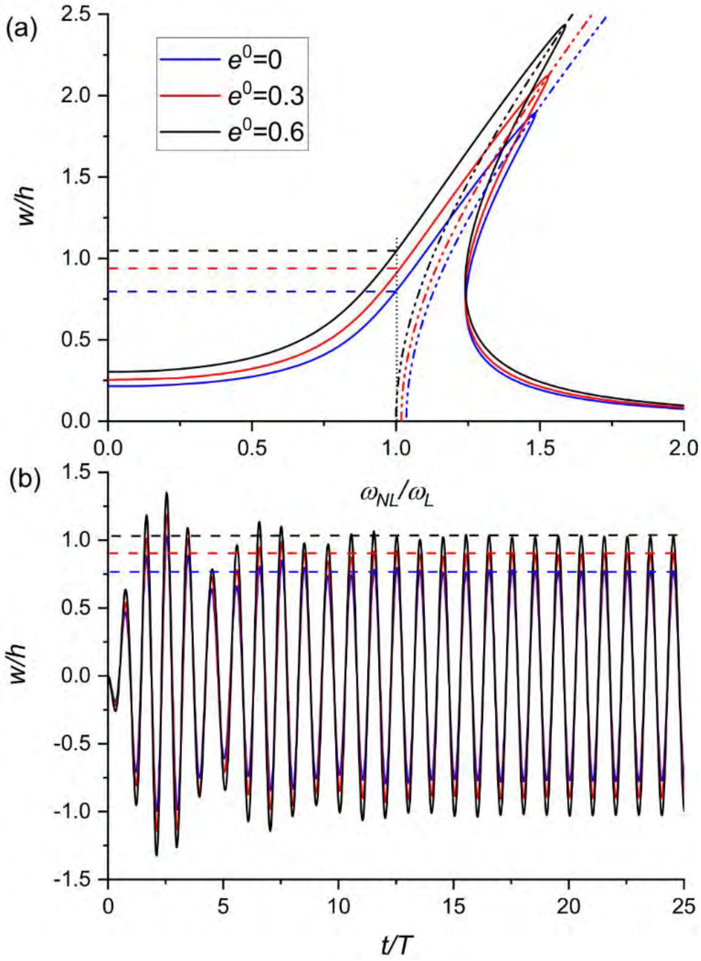

Fig. 6.10 Effect of porosity coefficient on (a)nonlinear vibration response, and (b)nonlinear dynamic response ((ω_{NL}/ω_L) =2 and w_0=0), for a damped PMREF (Symmetric Porosity; $\overline{K_w} = 10, \overline{K_p} = 10$; a/h=10; h/l=2; ζ_1=4% & ζ_2=2%; MSGT; SSSS; f_0 = 2x10^8 N/m^2; Centre {(a_l,b_l)= 0.5(a,b)}).

6.4.2 *Effect of Type of Porosity*

Fig. 6.11 depicts the effect of the kind of porosity distribution for various porosity coefficients on the nonlinear dynamic behaviour of the PMREF. The non-dimensional frequency ratio, (ω_{NL}/ω_L) and dimensionless time ratio (*t/T*) are assumed to be equal to the fundamental natural frequency and fundamental time period of PMREF with uniform porosity distribution and e_0=0.6. Fig. 6.11(a) demonstrates that as the distribution of porosity changes from symmetric to uniform, region 'B' shifts towards a lower excitation frequency ratio for a given porosity coefficient. Consequently, suggesting a decrease in linear stiffness. The difference in stiffness between uniform and symmetric porosity distribution is likewise more pronounced at higher porosity coefficient values. Following similar tendencies, the width of regions 'B' and 'C' is also observed to be greater for homogeneous porosity distribution. However, no substantial differences in hardening behaviour are seen, showing that nonlinear stiffness is unaffected. For each curve and initial amplitude near the top stability curve of PMREFs with $e_0=0.2$, the forcing frequency being in the region 'C', a time history plot is plotted. Consequently, it is seen that the steady-state amplitude is equivalent to the upper stable curves for PMREFs with $e_0=0.2$. Nevertheless, because the initial amplitude is not close to the steady-state amplitudes of PMREFs with $e_0=0.6$, the steady-state amplitude of the more stable, lower-stable curve is obtained.

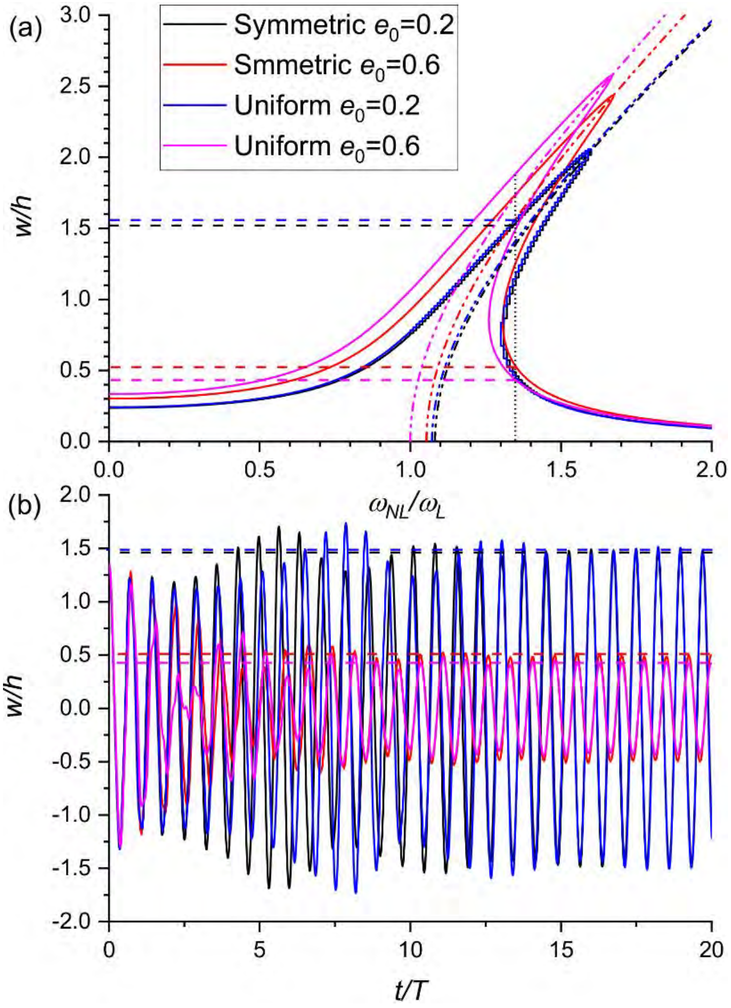

Fig. 6.11 Effect of type of porosity on (a)nonlinear vibration response, and (b)nonlinear dynamic response ((ω_{NL}/ω_L) =1.35 and w_0=1.35h), for a damped PMREF ($\overline{K_w} = 10, \overline{K_p} = 10$; a/h=10; h/l=2; ζ_1=4% & ζ_2=2%; MSGT; SSSS; f_0= 2x10^8 N/m^2; Centre {(a_l,b_l)= 0.5(a,b)}).

6.4.3 *Effect of Elastic Foundation Parameters*

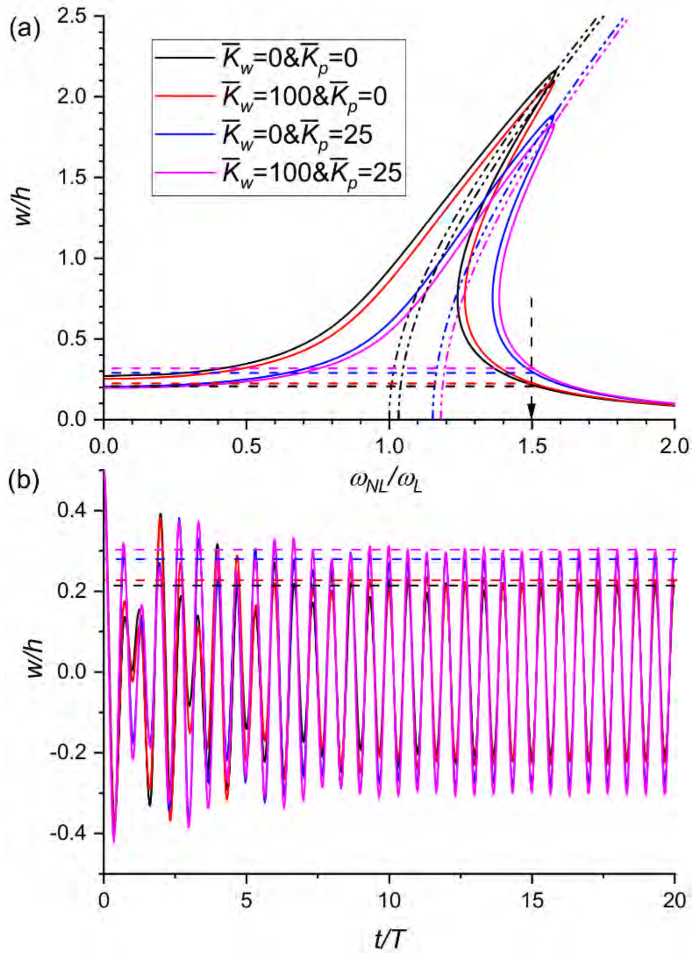

Fig. 6.12 Effect of Winkler-Pasternak elastic foundation parameters on (a)nonlinear vibration response, and (b)nonlinear dynamic response ((ω_{NL}/ω_L) =1.5 and w_0=0.5h), for a damped PMREF (e_0=0.2; symmetric porosity; a/h=10; h/l=2; ζ_1=4% & ζ_2=2%; MSGT; SSSS; f_0= 2x10^8 N/m^2; Centre {(a_l,b_l)= 0.5(a,b)})

Fig. 6.12 depicts the effect of Winkler-Pasternak elastic foundation parameters on the nonlinear dynamic behaviour of the PMREF under harmonic transverse loading. The ‘ω_L’ *for the* non-dimensional frequency ratio (ω_{NL}/ω_L) and *‘T’* for dimensionless time ratio (*t/T*) are assumed to be equal to the fundamental natural frequency and fundamental time period of PMREF with $\overline{K_w} = 0$, $\overline{K_p} = 0$. The origin of region 'B' shifts toward a higher excitation frequency ratio, and the width of regions 'B' and 'C' decreases as the corresponding elastic foundation parameters $\overline{K_w}$and $\overline{K_p}$ are increased (Fig. 6.12(a)). In contrast to the Pasternak parameter, the effect of the Winkler parameter on the enhancement of stiffness is observed to be minimal. As the forcing frequency rises, the difference between steady-state amplitudes of free vibration curves decreases, indicating that the hardening nature of the frequency amplitude curve is diminished for higher values of elastic foundation parameters. This suggests that the effect of geometric nonlinearity diminishes as the significance of the elastic foundation parameters increases. The time history response (Fig. 6.12(b)) is presented for all models with forcing frequency in region 'C' and an initial amplitude of $0.5h$. It can be noted that the response for all models decays until it reaches the steady state amplitude depicted by the lower stable curve. The steady-state amplitude for PMREFs with greater elastic foundation parameters and increased stiffness is attained sooner than for PMREFs with weaker values.

6.4.4 *Effect of Size-Dependent Theory*

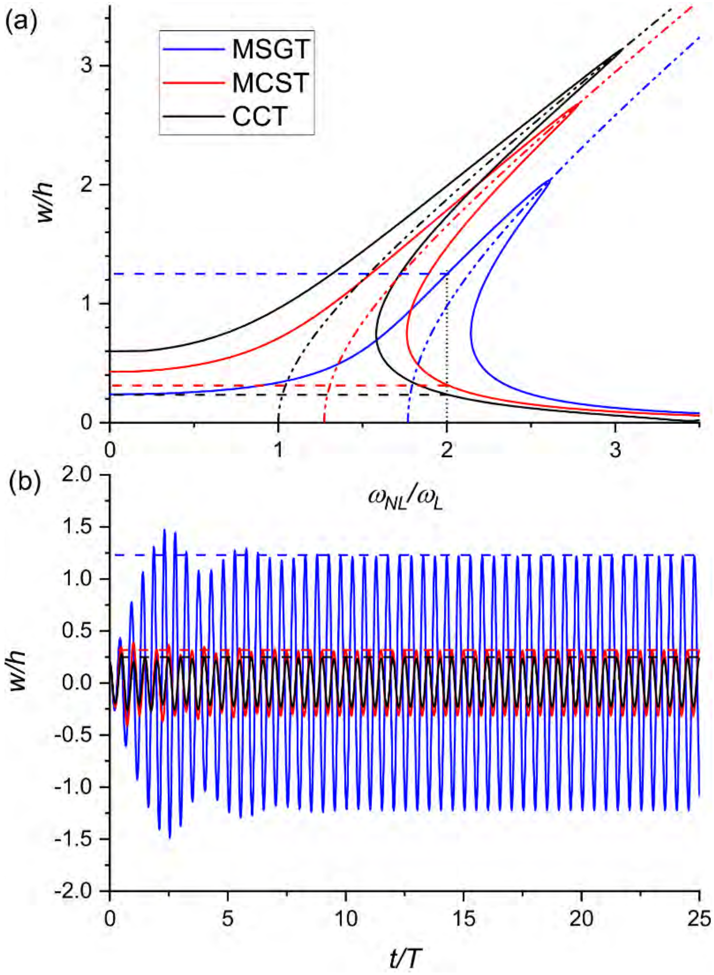

Fig. 6.13 Effect of different small-scale theories on (a)nonlinear vibration response, and (b)nonlinear dynamic response (ω_{NL}/ω_L =2 and w_0=0.2h), for a damped PMREF (e_0=0.2; symmetric porosity; $\overline{K_w} = 10$, $\overline{K_p} = 10$; a/h=10; h/l=2; ζ_1=4% & ζ_2=2%; SSSS; f_0 = 2x10^8 N/m^2; Centre {(a_l,b_l)= 0.5(a,b)})

Fig. 6.13(a) and Fig. 6.13(b) depict the nonlinear vibration and dynamic responses of PMREF with small-scale effects modelled using MSGT, MCST, and CCT, respectively. The *'ω_L' for the* non-dimensional frequency ratio (ω_{NL}/ω_L) and *'T'* for dimensionless time ratio (*t/T*) are taken equal to the fundamental natural frequency and fundamental time period of PMREF modelled using CCT. On including the effect of rotation gradients in the MCST model, the origin of region 'B' shifts toward a higher excitation frequency ratio. MSGT model indicates more contribution in stiffness due to dilatant and deviatoric stretch gradients. Consequently, the magnitude of the shift is bigger. Due to the inclusion of linear stiffness from the hardening of strain gradients in the MSGT and MCST models, the width of areas 'B' and 'C' is also minimal for MSGT and maximal for CCT. However, the hardening aspect of the free vibration curve is diminished in the MCST and MSGT models. Due to the availability of stiffer strain gradient models of MCST and MSGT, the effect of geometric nonlinearities is diminished. For the MSGT model, the forcing frequency utilized to generate the time history response plot lies in region 'B,' whereas for the MCST and CCT models, it lies in the region 'C'. Initial displacement amplitude is considered close to the upper stable curves of the CCT and MCST models. Fig. 6.13(b) demonstrates that while the initial amplitude is not close to the upper stable curve, the response decays to the steady state amplitude of the lower stable curve for MCST and CCT-modelled PMREFs. However, in the case of MSGT-modelled PMREF, despite the initial amplitude being distinct from the upper stable curve, the response develops to achieve the steady-state amplitude derived from the upper stable curve. This is because the excitation frequency for this model lies in region B.

6.4.5 *Load Concentration*

Fig. 6.14 demonstrates the effect of transverse patch load concentration, *'a_l'* and *'b_l'* on the nonlinear dynamic behaviour of the PMREF. The loading concentration has no influence on the PMREF's linear and nonlinear stiffness. Loading concentration has no effect on the origin of area 'B' and the hardening nature of the curve. However, it is noticed that the steady-state amplitude of the upper stable curve, as well as the width of regions 'B' and 'C', increases as the load concentration rises. The excitation frequency evaluated for the time-history response (Fig. 6.14(b)) falls within the region 'A' for all loading concentrations, and the initial perturbation amplitude was assumed to be 'h'. Thus, the response for all load concentrations decays to reach the steady-state amplitude of the single stable curve in the region 'A', where the steady-state amplitude for higher load concentrations is greater. In the case of transverse patch loading, unlike in-plane loading, the response does not die out completely due to the forcing frequencies in regions 'A' and 'D'. Since the linear stiffness is unaltered in all circumstances, the decline occurs simultaneously for all concentrations.

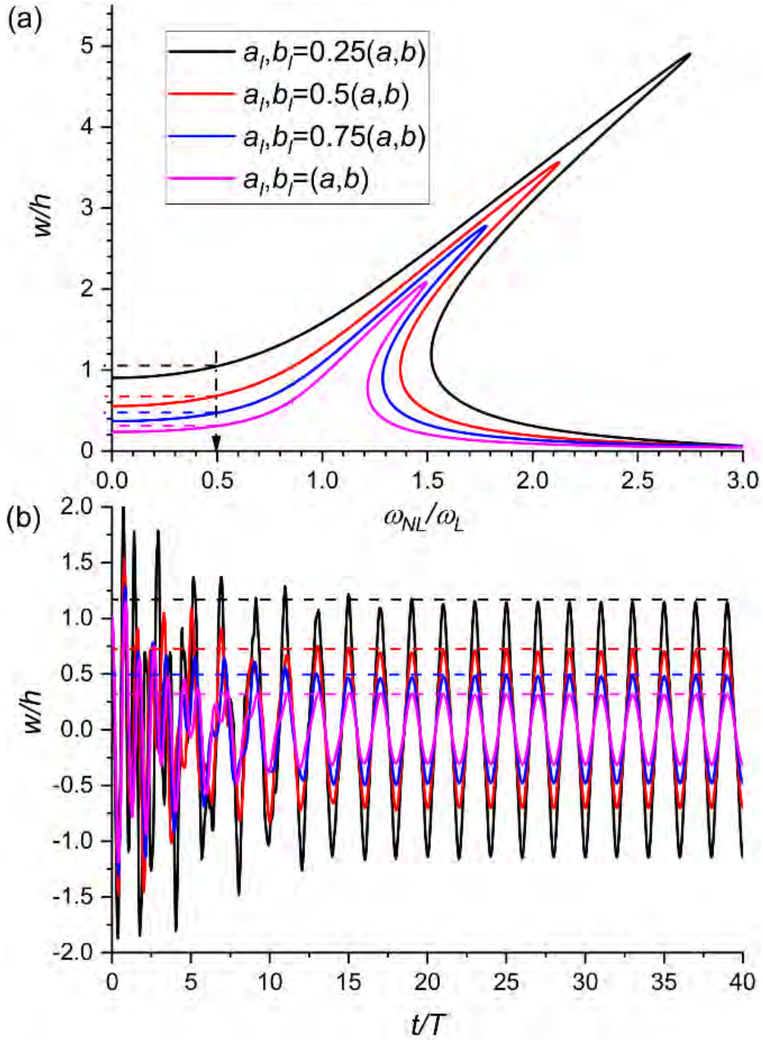

Fig. 6.14 Effect of Concentration of load on (a)nonlinear vibration response, and (b)nonlinear dynamic response (ω_{NL}/ω_L=0.5 and w_0=h), for a damped PMREF (e_0=0.2; symmetric porosity; $\overline{K_w} = 10$, $\overline{K_p} = 10$; a/h=10; h/l=2; ζ_1=4% & ζ_2=2%; MSGT; SSSS; f_0= 5x10^8 N/m^2; Centre)

6.4.6 *Effect of Load Position*

The influence of the loading profile of the in-plane harmonic load on the nonlinear dynamic behaviour of the PMREF is depicted in Fig. 6.15. The loading profile has no effect on the linear stiffness and nonlinear stiffness of the PMREF. Thus, the origin of region ‘B’ and the hardening nature of the curve remains unaffected by the loading profile. The width of region ‘B’ and region ‘C’ is maximum for the centre loading position and minimum for the corner loading position. This implies that the impact of loading decreases as the centroid of the load moves further away from the centre of the plate for the first mode with central deflection. The time history response is plotted for excitation frequency in the region ‘D’ for all the loading positions with no initial amplitude of perturbation (Fig. 6.15(b)). It is observed that even for forcing frequency far away from the fundamental natural frequency and with no initial perturbation, the response does not completely decay to zero. The steady-state amplitude, though very small, is maximum for the centre loading position and minimum for the corner loading position.

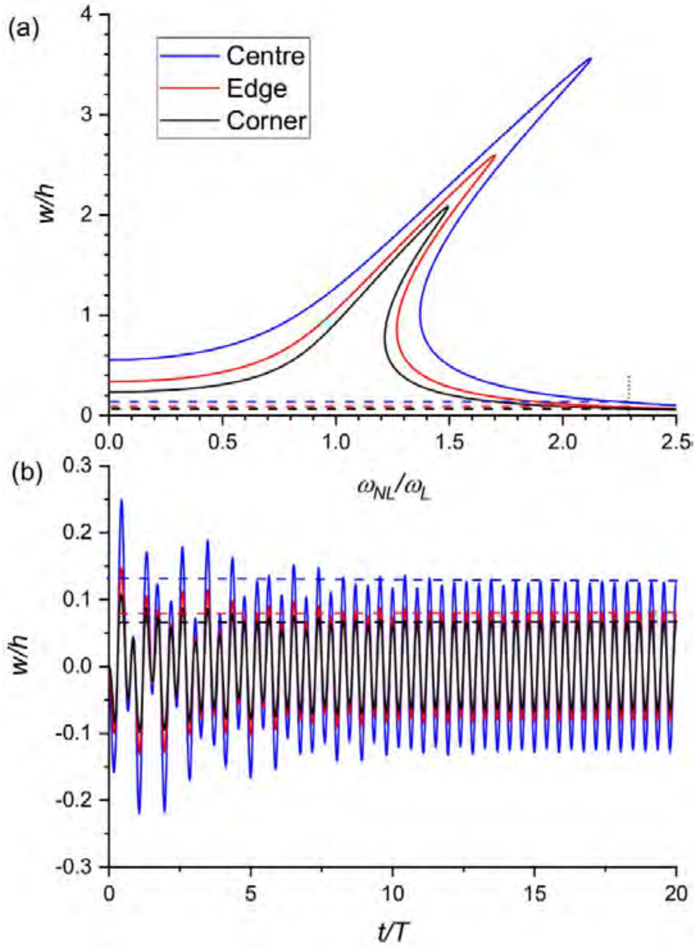

Fig. 6.15 Impact of loading position on (a)nonlinear vibration response, and (b)nonlinear dynamic response (ω_{NL}/ω_L=2.3 and w_0=0), for a damped PMREF (e_0=0.2; symmetric porosity; $\overline{K_w} = 10$, $\overline{K_p} = 10$; a/h=10; h/l=2; ζ_1=4% & ζ_2=2%; MSGT; SSSS; f_0= 5x10^8 N/m^2; {(a_l,b_l)= 0.5(a,b)})

6.4.7 *Effect of Damping*

Fig. 6.16 depicts the effect of modal damping ratios on the nonlinear dynamic behaviour of the PMREF. Fig. 6.16(a) demonstrates that an increase in modal damping ratios significantly reduces the width of region 'C'. The width of region 'B' is minimally altered. The forcing frequency for the time history response falls within region 'D' for the system with ζ_1=6% & ζ_2=3% and region 'C' for the remaining two systems. Initial amplitude is determined in close proximity to the upper stable curves. For ζ_1=4% & ζ_2=2%, and ζ_1=5% & ζ_2=2.5%, the time history response reaches the steady-state response. It decays fully for the ζ_1=6% & ζ_2=3% systems as it lies within the region 'D'. It is also noticed that systems with a greater modal damping ratio reach the steady state response earlier.

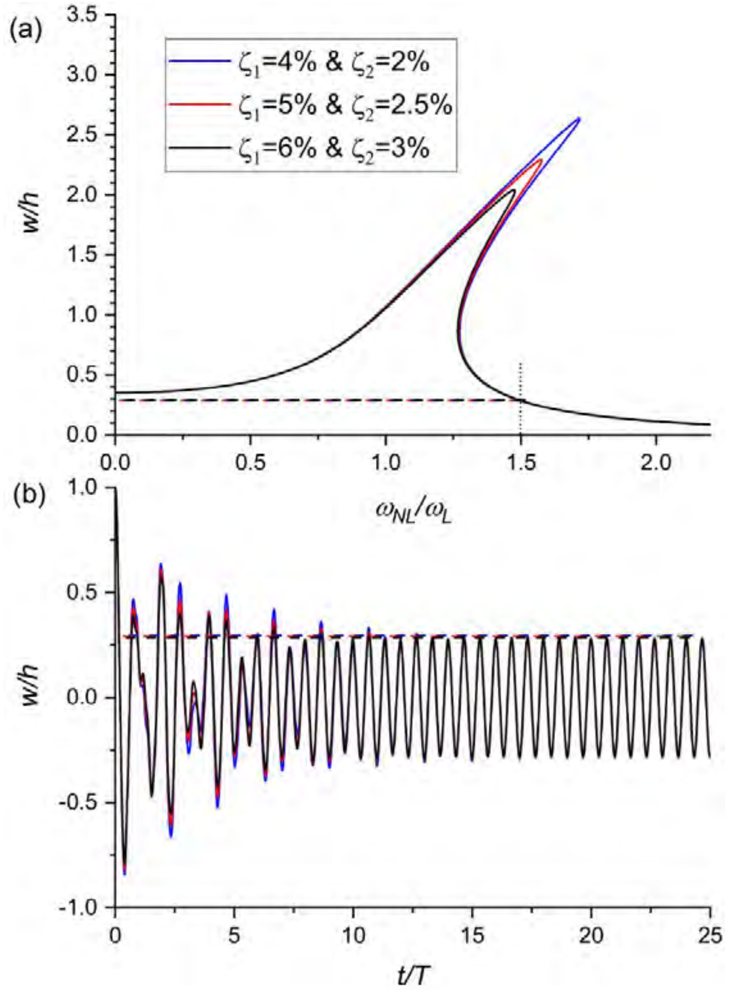

Fig. 6.16 Effect of modal damping ratios on (a)nonlinear vibration response, and (b)nonlinear dynamic response (ω_{NL}/ω_L=1.5 and w_0=*h*), for a damped PMREF (e_0=0.2; symmetric porosity; $\overline{K_w} = 10$, $\overline{K_p} = 10$; *a*/*h*=10; *h*/*l*=2; MSGT; SSSS; f_0= 3x10^8 N/m^2; Centre {(a_l,b_l)= 0.5(*a*,*b*)})

7

Thermal Buckling and Post-buckling analyses of Microplate: Results and Discussion

7.1 Introduction

In this chapter, a parametric study on the buckling and post-buckling analyses of porous microplates resting on elastic foundation (PMREF) subjected to localized heating (Fig. 3.3(c)) is presented. The developed semi-analytical expressions for pre-buckling stresses are validated by comparing with ABAQUS (FEM) results. The overall methodology is also validated by comparing its simpler version with previously published studies. The parametric response of mode shape at buckling load for different aspect ratios and boundary conditions of the microplates subjected to in-plane mechanical and thermal loads is performed. The properties of the PMREF plate considered in this study are given in column no. 1 of Table 7.1. These properties are considered throughout the study unless explicitly stated.

Table 7.1 Properties of the plates used in this chapter

Parameters	**Property**	**Sym.**	**Column No.**			
			1	**2**	**3**	**4**
			PMREF Plate	**(Fig. 3 and Table 2.)**	**(Fig.6)**	**(Table 3.)**
Material Properties	Young's Modulus	E	200 GPa	200 GPa	380 GPa	200 GPa
	Poisson's Ratio	v	0.33	0.33	0.33	0.33
	Coefficient of Thermal Expansion	α_T	2×10^{-6} 1/K	2×10^{-6} 1/K	7.4×10^{-6} 1/K	–
Porosity Parameters	Distribution		Uniform	None	None	Varying
	Porosity Coefficient	e_o	0.3	0	0	0.2
Elastic Foundation Parameters	Winkler	$\overline{K}_w$	25	0	0	0
	Pasternak	$\overline{K}_p$	50	0	0	0
Length Scale Parameters	$l_0 = l_1 = l_2 = l$		15μm	0	0	15μm
Dimensions	Thickness	h	$3l$	$a/30$	$a/100$	varying
	Edge	$a=b$	$30h$	1m	1m	$10h$

Note: For isotropic plate, $\alpha_T = \alpha_{xx}^T = \alpha_{yy}^T$, & $\alpha_{xy}^T = 0$.

The effect of different parameters such as porosity distributions, porosity coefficients, elastic foundation parameters, size-dependent theories, *a/h* ratio of microplate, *h/l* ratio of microplate, Winkler and Pasternak elastic foundation parameters, aspect ratio (*a/b*), loading concentration $\left(\frac{a_0}{a} = \frac{b_0}{b}\right)$, and boundary conditions on the buckling and post-buckling response of the PMREF are studied. In this study, $\frac{b_0}{b}$ ratio is considered equal to $\frac{a_0}{a}$ ratio. Also, the amount of heating is kept same for all cases of loading concentrations.

7.2 Validation and Convergence study

The semi-analytical technique used to compute the in-plane pre-buckling stresses due to the localized thermal load is tested by assessing these stresses and the buckling temperature difference (ΔT_{cr}) due to these stresses with those obtained from finite element (FE) based ABAQUS software (numerical method) results. The size-dependent effects cannot be considered in ABAQUS, thus a macro plate is considered. The properties of the plate are given in column no. 2 of Table 7.1. The normalized stresses $\left(\bar{\sigma}_{ij} = \sigma_{ij}.\frac{(1-\nu^2)a}{(1+\nu)E\alpha_T} \text{ where } i,j = (x,y)\right)$ are plotted at a particular section of an isotropic macro plate for $\frac{a_0}{a} = 0.6$ in Fig. 7.1. The stresses (σ_{ij}) are computed from the stress resultants (n_{ij}) using the relation: $\sigma_{ij} = \frac{n_{ij}}{h}$. The nondimensional buckling temperature difference $\left(\overline{\Delta T_{cr}} = \Delta T_{cr}.\alpha^T.\left(\frac{a}{h}\right)^2\right)$ due to various concentrations of the localized heating are compared with the outcomes of ABAQUS for this macro plate in Table 7.2. Fig. 7.1 and Table 7.2 show that the findings are in close accord with FE based ABAQUS results, thus validating the current Airy's stress approach used in this work.

Table 7.2 Comparison of non-dimensional buckling temperature difference $\overline{\Delta T_{cr}}$ obtained from finite element (FE) method and current semi-analytical methodology (Airy's stress approach) (SSSS; CCT)

$a_0/a = b_0/b$		0.2	0.4	0.6	0.8	1
$\overline{\Delta T}_{cr}$	**Finite Element Method (ABAQUS)**	0.669	0.773	0.894	1.045	1.226
	Semi-analytical (Airy's stress approach)	0.692	0.777	0.894	1.042	1.216

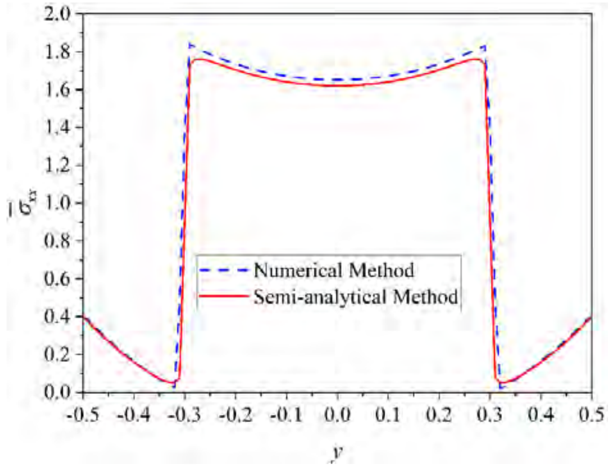

(a) Normal Stress $\bar{\sigma}_{xx}$ at x=0

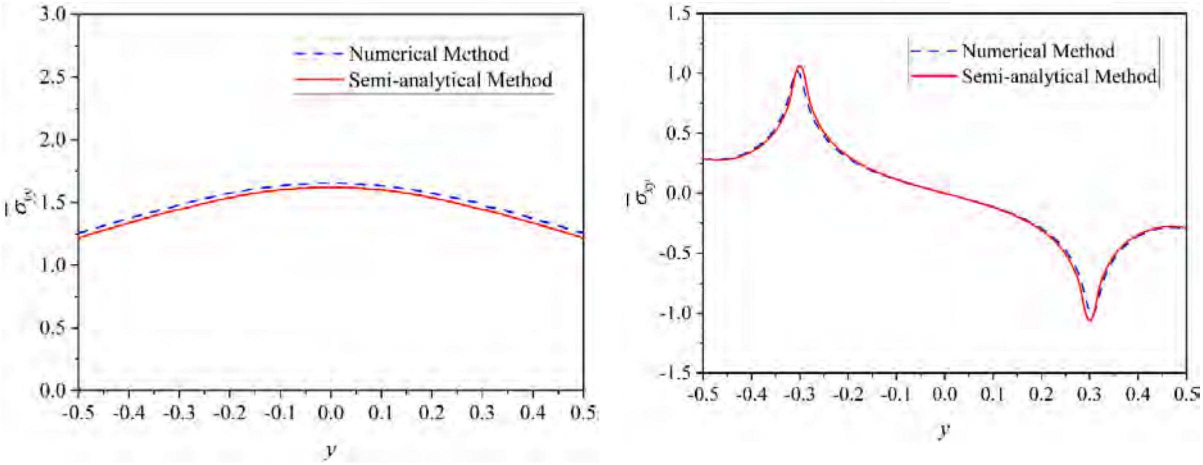

(b) Normal Stress $\bar{\sigma}_{yy}$ at x=0

(c) Shear Stress $\bar{\sigma}_{xy}$ at x=0.3

Fig. 7.1 Comparison of in-plane pre-buckling normalized (a) normal stress $\bar{\sigma}_{xx}$, (b) normal stress $\bar{\sigma}_{yy}$, and (c) shear stress $\bar{\sigma}_{xy}$ computed using the semi-analytical methodology (Airy's Stress Approach) used in this study with numerical method (ABAQUS) for a simply supported macro plate $\left(\frac{a_0}{a} = 0.6; \mathrm{CCT}\right)$

The expression for the in-plane stresses consists of trigonometric series. The optimum number of these terms need to be determined to save computational cost while maintaining accuracy. Convergence analysis is performed in Fig. 7.2 on PMREF with $\frac{a_0}{a} = 0.7$ to determine the optimum number of these terms. The non-dimensional stress $\bar{\sigma}_{xx}$ is computed using different number of these terms. It is observed from Fig. 7.2 that $\bar{\sigma}_{xx}$ computed with $\mathrm{NT}_1 = 20$ and $\mathrm{NT}_2 = 100$ coincides with that computed using $\mathrm{NT}_1 = 100$ and $\mathrm{NT}_2 = 100$. Thus $\mathrm{NT}_1 = 20$ and $\mathrm{NT}_2 = 100$ are adopted as the optimum number of terms in this study to compute in-plane pre-buckling stresses due to localized heating. Here, NT_1 and NT_2 are the number of terms taken in complimentary solution and particular integral used to compute the stress resultants.

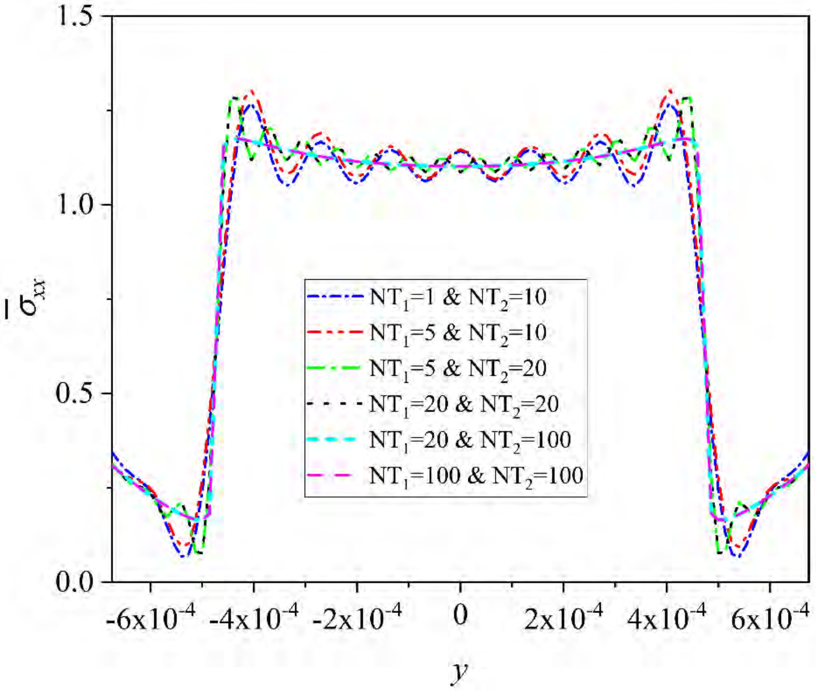

Fig. 7.2 Convergence analysis of the PMREF's pre-buckling normalized stress $\bar{\sigma}_{xx}$ with different number of terms in the trigonometric series expressions used to model these stresses $\left(\frac{a_0}{a} = 0.7; \mathrm{SSSS}; \mathrm{MSGT}\right)$

Table 7.3 Comparison of dimensionless buckling load for a SSSS square porous metal foam microplate subjected to uniaxial compressive mechanical loading with varying *l/h* ratios (MSGT)

Type of Porosity		**Symmetric**				**Uniform**			
l/h		**0.1**	**0.2**	**0.5**	**1**	**0.1**	**0.2**	**0.5**	**1**
$\widehat{N_{cr}}$	**Present Study**	3.66	4.98	14.25	47.35	3.47	4.78	13.96	46.69
	(Hung et al. 2022)	3.66	4.97	13.86	46.23	3.47	4.77	14.15	46.92

The contour plots of $\bar{\sigma}_{xx}$, $\bar{\sigma}_{yy}$, and $\bar{\sigma}_{xy}$ for this plate are presented in Fig. 7.3(a), Fig. 7.3(b), and Fig. 7.3(c), respectively. It can be observed from Fig. 7.3(a) and Fig. 7.3(b) that $\bar{\sigma}_{xx}$ and $\bar{\sigma}_{yy}$ are high in the localized heating region and outside the region these stresses gradually diminish. The shear stress (Fig. 7.3(c)), is almost negligible at all portions of the plate except the corners of the heating region, where it shows sudden increase.

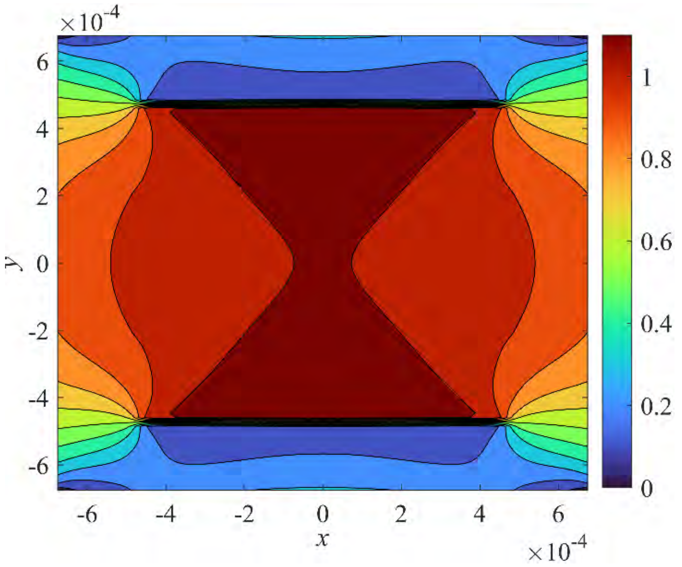

(a) Normal Stress $\bar{\sigma}_{xx}$

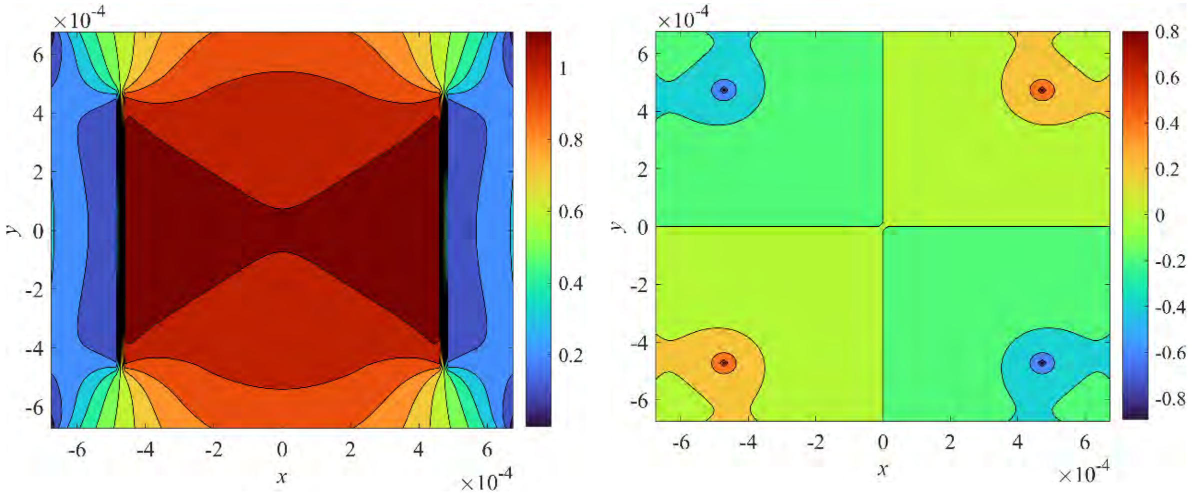

(b) Normal Stress $\bar{\sigma}_{yy}$

(c) Shear Stress $\bar{\sigma}_{xy}$

Fig. 7.3 Contour plots for in-plane pre-buckling normalized (a) normal stress $\bar{\sigma}_{xx}$, (b) normal stress $\bar{\sigma}_{yy}$, and (c) shear stress $\bar{\sigma}_{xy}$ for the PMREF used in this study$\left(\frac{a_0}{a} = 0.7; \mathrm{SSSS}; \mathrm{MSGT}\right)$

In order to validate the modified strain gradient theory formulation and porosity inclusion in the developed methodology, the dimensionless buckling load, $\widehat{N_{cr}} = \frac{N_{cr}a^2}{Eh^3}$ due to uniaxial compressive mechanical loading is compared with those given by ref. (Hung et al. 2022) in Table 7.3. The properties of the microplate used in this comparison are given in column no. 4 of Table 7.1. Hung et al. used MSGT and refined higher order shear deformation theory to model the plate. The results of $\widehat{\boldsymbol{N}_{cr}}$ for various values of *l/h* and different porosity distributions are compared. It is found that the findings of present investigation are consistent with those of Hung et al. (2022). Thus, the authenticity of the current methodology is validated.

The methodology adopted to compute the post-buckling path is validated by comparing the post-buckling response of a macro plate with that given by (Prakash et al. 2008). Since the post-buckling path of a isotropic microplate for constant temperature variation was not available in literature, macro plate is considered. The properties of the macro plate considered by Prakash et al. (2008) are given in column no. 3 of Table 7.1. The heating is assumed to be spread throughout the domain of the plate $\left(\frac{a_0}{a} = 1\right)$. They used the FSDT and modelled the plate using FE modelling. The thermal post-buckling path was obtained using direct iterative technique. It is observed from Fig. 7.4 that the post-buckling path found in this study is very close to that obtained by Prakash et al. (2008). Thus, the authenticity of the methodology adopted to acquire the post-buckling response is established.

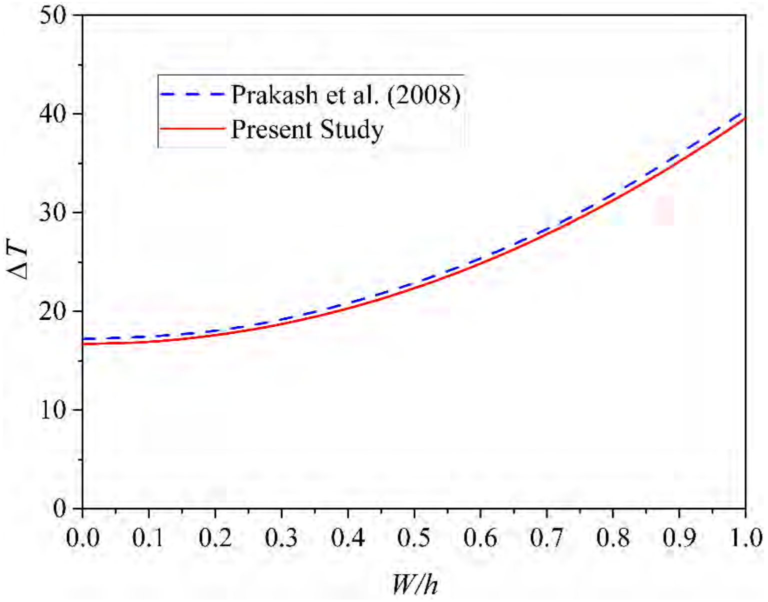

Fig. 7.4 Validation study of the plate's post-buckling response methodology by comparison of post-buckling equilibrium path of a macro-plate $\left(\frac{a_0}{a} = 1; \text{SSSS}; \text{CCT}\right)$ with results of Prakash et al. (2008)

Convergence analysis to determine the optimum count of terms in the trigonometric series for expressing basis functions is performed in Fig. 7.5. The thermal post-buckling equilibrium path is computed for a PMREF with $\frac{a_0}{a} = 0.6$ for different number of terms. It can be seen in Fig.

7.5, that the post-buckling path computed using $N^* = M^* = 4$ completely coincides with post-buckling path computed using $N^* = M^* = 6$. Thus, $N^* = M^* = 4$ is taken as the optimum count of terms in the basis functions for expressing the displacement fields.

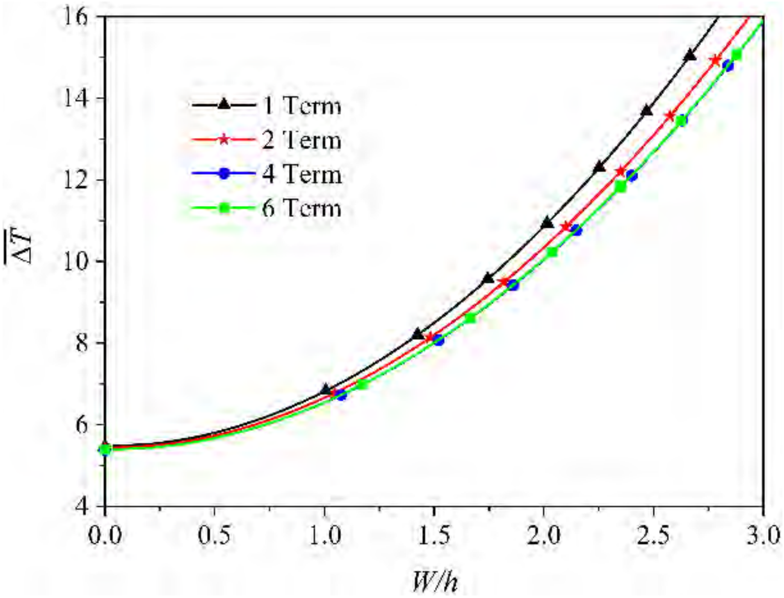

Fig. 7.5 Convergence analysis of the PMREF's ($\frac{a_0}{a} = 0.6$; SSSS; MSGT) post-buckling response by considering varying count of terms in the basis function associated with each displacement field

7.3 Parametric Analysis

The parametric investigation on the mode shape behaviour, critical buckling temperature difference and the thermal post-buckling strength of PMREF is illustrated in the following subsections. The effect of parameters such as size of plate, aspect ratio, thickness, support conditions, porosity distributions, elastic foundation parameters, and concentration of heating is analysed.

7.3.1 *Mode Shape Behaviour*

The mode shapes of PMREFs with uniaxial compressive mechanical loading and PMREFs with heating on the entire surface of the plate $\left(\frac{a_0}{a} = 1\right)$ at their buckling load/temperature are compared in Fig. 9 and Fig. 8 for CCCC and SSSS boundary conditions respectively.

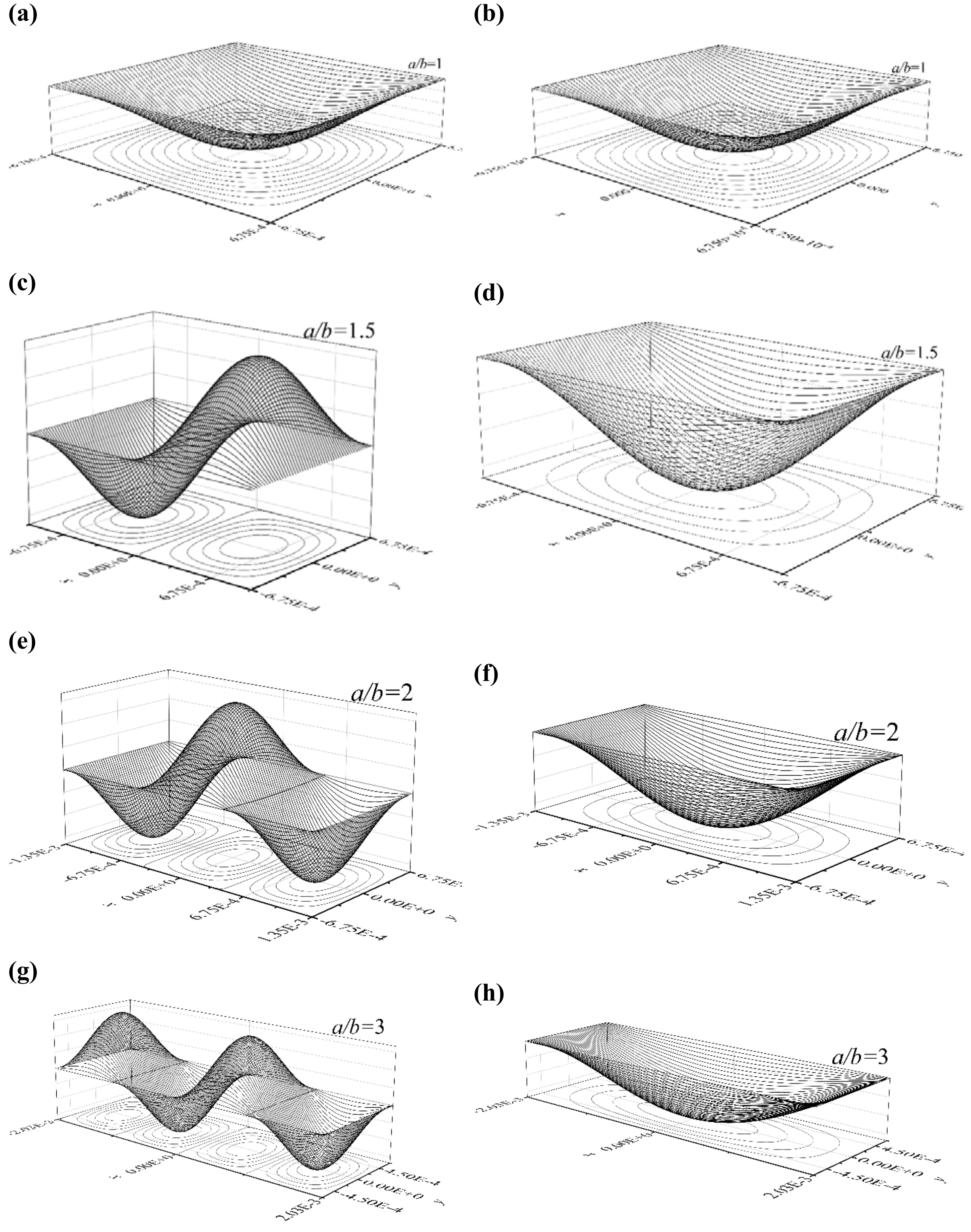

Fig. 7.6 Mode Shape at mechanical buckling load((a), (c), (e), and (g)) and thermal buckling load ((b), (d), (f), and (h)) for a SSSS type PMREF with different aspect ratios (MSGT).

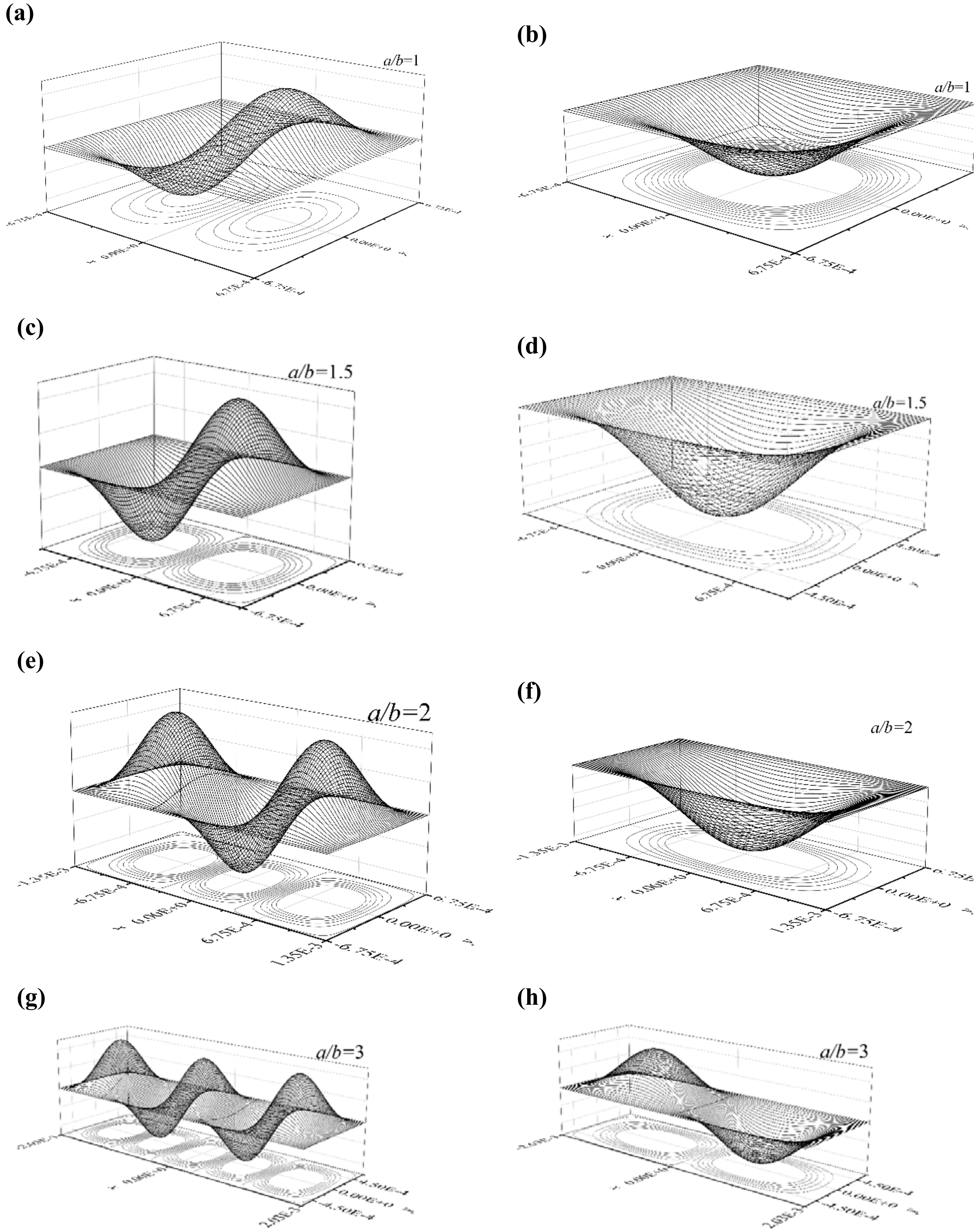

Fig. 7.7 Mode Shape at mechanical buckling load ((a), (c), (e), and (g)) and thermal buckling load ((b), (d), (f), and (h)) for an SSSS type PMREF with different aspect ratios (MSGT)

The mode shapes for various aspect ratios at buckling loads are presented. It is evident from

Fig. 7.6 and Fig.7.7 that the index of mode shape increases with the increase in aspect ratio for uniaxial compressive mechanical loading. In the case of SSSS type PMREFs with thermal load, the thermal buckling load occurs at the first mode itself for all the given aspect ratios of PMREFs. In the case of CCCC type PMREFs subjected to thermal load, mode index increases to (2,1) for aspect ratio 3. The PMREFs with lower aspect ratio buckle in the first mode only. This indicates that increase in index of buckling mode is more susceptible to increase in aspect ratio for uniaxial mechanical load in comparison to thermal load. This is because, pre-buckling stresses are more concentrated at the centre of the plate in the case of thermal load in comparison to uniaxial compression load, where loads are applied at the opposite edges. The loads along the edges induce bending in the direction perpendicular to the loading. Thus, making the plate susceptible to buckle at higher modes. However, in thermal loading, the stresses are concentrated more towards the center of the plate. Thus, there is less possibility of concentration of stresses at the nodal lines of higher modes. Therefore, buckling occurs at lower modes for thermal loading. It can also be noted on comparing Fig. 7.6 and Fig. 7.7 that for a particular aspect ratio of PMREF, the buckling load tends to occur at a higher mode for clamped restraints than simply supported PMREFs. This is because, the simply supported plates have more flexibility due to laterally free edges. This provides these plates a higher resistance to buckling at higher modes. In contrast, the CCCC type plates lack this flexibility, leading to less deformation and thus lower resistance to buckling at higher modes.

7.3.2 Buckling Temperature

The parametric variation on non-dimensional buckling temperature difference $\left(\overline{\Delta T_{cr}} = \Delta T\alpha\left(\frac{a}{h}\right)^2\right)$ is presented in this section. The influence of porosity distribution and porosity coefficient, e_0, is presented in Fig. 7.8. The augmentation in porosity coefficient results in an increase in $\overline{\Delta T_{cr}}$, as the in-plane thermal stresses induced due to heating diminish i.e., thermal resistivity increases. This decrease is more than the reduction in stiffness of the plate owing to increase in porosity. Thus, the overall stability of the system enhances and the $\overline{\Delta T_{cr}}$ increases. The effect of type of porosity distribution is not visible until e_0=0.7. However, the critical buckling temperature is higher for uniform porosity (UP) distribution than the non-uniform symmetric porosity (NSP) distribution at e_0>0.7. This is because concentration of voids at the central portion of the PMREF increases too much for NSP distribution, leading to considerable loss of effective material volume and consequently, its strength. The $\overline{\Delta T_{cr}}$

increases with increase in $\frac{a_0}{a}$ as the concentration of stresses decreases (Fig. 7.9). Due to the greater stiffness provided by clamped restraints, the increase is maximum for CCCC type PMREF and minimum for SSSS type PMREF. The amount of heat is kept constant for all $\frac{a_0}{a}$ ratios.

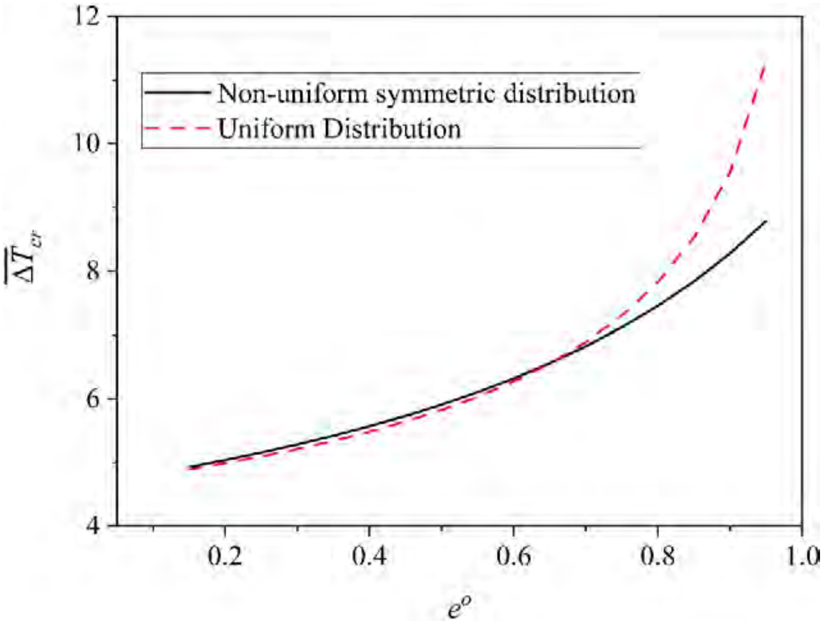

Fig. 7.8 Modification in $\overline{\Delta T}_{cr}$ with change in porosity coefficient of a PMREF ($\frac{a_0}{a} = 0.6$; SSSS; MSGT) with different porosity distributions

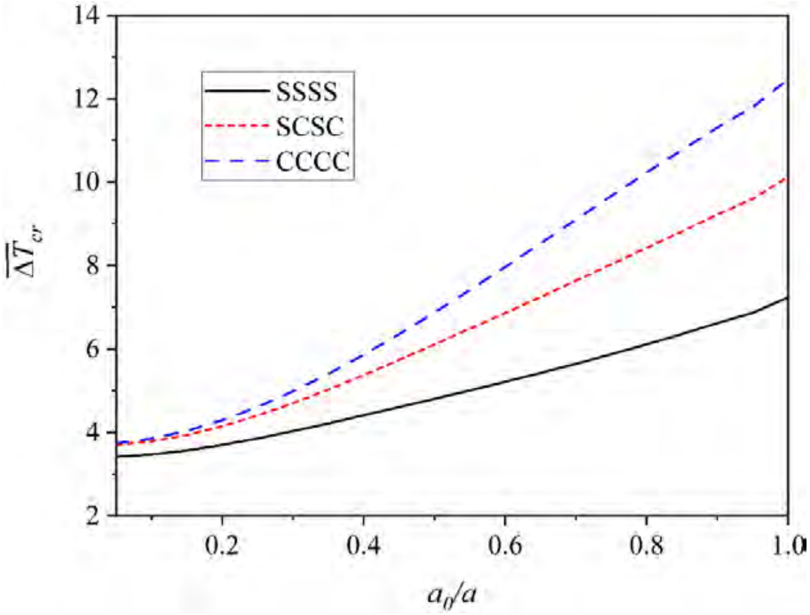

Fig. 7.9 Modification in nondimensional buckling temperature difference with change in loading concentration of a PMREF (MSGT) for various boundary conditions

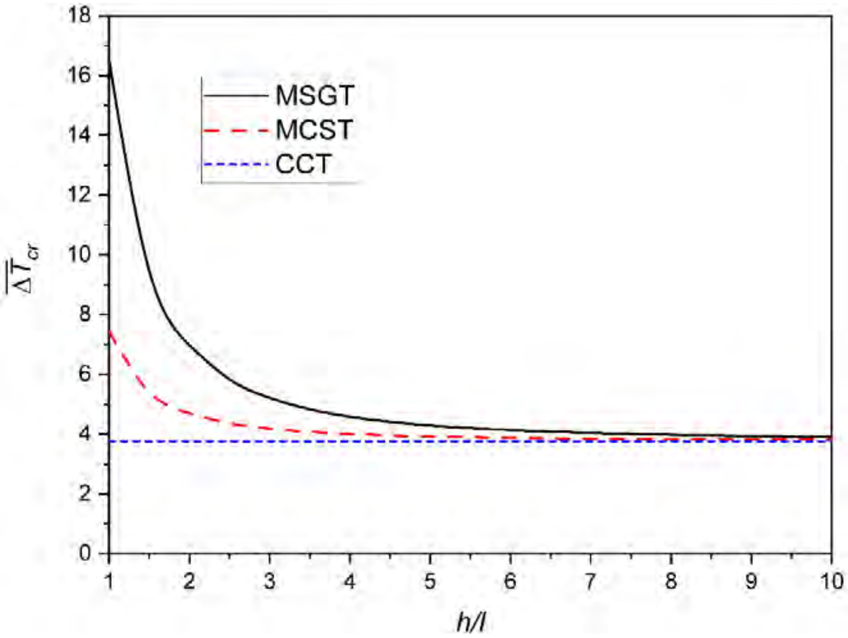

Fig. 7.10 Variation of $\overline{\Delta T_{cr}}$ with change in size (*h/l* ratio) of a PMREF (*h*=45μm; $\frac{a}{b}=1$; $\frac{a_0}{a}=0.6$; SSSS) modelled with different size-dependent theories

The impact of non-dimensional length scale parameter (*h/l*) on the PMREF modelled using different size-dependent theories is presented in Fig. 7.10. The thickness is kept constant and *l* is varied. It is found that the value of $\overline{\Delta T_{cr}}$ amplifies when the thickness is close to the value of *l* for MSGT and MCST. The amplification is more for MSGT than MCST. This is because size-dependent effects due to formation of dislocations (strain gradients) are also included in the MSGT along with the rotation of grains (couple stress) used in MCST. In the absence of size-dependent effects in CCT, there is no influence on the $\overline{\Delta T_{cr}}$.

It is observed from Fig. 7.11 that the $\overline{\Delta T_{cr}}$ decreases as the aspect ratio (*a/b*) of the PMREF increases. At aspect ratio unity, the SCSC and CSCS type PMREF are similar. As the aspect ratio increases, the stiffness of CSCS type PMREF dips more than the SCSC type PMREF. This is because, the clamped boundary conditions become dominant in SCSC PMREF and simply supported conditions in CSCS PMREF. The $\overline{\Delta T_{cr}}$ of SCSC becomes equal to CCCC PMREF at *a/b*=2 and CSCS becomes equal to SSSS PMREF at *a/b*=2.5. This is because at larger aspect ratios, the boundary condition of the longer side does not have much effect.

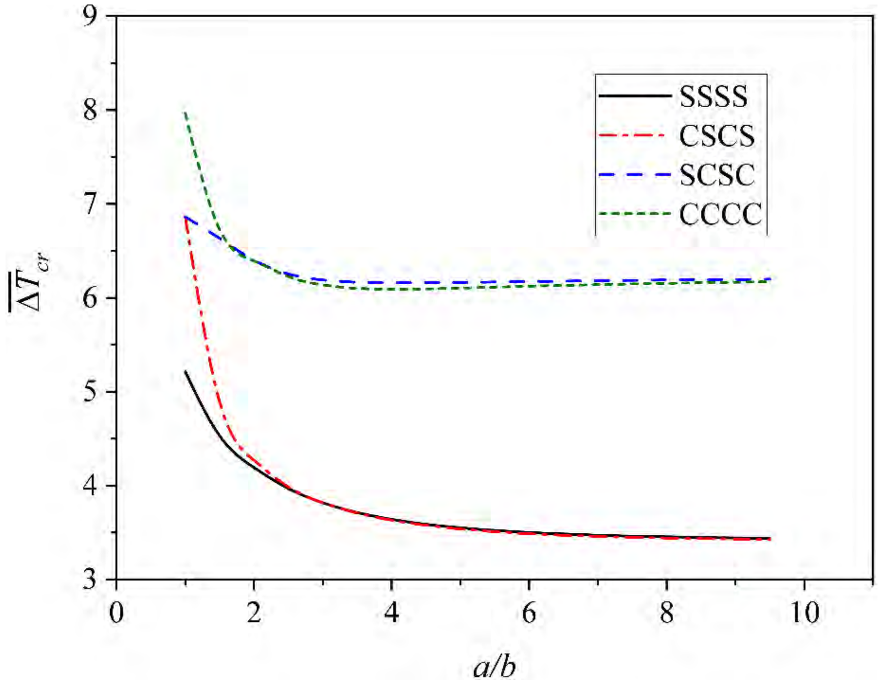

Fig. 7.11 Variation of $\overline{\Delta T}_{cr}$ with change in aspect ratio (*a/b*) of PMREF ($\frac{a_0}{a} = \frac{b_0}{b} = 0.6$; SSSS; MSGT) with different boundary conditions

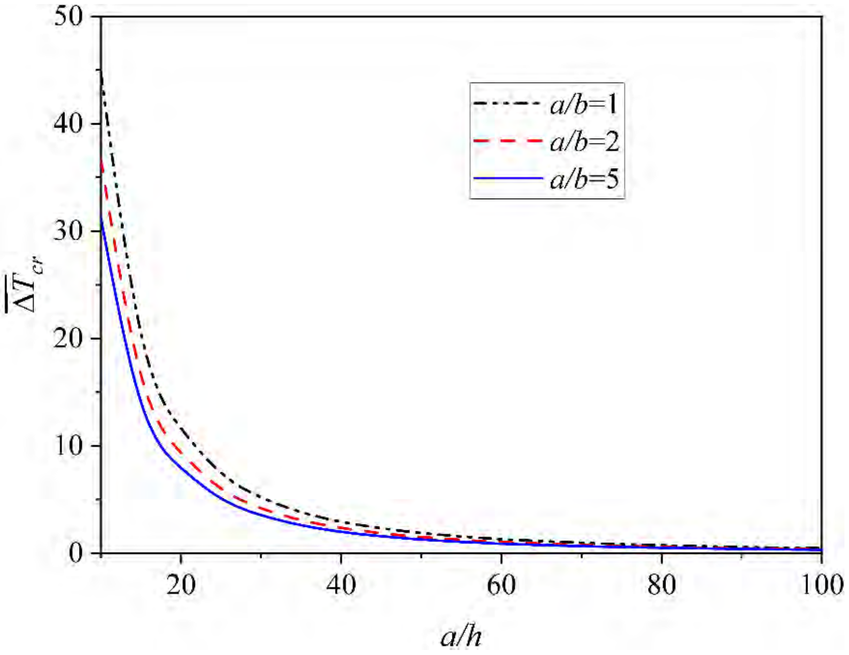

Fig. 7.12 Modification in $\overline{\Delta T}_{cr}$ with change in length to thickness ratio (*a/h)* of PMREF (*a*=1350μm; *l* varies; *h* varies; $\frac{a_0}{a} = 0.6$; SSSS) with different aspect ratios

The effect of change in length to thickness ratio (*a/h*) on $\overline{\Delta T}_{cr}$ is monitored in Fig. 7.12 for different aspect ratios of PMREF. It is observed that the $\overline{\Delta T}_{cr}$ amplifies for thicker plates (*a/h*<=40). This is due to the enhanced stiffness owing to the shear deformation effects and the increase in thermal resistance for thicker plates. In case of thin plates, this effect vanished and thus the variation in $\overline{\Delta T_{cr}}$on further decreasing the thickness is insignificant. It can also be seen that the change in aspect ratio does not alter the behaviour due to change in thickness.

7.3.3 Thermal Post-buckling Response

The parametric study of post-buckling response is presented in this section. The post-buckling strength with respect to different length to thickness (*a/h*) ratios (Fig. 7.13(a)), different size-dependent theories (Fig. 7.13(b)), various non-dimensional length scale parameters (*h/l* ratio) (Fig. 7.13(c)), different distribution and coefficient of porosity (Fig. 7.13(d)), and, different Winkler and Pasternak Elastic foundation parameters (Fig. 7.13(e)) are presented in Fig. 7.13. In all the above parametric studies, the post-buckling strength is proportional to the buckling strengths of these PMREFs. The difference between the post-buckling response for different curves in these figures remains equal to the difference in in their critical buckling temperature difference ($\overline{\Delta T_{cr}}$). Thus, it can be said that a change in these parameters has insignificant effect on the strain hardening of these PMREFs. The strain hardening in Fig. 7.13(a) remains unaffected with decrease in length to thickness ratio, as the increase in nonlinear stiffness is undermined by the increase in geometric stiffness due to the increase in thermal resistivity. The inclusion of strain gradients in size-dependent theories in Fig. 7.13(b) and the intensification of size-dependent effects on reduction in size (Fig. 7.13(c)) do not influence the strain hardening because the effect of geometric nonlinearity is subdued in stiffer models with greater size-dependent effects. Thus, even with large difference in buckling strengths, the differences in nonlinear geometric stiffness is not much. Both the linear and nonlinear stiffness of the PMREF and the thermal resistivity or the geometric stiffness due to thermal load of the PMREFs increases with the increase in porosity coefficient. The differences in nonlinear hardening characters of the curves in Fig. 7.13(d) is not much because of the undermined effect of geometric nonlinear stiffness by the thermal resistivity. In the case of elastic foundation parameters, it is observed from Fig. 7.13(e) that an increase in overall strength occurs on incrementing the value of these parameters. The increase in Pasternak parameter has a greater effect of the stiffness in comparison to the Winkler parameter. The PMREF with $\overline{K}_w = 0$ and $\overline{K}_p = 25$ has a much larger overall strength than the PMREF with $\overline{K}_w = 100$ and $\overline{K}_p = 0$. However, the difference in strain hardening characteristics of the curve is not visible as the nonlinear effects of the foundation parameters are not considered.

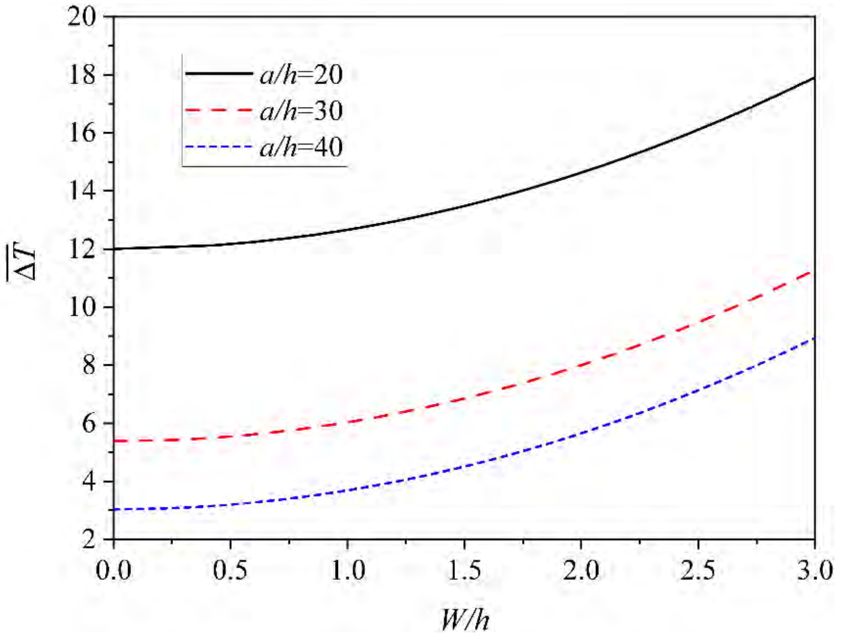

Fig. 7.13(a) Thermal post-buckling response of PMREF (a=1350μm; l varies; h varies; $\frac{a_0}{a}=0.6$; SSSS) with different length to thickness (a/h) ratios

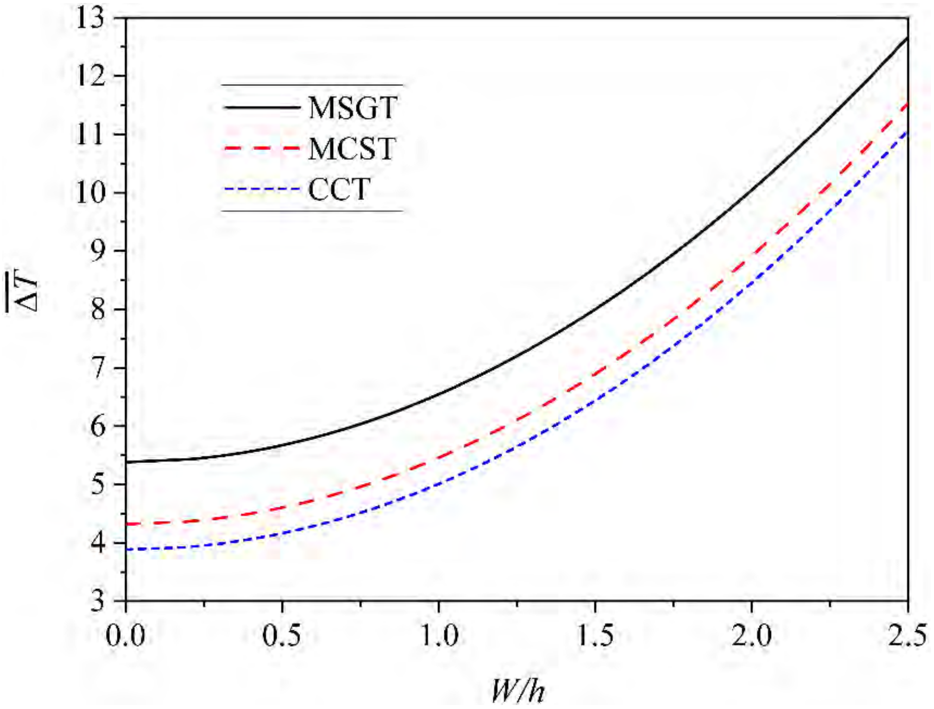

Fig. 7.13(b) Thermal post-buckling response of a PMREF ($\frac{a_0}{a}=0.6$; SSSS). modelled with different size-dependent theories

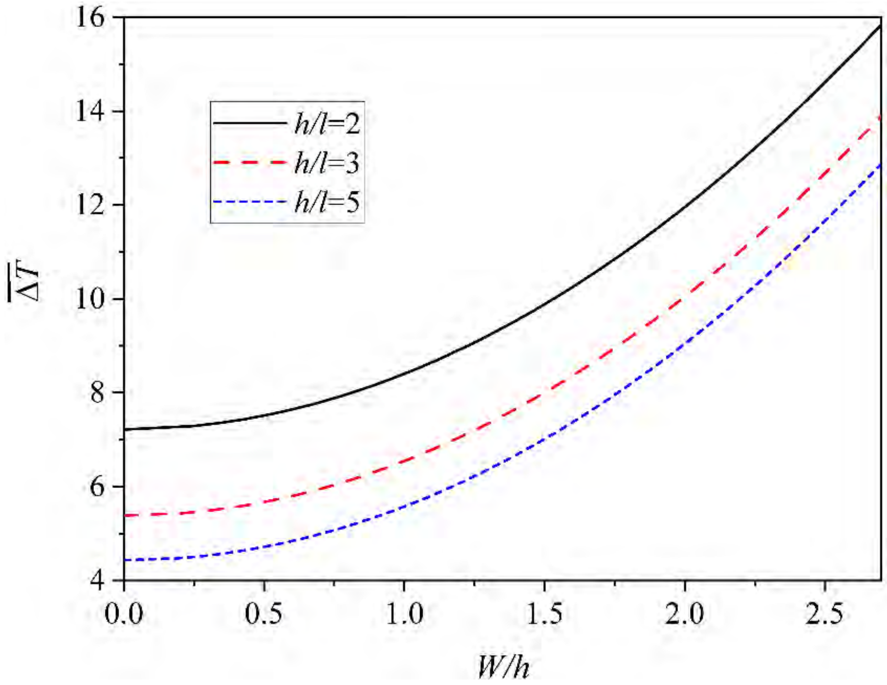

Fig. 7.13(c) Thermal post-buckling response of PMREF (h=45μm; $\frac{a}{b}=1$; $\frac{a_0}{a}=0.6$; SSSS) with different size (h/l ratios)

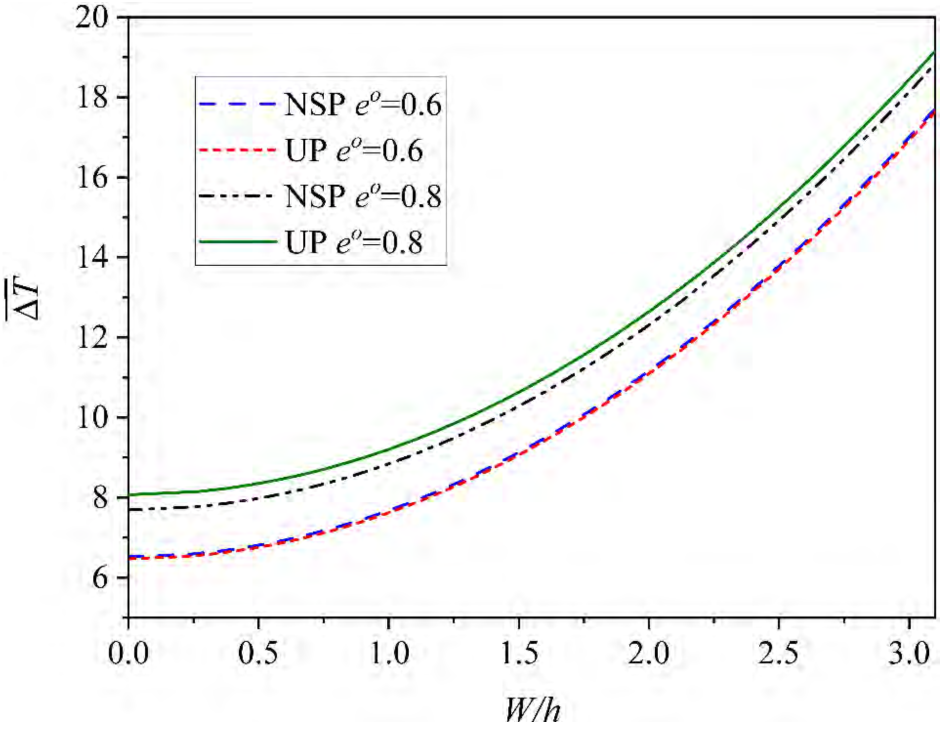

Fig. 7.13(d) Thermal post-buckling response of PMREF ($\frac{a_0}{a}=0.6$; SSSS; MSGT). with different porosity coefficients and porosity distributions

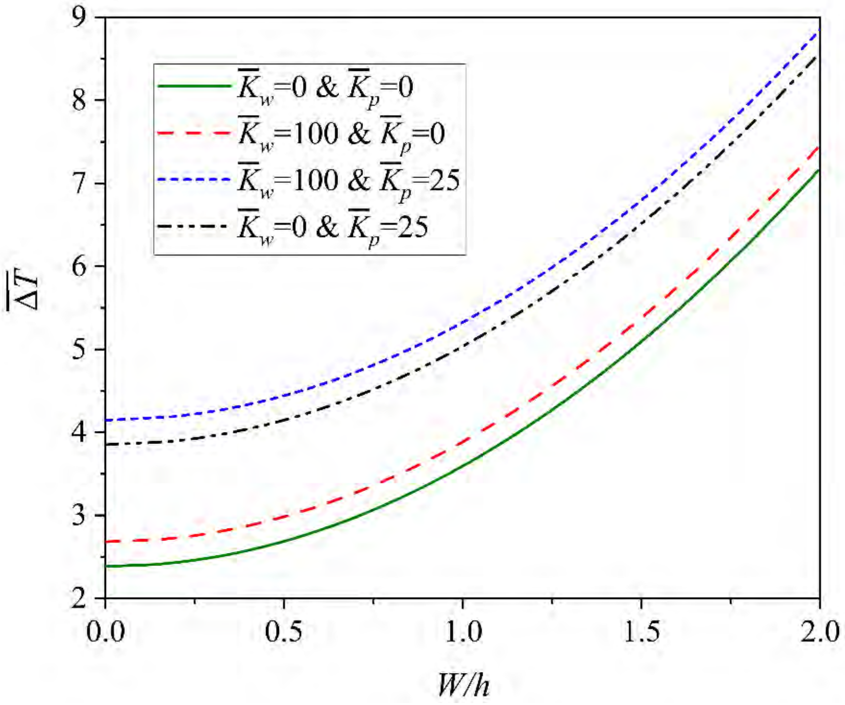

Fig. 7.13(e) Thermal post-buckling response of PMREF ($\frac{a_0}{a} = 0.6$; SSSS; MSGT).with different Winkler and Pasternak elastic foundation parameters

The effect of area of the heating region on the post-buckling strengths is illustrated in Fig. 7.14. It is observed that on decreasing the heating area such that the total thermal load remains the same, both the pre-buckling and post-buckling strength of the plate decreases. It is evident from the figure that for an equal increment in temperature from the critical buckling temperature, the deformation is more on PMREF which has a higher concentration of heating. Thus, the post-buckling strength of PMREF with heating on the entire region of the plate ($\frac{a_0}{a} = 1$) is maximum and plate with least area of heating ($\frac{a_0}{a} = 0.4$) is minimum. This is because, the nonlinear hardening characteristics of the curves increase as the geometric stiffness due to thermal load decreases on increasing the heating area. A similar trend can be seen in Fig. 7.15 for PMREF with different support conditions. The CCCC type PMREF has the maximum buckling and post-buckling strength followed by the SCSC and SSSS type PMREF. This is because the clamped restraints provide an increase in both linear and nonlinear stiffness, and decrease in flexibility. Thus, leading to less deformations on increase of temperature in comparison to SSSS type PMREF.

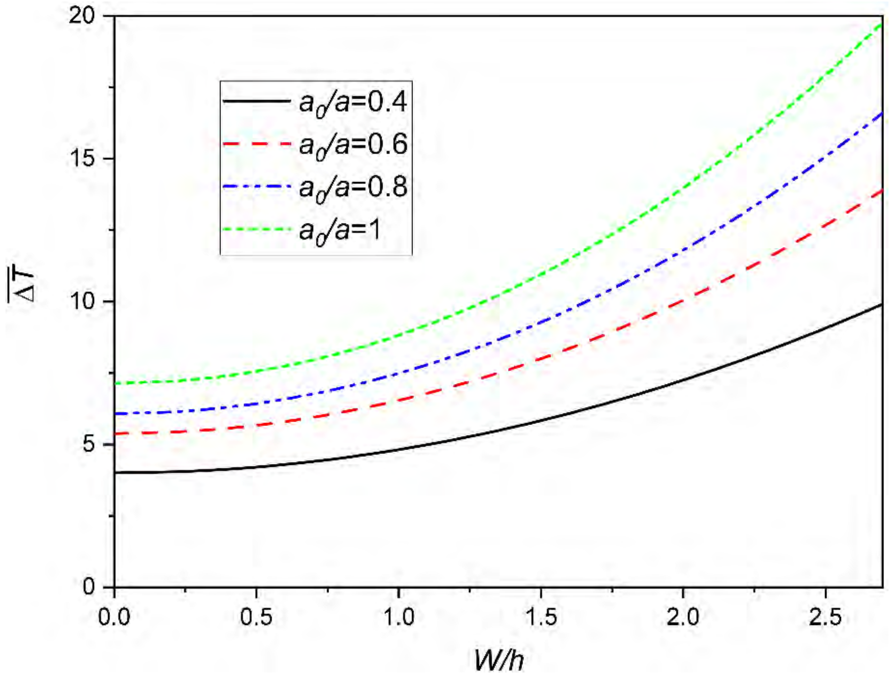

Fig. 7.14 Thermal post-buckling response of PMREF (SSSS; MSGT).with different loading concentrations

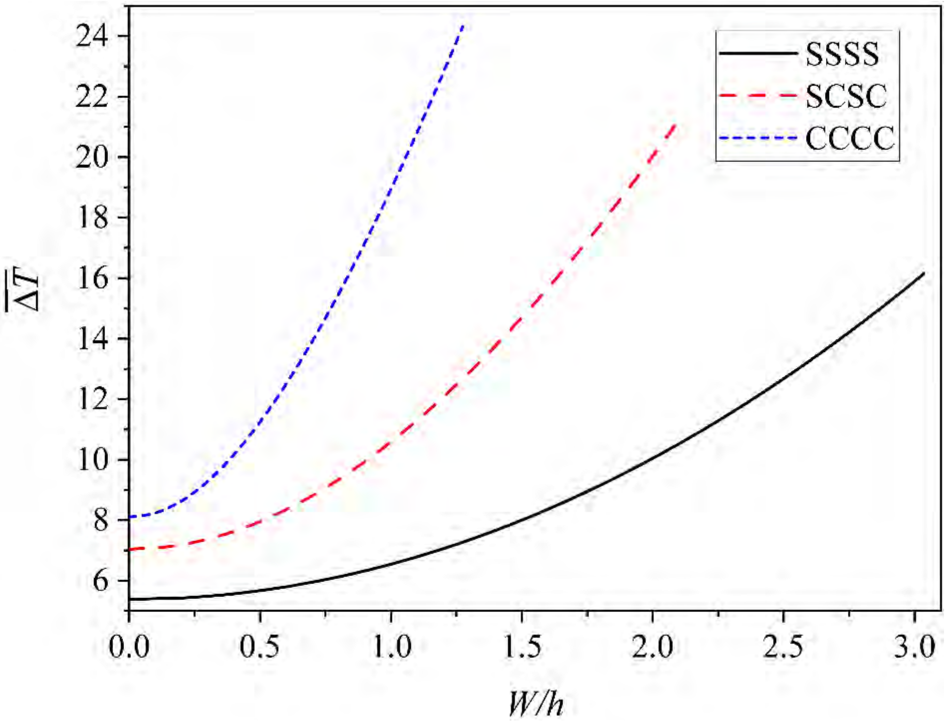

Fig. 7.15 Thermal post-buckling response of PMREF ($\frac{a_0}{a} = 0.6$; MSGT) with different boundary conditions

8

Conclusions

8.1 Introduction

This thesis has provided a comprehensive investigation into the analysis of micro-sized plate structures. Since Classical Continuum Theory (CCT) cannot be used to model these structures, a semi-analytical methodology is developed using the size-dependent modified strain gradient theory (MSGT) and the third-order shear deformation theory (TSDT). The MSGT is optimum to model micro-sized structures and the TSDT is best suited for thin and moderately thick plates. This thesis presents findings concerning a range of phenomena in microplate behaviour, including free vibration, buckling, dynamic instability, nonlinear free vibration, nonlinear forced vibration, nonlinear dynamic response, and post-buckling behaviours under diverse loading conditions. The investigation encompasses microplates made of both isotropic and functionally graded (FG) materials. Furthermore, the study delves into the behaviour of metal foam microplates while accounting for porosity effects, alongside the consideration of microplates resting on elastic foundations. The impact of viscous damping on these microplates is also included in the analysis.

In this investigation, the behaviour of microplates is analysed under uniform and non-uniform in-plane loadings, transverse patch loadings, and localized thermal loading. The analytical expressions for in-plane pre-buckling stresses due to in-plane non-uniform mechanical loading or localized thermal loading are obtained by solving the in-plane stress equilibrium equations and by solving the strain compatibility conditions in terms of the Airy's stress function (Φ). The validation of developed semi-analytical expressions against finite element analysis results has established the reliability and accuracy of the proposed methodology. The governing partial differential equations (PDEs) of motion are obtained using the Hamilton's principle for dynamic problems and the principle of minimization of total potential energy for the static problem. The PDEs are reduced to ordinary differential equations (ODEs) of motion (dynamic problem) or algebraic equations (static problem) using the Galerkin's weighted residual method. The buckling load/temperature and natural frequencies are calculated by solving the eigenvalue problem of these equations. The dynamic instability region is plotted using the Bolotin's method. The nonlinear free and forced vibration behaviours are presented using the frequency-amplitude curves obtained using the incremental harmonic balance (IHB) method. The post-buckling equilibrium path is obtained using the modified Newton-Raphson method. The nonlinear dynamic response is presented using the time history plots obtained using the intrinsic Newmark β direct integration method. By corroborating the simpler version of the methodology used in this thesis with prior studies, the validity and robustness of our approach have been reinforced.

A deep understanding of the intricate relationships of different parameters with the critical buckling load/temperature, natural frequencies, dynamic instability region, nonlinear dynamic instability regions, nonlinear dynamic responses and post-buckling response is achieved with the help of a detailed parametric analysis. The comparison of different size-dependent theories, such as CCT, MCST, and MSGT, has shed light on the small-scale effects that play a pivotal role in the nonlinear responses of microplates. The parametric studies undertaken have illuminated the multifaceted nature of microplate dynamics, revealing the intricate interplay among factors such as porosity coefficients, elastic foundation properties, plate dimensions, boundary conditions, and loading conditions. These findings have far-reaching implications for designing and optimizing microstructures, contributing to the advancing micro-electromechanical systems and related technologies. The effect of aspect ratios, boundary conditions and elastic foundation parameters on the mode shape of the plate at the critical buckling load is also assessed. The exploration of initial perturbation effects on steady-state responses has emphasized the sensitivity of dynamic behaviour to minor disturbances. Time history plots have provided visual insights into the transient phenomena that dictate the overall behaviour of the microplates, offering valuable considerations for design and operational scenarios.

In this chapter, the conclusions to this thesis are presented. The findings of the parametric studies conducted in chapters 4, 5, 6, and 7 are summarized and discussed in section 8.2. Furthermore, the potential impact of this research on both the industry and the academic community is explored in section 8.3. The strengths of this thesis are discussed in section 8.4 It is important to note that this research, while comprehensive, does not encompass an exhaustive analysis of small-scale structures. Addressing this, section 8.5 delves into the identified limitations of this study, while section 8.6 elucidates the future avenues for research in this domain.

8.2 Findings of this Study

The focus of this thesis is to study the behaviour of microplate structures under various conditions of loading. The microstructure devices have unique properties depending on the application, determining their resonant frequency, sensor bandwidth, sensitivity, frequency response, full-scale nonlinearities, and deflection. Controlling these properties mostly depends on microplate factors, including geometry, support conditions, and damping mass. Thus, a parametric analysis of all these parameters is presented to understand the influence of various parameters to allow efficient design of these structures. Moreover, due to the enormous strength/stiffness and displacement sensitivity of microstructures, they are frequently used in applications where they are subjected to large deflections. Thus, the inclusion of geometric nonlinearity becomes mandatory in the study of these structures. The function of many sensors, such as accelerometers, is to measure time-varying acceleration. This makes it necessary to investigate the microstructure's behaviour under dynamic loading. Responding to this, a parametric analysis of the linear and nonlinear dynamic instability regions due to periodic in-plane mechanical loadings is presented in Chapter 4. The load acting on the edges of microplates is not uniform due to irregular connections with neighbouring members, partially damaged boundaries during fabrication or connections between stiffened and unstiffened plates. Thus, the effect of non-uniform in-plane loadings are presented. In Chapter 5, the effect of various parameters on the nonlinear dynamic response due to non-uniform in-plane loading is presented. The microplates in chips or organic solar cells are often placed on a flexible medium. Thus, the stiffness provided by the elastic foundation is also included in the modelling. Moreover, the advantage of large surface area and specific capacity has led to the massive use of porous materials in various microplate applications. Thus, a porous microplate resting on elastic foundations (PMREF) is considered in this chapter. The change in width and onset points of various regions of frequency and the nonlinear hardening nature of frequency-amplitude curve due to various parameters are illustrated. The parametric change in mode shape at critical buckling load is also presented. The effect of the initial perturbation on the steady state response in various regions of frequency is also presented using the time history response curves. In Chapter 6, the parametric studies similar to Chapter 5 are presented, but due to periodic transverse loadings on PMREF as well as functionally graded (FG) microplate. Since practically, the transverse force gets transferred from components placed on these structures, and the loading is mostly localized. Thus, transverse patch loadings are considered. Over the course of their service life, the microplate elements are often subjected to large thermal stresses which may induce buckling. Thus, a parametric investigation of the buckling loads and post-buckling equilibrium path on PMREF is presented in Chapter 7. The hot microplate elements are often connected with cooler substrate elements which act as heat sinks.

The placement of electric components or sensors on the plate is localized. Thus, the region of heating often remains localized. Thus, the effect of localized heating is considered in the results for chapter 7. The parametric changes in mode shape at buckling load due to mechanical and thermal load are also shown. The major findings from this study are:

(1) The inclusion of strain gradients in the MSGT significantly increases the linear stiffness of the microplate at micro-sizes. However, the effect on nonlinear stiffness is minimal. Thereby, the geometric nonlinearity of the microplates gets suppressed on using the MSGT model.
(2) The impact of both non-uniform in-plane loading and transverse patch loadings is most when applied near the centre of the plate with higher concentrations. Its impact decreases as the concentration decreases or when it moves away from the centre.
(3) The frequency-amplitude curves for both in-plane periodic and transverse periodic loading can be segregated in four regions of excitation frequencies. In regions of excitation frequency where more than one stable curves are present, the steady state amplitude attained by the microplate depends on the amplitude of initial perturbation.
(4) Buckling occurs at lower modes for thermal loads compared to mechanical loads as the stresses are more concentrated at the centre of the plate in thermal loading. The increase in concentration of thermal loading leads to a decrease in post-buckling strength as the thermal stresses increase, which suppress the nonlinear geometric nonlinearity of the plate.

The detailed chapter wise findings from the current study are presented in the sub-sections below.

8.2.1 Nonlinear Vibration and Dynamic Instability of Microplate under In-Plane Mechanical Loading

The major findings from this chapter are:

(1) The strain hardening effect on critical buckling load and vibrational frequency is maximum using MSGT and null using Classical Continuum Theory (CCT). The small-scale effect vanishes for $h/l>7.5$ on using modified couple stress theory (MCST) and $h/l>15$ for MSGT. The dynamic stability behaviour and nonlinear vibration response also follow a similar trend, where the width of linear dynamic instability region

($wDIR^L$), width of nonlinear dynamic instability region ($wDIR^{NL}$), and peak amplitude are maximum from CCT and minimum from MSGT.

(2) The minimum dynamic load required for the onset of instability increases with an increase in the modal damping ratio. The peak amplitude is unbounded for the undamped plate and it decreases with an increase in the modal damping ratio. No significant difference is noticed in the width of stability regions.

(3) The instability region shifts towards the left with the increase in preloading due to a decrease in stiffness. The increase in width of the instability region on the increase in static load factor is nonlinear.

(4) The width of the instability region is maximum for the SSSS boundary condition and minimum for the CCCC boundary condition. The origin of instability is similar for SCSC and CSCS boundary conditions.

(5) The peak amplitude and width of the instability region are maximum for partial loading and minimum for uniform loading. The origin of instability is unaffected by the change in the loading profile.

8.2.2 Nonlinear Vibration and Dynamic Response of Microplate under In-plane Mechanical Loading

The major findings from this chapter are as follows:

(1) Both linear and nonlinear stiffness decreases on the increase in the porosity coefficient. The impact of uniform porosity distribution is more than symmetric distribution, and this difference in result is even more for higher porosity coefficients.

(2) While linear stiffness increases on increasing the elastic foundation parameters, the effect of geometric nonlinearity decreases. Moreover, the Winkler elastic foundation parameter's impact is insignificant compared to the impact of Pasternak parameter.

(3) The change in mode shape happens earlier with an increase in the Pasternak parameter compared to an increase in the Winkler parameter. The plate moves to higher modes of vibration with an increase in the aspect ratio of the PMREF.

(4) The effect of geometric nonlinearity gets suppressed in MCST and MSGT models due to the stiffer strain gradient models. Thus, the nonlinear hardening nature of the frequency-amplitude curves decreases when including the size-dependent effects using MCST and MSGT.

(5) The overall stiffness of the plate increases as the size-dependent effects and shear deformation effects become more prominent when decreasing the size and increasing the thickness of the PMREF. However, the nonlinear hardening nature of the curves decreases as these effects intensify.

(6) The impact of loading on the geometric stiffness due to in-plane loads increases as the concentration of loading increases near the centre of the plate. Following similar trends, the impact was found to be greater for the partial loading profile, followed by the parabolic and uniform loading profiles.

(7) The traced frequency amplitude curves consists of two branches, one stable and one unstable, both showing nonlinear hardening. There are three bifurcation points and the forcing frequencies are segregated into four zones (‘A’, ‘B’, ‘C’, and ‘D’) based on these points. There is no effect of the amplitude of initial perturbation on the steady-state response due to excitation frequencies from the region ‘A’, ‘B’ and ‘D’. However, in region ‘C’, due to the presence of two stable solutions, the initial displacement decides which solution will be attained.

(8) Region ‘B’ of excitation frequencies is the most vulnerable, followed by Region ‘C’. Large steady-state amplitude is attained from excitation frequencies in Region ‘B’, independent of the initial perturbation amplitude. Large steady-state amplitude is also found in Region ‘C’, but only if the initial perturbation amplitude is provided near the upper stable curve. Otherwise, the response decays completely. In zones ‘A’ and ‘D’, the response decays to zero independent of the initial perturbation amplitude.

8.2.3 Nonlinear Dynamic Analyses of Microplate under Transverse Loading

The following are the significant findings from this chapter:

(1) The traced frequency amplitude curves exhibits nonlinear hardening character and the curve consists of both stable and unstable regions, which are separated by two bifurcation points. The forcing frequencies are segregated into four zones (‘A’, ‘B’, ‘C’, and ‘D’) based on their vulnerability and dependence on initial perturbation.

(2) The most sensitive region of excitation frequencies is ‘B’, followed by ‘C’. Regardless of the initial perturbation amplitude, excitation frequencies in Region 'B' produce a large steady-state amplitude. Large steady-state amplitudes are also observed in Region 'C', but only if the initial perturbation amplitude is close to the upper stable curve.

Otherwise, the response decays to the steady-state amplitude of a more stable, lower stability curve. In regions 'A' and 'D', the steady-state amplitude of the curve is minimal but does not decay to zero and is independent of the perturbation's initial amplitude. In the case of transverse loading, the steady-state amplitude is non-zero, even in the absence of an initial perturbation.

(3) The effect of the power-law index on the hardening behaviour of the nonlinear free vibration response is insignificant.

(4) The clamped boundary conditions cause an increase in both the hardening nature of the nonlinear vibration response and stiffness of the plate.

(5) The transverse patch loading is most impactful when applied at the centre of the plate with higher concentrations. Its impact decreases as the concentration decreases or when it moves away from the centre. The excitation frequency ratio for resonance is also the least for centrally applied load with higher concentration and increases with a decrease in concentration or moving away from the centre of the plate.

8.2.4 Thermal Buckling and Post-buckling analyses of Microplate

The major findings from this chapter are:

(1) Buckling occurs at lower modes for thermal load compared to mechanical load as the stresses are more concentrated at the centre of the plate in thermal loading. The increase in aspect ratio of PMREF leads to higher buckling modes. The buckling occurs in higher buckling modes for clamped restraints in comparison to simply supported conditions due to the rigidity to deformations in these supports.

(2) The buckling strengths of the microplate decreases with the increase in loading concentration, *h/l* ratio, and *a/b* ratio. The buckling strength increases with an increase in porosity coefficient and elastic foundation parameters. The increase in buckling strength is more due to Pasternak parameter and uniform porosity distribution.

(3) In case of post-buckling strength, the increase in loading concentration leads to a decrease in post-buckling strength as the thermal stresses increase. The clamped supports also provide higher post-buckling strengths as the deformation for an increase in temperature decreases.

8.3 Impact of this Study

This analysis has not only enriched our theoretical knowledge but also highlighted the practical implications for engineering applications involving microscale structures. The nonlinear behaviours of microplates are studied comprehensively, shedding light on the complex interactions that govern their responses under various conditions. The major contribution of this research is to provide results of behaviour of microplates using a mesh-free semi-analytical methodology. This makes these results void of any discretization errors. Thus, the results provided in this thesis can be used as benchmarks to validate further numerical methodologies developed to study more complex microplates with irregular shapes, support conditions, and loading conditions. The insights gained from this thesis hold immense potential for influencing the design, analysis, and performance optimization of microscale systems in fields ranging from electronics to aerospace. As we delve deeper into the realm of miniaturized structures, the knowledge and methodologies developed herein will undoubtedly serve as essential tools for pushing the boundaries of modern engineering and technology.

8.4 Strengths of this Study

The notable strengths of the work adopted in this research are listed below.

(1) The methodology used in this research is ideal for microplates towards the lower end of the micro-scale as the MSGT takes care of the rotation of grains and accumulation of dislocations in such structures.

(2) The moderately thick/thin plates can be quite accurately modelled using the developed methodology as the shear deformation effects are quite accurately included using the TSDT.

(3) The governing equations are derived using the robust analytical approximation method in its strong form. This technique yields results that closely align with closed-form solutions, while also accommodating the incorporation of nonlinearity within the governing equations.

(4) This is unique research where the localized and nonuniform loadings are included in the semi-analytical solution methodology by deriving explicit analytical expressions for the localized mechanical/thermal loads and the corresponding pre-buckling stresses within the plate.

(5) The Incremental Harmonic Balance (IHB) method used in this research allows to plot both the stable and unstable regions of the frequency amplitude curve. Moreover, the arc-length continuation method used as the incremental method in this approach can pass through the juncture points and thus can easily trace the snap back and snap through cases. This allows to demonstrate the effect of damping on the nonlinear vibration.

(6) A comprehensive parametric study is done in this thesis where a variety of microplate material properties, geometries, supports and loading conditions are included.

8.5 Limitations of this Study

Although quite comprehensive, still there are some limitations to this research. These are listed in the points below.

(1) This research cannot be applied to nanoplates as the softening behaviour due to nonlocalities needs to be included to model such structures.

(2) Thick microplates cannot be modelled using this methodology as the three-dimensional (3D) analysis is required to model such structures to model the large variations in transverse strains along the thickness.

(3) This research cannot be applied to irregular geometries and boundary conditions of microplates. The approximating functions for the strong form method used in this research are very difficult to identify for such microplates. Secondly, the methodology applied to obtain the localized loading expressions can only be applied on rectangular plates.

(4) Currently, no experimental or atomistic simulation results are yet available to calibrate the length-scale parameters for functionally graded materials and porous materials. Therefore, in this study, the length scale parameters are assumed which only provide effective qualitative results and not actual quantitative ones.

(5) The analytical expressions for pre-buckling stresses due to localized heating are calculated only for the case when the heating is symmetric about the centre of the plate.

(6) The IHB method is suitable only for systems with smooth nonlinearities. In the case of strong nonlinearities, a higher order of harmonics is required which leads to substantial computational cost.

8.6 Future Scope

It is hopeful that the results of this study can serve as benchmark results to validate future numerical methods developed for MSGT based moderately thick microplates with nonlinearity considerations. Moving forward, this thesis opens doors to numerous promising avenues for future exploration. Some of these are listed below.

(1) The nonlocality effects can be included in the methodology to allow efficient nonlinear analysis of nanoplates using nonclassical continuum theory.
(2) Methodology incorporating 3D analysis can be developed to allow modelling of thick plates.
(3) In order to calibrate material length-scale parameters for functionally graded structures and porous structures, atomistic simulations or experimental investigations can be performed.
(4) Further numerical techniques can be developed to enable analysis of small-scale plates with irregular geometries, cut-outs, boundaries and loading conditions.
(5) Methodologies for other complex microstructures such as shells, sandwich microplates shall be developed.
(6) Analytical expressions for pre-buckling stresses for asymmetric loading cases shall be developed.
(7) Nonlinear vibrations shall be further investigated to study chaos and other complex operations.

Afshari, H., and Adab, N. (2020). "Size-dependent buckling and vibration analyses of GNP reinforced microplates based on the quasi-3D sinusoidal shear deformation theory." *Mechanics Based Design of Structures and Machines*, 50(1), 184–205.

Aikele, M., Bauer, K., Ficker, W., Neubauer, F., Prechtel, U., Schalk, J., and Seidel, H. (2001). "Resonant accelerometer with self-test." *Sensors and Actuators A: Physical*, 92(1–3), 161–167.

Akgöz, B., and Civalek, Ö. (2012). "Free vibration analysis for single-layered graphene sheets in an elastic matrix via modified couple stress theory." *Materials & Design*, 42, 164–171.

Akgöz, B., and Civalek, Ö. (2013). "Modeling and analysis of micro-sized plates resting on elastic medium using the modified couple stress theory." *Meccanica*, 48(4), 863–873.

Akgöz, B., and Civalek, Ö. (2015). "A microstructure-dependent sinusoidal plate model based on the strain gradient elasticity theory." *Acta Mechanica 2015*, 226(7), 2277–2294.

Alinaghizadeh, F., Shariati, M., and Fish, J. (2017). "Bending analysis of size-dependent functionally graded annular sector microplates based on the modified couple stress theory." *Applied Mathematical Modelling*, 44, 540–556.

Alunda, B. O., and Lee, Y. J. (2020). "Review: Cantilever-Based Sensors for High Speed Atomic Force Microscopy." *Sensors (Basel, Switzerland)*, 20(17), 1–39.

Amabili, M. (2008). *Nonlinear vibrations and stability of shells and plates*. Cambridge University Press.

Ansari, R., Ashrafi, M. A., and Arjangpay, A. (2015a). "An exact solution for vibrations of postbuckled microscale beams based on the modified couple stress theory." *Applied Mathematical Modelling*, 39(10–11), 3050–3062.

Ansari, R., Faghihshojaei, M., Mohammadi, V., Gholami, R., and Darabi, M. A. (2014a). "Size-dependent vibrations of post-buckled functionally graded Mindlin rectangular microplates." *Latin American Journal of Solids and Structures*, 11(13), 2351–2378.

Ansari, R., Gholami, R., Faghih Shojaei, M., Mohammadi, V., and Darabi, M. A. (2013). "Thermal Buckling Analysis of a Mindlin Rectangular FGM Microplate Based on the Strain Gradient Theory." *Journal of Thermal Stresses Journal of Thermal Stresses*, 36(5), 446–465.

Ansari, R., Gholami, R., Faghih Shojaei, M., Mohammadi, V., and Darabi, M. A. (2015b). "Size-dependent nonlinear bending and postbuckling of functionally graded Mindlin rectangular microplates considering the physical neutral plane position." *Composite Structures*, 127, 87–98.

Ansari, R., Gholami, R., Faghih Shojaei, M., Mohammadi, V., and Sahmani, S. (2015c). "Bending, buckling and free vibration analysis of size-dependent functionally graded circular/annular microplates based on the modified strain gradient elasticity theory." *European Journal of Mechanics - A/Solids*, 49, 251–267.

Ansari, R., Hasrati, E., Faghih Shojaei, M., Gholami, R., Mohammadi, V., and Shahabodini, A. (2016). "Size-Dependent Bending, Buckling and Free Vibration Analyses of Microscale Functionally Graded Mindlin Plates Based on the Strain Gradient Elasticity Theory." *Latin American Journal of Solids and Structures*, 13(4), 632–664.

Ansari, R., Shojaei, M. F., Mohammadi, V., Gholami, R., and Darabi, M. A. (2014b). "Nonlinear vibrations of functionally graded Mindlin microplates based on the modified couple stress theory." *Composite Structure*, 114, 124–134.

Ansari, R., Shojaei, M. F., Mohammadi, V., Gholami, R., and Rouhi, H. (2014c). "Size-dependent thermal buckling and postbuckling of functionally graded annular microplates based on the modified strain gradient theory." *Journal of Thermal Stresses*, 37(2), 174–201.

Arefi, M., and Kiani, M. (2020). "Magneto-electro-mechanical bending analysis of three-layered exponentially graded microplate with piezomagnetic face-sheets resting on

Pasternak's foundation via MCST." *Mechanics of Advanced Materials and Structures*, 27(5), 383–395.

Arefi, M., Mohammad-Rezaei Bidgoli, E., and Rabczuk, T. (2019). "Thermo-mechanical buckling behavior of FG GNP reinforced micro plate based on MSGT." *Thin-Walled Structures*, 142, 444–459.

Arefi, M., and Rabczuk, T. (2019). "A nonlocal higher order shear deformation theory for electro-elastic analysis of a piezoelectric doubly curved nano shell." *Composites Part B*, 168, 496–510.

Arefi, M., and Zenkour, A. M. (2017). "Vibration and bending analyses of magneto–electro–thermo-elastic sandwich microplates resting on viscoelastic foundation." *Applied Physics A: Materials Science and Processing*, 123(8), 1–17.

Arpanahi, R. A., Eskandari, A., Hosseini-Hashemi, S., Taherkhani, M., and Hashemi, S. H. (2023). "Surface Energy Effect on Free Vibration Characteristics of Nano-plate Submerged in Viscous Fluid." *Journal of Vibration Engineering and Technologies*. DOI: 10.1007/s42417-022-00828-x

Arpanahi, R. A., Hosseini-Hashemi, S., Rahmanian, S., Hashemi, S. H., and Ahmadi-Savadkoohi, A. (2019). "Nonlocal surface energy effect on free vibration behavior of nanoplates submerged in incompressible fluid." *Thin-Walled Structures*, 143, 106212.

Arshid, E., Amir, S., and Loghman, A. (2021). "Thermal buckling analysis of FG graphene nanoplatelets reinforced porous nanocomposite MCST-based annular/circular microplates." *Aerospace Science and Technology*, 111, 106561.

Asghari, M. (2012). "Geometrically nonlinear micro-plate formulation based on the modified couple stress theory." *International Journal of Engineering Science*, 51, 292–309.

Asghari, M., and Taati, E. (2012). "A size-dependent model for functionally graded micro-plates for mechanical analyses." *Journal of Vibration and Control*, 19(11), 1614–1632.

Ashby, M. F. (1970). "The deformation of plastically non-homogeneous materials." *The Philosophical Magazine: A Journal of Theoretical Experimental and Applied Physics*, 21(170), 399–424.

Ashoori, A. R., and Sadough Vanini, S. A. (2016a). "Thermal buckling of annular microstructure-dependent functionally graded material plates resting on an elastic medium." *Composites Part B: Engineering*, 87, 245–255.

Ashoori, A. R., and Sadough Vanini, S. A. (2016b). "Nonlinear thermal stability and snap-through behavior of circular microstructure-dependent FGM plates." *European Journal of Mechanics - A/Solids*, 59, 323–332.

Ashoori Movassagh, A., and Mahmoodi, M. J. (2013). "A micro-scale modeling of Kirchhoff plate based on modified strain-gradient elasticity theory." *European Journal of Mechanics - A/Solids*, 40, 50–59.

Askari, A. R., and Tahani, M. (2015). "Analytical determination of size-dependent natural frequencies of fully clamped rectangular microplates based on the modified couple stress theory." *Journal of Mechanical Science and Technology*, 29(5), 2135–2145.

Babu, B., and Patel, B. P. (2019a). "Analytical solution for strain gradient elastic Kirchhoff rectangular plates under transverse static loading." *European Journal of Mechanics, A/Solids*, 73, 101–111.

Babu, B., and Patel, B. P. (2019b). "A new computationally efficient finite element formulation for nanoplates using second-order strain gradient Kirchhoff's plate theory." *Composites Part B: Engineering*, 168, 302–311.

Baferani, A. H., Saidi, A. R., and Ehteshami, H. (2011). "Accurate solution for free vibration analysis of functionally graded thick rectangular plates resting on elastic foundation." *Composite Structures*, 93(7), 1842–1853.

Bajkowski, J., and Szemplińska-Stupnicka, W. (1986). "Internal resonances effects—

simulation versus analytical methods results." *Journal of Sound and Vibration*, 104(2), 259–275.

Bashir, R., Gupta, A., Neudeck, G. W., McElfresh, M., and Gomez, R. (2000). "On the design of piezoresistive silicon cantilevers with stress concentration regions for scanning probe microscopy applications." *J. Micromech. Microeng*, 10, 483–491.

Behera, L., and Chakraverty, S. (2017). "Recent Researches on Nonlocal Elasticity Theory in the Vibration of Carbon Nanotubes Using Beam Models: A Review." *Archives of Computational Methods in Engineering*, 24(3), 481–494.

Björkman, H., Rangsten, P., Hollman, P., and Hjort, K. (1999). "Diamond replicas from microstructured silicon masters." *Sensors and Actuators A: Physical*, 73(1–2), 24–29.

Cartmell, M. (1990). *Introduction to linear, parametric, and nonlinear vibrations*. Chapman and Hall.

Chen, W. J., Lin, P. D., and Chen, L. W. (1991). "Thermal buckling behavior of thick composite laminated plates under nonuniform temperature distribution." *Computers & Structures*, 41(4), 637–645.

Chen, W., Xu, M., and Li, L. (2012). "A model of composite laminated Reddy plate based on new modified couple stress theory." *Composite Structures*, 94(7), 2143–2156.

Cheung, Y. K., Chen, S. H., and Lau, S. L. (1990). "Application of the incremental harmonic balance method to cubic non-linearity systems." *Journal of Sound and Vibration*, 140(2), 273–286.

Chong, A. C. M., Yang, F., Lam, D. C. C., and Tong, P. (2001). "Torsion and bending of micron-scaled structures." *Journal of Materials Research*, 16(4), 1052–1058.

Cosserat, E., and Cosserat, F. (1909). "Théorie des Corps déformables." *Nature*, 81(2072), 67–67.

Darijani, H., and Mohammadabadi, H. (2014). "A new deformation beam theory for static and dynamic analysis of microbeams." *International Journal of Mechanical Sciences*, 89:3, 1–9.

Darijani, H., and Shahdadi, A. H. (2015). "A new shear deformation model with modified couple stress theory for microplates." *Acta Mechanica*, 226(8), 2773–2788.

Das, D. (2019). "Nonlinear forced vibration analysis of higher order shear-deformable functionally graded microbeam resting on nonlinear elastic foundation based on modified couple stress theory." *Proc IMechE Part L: Journal of Materials: Design and Applications*, 233(9), 1773–1790.

Dell'Isola, F., Andreaus, U., and Placidi, L. (2014). "At the origins and in the vanguard of peridynamics, non-local and higher-gradient continuum mechanics: An underestimated and still topical contribution of Gabrio Piola." *Mathematics and Mechanics of Solids*, 20(8), 887–928.

Dell'Isola, F., Della Corte, A., Esposito, R., and Russo, L. (2016). "Some cases of unrecognized transmission of scientific knowledge: From antiquity to gabrio piola's peridynamics and generalized continuum theories." *Advanced Structured Materials*, 42, 77–128.

Dhotarad, M. S., and Ganesan, N. (1978). "Vibration analysis of a rectangular plate subjected to a thermal gradient." *Journal of Sound and Vibration*, 60(4), 481–497.

Ebrahimi, F., Barati, M. R., and Civalek, Ö. (2020). "Application of Chebyshev – Ritz method for static stability and vibration analysis of nonlocal microstructure-dependent nanostructures." *Engineering with Computers*, 36(3), 953–964.

Emami, A. A., and Alibeigloo, A. (2016). "Thermoelastic damping analysis of FG Mindlin microplates using strain gradient theory." *Journal of Thermal Stresses*, 39(12), 1499–1522.

Eshraghi, I., Dag, S., and Soltani, N. (2015). “Consideration of spatial variation of the length scale parameter in static and dynamic analyses of functionally graded annular and circular micro-plates.” *Composites Part B: Engineering*, 78, 338–348.

Eshraghi, I., Dag, S., and Soltani, N. (2016). “Bending and free vibrations of functionally graded annular and circular micro-plates under thermal loading.” *Composite Structures*, 137, 196–207.

Fang, J., Yin, B., Li, L., and Zhang, D. (2023). “Thermal buckling and vibration analysis of rotating porous FG GNPs-reinforced Reddy microplates.” *Aerospace Science and Technology*, 137, 108298.

Farahmand, H., Ahmadi, A. R., and Arabnejad, S. (2011). “Thermal buckling analysis of rectangular microplates using higher continuity p-version finite element method.” *Thin-Walled Structures*, 49(12), 1584–1591.

Farokhi, H., and Ghayesh, M. H. (2015). “Nonlinear dynamical behaviour of geometrically imperfect microplates based on modified couple stress theory.” *International Journal of Mechanical Sciences*, 90, 133–144.

Farokhi, H., Ghayesh, M. H., and Amabili, M. (2013). “Nonlinear dynamics of a geometrically imperfect microbeam based on the modified couple stress theory.” *International Journal of Engineering Science*, 68, 11–23.

Farzam, A., and Hassani, B. (2018). “Thermal and mechanical buckling analysis of FG carbon nanotube reinforced composite plates using modified couple stress theory and isogeometric approach.” *Composite Structures*, 206, 774–790.

Farzam, A., and Hassani, B. (2019). “Size-dependent analysis of FG microplates with temperature-dependent material properties using modified strain gradient theory and isogeometric approach.” *Composites Part B: Engineering*, 161, 150–168.

Fleck, N. A., and Hutchinson, J. W. (1997). “Strain gradient plasticity.” *Advances in Applied Mechanics*, 33(C), 295 –361.

Fleck, N. A., Muller, G. M., Ashby, M. F., and Hutchinson, J. W. (1994). “Strain gradient plasticity: Theory and experiment.” *Acta Metallurgica Et Materialia*, 42(2), 475–487.

Fu, Y., Du, H., and Zhang, S. (2003). “Functionally graded TiN/TiNi shape memory alloy films.” *Materials Letters*, 57(20), 2995–2999.

Gad-el-Hak, M. (Ed.). (2006). *MEMS Design and Fabrication*. CRC Press, Boca Raton.

Gao, H., Huang, Y., Nix, W. D., and Hutchinson, J. W. (1999). “Mechanism-based strain gradient plasticity— I. Theory.” *Journal of the Mechanics and Physics of Solids*, 47(6), 1239–1263.

Gao, X. L., Huang, J. X., and Reddy, J. N. (2013). “A non-classical third-order shear deformation plate model based on a modified couple stress theory.” *Acta Mechanica*, 224(11), 2699–2718.

Gennissen, P. T. J., Bartek, M., French, P. J., and Sarro, P. M. (1997). “Bipolar-compatible epitaxial poly for smart sensors: stress minimization and applications.” *Sensors and Actuators A: Physical*, 62(1–3), 636–645.

George, N., Jeyaraj, P., and Murigendrappa, S. M. (2016). “Buckling and Free Vibration of Nonuniformly Heated Functionally Graded Carbon Nanotube Reinforced Polymer Composite Plate.” *International Journal of Structural Stability and Dynamics*, 17(06), 1750064.

Ghayesh, M. H. (2019). “Mechanics of viscoelastic functionally graded microcantilevers.” *European Journal of Mechanics - A/Solids*, 73, 492–499.

Ghayesh, M. H., Amabili, M., and Farokhi, H. (2013a). “Three-dimensional nonlinear size-dependent behaviour of Timoshenko microbeams.” *International Journal of Engineering Science*, 71, 1–14.

Ghayesh, M. H., and Farokhi, H. (2016). “Coupled size-dependent behavior of shear deformable microplates." *Acta Mechanica*, 227(3), 757–775.

Ghayesh, M. H., Farokhi, H., and Amabili, M. (2013b). "Coupled nonlinear size-dependent behaviour of microbeams." *Applied Physics A*, 112(2), 329–338.

Ghayesh, M. H., Farokhi, H., and Amabili, M. (2013c). "Nonlinear dynamics of a microscale beam based on the modified couple stress theory." *Composites Part B: Engineering*, 50, 318–324.

Ghayesh, M. H., Farokhi, H., and Farajpour, A. (2020). "Viscoelastically coupled in-plane and transverse dynamics of imperfect microplates." *Thin-Walled Structures*, 150, 106117.

Gholami, R., and Ansari, R. (2016). "A most general strain gradient plate formulation for size-dependent geometrically nonlinear free vibration analysis of functionally graded shear deformable rectangular microplates." *Nonlinear Dynamics*, 84(4), 2403–2422.

Gholami, R., Ansari, R., Darvizeh, A., and Sahmani, S. (2014). "Axial Buckling and Dynamic Stability of Functionally Graded Microshells Based on the Modified Couple Stress Theory." *International Journal of Structural Stability and Dynamics*, 15(4), 1–24.

Gholami, Y., Ansari, R., and Gholami, R. (2020). "Three-dimensional nonlinear primary resonance of functionally graded rectangular small-scale plates based on strain gradeint elasticity theory." *Thin-Walled Structures*, 150, 106681.

Ghorbani, K., Rajabpour, A., and Ghadiri, M. (2021). "Determination of carbon nanotubes size-dependent parameters: molecular dynamics simulation and nonlocal strain gradient continuum shell model." *Mechanics Based Design of Structures and Machines*, 49(1), 103–120.

Hahm, G., Kahn, H., Phillips, S. M., and Heuer, A. H. (2000). "Fully Microfabricated Silicon Spring Biased Shape Memory Actuated Microvalve." *Technical Digest: Solid-State Sensor and Actuator Workshop*, Hilton Head, SC, 230–233.

Haque, M. A., and Saif, M. T. A. (2003). "Strain gradient effect in nanoscale thin films." *Acta Materialia*, 51(11), 3053–3061.

Hayashi, I., Sato, M., and Kuroda, M. (2011). "Strain hardening in bent copper foils." *Journal of the Mechanics and Physics of Solids*, 59(9), 1731–1751.

He, D., Yang, W., and Chen, W. (2017). "A size-dependent composite laminated skew plate model based on a new modified couple stress theory." *Acta Mechanica Solida Sinica*, 30(1), 75–86.

He, L., Lou, J., Zhang, E., Wang, Y., and Bai, Y. (2015). "A size-dependent four variable refined plate model for functionally graded microplates based on modified couple stress theory." *Composite Structures*, 130, 107–115.

Hosseini, M., Bahreman, M., and Jamalpoor, A. (2016). "Using the modified strain gradient theory to investigate the size-dependent biaxial buckling analysis of an orthotropic multi-microplate system." *Acta Mechanica 2016 227:6*, 227(6), 1621–1643.

Hung, P. T., Phung-Van, P., and Thai, C. H. (2022). "A refined isogeometric plate analysis of porous metal foam microplates using modified strain gradient theory." *Composite Structures*, 289, 115467.

Hutchinson, J. (2000). "Plasticity at the micro scale." *International Journal of Solids and Structures*, 37(1-2), 225–238.

Jha, D. K., Kant, T., and Singh, R. K. (2013). "A critical review of recent research on functionally graded plates." *Composite Structures*, 96, 833–849.

Jing, Z., and Zhan, J. (2008). "Fabrication and Gas-Sensing Properties of Porous ZnO Nanoplates." *Advanced Materials*, 20(23), 4547–4551.

Jomehzadeh, E., Noori, H. R., and Saidi, A. R. (2011). "The size-dependent vibration analysis of micro-plates based on a modified couple stress theory." *Physica E: Low-dimensional Systems and Nanostructures*, 43(4), 877–883.

Jung, W. Y., and Han, S. C. (2015). “Static and eigenvalue problems of Sigmoid Functionally Graded Materials (S-FGM) micro-scale plates using the modified couple stress theory.” *Applied Mathematical Modelling*, 39(12), 3506–3524.

Jung, W. Y., Han, S. C., and Park, W. T. (2014a). “A modified couple stress theory for buckling analysis of S-FGM nanoplates embedded in Pasternak elastic medium.” *Composites Part B: Engineering*, 60, 746–756.

Jung, W. Y., Park, W. T., and Han, S. C. (2014b). “Bending and vibration analysis of S-FGM microplates embedded in Pasternak elastic medium using the modified couple stress theory.” *International Journal of Mechanical Sciences*, 87, 150–162.

Karamanli, A., Aydogdu, M., and Vo, T. P. (2021). “A comprehensive study on the size-dependent analysis of strain gradient multi-directional functionally graded microplates via finite element model.” *Aerospace Science and Technology*, 111, 106550.

Karamanli, A., and Vo, T. P. (2020). “Size-dependent behaviour of functionally graded sandwich microbeams based on the modified strain gradient theory.” *Composite Structures*, 246, 112401.

Karamanli, A., and Vo, T. P. (2021). “A quasi-3D theory for functionally graded porous microbeams based on the modified strain gradient theory.” *Composite Structures*, 257, 113066.

Ke, L. L., Wang, Y. S., Yang, J., and Kitipornchai, S. (2012a). “Nonlinear free vibration of size-dependent functionally graded microbeams.” *International Journal of Engineering Science*, 50(1), 256–267.

Ke, L. L., Wang, Y. S., Yang, J., and Kitipornchai, S. (2012b). “Free vibration of size-dependent Mindlin microplates based on the modified couple stress theory.” *Journal of Sound and Vibration*, 331(1), 94–106.

Ke, L. L., Yang, J., Kitipornchai, S., and Bradford, M. A. (2012c). “Bending, buckling and vibration of size-dependent functionally graded annular microplates.” *Composite Structures*, 94(11), 3250–3257.

Ke, L. L., Yang, J., Kitipornchai, S., Bradford, M. A., and Wang, Y. S. (2013). “Axisymmetric nonlinear free vibration of size-dependent functionally graded annular microplates.” *Composites Part B: Engineering*, 53, 207–217.

Ke, L. L., Yang, J., Kitipornchai, S., and Wang, Y. S. (2014). “Axisymmetric postbuckling analysis of size-dependent functionally graded annular microplates using the physical neutral plane.” *International Journal of Engineering Science*, 81, 66–81.

Ke, L., and Wang, Y. (2011). “Size effect on dynamic stability of functionally graded microbeams based on a modified couple stress theory.” *Composite Structures*, 93(2), 342–350.

Khorshidi, K., Ghasemi, M., and Fallah, A. (2018). “Buckling analysis of functionally graded rectangular microplate in thermal environment based on exponential shear deformation theory using the modified couple stress theory.” *Journal of Solid and Fluid Mechanics*, 8(4), 179–196.

Kitazono, K., Sato, E., and Kuribayashi, K. (2004). “Novel manufacturing process of closed-cell aluminum foam by accumulative roll-bonding.” *Scripta Materialia*, 50(4), 495–498.

Ko, W. L. (2004). “Thermal buckling analysis of rectangular panels subjected to humped temperature profile heating.” https://ntrs.nasa.gov/citations/20040021345

Koiter, W. T. (1964). “Couple stresses in the theory of elasticity.” *I and II. Proc. K. Ned. Akad. Wet. (B) 67*, 17–44.

Kumar, R., Ramachandra, L. S., and Banerjee, B. (2017). “Semi-analytical approach for thermal buckling and postbuckling response of rectangular composite plates subjected to localized thermal heating.” *Acta Mechanica*, 228(5), 1767–1791.

Kumar, R., Singh, V., Dey, T., Bhunia, D., Patel, S. N., and Jain, V. (2022). “Nonlinear analysis of sandwich plate with FG porous core and RD-CNTCFRC face sheets under transverse patch loading." *Acta Mechanica*, 233, 4589–4614.

Kumar, V., Singh, S. J., Saran, V. H., and Harsha, S. P. (2021). "Vibration characteristics of porous FGM plate with variable thickness resting on Pasternak's foundation." *European Journal of Mechanics - A/Solids*, 85, 104124.

Lal, A., and Singh, B. N. (2010). "Effect of uncertain system properties on thermo-elastic stability of laminated composite plates under nonuniform temperature distribution." *International Journal of Applied Mechanics*, 02(02), 399–420.

Lam, D. C. C., Yang, F., Chong, A. C. M., Wang, J., and Tong, P. (2003). "Experiments and theory in strain gradient elasticity." *Journal of Mechanics and Physics of Solids*, 51, 1477–1508.

Lau, S. L., and Cheung, Y. K. (1981). "Amplitude Incremental Variational Principle for Nonlinear Vibration of Elastic Systems." *Journal of Applied Mechanics*, 48(4), 959–964.

Lee, B. H. K., Gong, L., and Wong, Y. S. (1997). "Analysis and computation of nonlinear dynamic response of a two-degree-of-freedom system and its application in aeroelasticity." *Journal of Fluids and Structures*, 11(3), 225–246.

Lee, Z., Ophus, C., Fischer, L. M., Nelson-Fitzpatrick, N., Westra, K. L., Evoy, S., Radmilovic, V., Dahmen, U., and Mitlin, D. (2006). "Metallic NEMS components fabricated from nanocomposite Al–Mo films." *Nanotechnology*, 17(12), 3063.

Lei, J., He, Y., Zhang, B., Liu, D., Shen, L., and Guo, S. (2015). "A size-dependent FG micro-plate model incorporating higher-order shear and normal deformation effects based on a modified couple stress theory." *International Journal of Mechanical Sciences*, 104, 8–23.

Li, C., Lai, S. K., and Yang, X. (2019a). "On the nano-structural dependence of nonlocal dynamics and its relationship to the upper limit of nonlocal scale parameter." *Applied Mathematical Modelling*, 69, 127–141.

Li, J., Narita, Y., and Wang, Z. (2015). "The effects of non-uniform temperature distribution and locally distributed anisotropic properties on thermal buckling of laminated panels." *Composite Structures*, 119, 610–619.

Li, Q., Wu, D., Gao, W., Tin-Loi, F., Liu, Z., and Cheng, J. (2019b). "Static bending and free vibration of organic solar cell resting on Winkler-Pasternak elastic foundation through the modified strain gradient theory." *European Journal of Mechanics - A/Solids*, 78, 103852.

Lin, L., Howe, R. T., and Pisano, A. P. (1998). "Microelectromechanical filters for signal processing." *Journal of Microelectromechanical Systems*, 7(3), 286–294.

Liu, C., Ke, L. L., Wang, Y. S., Yang, J., and Kitipornchai, S. (2014). "Buckling and post-buckling of size-dependent piezoelectric Timoshenko nanobeams subject to thermo-electro-mechanical loadings." *International Journal of Structural Stability and Dynamics*, 14(3), 1–22.

Liu, D., He, Y., Dunstan, D. J., Zhang, B., Gan, Z., Hu, P., and Ding, H. (2013). "Toward a further understanding of size effects in the torsion of thin metal wires: An experimental and theoretical assessment." *International Journal of Plasticity*, 41, 30–52.

Liu, H. R., Li, J. Z., Hou, D. X., Yin, R. R., and Jiang, J. S. (2015). "Analysis of dynamical characteristic of piecewise-nonlinear asymmetric hysteretic system based on incremental harmonic balance method." *Discrete Dynamics in Nature and Society*, 2015.

Liu, R. H., Vasile, M. J., and Beebe, D. J. (1999). "The Fabrication of nonplanar spin-on glass microstructures." *Journal of Microelectromechanical Systems*, 8(2), 146–151.

Liu, Y., Qin, Z., and Chu, F. (2021). "Nonlinear forced vibrations of functionally graded piezoelectric cylindrical shells under electric-thermo-mechanical loads." *International Journal of Mechanical Sciences*, 201, 106474.

Loghman, E., Bakhtiari-Nejad, F., Kamali E., A., Abbaszadeh, M., and Amabili, M. (2021).

"Nonlinear vibration of fractional viscoelastic micro-beams." *International Journal of Non-Linear Mechanics*, 137, 103811.

Lou, J., and He, L. (2015). "Closed-form solutions for nonlinear bending and free vibration of functionally graded microplates based on the modified couple stress theory." *Composite Structures*, 131, 810–820.

Lou, J., He, L., Du, J., and Wu, H. (2016). "Nonlinear analyses of functionally graded microplates based on a general four-variable refined plate model and the modified couple stress theory." *Composite Structures*, 152, 516–527.

Love, A. E. H. (1888). "The Small Free Vibrations and Deformation of a Thin Elastic Shell." *RSPTA*, The Royal Society, 179, 491–546.

Ma, H. M., Gao, X. L., and Reddy, J. N. (2011). "A non-classical Mindlin plate model based on a modified couple stress theory." *Acta Mechanica*, 220(1–4), 217–235.

Mahmud, A. S., Liu, Y., and Nam, T. H. (2008). "Gradient anneal of functionally graded NiTi." *Smart Materials and Structures*, 17(1), 015031.

Malekzadeh, P., Ghorbani Shenas, A., and Ziaee, S. (2018). "Thermal buckling of functionally graded triangular microplates." *Journal of the Brazilian Society of Mechanical Sciences and Engineering*, 40(9), 1–15.

Malikan, M. (2018). "Buckling Analysis of a Micro Composite Plate with Nano Coating Based on the Modified Couple Stress Theory." *Journal of Applied and Computational Mechanics*, 4(1), 1–15.

Mindlin, R.D., Tiersten, H. F. (1962). "Effects of couple-stresses in linear elasticity." *Archive for Rational Mechanics and Analysis*, 11, 415–448.

Mindlin, R. D. (1951). "Influence of Rotatory Inertia and Shear on Flexural Motions of Isotropic, Elastic Plates." *Journal of Applied Mechanics*, 18(1), 31–38.

Mindlin, R. D. (1964). "Micro-structure in linear elasticity." *Archive for Rational Mechanics and Analysis*, 16(1), 51–78.

Mindlin, R. D. (1965). "Second gradient of strain and surface-tension in linear elasticity." *International Journal of Solids and Structures*, 1(4), 417–438.

Mindlin, R. D., and Tiersten, H. F. (1962). "Effects of couple-stresses in linear elasticity." *Archive for Rational Mechanics and Analysis*, 11(1), 415–448.

Mindlin R.D. (1964). "Micro-structure in linear elasticity." *Archive for Rational Mechanics and Analysis*, 16, 51–78.

Mirjavadi, S. S., Afshari, B. M., Barati, M. R., and Hamouda, A. M. S. (2019). "Nonlinear free and forced vibrations of graphene nanoplatelet reinforced microbeams with geometrical imperfection." *Microsystem Technologies*, 25(8), 3137–3150.

Mirsalehi, M., Azhari, M., and Amoushahi, H. (2015). "Stability of thin FGM microplate subjected to mechanical and thermal loading based on the modified couple stress theory and spline finite strip method." *Aerospace Science and Technology*, 47, 356–366.

Mirsalehi, M., Azhari, M., and Amoushahi, H. (2017). "Buckling and free vibration of the FGM thin micro-plate based on the modified strain gradient theory and the spline finite strip method." *European Journal of Mechanics, A/Solids*, 61, 1–13.

Miyoshi, T., Itoh, M., Akiyama, S., and Kitahara, A. (1998). "Aluminum foam, 'ALPORAS': the production process, properties and applications." *Materials Research Society Symposium - Proceedings*, 521, 133–137.

Mohamad, A. A. (2005). "Combustion in porous media: fundamentals and applications." *Transport Phenomena in Porous Media III*, D. B. Ingham and I. Pop, eds., Elsevier, Oxford, 287–304.

Mohammadi, M., and Fooladi Mahani, M. (2015). "An analytical solution for buckling analysis of size-dependent rectangular micro-plates according to the modified strain gradient and couple stress theories." *Acta Mechanica*, 226(10), 3477–3493.

Morimoto, T., Tanigawa, Y., and Kawamura, R. (2006). “Thermal buckling of functionally graded rectangular plates subjected to partial heating.” *International Journal of Mechanical Sciences*, 48(9), 926–937.

Mukherjee, S., and Aluru, N. R. (2006). “Applications in micro- and nanoelectromechanical systems.” *Engineering Analysis with Boundary Elements*, 30, 909.

Mustafa, J., Alqaed, S., and Sharifpur, M. (2022). “Enhancing the energy and exergy performance of a photovoltaic thermal system with ∇-shape collector using porous metal foam.” *Journal of Cleaner Production*, 368, 133121.

Nakajima, H. (2007). “Fabrication, properties and application of porous metals with directional pores.” *Progress in Materials Science*, 52(7), 1091–1173.

Nateghi, A., and Salamat-talab, M. (2013). “Thermal effect on size dependent behavior of functionally graded microbeams based on modified couple stress theory.” *Composite Structures*, 96, 97–110.

Nguyen, C. T. C. (1995). “Micromechanical resonators for oscillators and filters.” *Proceedings of the IEEE Ultrasonics Symposium*, IEEE, 1, 489–499.

Nguyen, H. X., Atroshchenko, E., Ngo, T., Nguyen-Xuan, H., and Vo, T. P. (2019). “Vibration of cracked functionally graded microplates by the strain gradient theory and extended isogeometric analysis.” *Engineering Structures*, 187, 251–266.

Nix, W. D. (1989). “Mechanical properties of thin films.” *Metallurgical Transactions A*, 20(11), 2217–2245.

Noor, A. K. (1975). “Stability of Multilayered Composite Plates.” *Fibre Science and Technology*, 37, 81–89.

Park, S. K., and Gao, X. L. (2006). “Bernoulli–Euler beam model based on a modified couple stress theory.” *Journal of Micromechanics and Microengineering*, 16(11), 2355.

Pasternak, P. L. (1954). “New method of calculation for flexible substructures on two-parameter elastic foundation.” *Gasudarstvennoe Izdatelstoo. Literatury po Stroitelstvu I Architekture*, 1, 56.

Patkar, R. S., Vinchurkar, M., Ashwin, M., Adami, A., Giacomozzi, F., Lorenzelli, L., Baghini, M. S., and Ramgopal Rao, V. (2020). “Microcantilever Based Dual Mode Biosensor for Agricultural Applications.” *IEEE Sensors Journal*, 20(13), 6826–6832.

Peeters, E., Vergote, S., Puers, B., and Sansen, W. (1992). “A highly symmetrical capacitive micro-accelerometer with single degree-of-freedom response.” *Journal of Micromechanics and Microengineering*, 2(2), 104.

Piekarski, B., DeVoe, D., Dubey, M., Kaul, R., and Conrad, J. (2001). “Surface micromachined piezoelectric resonant beam filters.” *Sensors and Actuators, A: Physical*, 91(3), 313–320.

Prakash, T., Singha, M. K., and Ganapathi, M. (2008). “Thermal postbuckling analysis of FGM skew plates.” *Engineering Structures*, Elsevier, 30(1), 22–32.

Qiu, J., Sahmani, S., and Safaei, B. (2020). “On the NURBS-based isogeometric analysis for couple stress-based nonlinear instability of PFGM microplates.” *Mechanics Based Design of Structures and Machines*, 51(2), 816-840.

Raskin, J. P., Brown, A. R., Khuri-Yakub, B. T., and Rebeiz, G. M. (2000). “Novel parametric-effect MEMS amplifier.” *Journal of Microelectromechanical Systems*, 9(4), 528–537.

Reddy, J. (2006). *Theory and analysis of elastic plates and shells*. CRC Press.

Reddy, J. N. (2017). *Energy Principles and Variational Methods in Applied Mechanics.* John Wiley & Sons, Incorporated.

Reddy, J. N., and Berry, J. (2012). “Nonlinear theories of axisymmetric bending of functionally graded circular plates with modified couple stress.” *Composite Structures*, 94(12), 3664–3668.

Reddy, J. N., and Kim, J. (2012). “A nonlinear modified couple stress-based third-order theory of functionally graded plates." *Composite Structures*, 94(3), 1128–1143.

Reddy, J. N., and Liu., C. F. (1985). "A higher-order shear deformation theory of laminated elastic shells." *International Journal of Engineering Science*, 23(3), 319–330.

Reissner, E. (1945). "The Effect of Transverse Shear Deformation on the Bending of Elastic Plates." *Journal of Applied Mechanics*, 12(2), A69–A77.

Ren, Y., Huo, R., and Zhou, D. (2023). "Thermo-mechanical buckling analysis of non-uniformly heated rectangular plates with temperature-dependent material properties." *Thin-Walled Structures*, 186, 110653.

Rhoads, J. F., Shaw, S. W., Turner, K. L., and Baskaran, R. (2005). "Tunable Microelectromechanical Filters that Exploit Parametric Resonance." *Journal of Vibration and Acoustics*, 127(5), 423–430.

Roque, C. M. C., Ferreira, A. J. M., and Reddy, J. N. (2013). "Analysis of Mindlin micro plates with a modified couple stress theory and a meshless method." *Applied Mathematical Modelling*, 37(7), 4626–4633.

Rosler, R. S. (1977). "Low Pressure CVD Production Processes for Poly, Nitride, and Oxide." *Solid State Technology*, 20, 63–70.

Roylance, L. M., and Angell, J. B. (1979). "A Batch-Fabricated Silicon Accelerometer." *IEEE Transactions on Electron Devices*, 26(12), 1911–1917.

Rudd, R. E., and Broughton, J. Q. (1998). "Coarse-Grained molecular dynamics and the atomic limit of Finite Elements." *Physical Review B*, 58(10), R5893-R5896.

Saghir, S., and Younis, M. I. (2018). "An investigation of the mechanical behavior of initially curved microplates under electrostatic actuation." *Acta Mechanica 2018 229:7*, 229(7), 2909–2922.

Sahmani, S., and Ansari, R. (2013). "On the free vibration response of functionally graded higher-order shear deformable microplates based on the strain gradient elasticity theory." *Composite Structures*, 95, 430–442.

Sahmani, S., Ansari, R., Gholami, R., and Darvizeh, A. (2013). "Dynamic stability analysis of functionally graded higher-order shear deformable microshells based on the modified couple stress elasticity theory." *Composites Part B*, 51, 44–53.

Salehipour, H., and Shahsavar, A. (2018). "A three dimensional elasticity model for free vibration analysis of functionally graded micro/nano plates: Modified strain gradient theory." *Composite Structures*, 206, 415–424.

Seidel, H., Riedel, H., Kolbeck, R., Mück, G., Kupke, W., and Königer, M. (1990). "Capacitive silicon accelerometer with highly symmetrical design." *Sensors and Actuators A: Physical*, 21(1–3), 312–315.

Severi, S., Heck, J., Chou, T. K. A., Belov, N., Park, J. S., Harrar, D., Jain, A., Van Hoof, R., Du Bois, B., De Coster, J., Pedreira, O. V., Willegems, M., Vaes, J., Jamieson, G., Haspeslagh, L., Adams, D., Rao, V., Decoutere, S., and Witvrouw, A. (2009). "CMOS-integrated poly-sige cantilevers with read/write system for probe storage device." *TRANSDUCERS 2009 - 15th International Conference on Solid-State Sensors, Actuators and Microsystems*, 2409–2412.

Shenas, A. G., and Malekzadeh, P. (2016). "Free vibration of functionally graded quadrilateral microplates in thermal environment." *Thin-Walled Structures*, 106, 294–315.

Shenas, A. G., Ziaee, S., and Malekzadeh, P. (2022). "Nonlinear free vibration of rotating FG trapezoidal microplates in thermal environment." *Thin-Walled Structures*, 170, 108614.

Sheng, G. G., and Wang, X. (2019). "Nonlinear forced vibration of size-dependent functionally graded microbeams with damping effects." *Applied Mathematical Modelling*, 71, 421–437.

Sheykhi, M., Eskandari, A., Ghafari, D., Ahmadi Arpanahi, R., Mohammadi, B., and Hosseini Hashemi, S. (2023). "Investigation of fluid viscosity and density on vibration of nano beam submerged in fluid considering nonlocal elasticity theory." *Alexandria Engineering Journal*, 65, 607–614.

Shimpi, R. P. (2002). "Refined plate theory and its variants." *AIAA Journal*, American Inst. Aeronautics and Astronautics Inc., 40(1), 137–146.

Şimşek, M. (2014). "Nonlinear static and free vibration analysis of microbeams based on the nonlinear elastic foundation using modified couple stress theory and He's variational method." *Composite Structures*, 112(1), 264–272.

Şimşek, M., and Aydın, M. (2017). "Size-dependent forced vibration of an imperfect functionally graded (FG) microplate with porosities subjected to a moving load using the modified couple stress theory." *Composite Structures*, 160, 408–421.

Şimşek, M., Aydın, M., Yurtcu, H. H., and Reddy, J. N. (2015). "Size-dependent vibration of a microplate under the action of a moving load based on the modified couple stress theory." *Acta Mechanica 2015 226:11*, 226(11), 3807–3822.

Sobhy, M. (2020). "Size-Dependent Hygro-Thermal Buckling of Porous FGM Sandwich Microplates and Microbeams Using a Novel Four-Variable Shear Deformation Theory." *International Journal of Applied Mechanics*, 12(2), 2050017.

Sobhy, M., and Zenkour, A. M. (2019). "A comprehensive study on the size-dependent hygrothermal analysis of exponentially graded microplates on elastic foundations." *Mechanics of Advanced Materials and Structures*, 27(10), 816–830.

Soldatos, K. P. (1991). "A refined laminated plate and shell theory with applications." *Journal of Sound and Vibration.*, 144(1), 109–129.

Soldatos, K. P. (1992). "A transverse shear deformation theory for homogeneous monoclinic plates." *Acta Mechanica*, 94(3–4), 195–220.

Song, J., and Wei, Y. (2020). "A Method to Determine Material Length Scale Parameters in Elastic Strain Gradient Theory." *Journal of Applied Mechanics, Transactions ASME*, 87(3), 1–7.

Srinivas, S., and Rao, A. K. (1970). "Bending, vibration and buckling of simply supported thick orthotropic rectangular plates and laminates." *International Journal of Solids and Structures*, 6(11), 1463–1481.

Stelmashenko, N. A., Walls, M. G., Brown, L. M., and Milman, Y. V. (1993). "Microindentations on W and Mo oriented single crystals: An STM study." *Acta Metallurgica et Materialia*, 41(10), 2855–2865.

Stolarski, T., Nakasone, Y., and Yoshimoto, S. (2018). "Fundamentals of the finite element method." *Engineering Analysis with ANSYS Software* (Second Edition), 1–35. DOI:10.1016/B978-0-08-102164-4.00001-7

Stölken, J. S., and Evans, A. G. (1998). "A microbend test method for measuring the plasticity length scale." *Acta Materialia*, 46(14), 5109–5115.

Subbaraj, K., and Dokainish, M. A. (1989). "A survey of direct time-integration methods in computational structural dynamics—II. Implicit methods." *Computers & Structures*, 32(6), 1387–1401.

Swaminathan, K., Hirannaiah, S., and Rajanna, T. (2022). "Vibration and stability characteristics of functionally graded sandwich plates with/without porosity subjected to localized edge loadings." *Mechanics Based Design of Structures and Machines*, 51(11), 6254-6292.

Swaminathan, K., Naveenkumar, D. T., Zenkour, A. M., and Carrera, E. (2015). "Stress, vibration and buckling analyses of FGM plates—A state-of-the-art review." *Composite Structures*, 120, 10–31.

Taati, E. (2016). "Analytical solutions for the size dependent buckling and postbuckling behavior of functionally graded micro-plates." *International Journal of Engineering*

Science, 100, 45–60.

Thai, C. H., Ferreira, A. J. M., and Phung-van, P. (2020a). “Free vibration analysis of functionally graded anisotropic microplates using modified strain gradient theory.” *Engineering Analysis with Boundary Elements*, 117, 284–298.

Thai, C. H., Ferreira, A. J. M., and Phung-Van, P. (2019). “Size dependent free vibration analysis of multilayer functionally graded GPLRC microplates based on modified strain gradient theory.” *Composites Part B: Engineering*, 169, 174–188.

Thai, C. H., Ferreira, A. J. M., and Phung-Van, P. (2020b). “Free vibration analysis of functionally graded anisotropic microplates using modified strain gradient theory.” *Engineering Analysis with Boundary Elements*, 117, 284–298.

Thai, C. H., Ferreira, A. J. M., Rabczuk, T., and Nguyen-Xuan, H. (2018). “Size-dependent analysis of FG-CNTRC microplates based on modified strain gradient elasticity theory.” *European Journal of Mechanics - A/Solids*, 72, 521–538.

Thai, H. T., and Choi, D. H. (2012). “A refined shear deformation theory for free vibration of functionally graded plates on elastic foundation.” *Composites Part B: Engineering*, 43(5), 2335–2347.

Thai, H. T., and Choi, D. H. (2013). “Size-dependent functionally graded Kirchhoff and Mindlin plate models based on a modified couple stress theory.” *Composite Structures*, 95, 142–153.

Thai, H. T., and Kim, S. E. (2013). “A size-dependent functionally graded Reddy plate model based on a modified couple stress theory.” *Composites Part B: Engineering*, 45(1), 1636–1645.

Thai, H. T., and Kim, S. E. (2015). “A review of theories for the modeling and analysis of functionally graded plates and shells.” *Composite Structures*, 128, 70–86.

Thai, H. T., and Vo, T. P. (2013). “A size-dependent functionally graded sinusoidal plate model based on a modified couple stress theory.” *Composite Structures*, 96, 376–383.

Thai, S., Thai, H. T., Vo, T. P., and Nguyen-Xuan, H. (2017a). “Nonlinear static and transient isogeometric analysis of functionally graded microplates based on the modified strain gradient theory.” *Engineering Structures*, 153, 598–612.

Thai, S., Thai, H. T., Vo, T. P., and Patel, V. I. (2017b). “Size-dependant behaviour of functionally graded microplates based on the modified strain gradient elasticity theory and isogeometric analysis.” *Computers & Structures*, 190, 219–241.

Thai, S., Thai, H. T., Vo, T. P., and Reddy, J. N. (2017c). “Post-buckling of functionally graded microplates under mechanical and thermal loads using isogeomertic analysis.” *Engineering Structures*, 150, 905–917.

Thorby, D. (2008). *Structural Dynamics and Vibration in Practice, An engineering handbook.* ISBN: 978-0-7506-8002-8

Tien, D. M., Thom, D. Van, Minh, P. Van, Tho, N. C., Doan, T. N., and Mai, D. N. (2023). “The application of the nonlocal theory and various shear strain theories for bending and free vibration analysis of organic nanoplates.” *Mechanics Based Design of Structures and Machines*, DOI: 10.1080/15397734.2023.2186893.

Timoshenko, S. P. (1953). *History of Strength of Materials*. McGraw-Hill, New York. ISBN:9780486611877

Timoshin, A., Kazemi, A., Beni, M. H., Jam, J. E., and Pham, B. (2021). “Nonlinear strain gradient forced vibration analysis of shear deformable microplates via hermitian finite elements.” *Thin-Walled Structures*, 161, 107515.

Torabi, J., Niiranen, J., and Ansari, R. (2021). “Nonlinear finite element analysis within strain gradient elasticity: Reissner-Mindlin plate theory versus three-dimensional theory.” *European Journal of Mechanics - A/Solids*, 87, 104221.

Tortonese, M. (1997). “Cantilevers and tips for atomic force microscopy.” *IEEE engineering* *in medicine and biology magazine : the quarterly magazine of the Engineering in Medicine & Biology Society*, 16(2), 28–33.

Toupin, R. A. (1962). “Elastic materials with couple-stresses.” *Archive for Rational Mechanics and Analysis*, 11(1), 385–414.

Toupin, R. A., and Gazis, D. C. (1965). “Surface Effects And Initial Stress in Continuum and Lattice Models of Elastic Crystals.” R. F. B. T.-L. D. WALLIS, ed., 597–605.

Touratier, M. (1991). “An efficient standard plate theory.” *International Journal of Engineering Science*, 29(8), 901–916.

Tran, V. T., Nguyen, T. K., Nguyen, P. T. T., and Vo, T. P. (2022). “Stochastic vibration and buckling analysis of functionally graded microplates with a unified higher-order shear deformation theory.” *Thin-Walled Structures*, 177, 109473.

Trinh, L. C., Vo, T. P., Thai, H. T., and Mantari, J. L. (2017). “Size-dependent behaviour of functionally graded sandwich microplates under mechanical and thermal loads.” *Composites Part B: Engineering*, 124, 218–241.

Tsiatas, G. C. (2009). “A new Kirchhoff plate model based on a modified couple stress theory.” *International Journal of Solids and Structures*, 46(13), 2757–2764.

Tsiatas, G. C., and Yiotis, A. J. (2015). “Size effect on the static , dynamic and buckling analysis of orthotropic Kirchhoff-type skew micro-plates based on a modified couple stress theory : comparison with the nonlocal elasticity theory.” *Acta Mechanica,* 226, 1267–1281.

Turner, K. L., and Zhang, W. (2001). “Design and analysis of a dynamic MEM chemical sensor.” *Proceedings of the American Control Conference*, Institute of Electrical and Electronics Engineers Inc., 2, 1214–1218.

Vashist, S. K., and Holthofer, H. (2010). “Microcantilevers for Sensing Applications.” *Measurement and Control*, 43(3), 84–88.

Voyiadjis, G., and Almasri, A. (2009). “Variable Material Length Scale Associated with Nanoindentation Experiments.” *Journal of Engineering Mechanics*, 135(3), 139–148.

Wang, B., Huang, S., Zhao, J., and Zhou, S. (2016). “Reconsiderations on boundary conditions of Kirchhoff micro-plate model based on a strain gradient elasticity theory.” *Applied Mathematical Modelling*, 40(15–16), 7303–7317.

Wang, B., Zhou, S., Zhao, J., and Chen, X. (2011). “A size-dependent Kirchhoff micro-plate model based on strain gradient elasticity theory.” *European Journal of Mechanics - A/Solids*, 30(4), 517–524.

Wang, Y. G., Lin, W. H., and Liu, N. (2013a). “Nonlinear free vibration of a microscale beam based on modified couple stress theory.” *Physica E: Low-Dimensional Systems and Nanostructures*, 47, 80–85.

Wang, Y. G., Lin, W. H., and Liu, N. (2013b). “Large amplitude free vibration of size-dependent circular microplates based on the modified couple stress theory.” *International Journal of Mechanical Sciences*, 71, 51–57.

Wang, Y. G., Lin, W. H., and Liu, N. (2015a). “Nonlinear bending and post-buckling of extensible microscale beams based on modified couple stress theory.” *Applied Mathematical Modelling*, 39(1), 117–127.

Wang, Y. G., Lin, W. H., and Zhou, C. L. (2014). “Nonlinear bending of size-dependent circular microplates based on the modified couple stress theory.” *Archive of Applied Mechanics*, 84(3), 391–400.

Wang, Y. G., Lin, W. H., Zhou, C. L., and Liu, R. X. (2015b). “Thermal postbuckling and free vibration of extensible microscale beams based on modified couple stress theory.” *Journal of Mechanics*, 31(1), 37–46.

Warburton, G. B. (1954). “The Vibration of Rectangular Plates.” *Proceedings of the Institution* *of Mechanical Engineers*, 168(1), 371–384.

Winkler, E. (1867). "Die Lehre von Elastizitat und Festigkeit (The theory of elasticity and stiffness)." *H. Domenicus. Prague*.

Witvrouw, A., and Mehta, A. (2005). "The Use of Functionally Graded Poly-SiGe Layers for MEMS Applications." *Materials Science Forum*, 492–493, 255–260.

Wu, C., Lou, J., He, L., Du, J., and Wu, H. (2018). "Buckling and Post-Buckling of Symmetric Functionally Graded Microplate Lying on Nonlinear Elastic Foundation Based on Modified Couple Stress Theory." *International Journal of Structural Stability and Dynamics*, 18(9), 1850110.

Wu, J., Hong, L., and Jiang, J. (2022). "A robust and efficient stability analysis of periodic solutions based on harmonic balance method and Floquet-Hill formulation." *Mechanical Systems and Signal Processing*, 173, 109057.

Xu, L. L., Kang, C. C., Zheng, Y. F., and Chen, C. P. (2021). "Analysis of nonlinear vibration of magneto-electro-elastic plate on elastic foundation based on high-order shear deformation." *Composite Structures*, 271, 114149.

Yadav, A., Amabili, M., Panda, S. K., Dey, T., and Kumar, R. (2021). "Forced nonlinear vibrations of circular cylindrical sandwich shells with cellular core using higher-order shear and thickness deformation theory." *Journal of Sound and Vibration*, 510, 116283.

Yang, F., Chong, A. C. M., Lam, D. C. C., and Tong, P. (2002). "Couple stress based strain gradient theory for elasticity." *International Journal of Solids and Structures*, 39(10), 2731–2743.

Yang, Q., and Lim, C. W. (2012). "Thermal effects on buckling of shear deformable nanocolumns with von Kármán nonlinearity based on nonlocal stress theory." *Nonlinear Analysis: Real World Applications*, 13(2), 905–922.

Yazdi, N., Ayazi, F., and Najafi, K. (1998). "Micromachined inertial sensors." *Proceedings of the IEEE*, Institute of Electrical and Electronics Engineers Inc., 86(8), 1640–1658.

Yazdi, N., and Najafi, K. (1997). "All-silicon single-wafer fabrication technology for precision microaccelerometers." *International Conference on Solid-State Sensors and Actuators, Proceedings*, IEEE, 2, 1181–1184.

Yin, L., Qian, Q., Wang, L., and Xia, W. (2010). "Vibration analysis of microscale plates based on modified couple stress theory." *Acta Mechanica Solida Sinica*, 23(5), 386–393.

Zandekarimi, S., Asadi, B., and Rahaeifard, M. (2017). "Size dependent thermal buckling and postbuckling of functionally graded circular microplates based on modified couple stress theory." *Journal of Thermal Stresses*, 41(1), 1–16.

Zhang, B., He, Y., Liu, D., Lei, J., Shen, L., and Wang, L. (2015a). "A size-dependent third-order shear deformable plate model incorporating strain gradient effects for mechanical analysis of functionally graded circular/annular microplates." *Composites Part B: Engineering*, 79, 553–580.

Zhang, B., He, Y., Liu, D., Shen, L., and Lei, J. (2015b). "An efficient size-dependent plate theory for bending, buckling and free vibration analyses of functionally graded microplates resting on elastic foundation." *Applied Mathematical Modelling*, 39(13), 3814–3845.

Zhang, B., Li, H., Kong, L., Shen, H., and Zhang, X. (2020). "Size-dependent static and dynamic analysis of Reddy-type micro-beams by strain gradient differential quadrature finite element method." *Thin-Walled Structures*, 148, 106496.

Zhang, W., Baskaran, R., and Turner, K. L. (2002). "Effect of cubic nonlinearity on auto-parametrically amplified resonant MEMS mass sensor." *Sensors and Actuators A: Physical*, 102(1–2), 139–150.

Zhang, X., Qian, Y., Zhu, Y., and Tang, K. (2014). "Synthesis of Mn2O3 nanomaterials with controllable porosity and thickness for enhanced lithium-ion batteries performance."

Nanoscale, The Royal Society of Chemistry, 6(3), 1725–1731.

Zhou, S. S., and Gao, X. L. (2014). "A nonclassical model for circular mindlin plates based on a modified couple stress theory." *Journal of Applied Mechanics, Transactions ASME*, 81(5).

Zuo, D., Sahmani, S., Safaei, B., and Ma, G. (2021). "Influence of couple stress size dependency in thermal instability of porous functionally graded composite microplates having different central cutouts." *Waves in Random and Complex Media*. DOI: 10.1080/17455030.2021.2003474

Biography of Dr Rajesh Kumar

Dr. Rajesh Kumar is currently working as an Assistant Professor in the Department of Civil Engineering, Birla Institute of Technology and Science (BITS), Pilani (Rajasthan). He received his B. Tech (Civil) in 2006 from National Institute of Technology (NIT) Jamshedpur, M. Tech in Structural Engineering from Indian Institute of Technology (IIT) Kharagpur in 2009, and Ph.D. in Structural Engineering from IIT Kharagpur in 2017. His current areas of research are Nonlinear Solid Mechanics, Micro-mechanics, Computational Mechanics, Nonlinear Dynamics and Chaos, Nonlinear Vibration, Stability, and Dynamic Instability. He has 6 years of teaching and research experience. Also, he has 3.5 years of industrial experience. He has been awarded the best employee award in a group by the Indian Register of Shipping, Mumbai in November 2011 for a research project "ICAS fatigue harmonized common structural rule". Besides, he has 45 peer-reviewed international journal papers and 1 national journal paper, 8 international conferences, and 10 book chapters.

Biography of Mr Varun Jain

Mr. Varun Jain hails from Agra, a district in Uttar Pradesh, India. He earned his Bachelor of Technology (B.Tech.) in Civil Engineering from Vellore Institute of Technology, Vellore, in 2017. Building on this foundation, he went on to pursue his Master of Engineering (M.E.) in Civil Engineering, specializing in Infrastructure Engineering and Management, at Birla Institute of Technology and Science, Pilani, Rajasthan, India, which he successfully completed in 2019.

His professional journey began with a role as a structural designer for bridges at Delhi Integrated Multimodal Transit Systems (DIMTS) Ltd. Following this, Mr. Jain embarked on a path of academic exploration, enrolling in the doctoral program (Ph.D.) within the Department of Civil Engineering at BITS Pilani, Pilani Campus, Rajasthan, India. His research endeavours were guided by the expertise of Dr. Rajesh Kumar, Assistant Professor at BITS Pilani.

During his Ph.D. journey, Mr. Jain and Dr. Rajesh Kumar collaborated to publish four research papers in esteemed international journals, alongside presenting one significant contribution in the form of a conference paper. This academic and professional journey exemplifies his dedication and passion for making significant strides in the realm of his chosen discipline.